國立臺灣大學工學院工程科學及海洋工程學系
碩士論文

Department of Engineering Science and Ocean Engineering
College of Engineering
National Taiwan University
Master's Thesis

浮式風機跡流行為之數值研究

Numerical Study on Wake Behavior of a Floating Wind Turbine

蕭琮祐

Tsung-Yu Hsiao

指導教授：趙修武 博士

Advisor: Dr.-Ing. Shiu-Wu Chau

中華民國 114 年 7 月

July, 2025

doi:10.6342/NTU202503576

Abstract

This study investigates the wake behavior of the Vestas V80 floating offshore wind turbine (FOWT) using numerical methods. The simulations were conducted with STAR-CCM+ by solving the three-dimensional unsteady continuity and momentum equations, coupled with the SST $k-\omega$ turbulence model. An actuator disk model was employed to model the rotor thrust where the flow field around the wind turbine under six degrees of freedom platform motions are considered. Both fixed-bottom and floating turbine configurations are examined under the wind speeds of 9 m/s, 15 m/s, and 21 m/s. The motion modes considered include translational motions ranging from 0.5 m to 2.5 m and rotational motions from 1° to 5°, with motion periods between 40 and 50 s. Based on the difference in normalized time-average velocity ($\Delta\overline{U}^*_{avg}$) in the wake region, pitch and yaw motions were found to induce strong downstream disturbances, enhancing wake mixing and wind speed recovery, whereas its standard deviation ($\Delta\bar{\sigma}^*_{avg}$) suggests that sway and roll motions should be minimized to mitigate fatigue damage possibly arising in downstream turbines. At high wind speeds, the increased flow inertia and stability significantly suppress the wake effects induced by platform motions. Among the parameters examined, wind speed and motion amplitude were identified as the primary factors influencing the downstream wake, whereas the effect of motion period was relatively minor. Furthermore, the motions of the FOWT were found to enhance wake recovery, thereby potentially enabling reduced inter-turbine spacing and improving power generation efficiency per unit area. Although platform motions may decrease the power output of the turbine itself, they can enhance the performance of downstream turbines. Finally, the correlation among motion amplitude, downstream distance, and $\Delta\overline{U}^*_{avg}$ is described by a quadratic polynomial.

Keywords: Wind Turbine Wake, Floating Offshore Wind Turbine, Actuator Disk Model, 6DOF Motion, Wake Recovery, Power Output, Quadratic Polynomial Fitting

doi:10.6342/NTU202503576

摘要

本研究以數值方法探討 Vestas V80 浮式風機之跡流行為，採用 STAR-CCM+ 軟體求解三維暫態連續方程與動量方程，並結合 SST $k-\omega$ 紊流模型與致動盤模型，模擬風機進行六自由度運動時轉子周圍及下游的流場特性。研究中比較固定式與浮式風機，模擬條件涵蓋風速 9 m/s、15 m/s 及 21 m/s，平移運動振幅為 0.5 至 2.5 公尺，旋轉運動振幅為 1° 至 5°，運動週期則介於 40 至 50 秒。分析結果顯示，根據無因次化時間平均風速差異，縱搖與平擺運動會在距離風機下游引發強烈擾動，促進跡流混合並加速風速恢復；而其標準差分析則顯示，橫搖與橫移運動應予以抑制，以減輕下游風機的疲勞損傷。在高風速條件下，流場慣性與穩定性顯著削弱平台運動對跡流的影響。在所分析的各項參數中，風速與運動振幅為影響下游跡流行為的主要因素，而運動週期的影響相對較小。此外，浮式風機的六自由度運動有助於提高跡流的風速恢復效果，進而縮短風機間距、提升單位面積發電效率。雖然平台運動可能降低自身風機的功率輸出，但能改善下游風機的發電性能。浮式風機的運動振幅、下游距離與標準化時間平均風速差異三者之間的關係可以透過二次多項式加以描述。

關鍵字：風機跡流、浮式風機、制動盤模型、六自由度運動、跡流恢復、發電功率、二次多項式擬合

doi:10.6342/NTU202503576

Content

doi:10.6342/NTU202503576

doi:10.6342/NTU202503576

Nomenclature

Latin Symbols

A_r	Rotor area	[m^2]
a_1	Model coefficient	[-]
b	Empirical blending constant	[-]
C	Empirical blending constant	[-]
C_G	Normalized turbulence generation	[-]
C_P	Power coefficient	[-]
C_R	Total resistance coefficient	[-]
C_0	Constant coefficient of the quadratic polynomial model	[-]
C_1	Linear coefficient of motion amplitude in the quadratic polynomial model	[-]
C_2	Linear coefficient of downstream distance in the quadratic polynomial model	[-]
C_3	Quadratic coefficient of motion amplitude in the quadratic polynomial model	[-]
C_4	Quadratic coefficient of downstream distance in the quadratic polynomial model	[-]
C_5	Interaction coefficient between motion amplitude and downstream distance in the quadratic polynomial model	[-]
$CD_{k\omega}$	Cross diffusion coefficient	[-]
D	Rotor diameter	[m]
dx	Dimensionless grid size	[-]
d	Shortest distance to the wall	[m]
E	Ideal error	[-]
E'	Wall function offset	[-]
E^d	Temporal discretization error	[-]
E_d	Spatial discretization error	[-]
F_1	Blending function	[-]
F_2	Blending function	[-]
f_a	Axial force	[N]
f_i	Body force term	[N]
f_t	Tangential force	[N]
H_{hub}	Hub height	[m]
I	Turbulence intensity	[-]
k	Turbulence kinetic energy	[m^2/s^2]
k_0	Ambient turbulence kinetic energy	[m^2/s^2]
k_1	Wind turbine correlated coefficient	[-]
k_2	Wind turbine correlated coefficient	[-]

doi:10.6342/NTU202503576

k_3	Wind turbine correlated coefficient	[-]
N_n	Grid number of *n*th grid	[-]
N_T	Number of periods	[-]
$\mathbf{n}$	Normal vector	[-]
P	Power generated by wind turbine	[W]
P^*	Dimensionless power	[-]
P_k	Turbulence production	[m^2/s^3]
P_1	First turbine power	[W]
p	Pressure	[Pa]
R	Rotor Radius	[m]
R^2	Determination coefficient	[-]
$\mathbf{S}$	Modulus of the mean strain rate tensor	[-]
S_{ij}	Mean strain rate tensor	[1/s]
T_t	Turbulent time scale	[-]
T_P	Motion period	[s]
t	Time	[s]
$\mathbf{U}$	Velocity vector	[m/s]
U^*	Normalized average axial velocity of rotor surface	[m/s]
U_{avg}	Axial-averaged wind speed	[m/s]
U_{hub}	Velocity at hub height	[m/s]
U_{in}	Reference wind velocity	[m/s]
U_{avg}^t	Instantaneous axial-averaged velocity	[m/s]
$\overline{U}_{avg}^*$	Normalized time-averaged velocity	[m/s]
$\overline{U}_{avg}^s$	Time-averaged velocity within one period	[m/s]
$\overline{U}_{avg}^0$	Time-averaged velocity of fixed turbine	[m/s]
U_x	Axial velocity in *x* direction	[m/s]
u	Velocity component in the *x* direction	[m/s]
u^+	Dimensionless quantity	[-]
u_*	Dimensionless friction velocity	[m/s]
u_i	Mean velocity component in *i* direction	[m/s]
$\mathbf{u_p}$	Velocity vector at symmetry boundary	[-]
v	Velocity component in the *y* direction	[m/s]
w	Velocity component in the *z* direction	[m/s]
x	Downstream distance measured from the turbine	[m]
x_i	Coordinate in the *i* direction	[m]
x_j	Coordinate in the *j* direction	[m]
y	Distance from the wall	[m]
y^+	Dimensionless wall distance	[-]
y_m^+	Empirical blending parameter	[-]
z	height	[m]

doi:10.6342/NTU202503576

Greek Symbols

α^*	Model coefficient	[-]
α_1^*	Model coefficient	[-]
α_2^*	Model coefficient	[-]
β	Model coefficient	[-]
β^*	Model coefficient	[-]
β_1	Model coefficient	[-]
β_2	Model coefficient	[-]
γ	Model coefficient	[-]
γ_1	Model coefficient	[-]
γ_2	Model coefficient	[-]
Δt	Time step size	[s]
$\Delta \bar{U}_{avg}^*$	Difference in normalized time-average velocity	[-]
$\Delta \bar{U}_{avg}^F$	Predicted difference in normalized time-averaged velocity	[-]
$\Delta \bar{\sigma}_{avg}^*$	Difference in normalized time-averaged velocity standard deviation	[-]
δ_{ij}	Kronecker delta	[-]
ζ_T	Amplitude of platform motion in translation	[m]
ζ_R	Amplitude of platform motion in rotation	[°]
θ_w	Wind direction	[°]
κ	Von Kármán constant	[-]
λ	Tip speed ratio	[-]
μ	Dynamic viscosity of the fluid	[kg/(m·s)]
μ_t	Turbulent eddy viscosity	[kg/(m·s)]
ν	Kinematic viscosity	[m^2/s]
ρ	Fluid density	[kg/m^3]
σ	Velocity standard deviation of rotor surface	[m/s]
σ_{avg}^t	Instantaneous axial-averaged velocity standard deviation	[-]
$\bar{\sigma}_{avg}^*$	Normalized time-averaged velocity standard deviation	[-]
$\bar{\sigma}_{avg}^S$	Time-averaged velocity standard deviation within one period	[-]
$\bar{\sigma}_{avg}^0$	Time-averaged velocity standard deviation of fixed turbine	[-]
σ_k	Model coefficient	[-]
σ_{k1}	Model coefficient	[-]
σ_{k2}	Model coefficient	[-]
σ_ω	Model coefficient	[-]
$\sigma_{\omega 1}$	Model coefficient	[-]
$\sigma_{\omega 2}$	Model coefficient	[-]
τ_w	Wall shear stress	[Pa]
Φ^∞	Temporal ideal solution	[-]
Φ_∞	Spatial ideal solution	[-]

doi:10.6342/NTU202503576

Φ_n^s	Spatial numerical solution	[-]
Φ_n^t	Temporal numerical solution	[-]
ω	Turbulent dissipation rate	[1/s]
ω_r	Angular velocity of the rotor rotation	[rpm]
ω_0	Ambient turbulence dissipation rate	[1/s]

doi:10.6342/NTU202503576

List of Figures

doi:10.6342/NTU202503576

doi:10.6342/NTU202503576

doi:10.6342/NTU202503576

List of Tables

doi:10.6342/NTU202503576

1 Introduction

1.1 Motivation

In light of the escalating and increasingly urgent threat that climate change poses to the global environment, more than 130 countries have committed to achieving net-zero emissions by 2050. In alignment with this global initiative, the Taiwanese government has pledged to reach the same target by 2050 through a multi-faceted strategy that includes expanding renewable energy infrastructure, increasing the proportion of domestically produced energy, and prioritizing wind power as a central component of the national energy transition process.

To fulfill this commitment, Taiwan has set an ambitious target of installing 20.7 GW of offshore wind capacity by 2035. Beginning in 2028, offshore wind development will expand into waters deeper than 60 meters, making the deployment of floating offshore wind turbines an urgent and essential strategic direction. According to the Global Wind Energy Council (GWEC), over 10.8 GW of new offshore wind capacity was installed globally in 2023, bringing the cumulative total to more than 75.2 GW, a 24% increase compared to the previous year. By the end of 2023, 41 GW of offshore wind capacity were in operation across Asia, including 692 MW in Taiwan. [1] Although offshore wind power currently lags behind onshore wind in terms of installed capacity, its growth rate is significantly faster, underscoring its emergence as a strategic priority for many nations. Offshore wind farms offer compelling advantages in terms of energy yield and geographic flexibility, particularly in regions characterized by strong and consistent marine wind resources.

doi:10.6342/NTU202503576

1. Introduction

To capitalize on the vast wind energy potential of the Taiwan Strait, Taiwan has actively advanced the deployment of offshore wind farms in waters exceeding 50 meters in depth, as illustrated in Figure 1. [2] However, the installation of fixed-bottom wind turbines in such deep-sea environments presents significant technical and economic challenges. In response, floating offshore wind turbines have emerged as a technically feasible and cost-effective alternative, allowing deployment at greater depths and in farther offshore region. Unlike fixed-bottom structures, floating turbines experience six degrees of freedom (6DOF) motions driven by the combined effects of wind, waves, and ocean currents. These coupled motions profoundly affect both the power generation performance and the wake dynamics of turbines. In the marine environment, the 6DOF motions not only affect the inflow conditions at the rotor but also disturb the wake flow structure downstream. Compared to stationary fixed-bottom turbines, the dynamic behavior of floating turbines tends to increase turbulence intensity and shorten the wake recovery distance, thereby intensifying wake interactions within the wind farm.

In offshore wind farms, the wake flow generated by a floating turbine not only affects its own energy output but also alters the inflow velocity conditions encountered by downstream turbines, thereby influencing their wake behavior and power performance. Consequently, it is necessary to develop a numerical framework that couples the turbine's motion responses under metocean conditions with the evolution of wake characteristics. This study presents a coupled model that integrates viscous-effect motion response analysis with three-dimensional CFD-based wake prediction for floating offshore wind turbines, enabling the concurrent simulation of turbine dynamics and far-field wake behavior. The proposed framework provides a foundation for more accurate power performance assessment of floating offshore wind turbines, supports array layout optimization, and enhances the overall efficiency and energy yield of offshore wind farms.

doi:10.6342/NTU202503576

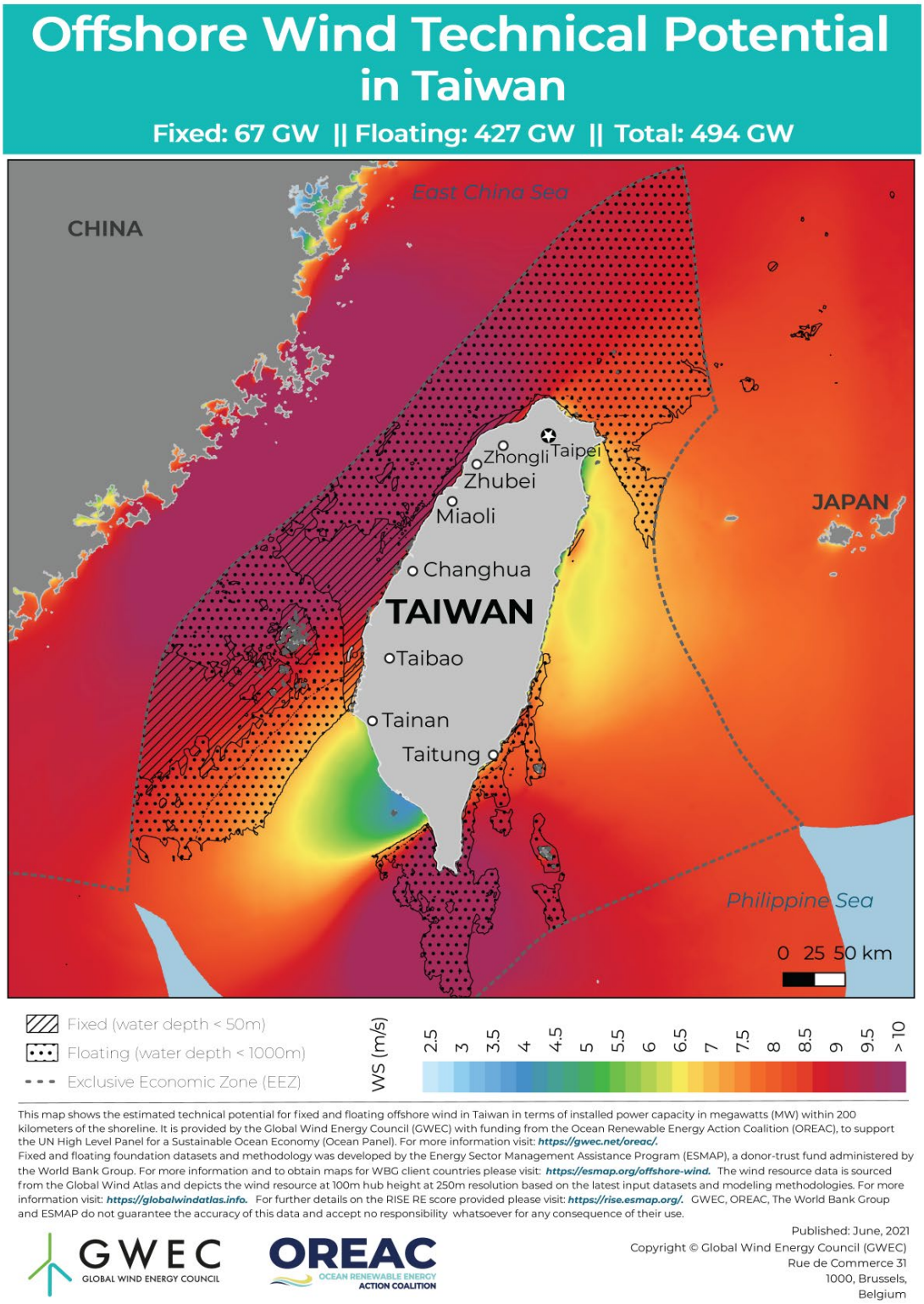

Figure 1 Wind energy potential in Taiwan [2]

doi:10.6342/NTU202503576

1.2 Literature Review

To accurately describe the influence of a wind turbine on the surrounding and downstream wake flow, an appropriate aerodynamic model must first be introduced. The most fundamental approach is the actuator disk model, originally developed from the pioneering work of Rankine [3] and Froude [4]. In this simplified model, the wind turbine is represented as a permeable circular disk onto which aerodynamic forces, such as thrust, are applied. This model predicts that the maximum fraction of kinetic energy that can be extracted from the wind is 16/27, or approximately 59%, a theoretical limit commonly known as the Betz limit.

Recent advances in computational modeling have enhanced the understanding of offshore wind farm wake dynamics. Lee [5] proposed a wake model combining actuator disk forcing and additional turbulence sources within a modified $k-\varepsilon$ framework, showing good agreement with experimental data. Chiang [6] applied an actuator disk model with corrected power curves to estimate the performance of three onshore wind farms in Taiwan, achieving close alignment with long-term observations based on wind direction distributions. Hsu [7] employed a large eddy simulation (LES) with actuator disk modeling, accurately capturing wake velocity deficits at Horns Rev, though underestimating turbulence levels. The study showed that turbulence generation scales with the turbine's power coefficient $C_p^{3/2}$ and tip-speed ratio $\lambda^{1/3}$, emphasizing the role of operational parameters. Pan [8] used a RANS-based actuator disk model to analyze wake effects at Taiwan's Zhangbin offshore wind farm, revealing up to 18.8% energy loss due to upstream interference. Lam [9] developed an LES framework with symmetry-preserving discretization and a dynamic subgrid-scale model, incorporating shifted-periodic boundaries for improved agreement with SCADA data in both ABL and offshore

doi:10.6342/NTU202503576

conditions. Nedjari et al. [10] used URANS with sliding mesh for full-rotor simulations of Nibe B turbine, showing that fine mesh is essential for accurate wake and turbulence predictions. Rezaeiha and Micallef [11] demonstrated that actuator disks can replicate key far-wake turbulence features of real turbines beyond three rotor diameters, validating their use as reliable surrogates under varying inflow conditions for wind tunnel and CFD studies. Neunaber et al. [12] used CFD simulations to demonstrate that upstream surge motion in tandem floating offshore wind turbines (FOWTs) enhances wake recovery and power performance, indicating that compact wind farm layouts may be more viable than those for fixed turbines under dynamic operating conditions. Dong et al. [13] compared actuator disk (AD) and actuator surface (AS) models across three turbine designs. Although the AD models matched the performance of the AS models for the NREL turbine, they underperformed for EOLOS and NREL-V, particularly in the prediction of far-wake turbulence. Meng et al. [14] proposed a SPAD actuator disk model with the $k-\varepsilon-f_{\mathrm{p}}$ turbulence model, improving near-wake predictions and reducing wake-induced power loss compared to actuator line and field data. The aforementioned research has provided a solid foundation for the numerical analysis of aerodynamic performance and wake dynamics associated with the wind turbine actuator disk model.

Recent studies have extensively investigated the aerodynamic effects of platform-induced motions in FOWTs, particularly focusing on surge, pitch, and their coupled dynamics. Kyle et al. [15] reported that large-amplitude surge motion can induce propeller and vortex ring states, leading to thrust reversal and vortex recirculation near the rotor plane. Sun et al. [16] showed that surge motion, when coupled with tower shadow effects, amplifies load fluctuations in downwind FOWTs, increasing torque variability and structural fatigue risks. Wang et al. [17], employing Improved Delayed Detached Eddy Simulation (IDDES) with overset mesh, found that damping effects dominate

doi:10.6342/NTU202503576

aerodynamic load fluctuations, and that higher surge amplitudes significantly enhance downstream wake recovery. In terms of pitch motion, Fang et al. [18], also using IDDES, demonstrated that it amplifies wake asymmetry and thrust variation, primarily through enhanced flow separation and complex vortex evolution near the rotor. Shi et al. [19] further revealed that pitch-induced platform motion results in cyclic fluctuations in blade surface pressure and turbine thrust, with a measurable phase shift between platform motion and aerodynamic response. Fu et al. [20] confirmed that both pitch amplitude and frequency strongly influence wake morphology, thrust oscillations, and vortex interactions, particularly in fully configured turbine setups.

Several studies have also explored the coupled effects of surge and pitch motion. Lin et al. [21] showed that their interaction generates asymmetric wake structures and considerable power overshoot, challenging the accuracy of conventional aerodynamic models. Chen et al. [22] found that these combined motions introduce substantial unsteady aerodynamic loads and reduce the average power output due to fluctuating blade angles. To address these complex flow phenomena, Alireza et al. [23] implemented an actuator line model (ALM) within a CFD framework and successfully captured vortex ring states and wake deformation under combined motions, while maintaining computational efficiency.

doi:10.6342/NTU202503576

2 Numerical Methods

The present study conducts numerical simulations using the commercial CFD software STAR-CCM+. This numerical platform is chosen for its integrated finite volume framework, robust turbulence modeling capabilities, and efficient handling of complex boundary conditions. The governing equations, comprising continuity and momentum conservation, are presented in Section 2.1, where they are discretized using the finite volume method (FVM) and solved with a segregated algorithm. The turbulence model, including its mathematical formulation and near-wall treatment strategy, is described in Section 2.2. Section 2.3 details the actuator disk model adopted to simulate rotor-induced aerodynamic loading, including the body force approach applied within the flow field. Section 2.4 outlines the overall numerical framework, covering the spatial and temporal discretization schemes as well as solver settings. Section 2.5 defines the computational domain and boundary conditions, while Section 2.6 describes the mesh generation and distribution strategy. Finally, Section 2.7 presents the results of the grid and time step independence study, which verifies the numerical stability and convergence of the simulation setup.

The flow is assumed to be governed by the unsteady Reynolds-Averaged Navier-Stokes equations under the following modeling assumptions:

- The fluid is Newtonian and the flow is considered three-dimensional.
- The flow is incompressible and isothermal, with density and viscosity variation ignored.
- Transient effects are included to capture unsteady wake and rotor flow structures.
- Gravity is neglected, as its influence is negligible compared to inertia effect.
- Heat transfer and buoyancy effects are not considered.

doi:10.6342/NTU202503576

2.1 Governing Equation

In this study, the Reynolds-Averaged Navier-Stokes (RANS) approach is employed to simulate the turbulent flow behavior around a wind turbine. RANS turbulence models provide closure relations for the RANS equations, which govern the transport of mean flow quantities by accounting for the effects of turbulence through modeled Reynolds stresses. To derive the RANS equations, each instantaneous flow variable in the Navier-Stokes equations is decomposed into a mean (time-averaged) component and a fluctuating component. Substituting the decomposed velocity field into the incompressible Navier-Stokes equations and applying ensemble averaging leads to the Reynolds-averaged continuity and momentum equations, expressed as follows:

$$\frac{\partial u_i}{\partial x_i} = 0, \tag{1}$$

$$\frac{\partial(\rho u_i)}{\partial t} + \frac{\partial(\rho u_i u_j)}{\partial x_j} = -\frac{\partial p}{\partial x_i} + \frac{\partial}{\partial x_j}\left[\mu\left(\frac{\partial u_i}{\partial x_j} + \frac{\partial u_j}{\partial x_i}\right)\right] + \frac{\partial(-\rho\overline{u_i' u_j'})}{\partial x_j} + f_i, \tag{2}$$

where ρ is the fluid density, p is the mean pressure, and μ is the dynamic viscosity of the fluid. The term u_i and f_i represent the mean velocity and the body force in the i-th direction, respectively. The fluctuating velocity component in the i-th direction is denoted by u_i', and the term $-\rho\overline{u_i' u_j'}$ corresponds to the Reynolds stress tensor, which arises from averaging the nonlinear convective term. To close the momentum equation, the Reynolds stresses must be modeled. Based on the Boussinesq approximation, the Reynolds stress tensor is related to the mean strain rate and turbulent viscosity as

$$-\rho\overline{u_i' u_j'} = \mu_t\left(\frac{\partial u_i}{\partial x_j} + \frac{\partial u_j}{\partial x_i}\right) - \frac{2}{3}\rho k\delta_{ij}, \tag{3}$$

where μ_t is the turbulent viscosity, k is the turbulent kinetic energy, and δ_{ij} is the Kronecker delta. Both quantities are obtained from the turbulence model and are used to close the RANS equations.

doi:10.6342/NTU202503576

2.2 Turbulence Model

The Shear Stress Transport (SST) $k-\omega$ turbulence model [24] is employed to compute μ_t and k, which are required for closing the RANS equations. The SST model combines the strengths of the standard $k-\omega$ model and the standard $k-\varepsilon$ model by blending them across the computational domain. Specifically, it uses the $k-\omega$ model in the near-wall region to accurately resolve the boundary layer, and transitions to the $k-\varepsilon$ model in the free shear flow region for improved stability and performance in the outer flow. This hybrid formulation enhances the model's ability to capture flow separation and adverse pressure gradients.

The SST model solves transport equations for the k and its specific dissipation rate (ω), which define the turbulence time and length scales. The turbulent viscosity is calculated as

$$\mu_t = \rho k T_t, \tag{4}$$

where the turbulence time scale T_t is defined as

$$T_t = \min\left(\frac{1}{\max\left(\frac{\omega}{\alpha^*}\right), \left(\frac{SF_2}{a_1}\right)}, \frac{C_R}{\sqrt{3}S}\right), \tag{5}$$

where F_2 is a blending function shown in Table 1, while S is the modulus of the mean strain rate tensor which related to the velocity gradient. It is defined as

$$S = \sqrt{2S_{ij}S_{ij}}, \tag{6}$$

where the mean strain rate tensor S_{ij} is given by

$$S_{ij} = \frac{1}{2}\left(\frac{\partial u_i}{\partial x_j} + \frac{\partial u_j}{\partial x_i}\right). \tag{7}$$

doi:10.6342/NTU202503576

2. Numerical Methods

The transport equations for k and ω are written as

$$\frac{\partial(\rho k)}{\partial t}+\frac{\partial\left(\rho k u_j\right)}{\partial x_j}= \frac{\partial}{\partial x_j}\left[(\mu+\sigma_k\mu_t)\frac{\partial k}{\partial x_j}\right]+P_k+\mu_t S^2-\rho\beta^*(\omega k-\omega_0 k_0), \tag{8}$$

$$\frac{\partial(\rho\omega)}{\partial t}+\frac{\partial\left(\rho\omega u_j\right)}{\partial x_j}= \frac{\partial}{\partial x_j}\left[(\mu+\sigma_\omega\mu_t)\frac{\partial\omega}{\partial x_j}\right]+\rho\gamma S^2+2\rho(1-F_1)\frac{\sigma_{\omega2}}{\omega}\frac{\partial k}{\partial x_j}\frac{\partial\omega}{\partial x_j}-\rho\beta(\omega^2-\omega_0^2), \tag{9}$$

where P_k represents the total turbulent kinetic energy production attributed specifically to blade-induced motion. The model constants used in the SST $k-\omega$ formulation, such as α^*, a_1, β, β^*, γ, σ_k, σ_ω and C_R are listed in Table 1.

The turbulence production due to blade motion, P_k, in Equation (8) can be expressed as follows [8]:

$$P_k=-\overline{u_i'u_j'}\frac{\partial u_i}{\partial x_j}+\frac{0.5C_G\rho U_{hub}^3A_r}{10^2}, \tag{10}$$

where U_{hub} is the hub-height wind velocity, A_r is the rotor swept area, and C_G is the dimensionless turbulence generation coefficient. The coefficient C_G is defined as a function of the turbine's aerodynamic characteristics

$$C_G=k_1C_P^{k_2}\lambda^{k_3}, \tag{11}$$

where the power coefficient (C_P) and tip-speed ratio (λ) represent key aerodynamic performance parameters of the wind turbine, which are described as

$$C_P=\frac{P}{0.5\rho U_{hub}^3A_r}, \tag{12}$$

$$\lambda=\frac{\omega_r D}{2U_{hub}}, \tag{13}$$

where P is the power generated by wind turbine, ω_r is the rotor speed, and D is the rotor diameter. The empirical coefficients k_1, k_2 and k_3 used in Equation (11) are listed in Table 2.

doi:10.6342/NTU202503576

For turbulence models, wall treatment provides the necessary boundary conditions for velocity, pressure, and turbulence quantities near solid boundaries, especially within turbulent boundary layers. In addition to enforcing no-slip conditions, the wall treatment framework specifies appropriate values for turbulence variables at the centroids of near-wall cells. In turbulent flows, the wall shear stress (τ_w) must account for both viscous and turbulent contributions. This is commonly modeled through the dimensionless friction velocity (u_*), from which τ_w is computed as

$$\tau_w = \rho u_*^2. \tag{14}$$

When modeling the turbulence characteristics of the boundary layer, a wall function is used to approximate the velocity distribution near solid surfaces. The dimensionless friction velocity (u_*) is derived from near-wall velocity gradients and turbulence quantities and is closely related to the non-dimensional wall distance (y^+), which is given by

$$y^+ = y\frac{u_*}{\nu}, \tag{15}$$

where y is the distance from the wall, and ν is the kinematic viscosity of the fluid. The near-wall velocity distribution is modeled differently depending on the value of y^+. The wall function describes the distribution of the non-dimensional quantity (u^+) in the three sublayers of the boundary layer. The wall function for u^+ is defined as follows:

$$u^+ = \frac{1}{\kappa}\ln(1+\kappa y^+) + C\left(1 - e^{-y^+/y_m^+} - \frac{y^+}{y_m^+}e^{-by^+}\right), \tag{16}$$

$$C = \frac{1}{\kappa}\ln\left(\frac{E'}{\kappa}\right), \tag{17}$$

$$b = \frac{1}{2}\left(y_m^+\frac{\kappa}{C} + \frac{1}{y_m^+}\right), \tag{18}$$

$$y_m^+ = \max\left[3, 267(2.64 - 3.9\kappa)E'^{0.0125}\right] - 0.987, \tag{19}$$

where κ is the von Kármán constant, and E' is the wall function offset. This

doi:10.6342/NTU202503576

formulation allows a smooth transition between the viscous sublayer and log layer. The relationship between u^+ and y^+ is illustrated in Figure 2.

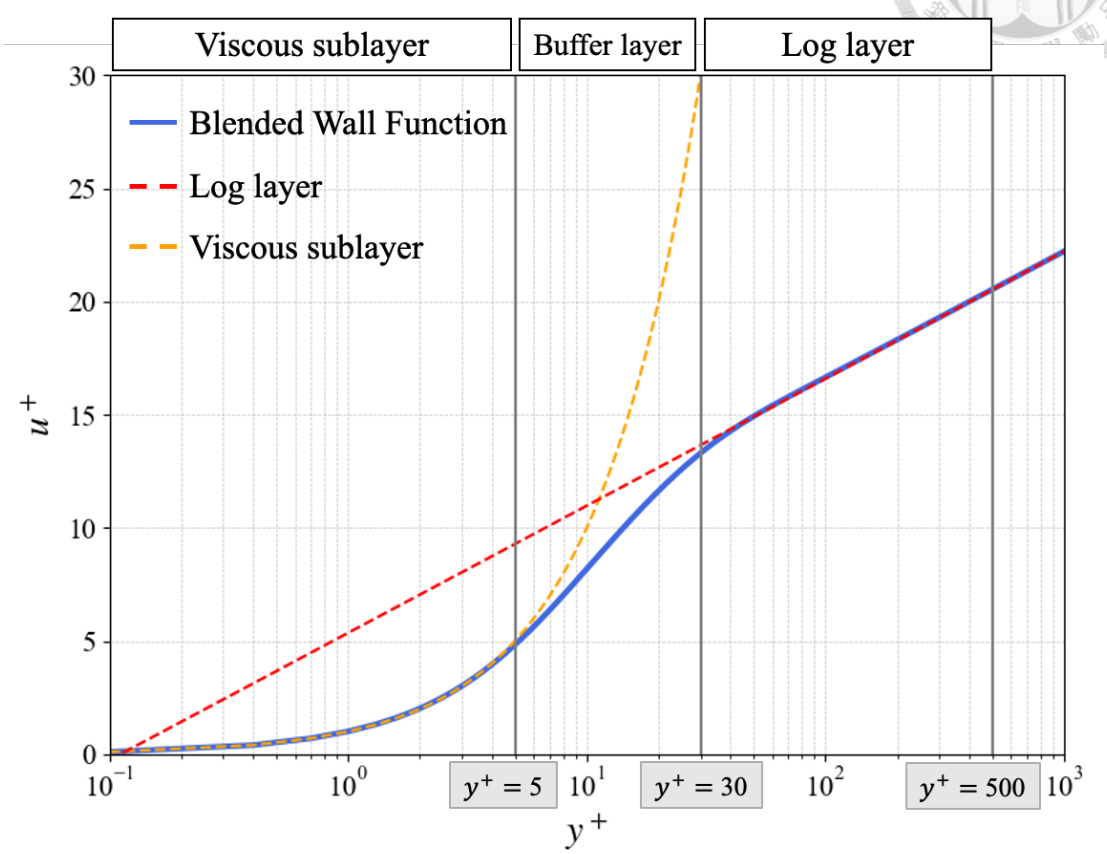

Figure 2 Wall function for turbulent boundary layers

doi:10.6342/NTU202503576

Table 1 Constants used in the SST $k-\omega$ turbulence model

F_1	$\tanh\left(\left[\min\left(\max\left(\frac{\sqrt{k}}{0.09\omega d},\frac{500\nu}{d^2\omega}\right),\frac{2k}{d^2\mathrm{CD}_{k\omega}}\right)\right]^4\right)$		
F_2	$\tanh\left(\left[\max\left(\frac{2\sqrt{k}}{\beta^*\omega d},\frac{500\nu}{d^2\omega}\right)\right]^2\right)$		
$\mathrm{CD}_{k\omega}$	$\max\left(\frac{1}{\omega}\frac{\partial k}{\partial x_j}\frac{\partial \omega}{\partial x_j},10^{-20}\right)$		
α^*	$F_1\alpha_1^*+(1-F_1)\alpha_2^*$		
β	$F_1\beta_1+(1-F_1)\beta_2$		
γ	$F_1\gamma_1+(1-F_1)\gamma_2$		
σ_k	$F_1\sigma_{k_1}+(1-F_1)\sigma_{k_2}$		
σ_ω	$F_1\sigma_{\omega_1}+(1-F_1)\sigma_{\omega_2}$		
α_1^*	1	α_2^*	1
β_1	0.075	β_2	0.0828
γ_1	$\frac{\beta_1}{\beta^*}-\frac{\sigma_{\omega_1}\kappa^2}{\sqrt{\beta^*}}$	γ_2	$\frac{\beta_2}{\beta^*}-\frac{\sigma_{\omega_2}\kappa^2}{\sqrt{\beta^*}}$
σ_{k_1}	0.85	σ_{k_2}	1
σ_{ω_1}	0.5	σ_{ω_2}	0.856
a_1	0.31	β^*	0.09
κ	0.41	C_R	0.6

$*$ d is the shortest distance to the wall, and the blending function F_1 combines the contributions near to and far away from the wall.

Table 2 Constants used in the C_G equation

k_1	k_2	k_3
1	1.2508	-0.1019

doi:10.6342/NTU202503576

2.3 Actuator Disk Model

The adopted Actuator Disk Model (ADM) is a simplified modeling approach that replaces the physical volume of wind turbine blades by an idealized disk positioned at the rotor plane. The complex blade-induced aerodynamic forces are approximated by applying distributed axial and tangential forces on the disk. The axial load imposed on the disk represents the thrust generated in actual turbine operation, thereby enabling simulation of the wake flow downstream. The principal advantage of ADM lies in its computational efficiency, making it particularly well-suited for simulating large-scale, multi-turbine wind farms.

In the present implementation, the actuator disk is described by the hub height H_{hub} and the rotor diameter D, are illustrated in Figure 3 [25]. The rotor swept area is defined as the actuator disk. Within this area, body forces equivalent to the aerodynamic forces exerted by the blades on the airflow are imposed, along with turbulence production terms to account for blade-induced fluctuations. The rotor disk is subdivided into multiple cells. Assuming a uniform distribution of blade forces over the rotor area, the total aerodynamic force is decomposed into axial and tangential components, f_a and f_t, respectively, which are defined as follows and illustrated in Figure 4:

$$f_a = \frac{P}{U_{avg}}, \tag{20}$$

$$f_t = \frac{3P}{4\pi R\omega_r}. \tag{21}$$

Since the undisturbed reference inflow velocity at the far-wake location cannot be directly obtained from the computational domain, the reference wind speed (U_{in}) used in the turbine power and rotor speed curves is replaced by the averaged axial wind speed U_{avg}, which can be directly extracted from the flow field, as shown in Figure 5.

doi:10.6342/NTU202503576

Consequently, both the power output and the body forces applied to the actuator disk are expressed as functions of U_{avg}. It is further assumed that the force distribution over the disk is uniform. The momentum source term is used to represent the axial and tangential forces exerted by the wind turbine on the flow field.

The calculation of these forces is based on the turbine's geometric parameters, such as rotor radius R, and operating parameters, including P, ω_r, and U_{avg}. The operational parameters considered are the rotor-averaged streamwise velocity at the turbine center (U_{avg}), the angular velocity of the rotor (ω_r), and the output power (P). These quantities are used to characterize the aerodynamic loading and energy extraction performance of the actuator disk within the numerical simulation framework. The correlation among P, ω_r, and U_{avg} is presumed to be fixed, based on stand-alone turbine operating characteristics, and extended to represent turbines within large turbine arrays. The correlation among these parameters is depicted in Figure 6.

doi:10.6342/NTU202503576

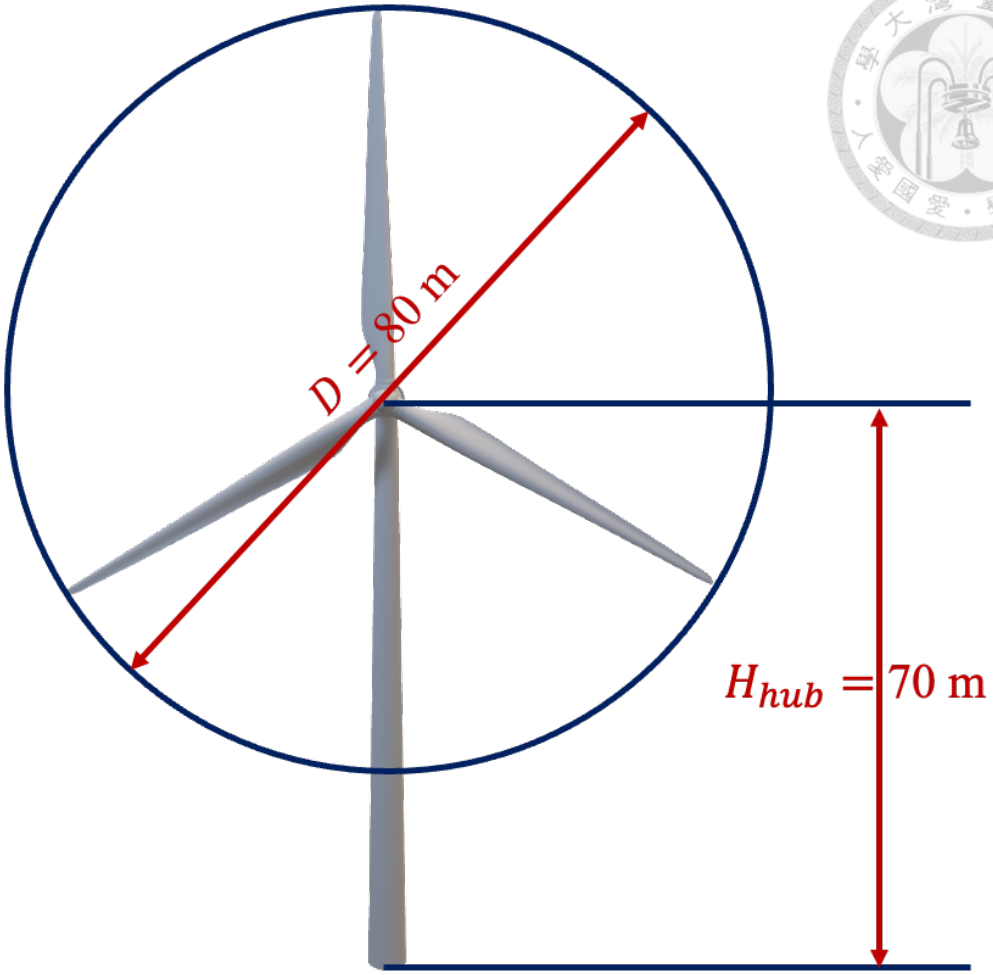

Figure 3 Geometric parameters of Vestas V80 2-MW wind turbine

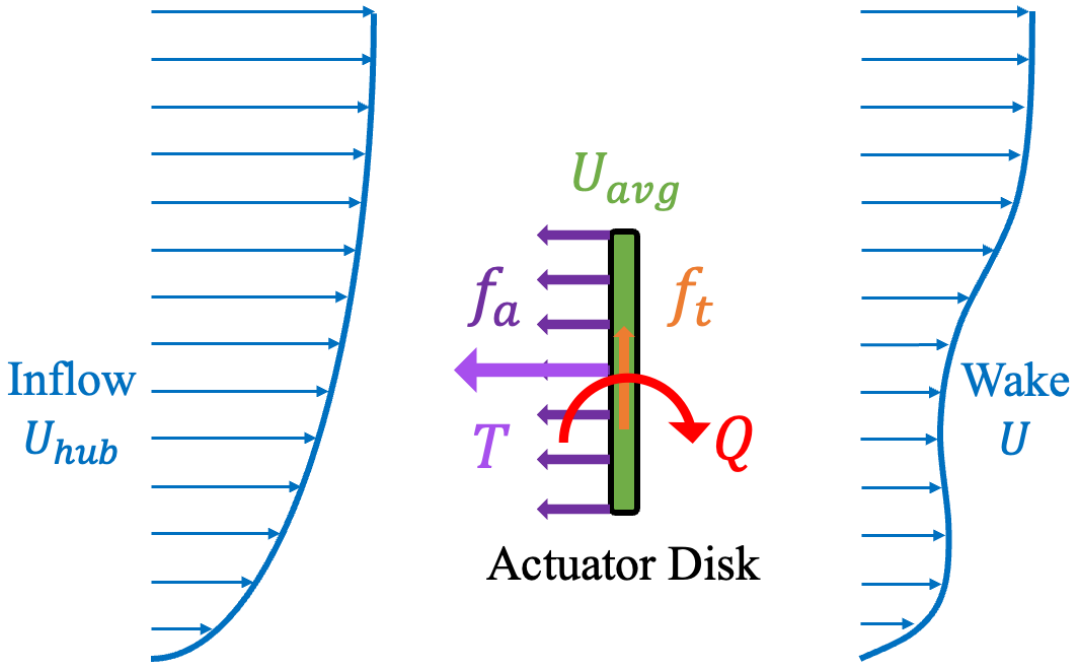

Figure 4 Relationship between thrust, torque, and rotor-averaged wind speed

doi:10.6342/NTU202503576

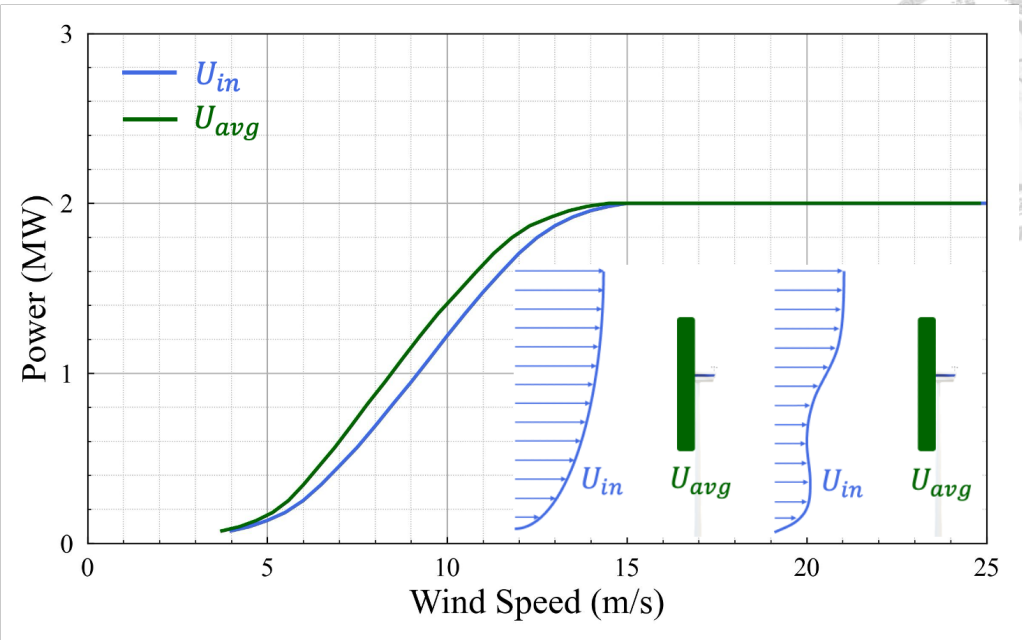

Figure 5 Dependence of P on U_{avg} and U_{in} for V80

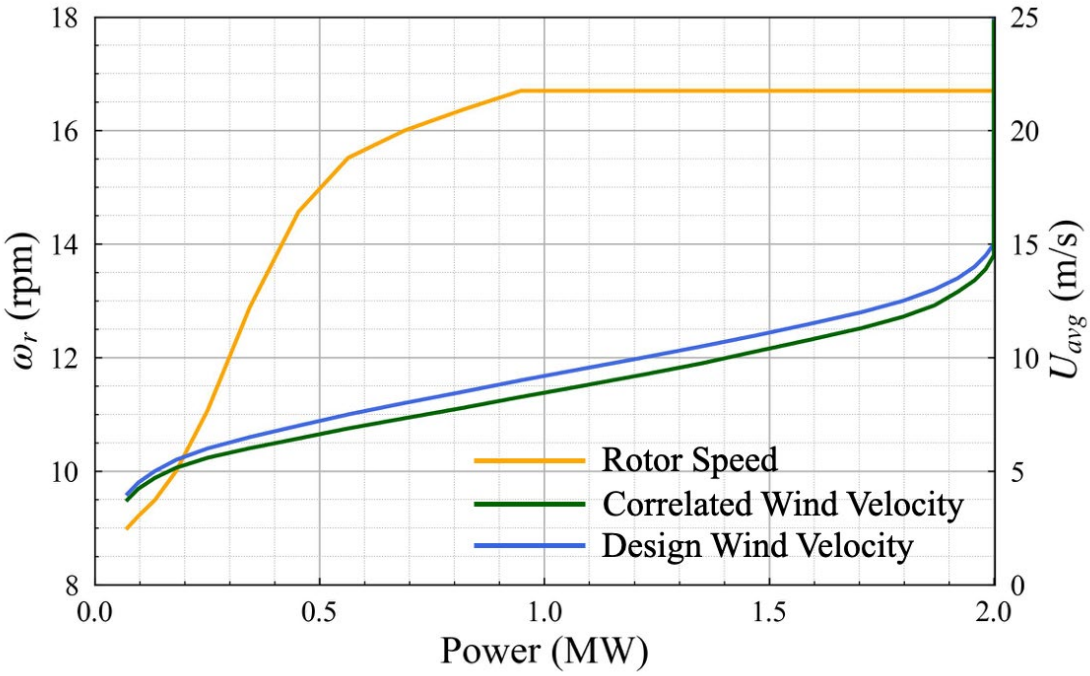

Figure 6 Correlation among U_{avg}, ω_r, and P for V80

doi:10.6342/NTU202503576

2.4 Numerical Framework

Here, STAR-CCM+ [26] is employed to perform numerical simulations based on the finite volume method (FVM). This method involves integrating the governing partial differential equations over discrete control volumes and approximating the flux terms using variable values at the centroids of neighboring cells. This procedure yields a linearized algebraic equation, which are solved iteratively to obtain the flow field variables.

Temporal discretization in the present simulations is performed using a first-order implicit scheme, which provides unconditional stability and allows for larger time steps while maintaining acceptable accuracy for unsteady flow calculations. This scheme is particularly advantageous in resolving the transient evolution of the flow field under platform motions, as it minimizes numerical instabilities associated with explicit time integration methods. Spatial discretization, on the other hand, is conducted using a second-order upwind scheme for the convective terms. Compared to first-order schemes, the second-order upwind approach significantly enhances the solution accuracy by reducing numerical diffusion and more accurately capturing steep flow gradients and vortical structures in the wake.

The coupling between the pressure and velocity fields is handled through the SIMPLE (Semi-Implicit Method for Pressure-Linked Equations) algorithm. This iterative procedure sequentially solves the discretized momentum equations to obtain an intermediate velocity field, followed by the solution of a pressure correction equation derived from the continuity constraint, which ensures mass conservation throughout the computational domain. The corrected pressure and velocity fields are then updated iteratively until convergence is achieved within each time step. This algorithm is widely

doi:10.6342/NTU202503576

adopted in incompressible flow computations due to its robustness and efficiency in handling pressure–velocity coupling. By solving the fully discretized system with the aforementioned temporal and spatial approximations, the simulation yields detailed distributions of key physical quantities, including velocity, pressure, and turbulence properties, across the entire computational domain, thereby enabling a comprehensive analysis of the wake behavior and flow dynamics around the floating offshore wind turbine.

doi:10.6342/NTU202503576

2.5 Computational Domain and Boundary Conditions

The computational domain is constructed based on the diameter of the wind turbine (D), which serves as the reference length scale. The inflow boundary is positioned at a distance of $2D$ upstream from the rotor, while the outflow boundary is placed at $20D$ downstream to ensure sufficient space for wake development. The top boundary is located at $5D$ above the mean sea level, allowing vertical development of the flow. The side boundaries on both lateral directions are placed at a distance of $2.5D$ from the center plane, providing enough clearance to avoid artificial blockage and lateral interactions, as illustrated in Figure 7.

A logarithmic wind profile is imposed at the inlet and top boundaries to represent the feature of the atmospheric boundary layer (ABL), using a power-law formulation with exponent $\alpha = 0.1$, representing smooth terrain conditions such as offshore sea surfaces [8]. The bottom boundary is treated as a no-slip wall, and the outlet is assigned a pressure outlet condition. Symmetry boundary conditions are applied at the lateral sides of the domain to reduce computational cost, where $\mathbf{u_p}$ denotes the velocity vector at the symmetry boundary and **n** represents the normal vector. The boundary condition used in this simulation are summarized in Table 3.

doi:10.6342/NTU202503576

Table 3 Boundary Condition Settings

Boundary Type	$\mathbf{U} = (u, v, w)$	p	k	ω
Velocity Inlet (Inflow, Top)	$\left(U_{hub}\left(\frac{z}{H_{hub}}\right)^{0.1}, 0, 0\right)$	$\frac{\partial p}{\partial n} = 0$	$\frac{3}{2}(I\lvert\mathbf{U}\rvert)^2$	$\frac{\rho k}{(\mu_t/\mu)\mu}$
Pressure Outlet (Outflow)	$\frac{\partial \mathbf{U}}{\partial n} = 0$	$p = p_{out}$	$\frac{\partial k}{\partial n} = 0$	$\frac{\partial \omega}{\partial n} = 0$
Wall (bottom)	$\mathbf{U} = 0$	$\frac{\partial p}{\partial n} = 0$	$\frac{\partial k}{\partial n} = 0$	$\frac{\partial \omega}{\partial n} = 0$
Symmetry (side)	$\mathbf{u_p} - (\mathbf{u_p} \cdot \mathbf{n})\mathbf{n}$	$\frac{\partial p}{\partial n} = 0$	$\frac{\partial k}{\partial n} = 0$	$\frac{\partial \omega}{\partial n} = 0$

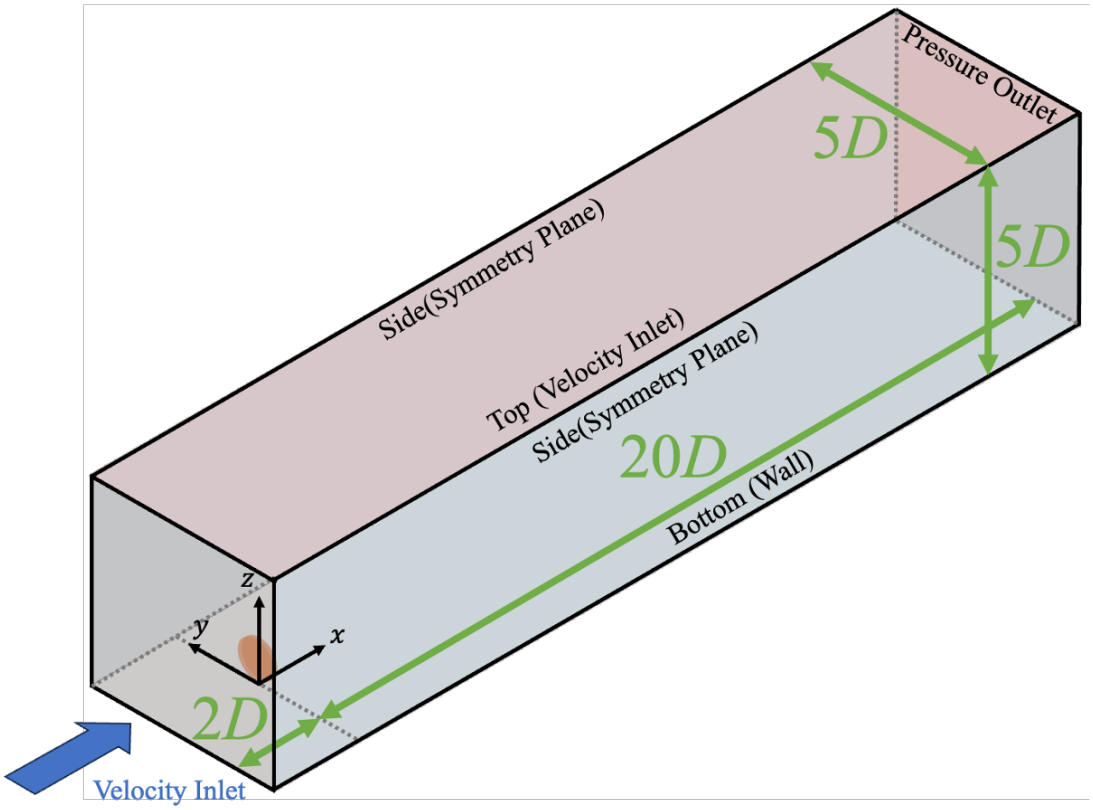

Figure 7 Computational domain and boundary condition

doi:10.6342/NTU202503576

2.6 Mesh Distribution

An overset mesh technique is employed to facilitate the integration of the actuator disk model into the computational domain. Compared to fully resolving turbine blade geometry, the actuator disk approach captures the rotor-induced flow effects while significantly reducing the computational cost. The overset strategy involves embedding a fine, body-conforming mesh around the actuator disk within a coarser background mesh. This configuration enables local mesh refinement near the rotor and wake regions, allowing accurate resolution of wake development while maintaining a manageable total cell count.

Communication between the background mesh and the overset mesh is handled automatically through an interpolation algorithm. The adopted grid sizes and the mesh layout are illustrated in Figure 8.

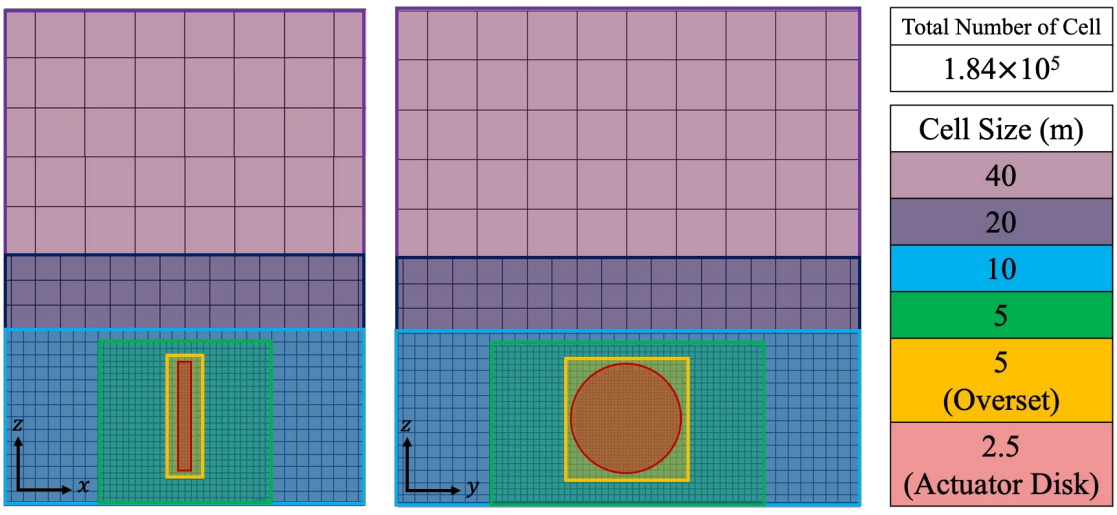

Figure 8 Distribution of grid sizes and mesh setting

doi:10.6342/NTU202503576

2.7 Time Step and Grid Dependency

The choice of time step size (Δt) is critical in transient simulations, affecting both accuracy and stability. In this study, six different time step sizes are examined, corresponding to a range from 25 to 800 time steps per encounter period. The time step sensitivity study reveals that as the time step size is reduced by a factor of 2, the solution demonstrates a consistent converging refinement behavior. To further evaluate the time discretization error, two simulation results with different time step sizes are used to approximate the converged solution Φ^{∞}, using the following Richardson is extrapolation formula:

$$\Phi^{\infty} \cong \Phi_1^t + \frac{\Phi_1^t - \Phi_2^t}{(\frac{\Delta t_2}{\Delta t_1})^n - 1}, \tag{22}$$

where n is the order of the temporal discretization scheme, Φ_1^t and Φ_2^t are the numerical solutions obtained using Δt_1 and Δt_2, and $\Delta t_1/\Delta t_2$ is the time step size refinement ratio. The corresponding discretization error E^d is then defined as

$$E^d = \left|\frac{\Phi^{\infty} - \Phi_m^t}{\Phi^{\infty}}\right| \times 100\% . \tag{23}$$

The ideal error (E) scales with the time step size to the power of n

$$E \propto (\Delta t)^n, \tag{24}$$

$$\log(E) = n\log(\Delta t) + C, \tag{25}$$

where C is a constant. Figure 9 and Figure 10 illustrate the variation of U_{avg} with respect to Δt, and the corresponding time discretization errors. The discretization error under the time step of 0.1125 s used in this study is approximately 0.3%. Therefore, a time step of 0.1125 s is adopted in the following simulations, providing a balance between computational efficiency and high-fidelity resolution of wake flows.

doi:10.6342/NTU202503576

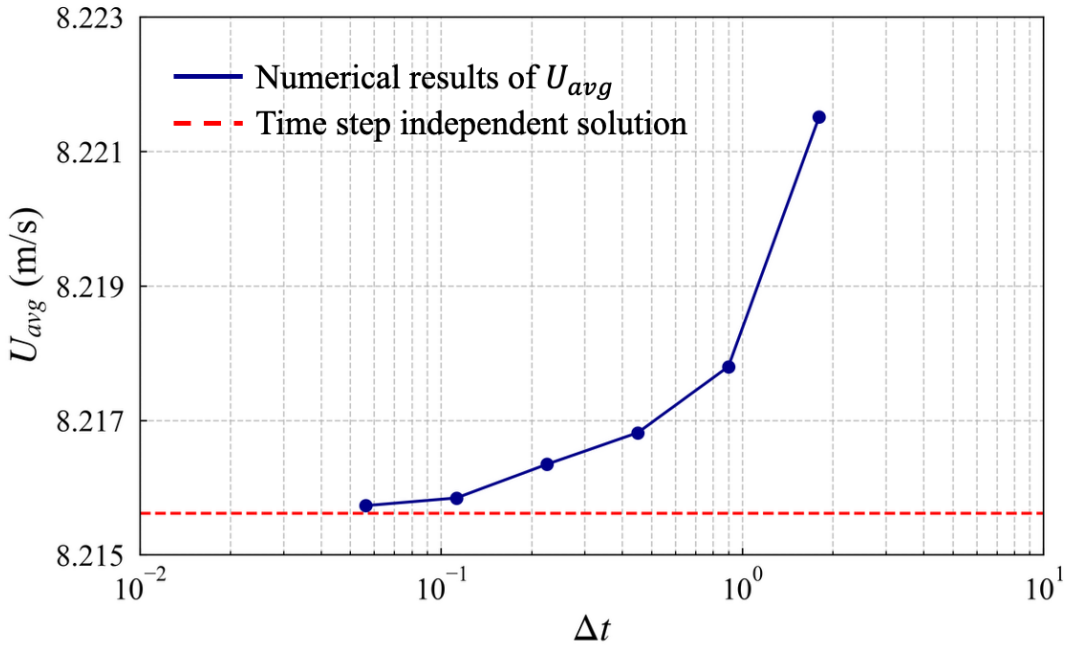

Figure 9 The dependence of U_{avg} on Δt

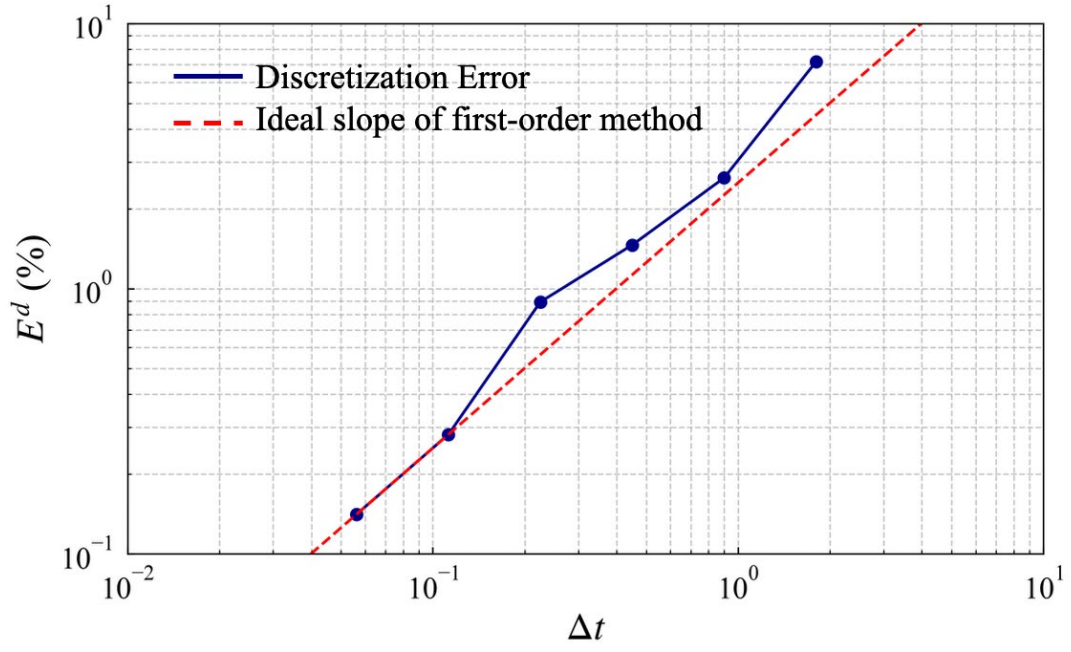

Figure 10 The dependence of E^d on Δt

doi:10.6342/NTU202503576

To balance numerical accuracy and computational efficiency, fine mesh regions are applied to the wind turbine rotor and the immediate wake zone to capture detailed vortex structures and wake dynamics. Coarser meshes are used in regions far from the rotor and wake to reduce computational cost. A controlled grid growth rate is implemented to ensure smooth transitions between adjacent mesh densities, thereby ensuring the numerical stability throughout the domain.

To verify the robustness and accuracy of the simulation, a grid independence study is performed using five different mesh resolutions categorized as Grid 1, Grid 2, Grid 3, Grid 4, and Grid 5. Each grid level is generated by increasing the total cell number by a refinement factor of approximately 1.1. The domain geometry and boundary conditions remain unchanged across all cases. The number of cells in each grid level is summarized in Table 4.

To estimate the grid discretization error, two adjacent mesh levels are used to approximate the ideal solution under infinite grid resolution, denoted as Φ_∞, using Richardson's extrapolation:

$$\Phi_\infty \cong \Phi_n + \frac{\Phi_n - \Phi_{n-1}}{(\sqrt[3]{\frac{N_n}{N_{n-1}}})^2 - 1}, \tag{26}$$

where Φ_n and Φ_{n-1} are the numerical solutions obtained using meshes with the cell number of N_n and N_{n-1}, respectively. The calculated U_{avg} evaluated in each grid level is shown in Figure 11. The corresponding discretization error E_d is then defined as

$$E_d = \left|\frac{\Phi_\infty - \Phi_n}{\Phi_\infty}\right| \times 100\%, \tag{27}$$

where Φ_n denotes the calculated result corresponding to the n-th grid. The dimensionless grid size (dx) for each level is given by

doi:10.6342/NTU202503576

$$dx_n = \sqrt[3]{\frac{1}{N_n}}. \tag{28}$$

As illustrated in Figure 12, E_d decreases with mesh refinement. When the grid is sufficiently fine, the slope of the error curve approaches that of a second-order method, indicated by the red reference line. This confirms that the numerical method delivers second-order spatial accuracy.

In this study, Grid 4 is selected for all subsequent simulations. With a discretization error of only 3.7%, further refinement offers marginal improvement at significantly higher computational cost. The selected mesh thus provides a good compromise between computational efficiency and accuracy. This assessment validates the credibility of the simulation framework.

Table 4 Number of grids in different grid levels

Grid Level	Total
Grid 1	1.38×10^5
Grid 2	1.52×10^5
Grid 3	1.67×10^5
Grid 4	1.84×10^5
Grid 5	2.03×10^5

doi:10.6342/NTU202503576

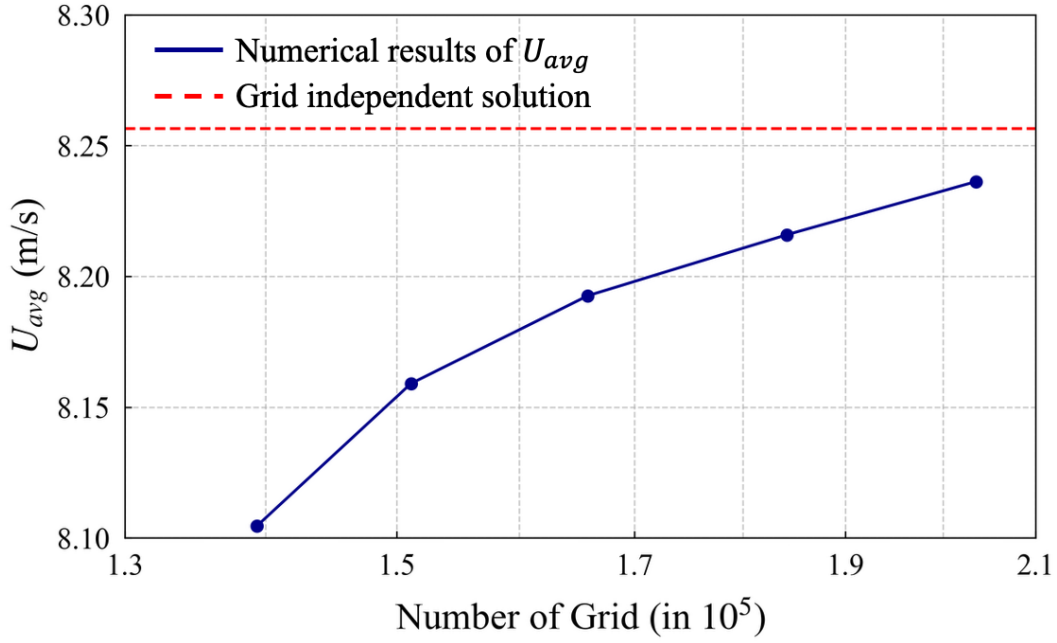

Figure 11 The dependence of U_{avg} on grid number

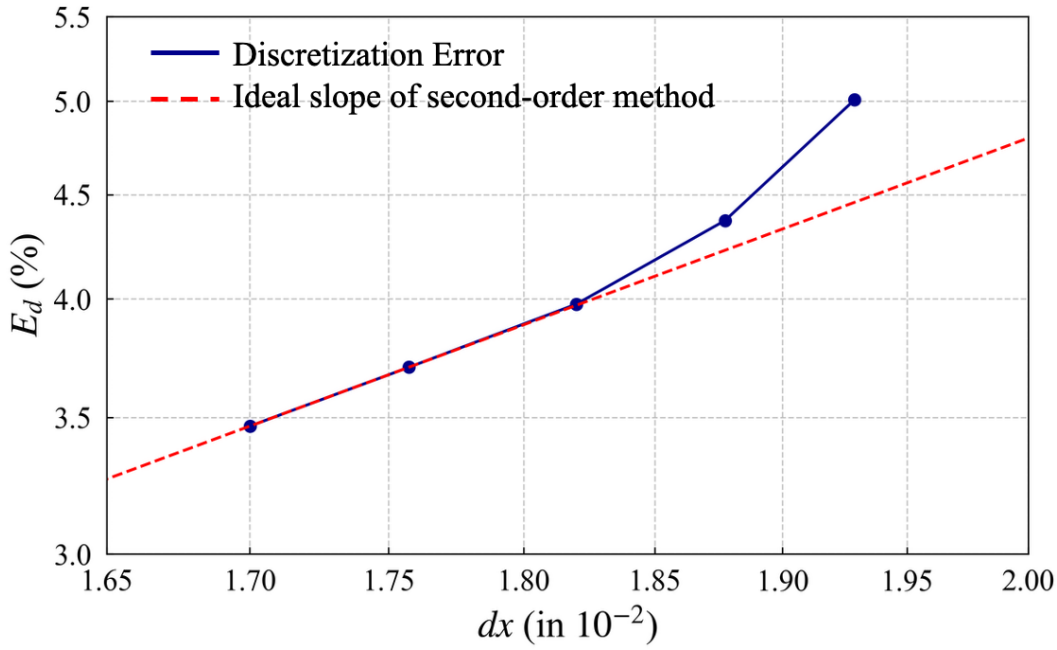

Figure 12 The dependence of E_d on dx

doi:10.6342/NTU202503576

3 Validation

3.1 Case Description

This study uses the time-averaged power output of the Horns Rev I offshore wind farm as a validation case. The wind farm comprises 80 Vestas V80 2-MW fixed-bottom wind turbines, arranged in a uniform grid configuration. Under three specific wind directions, the entire wind farm experiences full wake conditions, with the corresponding turbine spacings of $7.0D$, $9.3D$, and $10.4D$. The configuration is illustrated in Figure 13. Accordingly, in the simulation, wind turbines are arranged along these three wind directions to analyze wake interactions and power performance. The average wind speed at hub height is set to $U_{hub} = 8$ m/s, following the measurement condition.

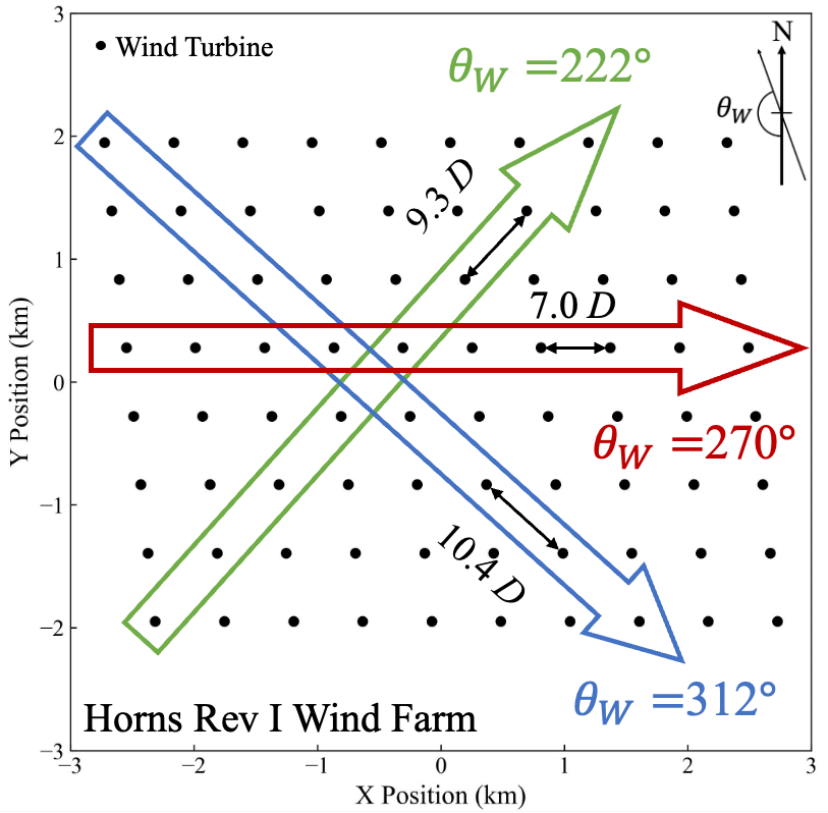

Figure 13 Wind turbine layouts in the Horns Rev I wind farm

doi:10.6342/NTU202503576

The computational domain for the three different turbine spacing scenarios is constructed using a bounding box to define the Horns Rev I wind farm layout. The corresponding numerical setup, including domain sizes, grid number, and boundary conditions, is summarized in Table 5 and Figure 14.

Table 5 Numerical setup for the Horns Rev I wind farm

Domain Size (m)	$\theta_w = 270°$	(6729.8, 4538.6, 400)
	$\theta_w = 222°$	(7275.4, 7298.7, 400)
	$\theta_w = 312°$	(7938.6, 6635.4, 400)
Grid Number	$\theta_w = 270°$	6.93×10^6
	$\theta_w = 222°$	1.10×10^7
	$\theta_w = 312°$	1.09×10^7
U_{hub} (m/s)		8.0
ρ (kg/m^3)		1.184
μ (Pa·s)		1.855×10^{-5}

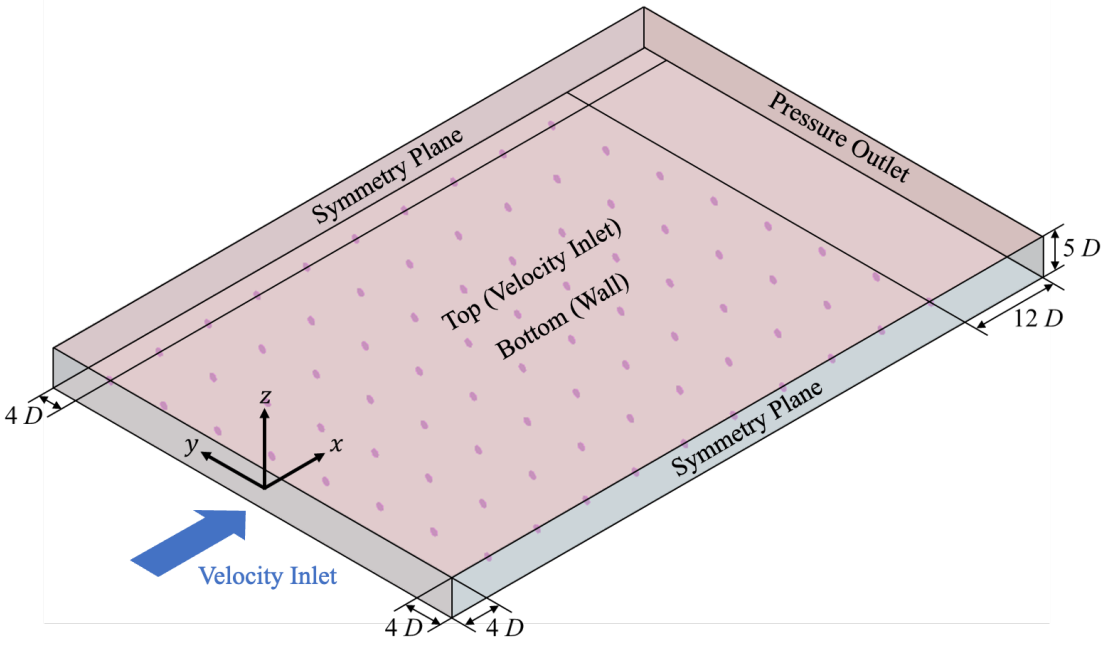

Figure 14 Computational Domain of the Horns Rev I wind farm under $\theta_w = 270°$

doi:10.6342/NTU202503576

3.2 Power Prediction

Steady-state RANS simulations are employed in this study to estimate the power output of each wind turbine in the Horns Rev I offshore wind farm. The power of the first row of turbines, denoted as P_1, is used as a reference, and the normalized power output of each downstream turbine rows are defined as:

$$P^* = \frac{P}{P_1}. \tag{29}$$

This normalization facilitates consistent comparisons of power attenuation under different wake conditions [27]. Under the wind direction of $\theta_w = 270°$ (Figure 15), the predicted power at the eighth row of turbines deviates by only 1.6% from the measured value. A similar pattern is observed for $\theta_w = 222°$ (Figure 16), where the second row of turbines exhibits a deviation of 7.25%, followed by excellent agreement with field data at downstream positions. In contrast, for $\theta_w = 312°$ (Figure 17) the simulation tends to underpredict the power output more significantly at the second row of turbines, with an error of 14%, but this discrepancy reduces to 3% by the fifth row of turbines. Figure 20 compare P^* values across three turbine spacings among four sources: SCADA field measurements [28], a referenced LES dataset [25], the WIFA3D-LES model [7], and the present STAR-CCM+ results. Based on comparisons with SCADA data, all numerical models exhibit power underprediction, e.g., the LES results have errors ranging from 3.3% to 20.7%. The largest deviation of 20.7% occurs in the LES simulation under the wind direction $\theta_w = 312°$. In contrast, the WIFA3D-LES approach shows even more pronounced underprediction, with errors ranging from 14.3% to 32.8%, reaching its maximum at $\theta_w = 270°$. As illustrated in Figure 21, the present simulation slightly overpredicts the power output at the second row of turbines compared to SCADA

doi:10.6342/NTU202503576

measurements, with a maximum error of approximately 12.7% at $\theta_w = 270°$. However, better agreement is achieved further downstream.

These results indicate that the proposed actuator disk model used in this study can reasonably capture turbine-level power production trends within large offshore wind farms. While discrepancies occur near the front-row turbines due to strong wake interactions, the model performs well downstream, where wake recovery becomes dominant.

doi:10.6342/NTU202503576

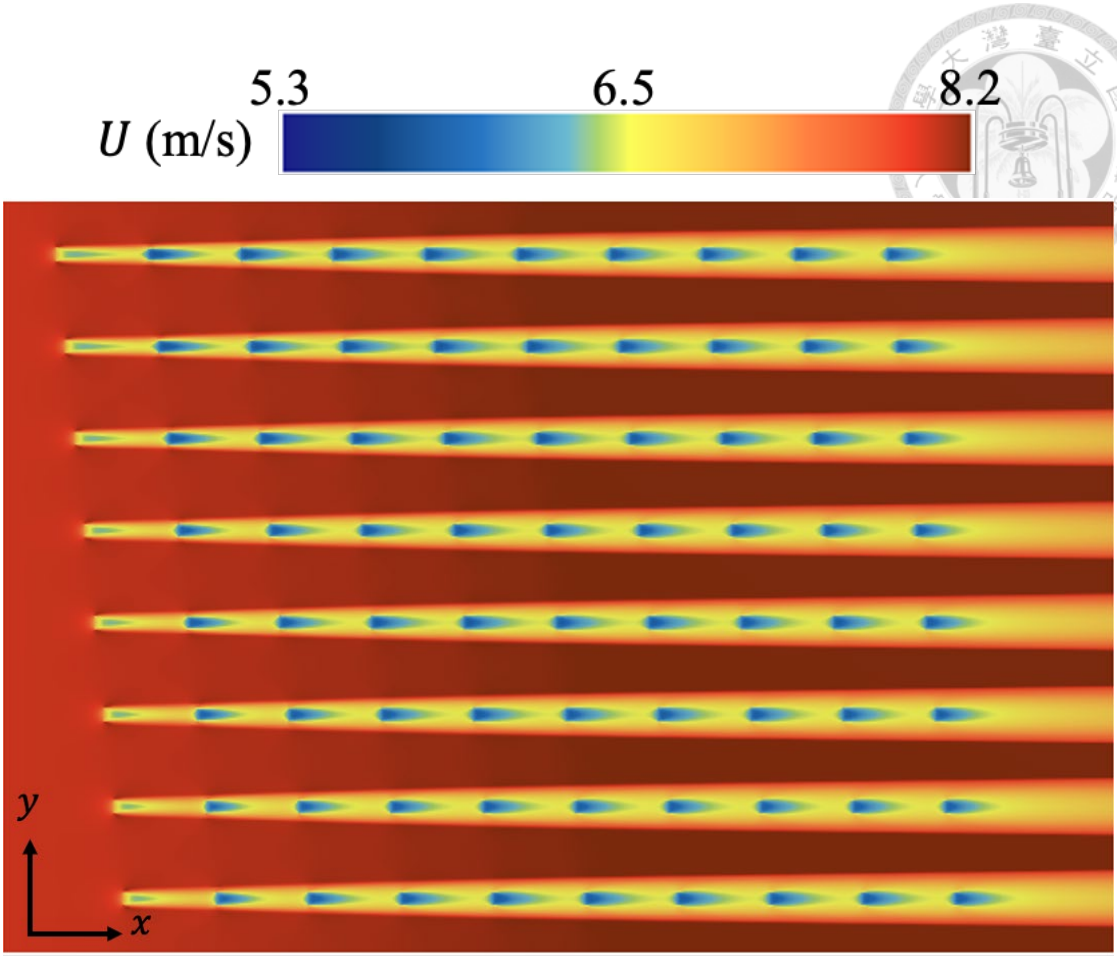

(a)

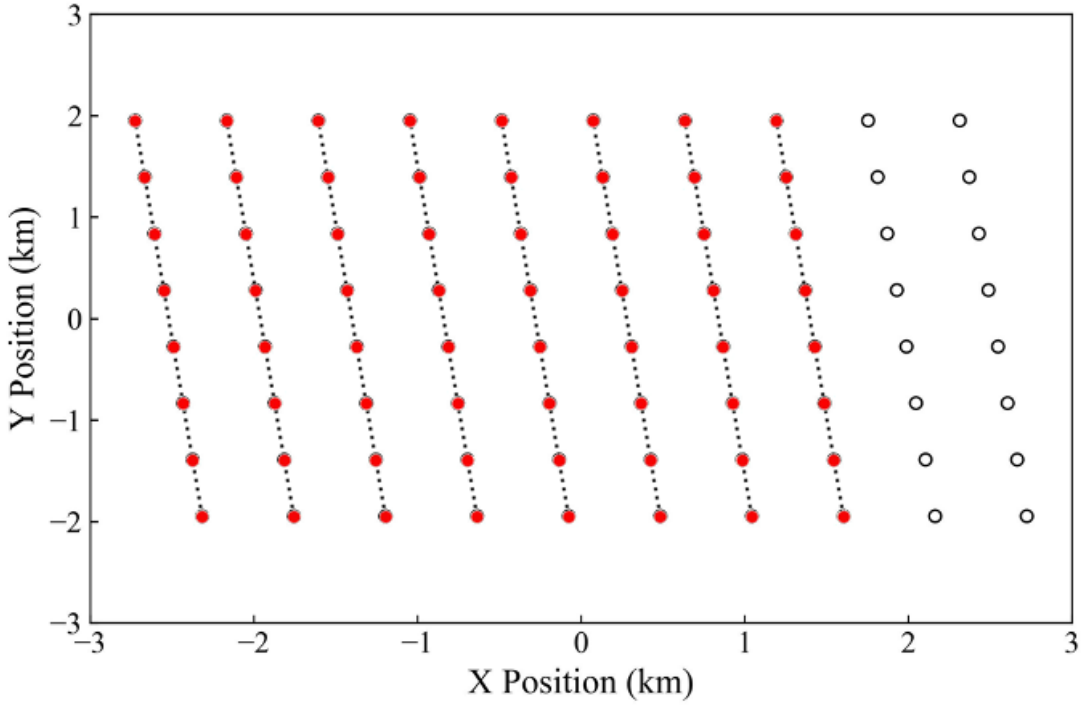

(b)

Figure 15 Flow field and turbine selection for θ_w =270°: (a) Contour of U at H_{hub} and (b) Wind turbines selected for P^*

doi:10.6342/NTU202503576

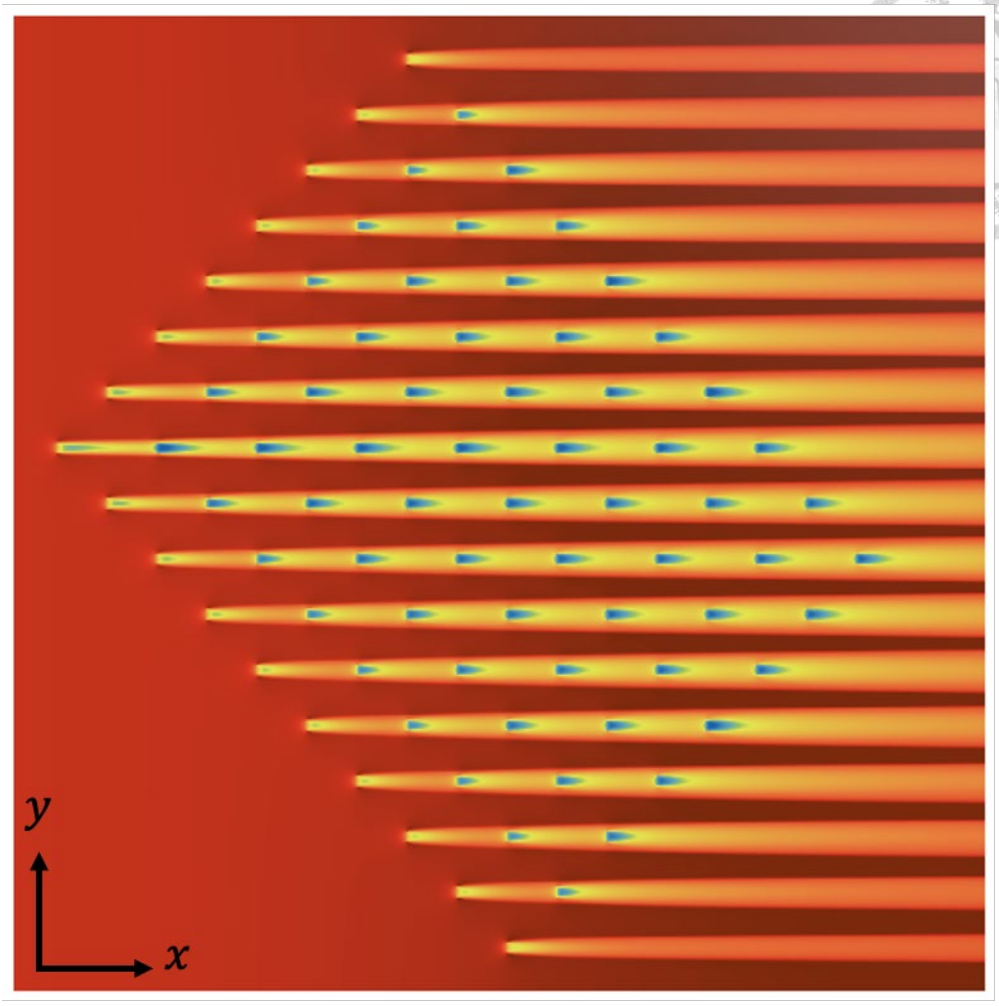

(a)

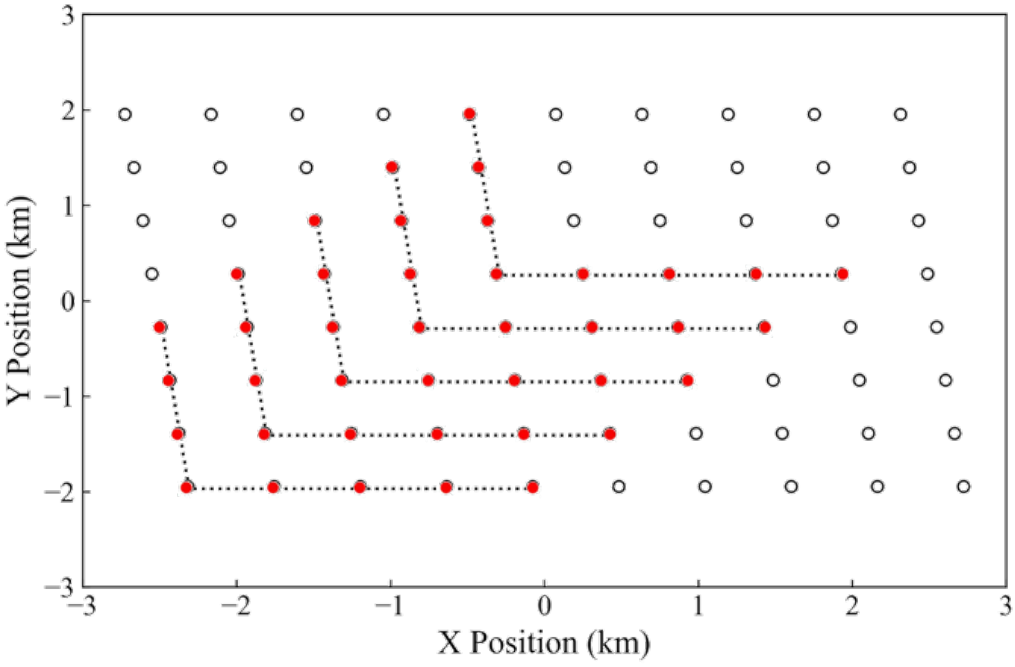

(b)

Figure 16 Flow field and turbine selection for θ_w =222°: (a) Contour of U at H_{hub} and (b) Wind turbines selected for P^*

doi:10.6342/NTU202503576

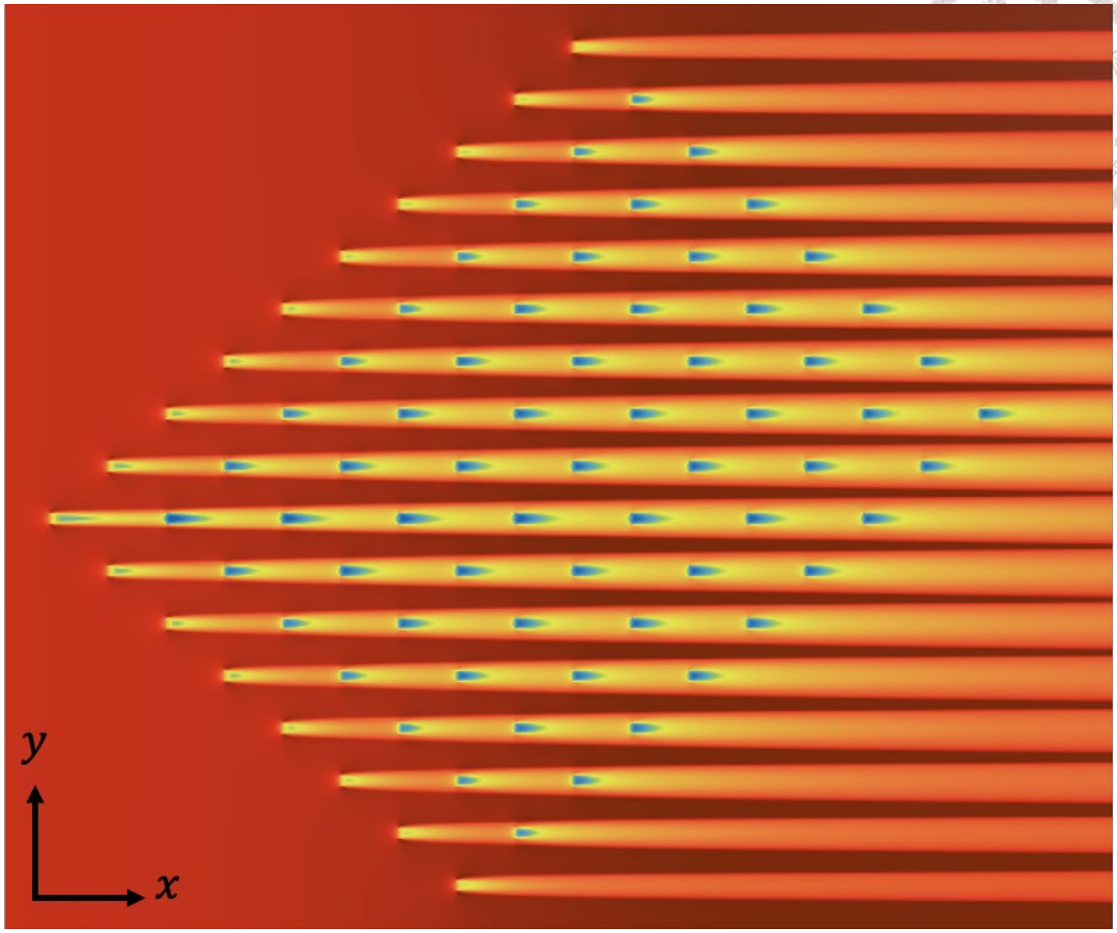

(a)

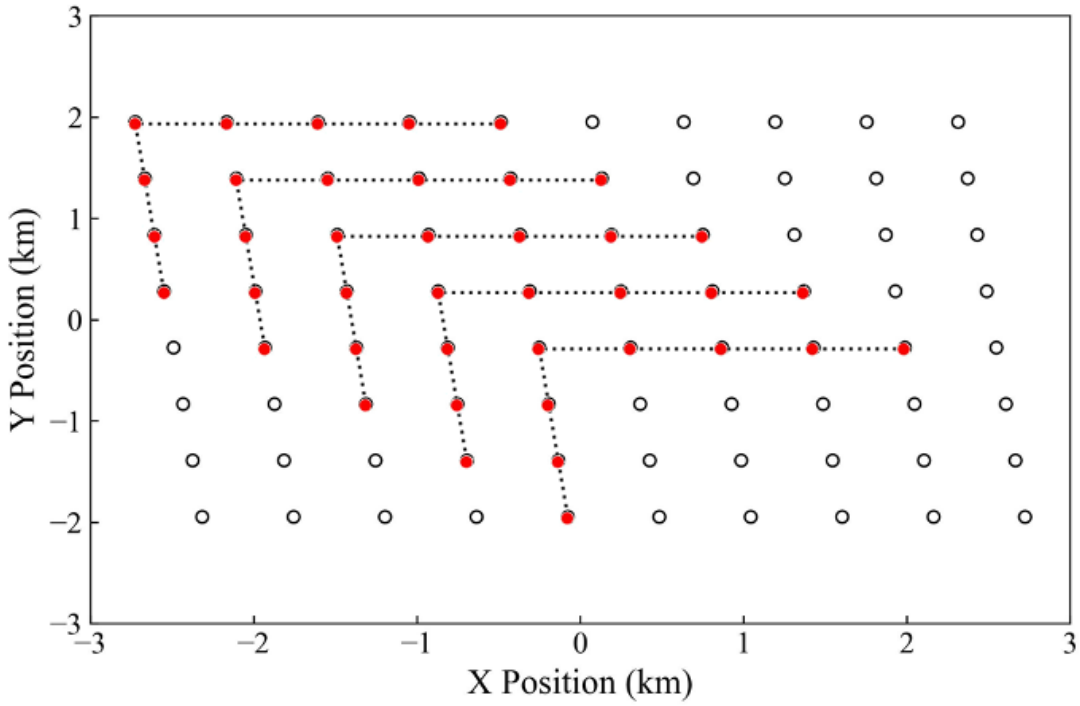

(b)

Figure 17 Flow field and turbine selection for θ_w =312°: (a) Contour of U at H_{hub} and (b) Wind turbines selected for P^*

doi:10.6342/NTU202503576

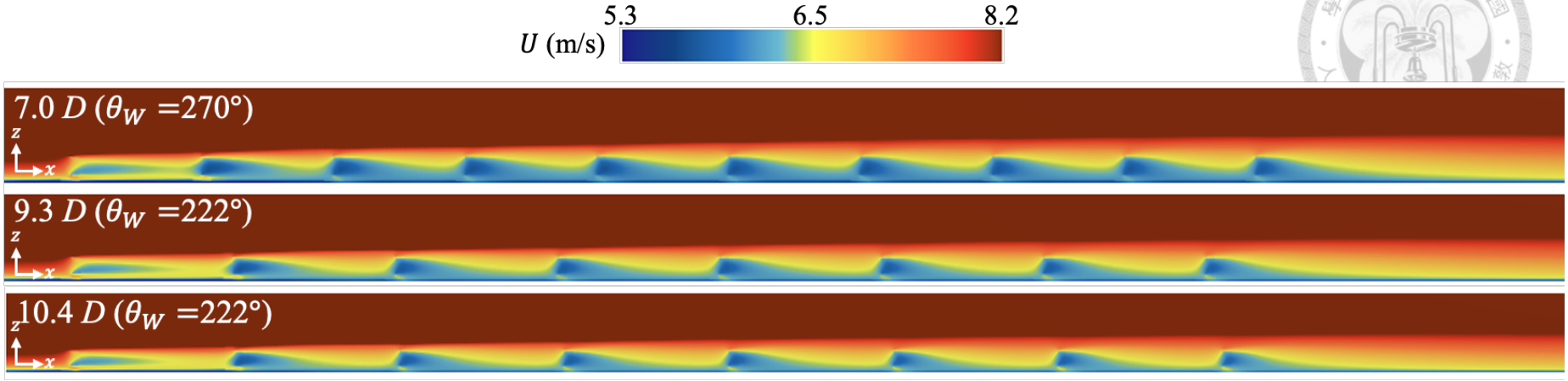

Figure 18 Contour of U for three wind directions at $y = 0$

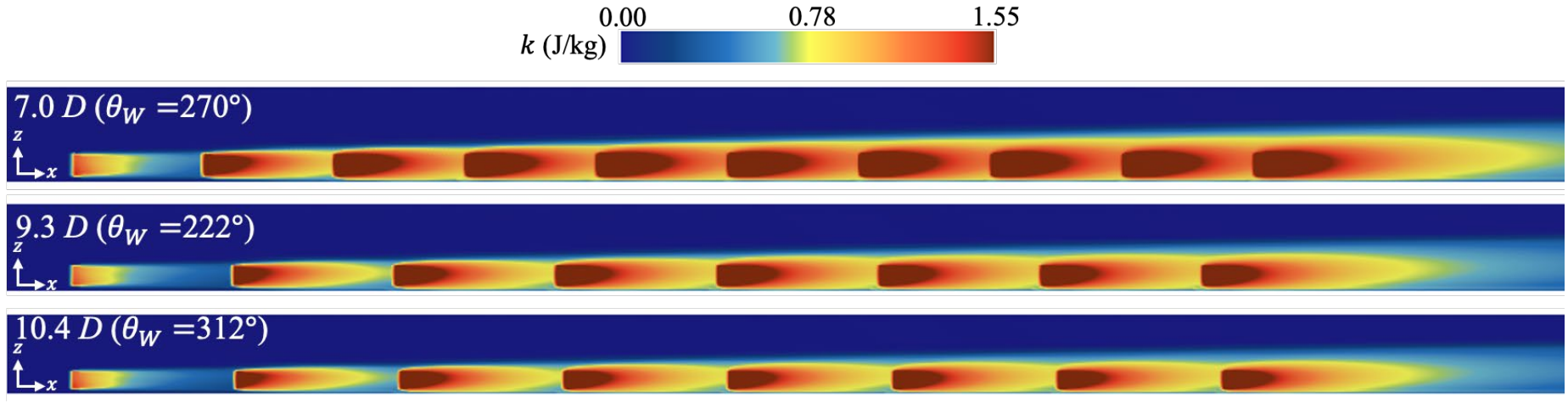

Figure 19 Contour of k for three wind direction at $y = 0$

doi:10.6342/NTU202503576

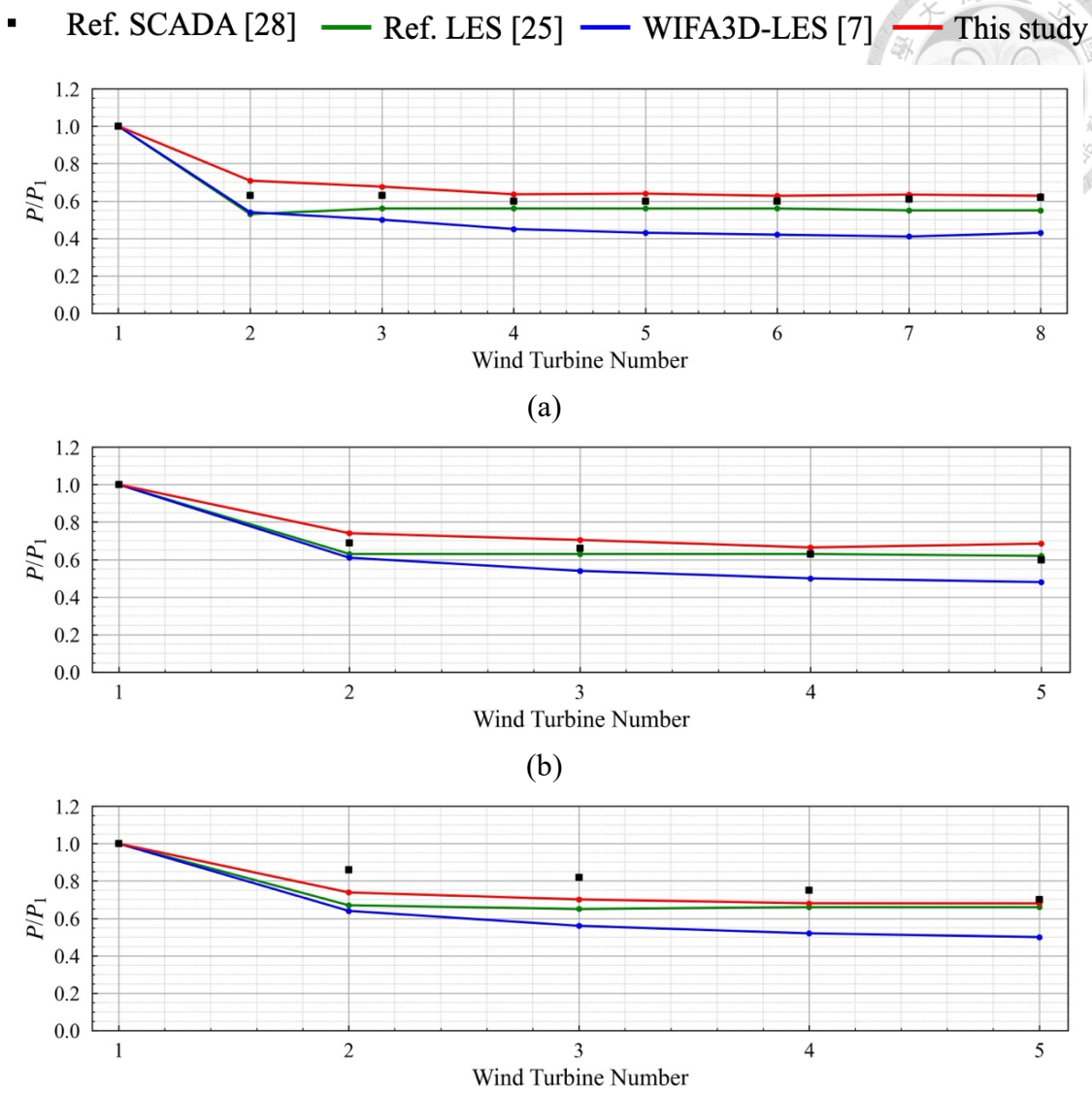

Figure 20 Comparison of P^*: (a) θ_w =270°, (b) θ_w =222°, and (c) θ_w =312°

doi:10.6342/NTU202503576

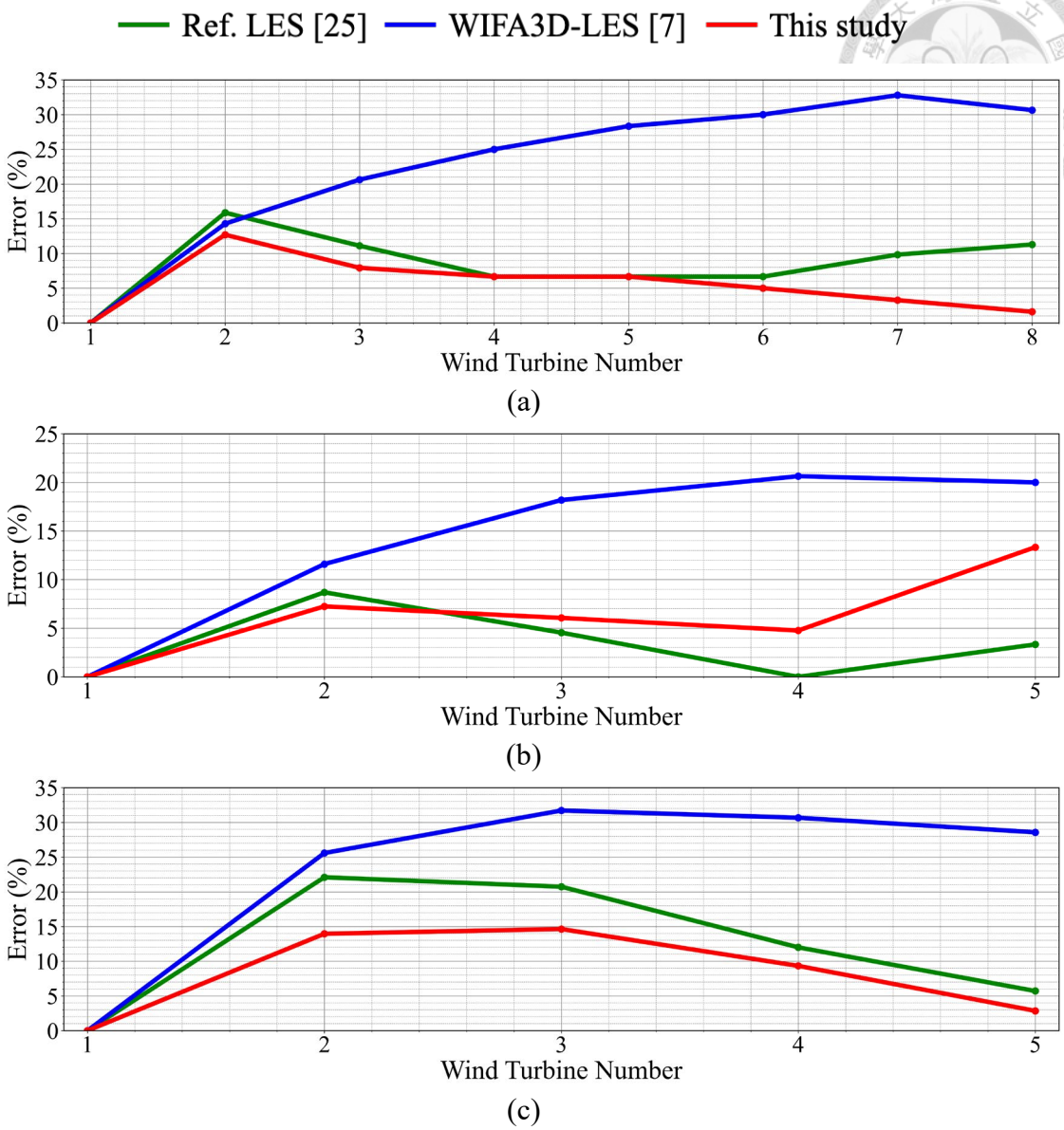

Figure 21 Error comparison between measured and simulated results: (a) $\theta_w = 270°$, (b) $\theta_w = 222°$, and (c) $\theta_w = 312°$

doi:10.6342/NTU202503576

4 Design Requirements

In this study, the investigated FOWT is assumed to adopt a semi-submersible platform. The natural periods of four typical FOWT types are summarized in Table 6, as reviewed by Subbulakshmi et al. [29]. To avoid the resonance in the platform's 6-DOF motions, a period range of 40-50 seconds is selected as the simulation condition of forced motions.

Several international standards have established operational thresholds to ensure the structural integrity and functional efficiency of FOWTs. According to DNV-RP-0286 [30], the mean tilt angle of a FOWT under normal operating conditions should not exceed 5°, a constraint designed to maintain platform stability and preserve consistent aerodynamic performance. In parallel, the COREWIND project [31] recommends that for deployment sites with water depths between 60 and 100 meters, the maximum horizontal offset of the floating platform should remain within 30 meters. This limitation ensures the continued effectiveness of slender mooring lines and dynamic cable configurations, enabling the floating structure to operate within a safe and controllable range. Exceeding these limits may not only degrade power generation efficiency due to rotor-wind misalignment, but also accelerate fatigue damage accumulation in the dynamic cable system, thereby jeopardizing the long-term structural reliability of the mooring infrastructure.

In addition, since existing international guidelines do not specify the mean translational excursion of semi-submersible FOWTs during normal operation, this study refers to Ishihara et al. [32], who conducted both simulation and water tank experiments on a 2 MW semi-submersible platform under representative operational sea states. Their results indicate that the maximum surge amplitude is approximately 2.5 meters. This

doi:10.6342/NTU202503576

study also uses the translational motions amplitude between 0.5 and 2.5 meters to investigate the small displacements effect on the wake behavior downstream of the rotor.

Table 6 Typical natural periods for different floating platforms [29]

6DOFs	Spar	Semi-submersible	Barge	TLP
Surge	>100 s	>100 s	>100 s	15-60 s
Sway				
Heave	25-40 s	15-25 s	5-10 s	1-2 s
Roll	25-40 s	25-40 s	9-16 s	2-5 s
Pitch				
Yaw	5-20 s	50-80 s	50-100 s	8-20 s

doi:10.6342/NTU202503576

5 Simulation Results

In this study, the inflow wind speed at U_{hub} is set to 9 m/s, 15 m/s, and 21 m/s, representing low, medium, and high wind conditions, respectively. The rotor speed (ω_r) is assumed to be 16.7 RPM. Initially, the simulation is performed under a stationary condition for 8 periods, allowing the wake to fully develop and reach the outflow boundary of the computational domain [33]. Following this, 18 periods are simulated under various 6-DOF motion scenarios to investigate the influence of platform dynamics on wake behavior. To facilitate detailed analysis of the wake behavior, a downstream region of area A_r is defined in the wake region. To facilitate a meaningful comparison with the wind turbine wake under stationary conditions, the wake obtained from the wind turbine in motion are evaluated based on the average velocity and the standard deviation over a complete operational cycle. These statistical measures, namely the time-averaged velocity and the standard deviation within one period, are defined as follows [34]:

$$\overline{U}_{avg}^{s} = \frac{1}{T}\int U_{avg}^{t} dt \,, \tag{30}$$

$$\bar{\sigma}_{avg}^{s} = \frac{1}{T}\int \sigma_{avg}^{t} dt \,, \tag{31}$$

where s denotes the number of periods. The quantity $\overline{U}_{avg}^{0}$ thus corresponds to the time-averaged velocity when the turbine is fixed. The velocity U_{avg}^{t} denotes the instantaneous velocity and σ_{avg}^{t} denotes the corresponding standard deviation are defined as follows:

$$U_{avg}^{t} = \frac{1}{A_r}\int U_x dA \,, \tag{32}$$

$$\sigma_{avg}^{t} = \sqrt{\frac{1}{A_r}\int (U_x - U_{avg})^2 \, dA} \,, \tag{33}$$

doi:10.6342/NTU202503576

where U_x is the axial velocity of the flow field in the x-direction. To evaluate the influence of 6-DOF platform motions on the wake behavior, the differences in $\overline{U}_{avg}^{s}$ and $\bar{\sigma}_{avg}^{s}$ between the fixed and floating wind turbine configurations are computed. These differences are denoted as $\Delta\overline{U}_{avg}^{*}$ and $\Delta\bar{\sigma}_{avg}^{*}$, respectively, as follows

$$\Delta\overline{U}_{avg}^{*} = \frac{\overline{U}_{avg}^{s} - \overline{U}_{avg}^{0}}{\overline{U}_{avg}^{0}} \times 100\% , \tag{34}$$

$$\Delta\bar{\sigma}_{avg}^{*} = \frac{\bar{\sigma}_{avg}^{s} - \bar{\sigma}_{avg}^{0}}{\bar{\sigma}_{avg}^{0}} \times 100\% . \tag{35}$$

The sinusoidal motions applied to the turbine platform are defined by varying amplitudes in both translational and rotational directions. The translational motion amplitudes (ζ_T) are set to 0.5 m, 1.0 m, 1.5 m, 2.0 m, and 2.5 m, while the rotational motion amplitudes (ζ_R) are set to 1°, 2°, 3°, 4°, and 5°. All motion cases are evaluated under three sinusoidal periods (T_p) of 40 s, 45 s, and 50 s. The detailed configurations and parameters for each case are summarized in Table 7 and Table 8.

Table 7 Translational motion case description

Parameter	Unit	Translational Motions
U_{hub}	m/s	9/15/21
ω_r	RPM	16.7
T_p	s	40/45/50
ζ_T	m	0.5/1.0/1.5/2.0/2.5

Table 8 Rotational motion case description

Parameter	Unit	Rotational Motions
U_{hub}	m/s	9/15/21
ω_r	RPM	16.7
T_p	s	40/45/50
ζ_R	°	1/2/3/4/5

doi:10.6342/NTU202503576

5. Simulation Results

To investigate wake behavior under large amplitude conditions, the surge and sway motion amplitudes of FOWT are varied from 5 to 30 m in increments of 5 m. A summary of the configuration for the large amplitude condition simulations is presented in Table 9.

Table 9 Large amplitude condition case description

Parameter	Unit	Surge and Sway Motion
U_{hub}	m/s	9/15/21
ω_r	RPM	16.7
T_p	s	40/45/50
ζ_T	m	5/10/15/20/25/30

doi:10.6342/NTU202503576

5.1 Translational Motions

In this section, the wake behavior of a FOWT is examined under three different wind speeds and three distinct platform motion periods. The investigation focuses on the effects of single DOF translational motions on wake characteristics. Specifically, both the normalized time-averaged velocity and the normalized time-averaged standard deviation are evaluated and compared. The results are presented and discussed in Section 5.1.1, Section 5.1.2, and Section 5.1.3, respectively, with a consolidated summary provided in Section 5.1.4.

To examine the transient development and convergence characteristics of $\Delta\overline{U}^*_{avg}$, the results of surge, sway, and heave motions are presented in Figure 22 (a), (b), and (c), respectively. In this example, the simulations are performed with an inflow wind speed of 9 m/s, $\zeta_T = 0.5$ m, and T_p = 45 s. The *x*-axis represents the number of period (N_T), and the *y*-axis indicates the corresponding $\Delta\overline{U}^*_{avg}$ in percentage. Each case includes 26 full motion cycles. In addition, all three translational motions of freedom exhibit a rapid change in $\Delta\overline{U}^*_{avg}$ within the initial 10 cycles. Subsequently, the values gradually stabilize and approach a steady plateau around $N_T = 15$. This indicates that the flow field has transitioned into a statistically steady state. Based on this fact, $N_T = 26$ is selected as the representative result for downstream wake analysis of this study. This practice ensures that all comparisons are based on time-converged data and reflects the long-term aerodynamic influence of each translational platform motion on the wake field.

doi:10.6342/NTU202503576

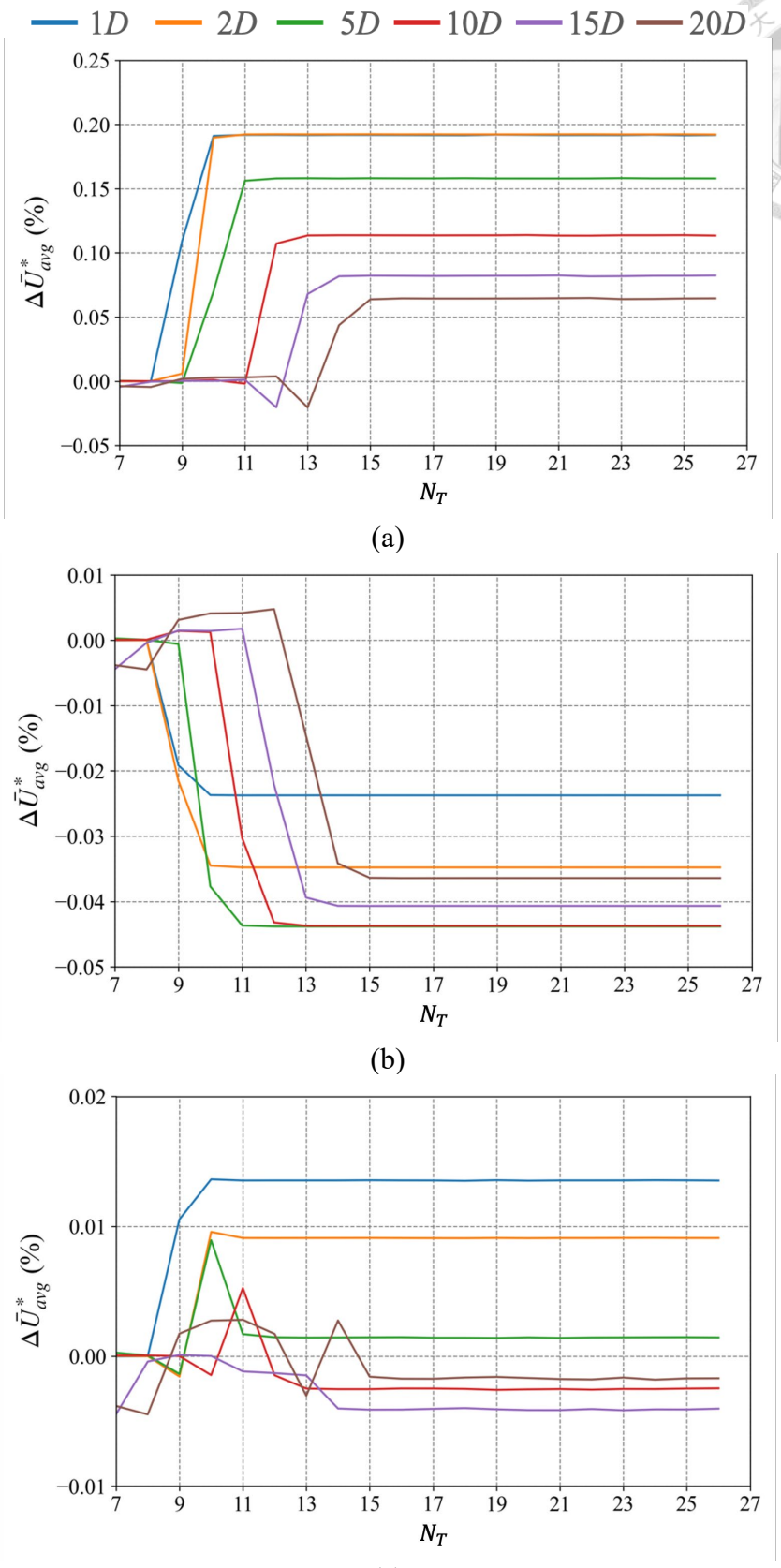

Figure 22 Evolution of $\Delta\bar{U}^*_{avg}$ over 26 periods under (a) surge, (b) sway and (c) heave motion with $U_{avg} = 9$ m/s, $T_p = 45$ s, and $\zeta_T = 0.5$ m

doi:10.6342/NTU202503576

5.1.1 Surging Behavior

Figure 23 illustrates $\Delta\overline{U}^{*}_{avg}$ along downstream direction induced by the surge motion with amplitudes ranging from 0.5 m to 2.5 m at the wind speed of 9, 15, and 21 m/s and T_p = 45 s. The results demonstrate that the effectiveness of surge-induced motion in promoting wake mixing is strongly dependent on both surge amplitude and ambient wind speed. At $U_{hub} = 9$ m/s, even small amplitudes produce significant and spatially persistent increases in downstream velocity, indicating high wake sensitivity to dynamic motion under low ambient momentum. Notably, the maximum velocity increment reaches 0.22% at $x = 2D$ downstream, followed by a gradual attenuation with distance. This behavior is attributed to lower flow inertia and momentum, which allow turbine-induced disturbances to propagate more effectively and foster wake recovery. Li et al. [35] and Guntur et al. [36] corroborated these findings, showing intensified shear-layer instabilities and improved wake diffusion under low wind conditions. At $U_{hub} =$ 15 m/s, a threshold-like response emerges, where only surge amplitudes exceeding 2.0 m generate meaningful wake recovery, suggesting that stronger motion is necessary to overcome the stabilizing influence of higher inflow momentum. At $U_{hub} = 21$ m/s, the wake response is minimal, with only marginal positive effects observed within a narrow amplitude range. These trends confirm that as inflow velocity increases, the wake becomes progressively less receptive to motion-induced perturbations due to elevated ambient inertia, leading to a more coherent and stable wake structure under moderate to high wind conditions.

Figure 24 illustrates the downstream behavior of $\Delta\overline{U}^{*}_{avg}$ induced by the surge motion with amplitudes ranging from 0.5 m to 2.5 m at a wind speed of 15 m/s and T_p = 40, 45, and 50 s, respectively. Across all three cases, the overall magnitude of the velocity

doi:10.6342/NTU202503576

recovery remains relatively small, and positive wake velocity increments emerge only when the surge amplitude exceeds 2.0 m, consistent with the threshold-like response observed under varying temporal conditions. At $U_{hub} = 9$ m/s, the maximum velocity increment occurs further downstream, approximately at $x = 7D$. For the $U_{hub} = 15$ m/s cases, the case of $T_p = 40$ s yields the highest recovery, reaching 0.065%, followed by 0.061% for the $T_p = 45$ s case, and 0.059% for the case of $T_p = 50$ s case. These results suggest that short-period surge motions may facilitate more intense energy transfer and turbulence generation within the near wake region. Nevertheless, despite the observable differences among these cases, the absolute values of $\Delta\overline{U}^*_{avg}$ remain on the order of 10^{-4} or lower. Consequently, the influence of surge period variation on wake recovery is suggested limited.

doi:10.6342/NTU202503576

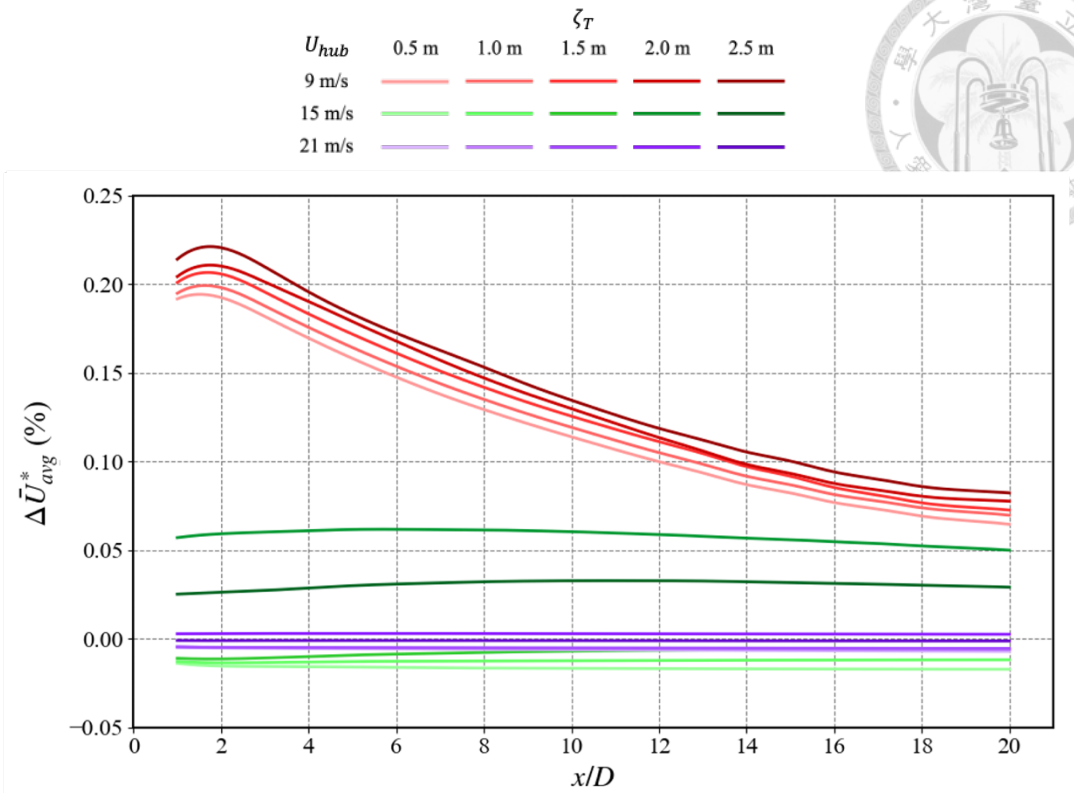

Figure 23 Downstream evolution of $\Delta\bar{U}^*_{avg}$ under surge motions at 9, 15, and 21 m/s with a fixed period of 45 s

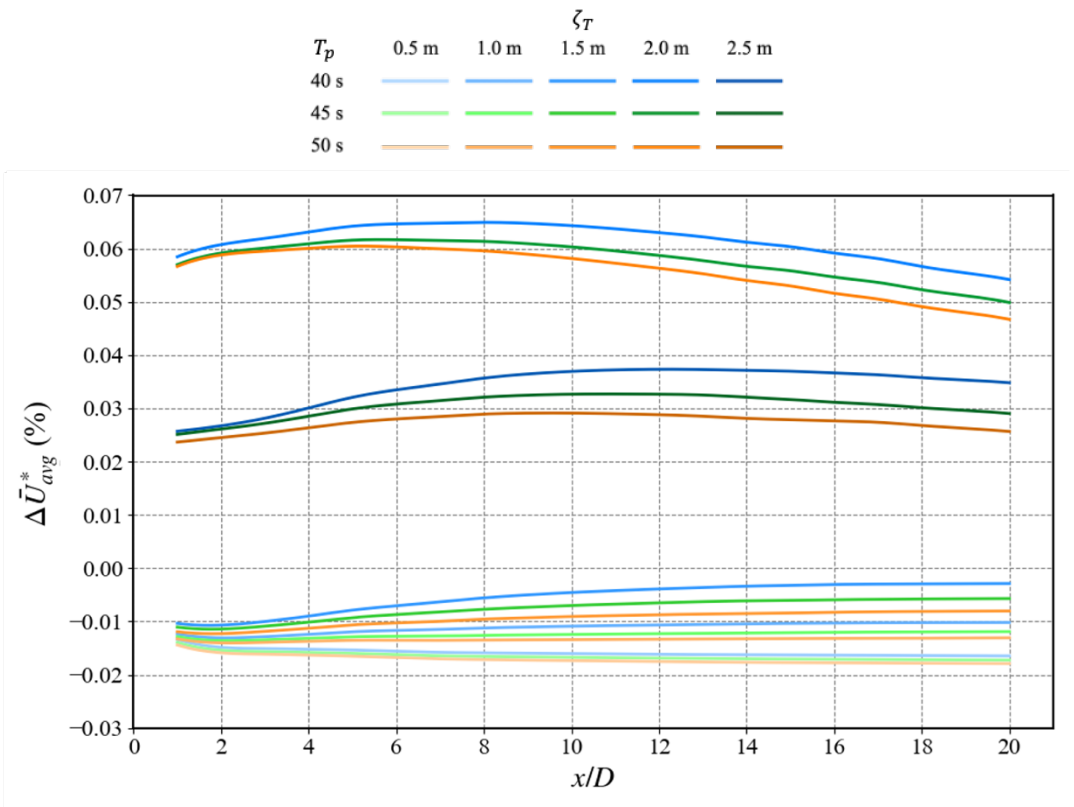

doi:10.6342/NTU202503576

Figure 24 Downstream evolution of $\Delta\overline{U}^*_{avg}$ under surge motions at 15 m/s with periods of 40, 45, and 50 s

doi:10.6342/NTU202503576

Figure 25 illustrates the $\Delta\bar{\sigma}^*_{avg}$ induced by the surge motion with amplitudes ranging from 0.5 m to 2.5 m at the wind speed of 9, 15, and 21 m/s and T_p = 45 s. At $U_{hub} = 9$ m/s, increasing surge amplitude leads to a pronounced rise in wake standard deviation, especially beyond $\zeta_T = 2.0$ m, indicating that dynamic motion effectively amplifies wake disturbance under low ambient momentum. At $U_{hub} = 15$ m/s, the response becomes more intricate small amplitudes initially increase wake variability, a local drop in standard deviation appears at $\zeta_T = 2.0$ m, followed by a slight rebound at $\zeta_T = 2.5$ m. This non-monotonic behavior suggests a transitional balance between disturbance generation by turbine motion and stabilization by the ambient flow. At $U_{hub} = 21$ m/s, the standard deviation remains consistently low across all amplitudes, demonstrating minimal wake sensitivity to surge-induced motion. These findings indicate that the capacity of surge motion to intensify wake disturbance diminishes with increasing wind speed, where stronger inflow inertia suppresses perturbation development. Overall, the response of $\Delta\bar{\sigma}^*_{avg}$ to surge motion varies significantly across the three inflow wind speeds, reflecting the dominant role of ambient momentum in regulating wake turbulence. As wind speed increases, the wake becomes progressively governed by inertial stability rather than by dynamic excitation.

Figure 26 illustrates the $\Delta\bar{\sigma}^*_{avg}$ induced by the surge motion with amplitudes ranging from 0.5 m to 2.5 m at a wind speed of 15 m/s and T_p = 40, 45, and 45 s, respectively. At a period of 40 s, large surge amplitudes lead to a pronounced increase in standard deviation along the downstream direction, indicating enhanced disturbance as a result of more frequent energy input. In contrast, the $T_p = 50$ s case exhibits a noticeable reduction in standard deviation at similar amplitudes, suggesting that longer-period oscillations may promote wake stabilization, particularly in the near-wake region. The

doi:10.6342/NTU202503576

$T_p = 45$ s case lies between these two extremes, displaying non-monotonic behavior characterized by partial suppression followed by a moderate recovery in disturbance. While observable differences exist across the tested surge periods, the overall magnitudes of $\Delta\bar{\sigma}^*_{avg}$ remain relatively small, typically on the order of 10^{-3} or less. Across all cases, small surge amplitudes yield stable and slightly positive standard deviation values, indicating only modest perturbation to the wake. These findings suggest that although surge period variation can influence wake disturbance to some extent, its practical impact is quite limited compared to that of surge amplitude.

doi:10.6342/NTU202503576

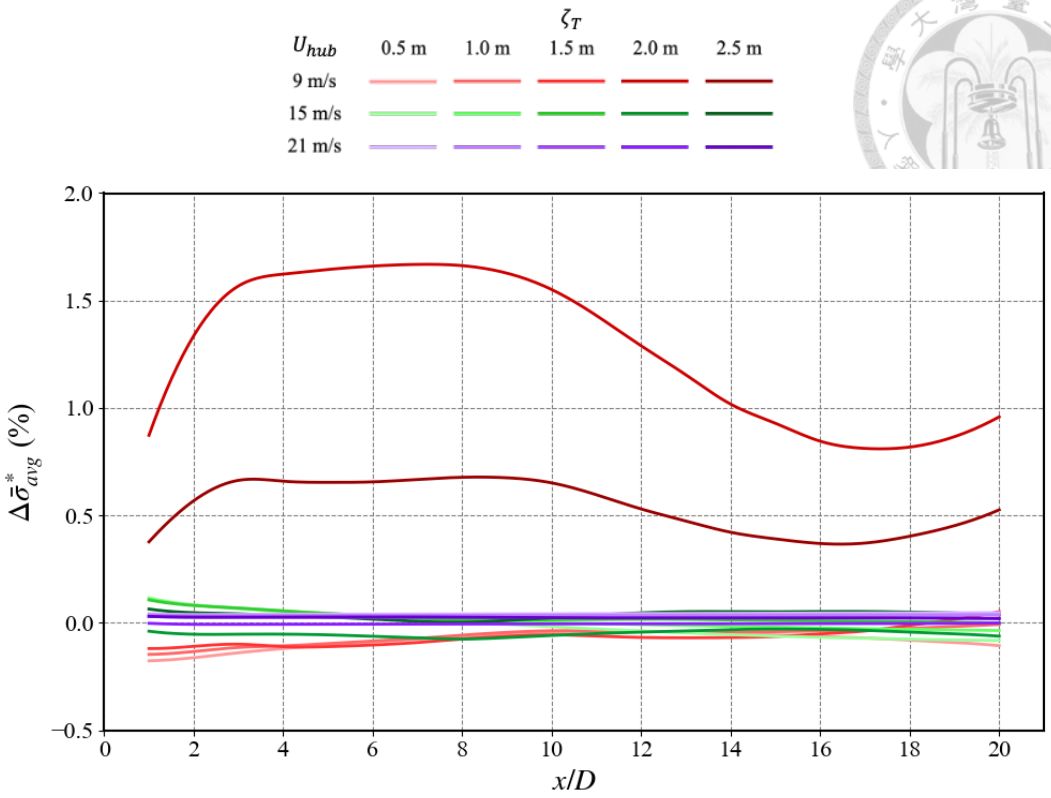

Figure 25 Downstream evolution of $\Delta\bar{\sigma}^*_{avg}$ under surge motions at 9, 15, and 21 m/s with a fixed period of 45 s

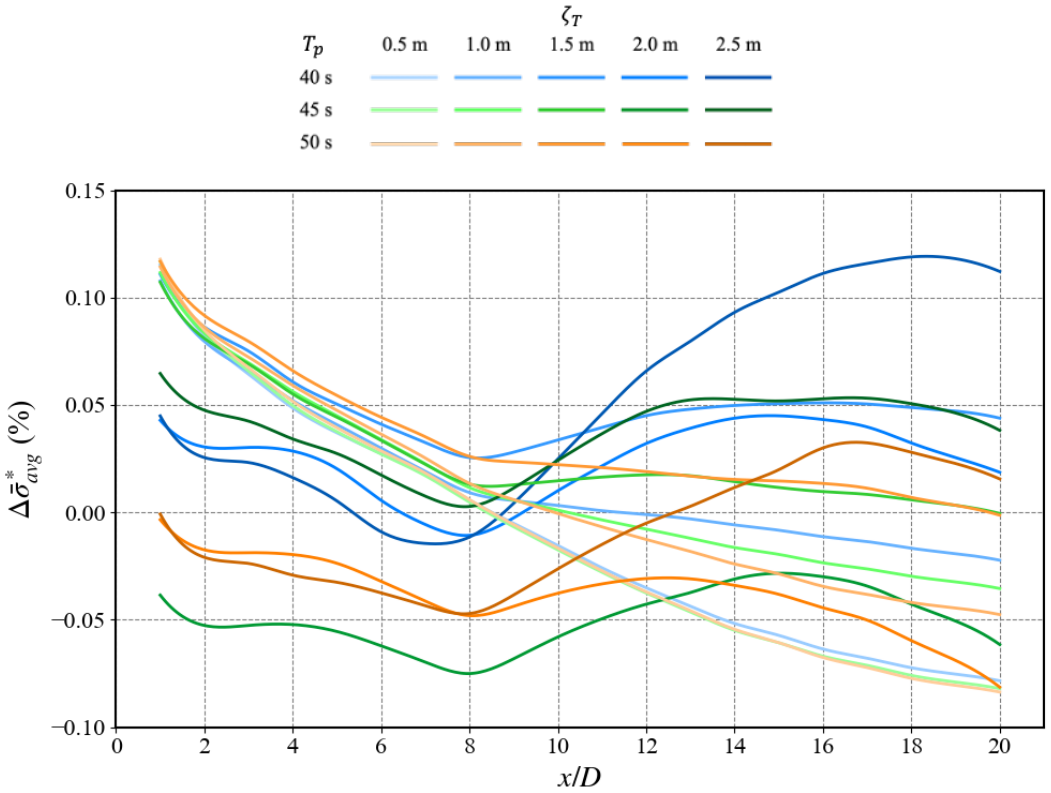

Figure 26 Downstream evolution of $\Delta\sigma^*_{avg}$ under surge motions at 15 m/s with periods of 40, 45, and 50 s

doi:10.6342/NTU202503576

Figure 27 illustrates the downstream behavior of $\Delta\overline{U}^*_{avg}$ induced by the large amplitude surge motion with amplitudes ranging from 5 to 30 m at the wind speed of 9, 15, 21 m/s and T_p = 45 s. At $U_{hub} = 9$ m/s, the velocity increment exhibits a consistently positive trend with increasing surge amplitude and downstream distance, reaching up to approximately 2.59% at a 30 m surge amplitude around $x = D$. At $U_{hub} = 15$ m/s, $\Delta\overline{U}^*_{avg}$ is initially negative in the near-wake region, particularly within $x = 6D$, reflecting a deeper velocity deficit. However, the values gradually become positive beyond $x = 7D$, attaining a maximum of approximately 0.425% at 30 m and $x = 20D$. At $U_{hub} = 21$ m/s, the influence of surge motion becomes minimal. The velocity increments remain mostly negative or close to zero throughout the domain, with only marginal positive values below 0.012% observed at the largest amplitudes and farthest downstream locations. These observations indicate that the effectiveness of surge-induced wake recovery diminishes as the wind speed increases. At low wind speed, strong flow interaction promotes efficient momentum entrainment, resulting in uniform and significant wake recovery. At moderate wind speed, wake response is delayed but shows noticeable downstream recovery. At high wind speed, the wake appears largely insensitive to surge motion due to increased flow inertia, leading to limited dynamic modulation. Overall, surge-induced wake recovery is most effective under low wind speed conditions and becomes progressively weaker as the turbine operates toward its rated regime.

Figure 28 illustrates the downstream behavior of $\Delta\overline{U}^*_{avg}$ induced by the large amplitude surge motion with amplitudes ranging from 5 to 30 m at a wind speed of 15 m/s and T_p = 40, 45, 50 s. Under a speed of 15 m/s, $\Delta\overline{U}^*_{avg}$ demonstrates clear sensitivity to the surge motion period. For a period of 40 seconds, the wake exhibits the

doi:10.6342/NTU202503576

earliest and most pronounced transition from negative to positive wake velocity increments, beginning around $x = 8D$ and reaching a peak of approximately 0.57% at ζ_T = 30 m and $x = 20D$. In comparison, the 45-second case yields a slightly small peak of 0.425%, with the transition occurring between $x = 6D$ and $x = 8D$. The 50-second case exhibits the weakest response, with positive increments appearing only beyond $x = 10D$ and peaking at about 0.32%. These trends suggest that short surge motion periods are more effective in reducing the wake deficit, likely due to an enhanced turbulent mixing. The 40-second case demonstrates vigorous flow modulation induced by higher-frequency motions, while the 45-second case represents a balance between motion frequency and wake response. In contrast, the 50-second case indicates a delayed and weak wake recovery. Despite the varying motion magnitudes, the overall trend is consistent: short surge periods result in early and strong wake recovery, while long periods reduce the impact of the surge motion.

doi:10.6342/NTU202503576

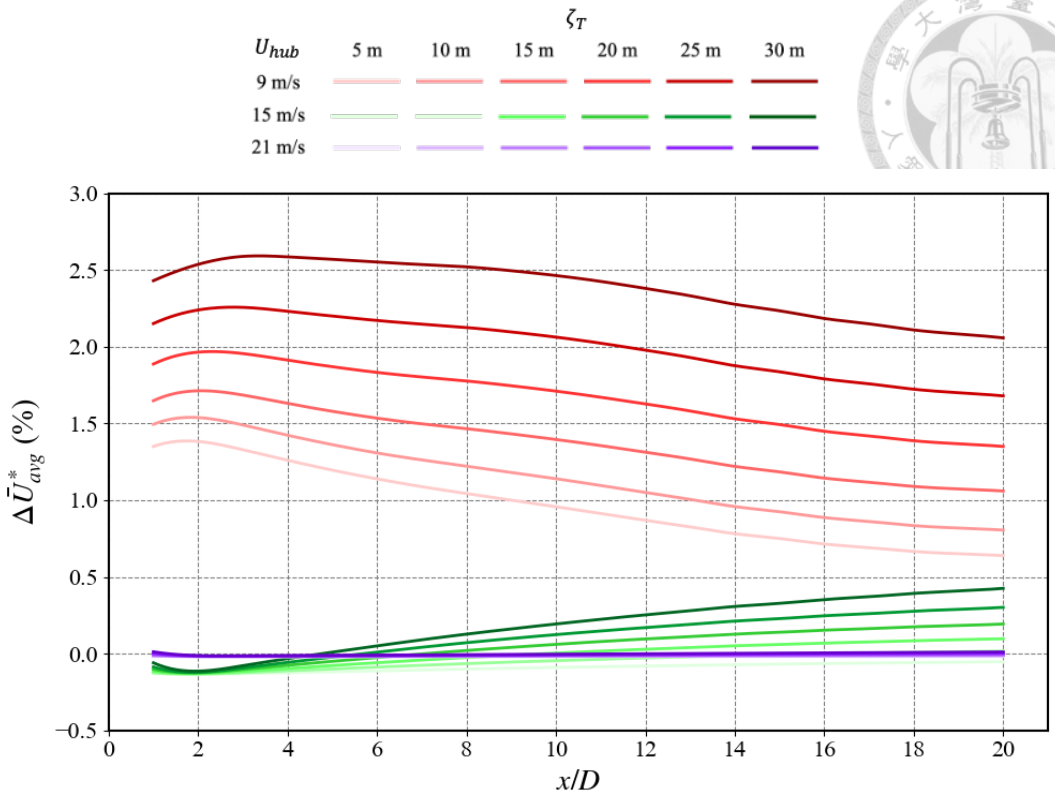

Figure 27 Downstream evolution of $\Delta\bar{U}^*_{avg}$ under large amplitude surge motions at 9, 15, and 21 m/s with a fixed period of 45 s

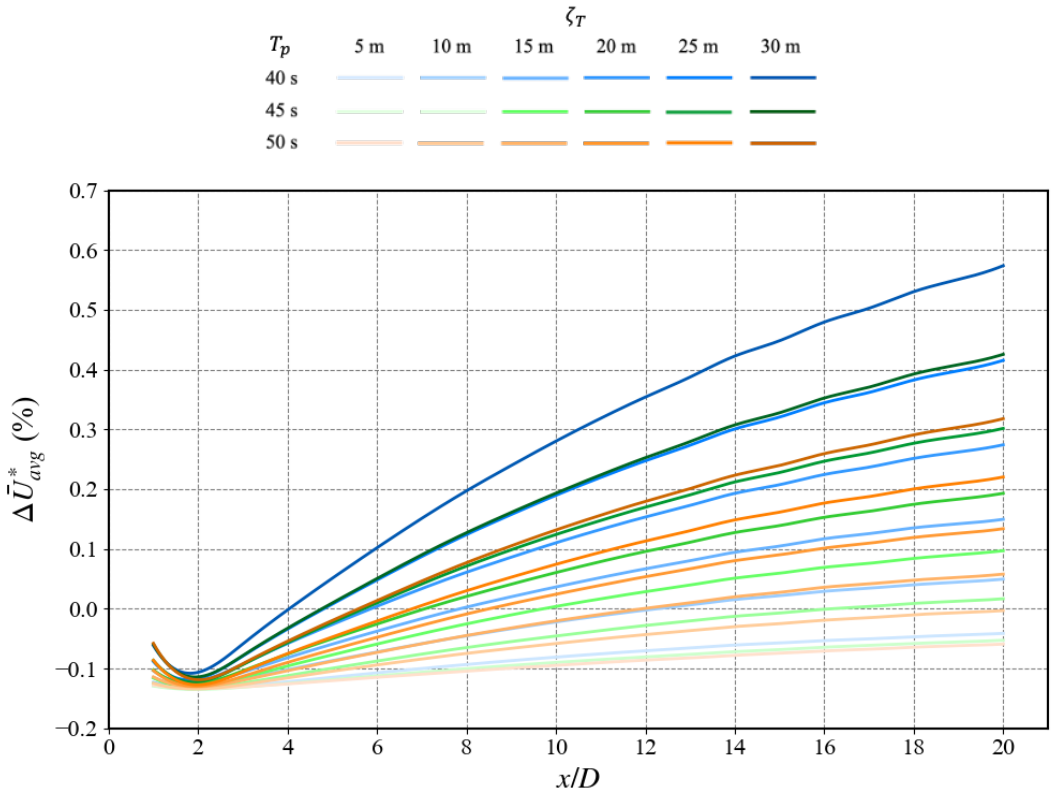

Figure 28 Downstream evolution of $\Delta\bar{U}^*_{avg}$ under large amplitude surge motions at 15 m/s with periods of 40, 45, and 50 s

doi:10.6342/NTU202503576

Figure 29 illustrates the downstream behavior of $\Delta\bar{\sigma}^*_{avg}$ induced by the large amplitude surge motion with amplitudes ranging from 5 to 30 m at the wind speed of 9, 15, 21 m/s and T_p = 45 s. At $U_{hub} = 9$ m/s, $\Delta\bar{\sigma}^*_{avg}$ is predominantly negative throughout most of the domain, reaching a minimum of approximately -5% at $x = 15D$ for a 30 m surge amplitude. A local change from negative to positive values occurs near the rotor, peaking at about 0.7% at $x = D$ under the same amplitude. At $U_{hub} = 15$ m/s, the standard deviation increases consistently with both surge amplitude and downstream distance. Starting at around 0.2% near the rotor, $\Delta\bar{\sigma}^*_{avg}$ rises steadily and reaches over 4.3% at $x = 20D$ and $\zeta_T = 30$ m, following a nearly linear growth pattern. In contrast, at $U_{hub} = 21$ m/s, the standard deviation remains uniformly low across all amplitudes and locations, with peak values below 0.12%, even at the farthest downstream positions. These results indicate that surge-induced wake recovery is most pronounced under moderate inflow wind conditions, where the wake demonstrates significant sensitivity to unsteady platform motion. At high wind speeds, the recovery effect diminishes due to high flow inertia which suppresses the development of unsteady flow. This trend highlights the nonlinear nature of the aerodynamic coupling between platform motion and wake response, which is strongly dependent on the incoming wind speed.

Figure 30 illustrates the downstream behavior of $\Delta\bar{\sigma}^*_{avg}$ induced by large amplitude surge motion with amplitudes ranging from 5 to 30 m at a wind speed of 15 m/s and T_p = 40, 45, 50 s. Among three cases, the 40-second period case produces the strongest and most rapid amplification of wake velocity fluctuation, with $\Delta\bar{\sigma}^*_{avg}$ peaking at approximately 5.09% at a 30 m surge amplitude near $x = 17D$. The 45-second period case follows closely, yielding a slightly lower peak of 4.47%. In contrast, the 50-second period case results in the weakest response, with a maximum value of 3.81% under the

doi:10.6342/NTU202503576

same conditions. While the case of three surge periods exhibits a broadly similar trend of increasing $\Delta\bar{\sigma}^{*}_{avg}$ with surge amplitude and downstream distance, the magnitude and rate of this increase vary significantly. The 40-second period case demonstrates the most pronounced and rapid recovery, suggesting that higher-frequency surge motion more effectively excites energy between the wake and the rotor region. The 45-second period case produces substantial but slightly dampened disturbance, whereas the 50-second period case displays a more gradual and subdued response, indicating that lower-frequency motion is less efficient in enhancing energy exchange to the wake. Under an identical wind speed and motion amplitude, the surge motion period plays a pivotal role in affecting the wake behavior.

doi:10.6342/NTU202503576

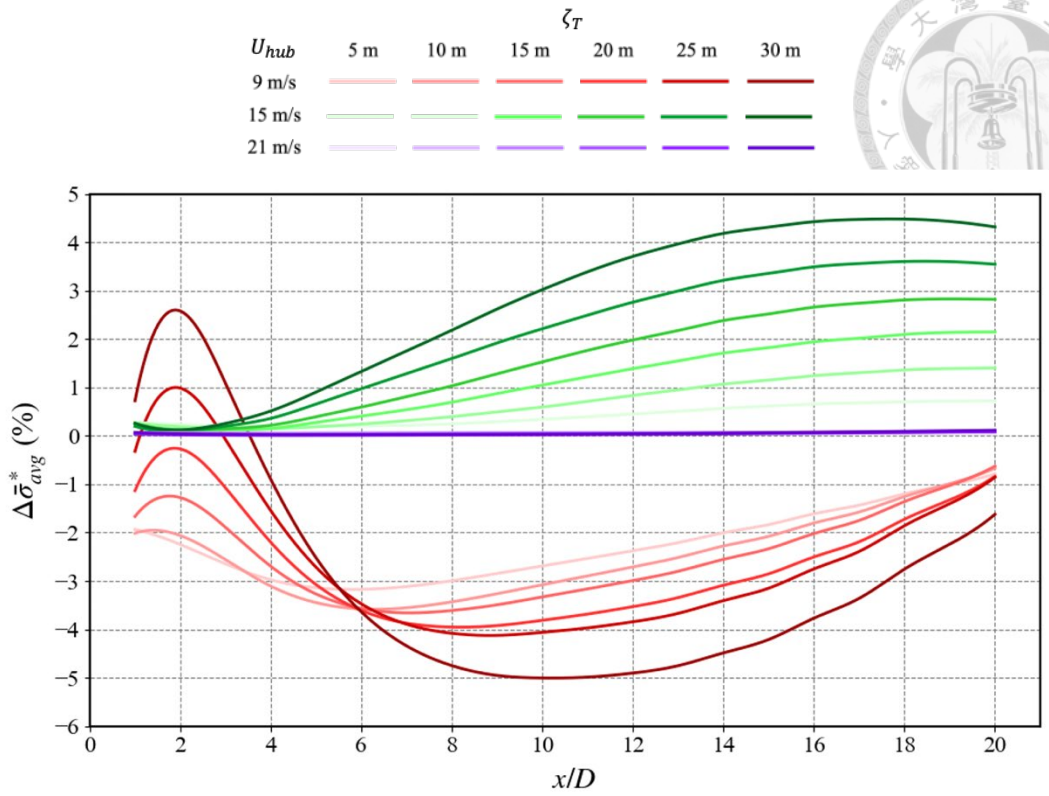

Figure 29 Downstream evolution of $\Delta\bar{\sigma}^*_{avg}$ under large amplitude surge motions at 9, 15, and 21 m/s with a fixed period of 45 s

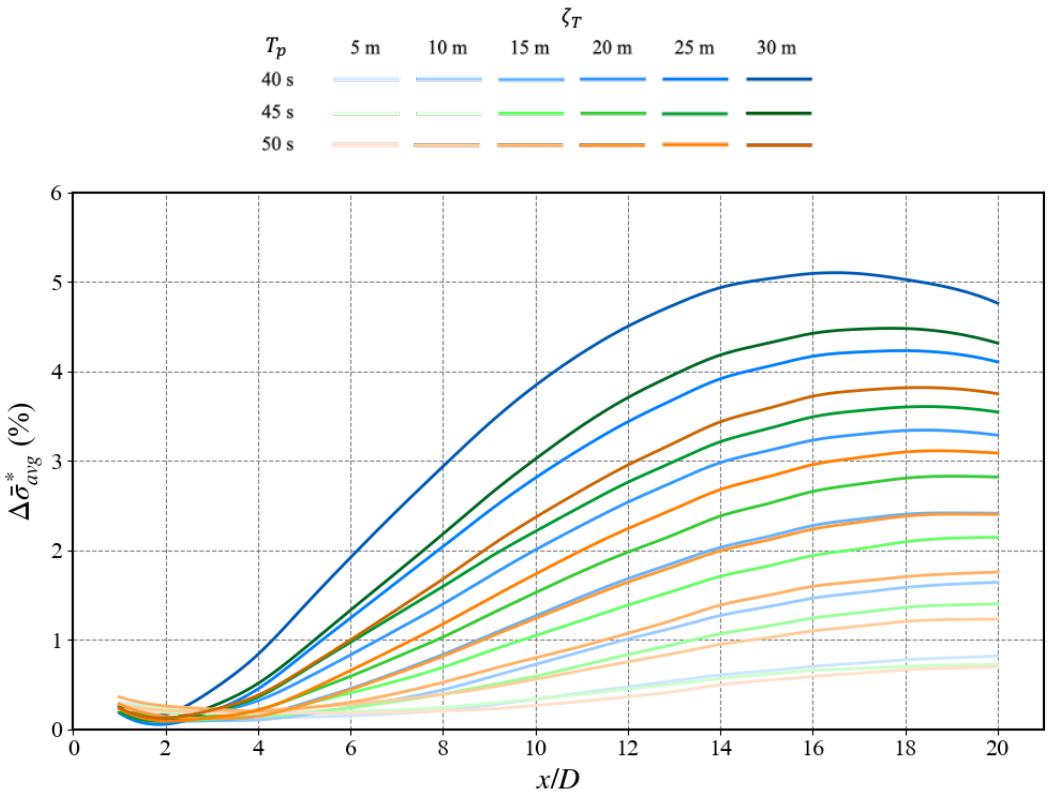

Figure 30 Downstream evolution of $\Delta\bar{\sigma}^*_{avg}$ under large amplitude surge motions at 15 m/s with periods of 40, 45, and 50 s

doi:10.6342/NTU202503576

5.1.2 Swaying Behavior

Figure 31 illustrates the downstream behavior of $\Delta\overline{U}^*_{avg}$ induced by the sway motion with amplitudes ranging from 0.5 m to 2.5 m at the wind speed of 9, 15, and 21 m/s and T_p = 45 s. The results demonstrate a consistent positive correlation between sway amplitude and wake velocity recovery across all tested wind speeds, although the magnitude of wake recovery is clearly influenced by the incoming flow condition. At $U_{hub} = 9$ m/s, the sway-induced motion leads to a substantial increase in downstream velocity, with the increment at $x = 1D$ rising from -0.023% at $\zeta_T = 0.5$ m to 0.219% at $\zeta_T = 2.5$ m. This trend persists throughout the wake but gradually diminishes with downstream distance. For example, at $x = 20D$, $\Delta\overline{U}^*_{avg}$ of $\zeta_T = 2.5$ m drops to 0.093%, while it becomes nearly negligible at $\zeta_T = 0.5$ m, indicating that the wake recovery is most prominent in the near-wake region. At $U_{hub} = 15$ m/s, the recovery remains moderate, where the velocity growth increases steadily with sway amplitude at $x = D$ and decays gradually downstream. In contrast, at $U_{hub} = 21$ m/s, the wake recovery is significantly weaker and begins from a small negative value at low amplitude, reflecting a limited influence of lateral motion in high freestream momentum. Although this effect is suppressed at high wind speeds, the spatial decay of wake recovery remains smooth, and the overall wake structure preserves its coherence over a longer distance. These observations indicate that while the sway-induced motion effectively promotes wake recovery under low wind speed conditions, its impact diminishes as the inflow inertia increases.

Figure 32 illustrates the downstream behavior of $\Delta\overline{U}^*_{avg}$ induced by the sway motion with amplitudes ranging from 0.5 m to 2.5 m at $U_{hub} = 15$ m/s and T_p = 40, 45, and 50 s. The results show that regardless of the period, the differences in wake velocity

doi:10.6342/NTU202503576

increment remain small across all amplitudes and downstream positions. In all cases, increasing the sway amplitude leads to higher downstream velocity increments, followed by a gradual decay along the streamwise direction. These findings suggest that under the tested flow conditions, changes in sway period have only a limited effect on wake recovery, while the motion amplitude remains the primary factor influencing wake behavior.

doi:10.6342/NTU202503576

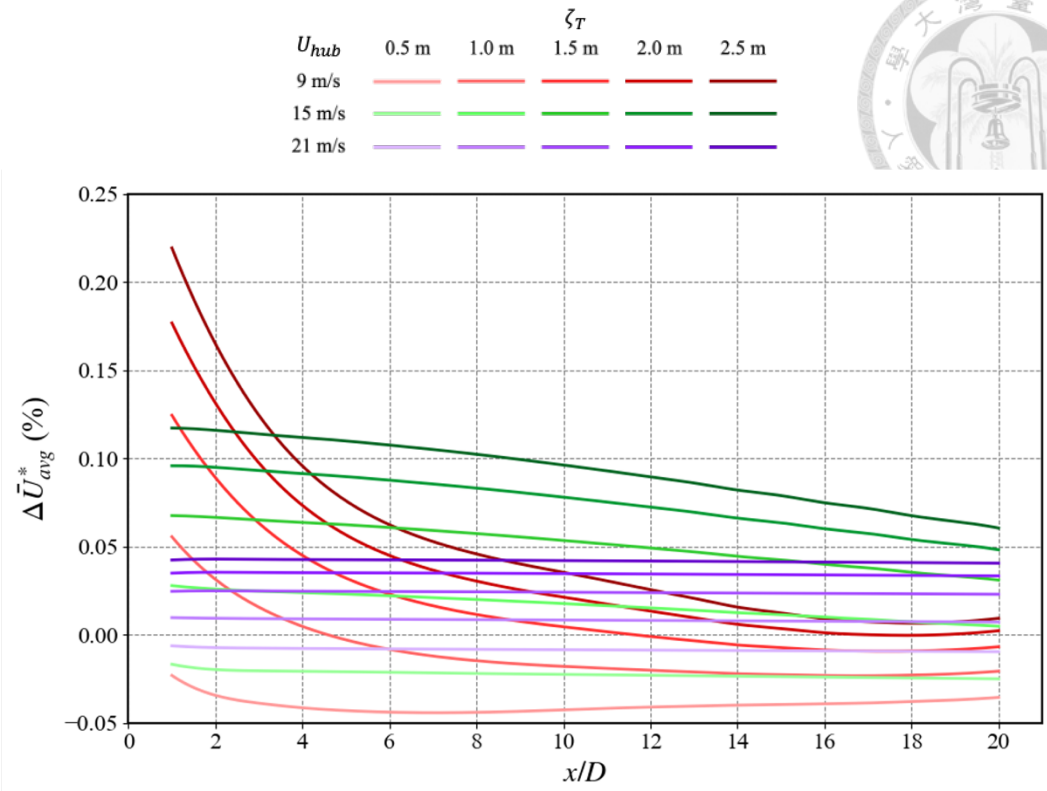

Figure 31 Downstream evolution of $\Delta\bar{U}^*_{avg}$ under sway motions at 9, 15, and 21 m/s with a fixed period of 45 s

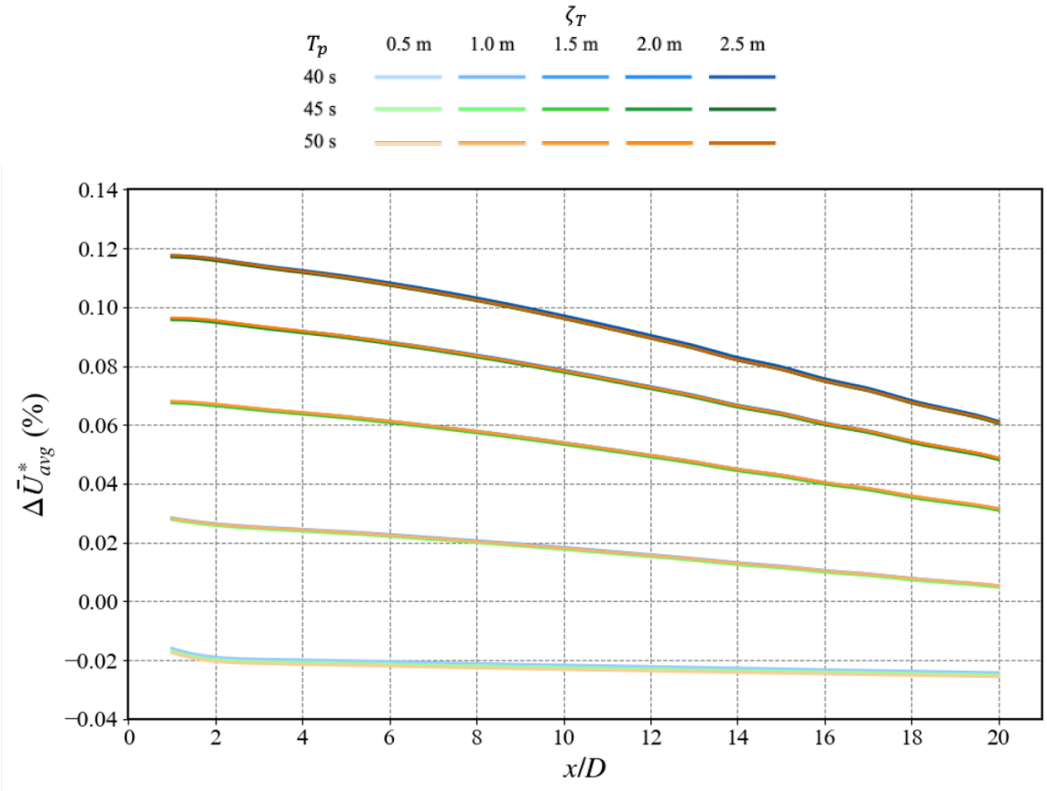

Figure 32 Downstream evolution of $\Delta\bar{U}^*_{avg}$ under sway motions at 15 m/s with periods of 40, 45, and 50 s

doi:10.6342/NTU202503576

Figure 33 illustrates $\Delta\bar{\sigma}^*_{avg}$ of the sway motion with amplitudes ranging from 0.5 m to 2.5 m at the wind speed of 9, 15, and 21 m/s and T_p = 45 s. At $U_{hub} = 9$ m/s, the standard deviation difference increases markedly with sway amplitude. For example, at an amplitude of 2.5 m, it reaches approximately 2.76% near $x = D$ downstream, indicating significant wake recovery induced by the imposed lateral motion. In contrast, for $\zeta_T = 0.5$ m, the standard deviation difference remains mostly negative or near zero before $x = 10D$, suggesting a weak influence of low-amplitude sway motions. As the wind speed increases to 15 m/s, $\Delta\bar{\sigma}^*_{avg}$ decrease noticeably. At $\zeta_T = 2.5$ m, the peak value at $x = D$ reduces to about 0.90% and continues declining downstream, while lower amplitudes exhibit values around 0.2% or less. At $U_{hub} = 21$ m/s, the wake recovery is further diminished. Even under the largest motion amplitude, the standard deviation difference at $x = D$ is limited to approximately 0.16%, falling below 0.1% beyond $x = 5D$, and consistently remaining under 0.05% for the motion amplitudes below 1.5 m. These results suggest that although large sway amplitudes can induce measurable wake disturbance, the absolute magnitude of the effect is highly sensitive to the background wind speed. As the ambient momentum increases, the development of velocity fluctuations becomes quite restricted, particularly in the far-wake region. Furthermore, the spatial decay of standard deviation becomes rather rapid at high wind speeds, reflecting strong damping effects of high wind speeds that suppress the persistence of motion-induced disturbances.

Figure 34 illustrates the $\Delta\bar{\sigma}^*_{avg}$ induced by the sway motion with amplitudes ranging from 0.5 m to 2.5 m at a wind speed of 15 m/s and T_p = 40, 45, and 50 s. At this fixed wind speed, changes in motion period have a noticeable impact on the level of wake disturbance. The motion with long sway periods generally leads to low $\Delta\bar{\sigma}^*_{avg}$ compared

doi:10.6342/NTU202503576

to those with short sway periods, although the overall trend of associated with the sway amplitude remains consistent. For instance, at $\zeta_T = 2.5$ m, $\Delta\bar{\sigma}^*_{avg}$ reaches approximately 0.884% near $x = D$ downstream for $T_p = 40$ s, increases slightly to about 0.906% at $T_p = 45$ s, and decreases to around 0.915% at $T_p = 50$ s. Despite these variations, all cases demonstrate that the growth of sway amplitude results in strong wake fluctuations near the turbine and these fluctuations decay gradually with downstream distance. At small sway amplitudes, $\Delta\bar{\sigma}^*_{avg}$ remains small and falls below 0.1% beyond $x = 10D$. These findings suggest the sway period negatively affects the degree of wake disturbance and the fundamental trend of amplitude-driven fluctuation and spatial decay is similar across all tested conditions. The combined influence of sway amplitude and oscillation frequency remains dominant in shaping both the intensity and the extend of wake disturbances.

doi:10.6342/NTU202503576

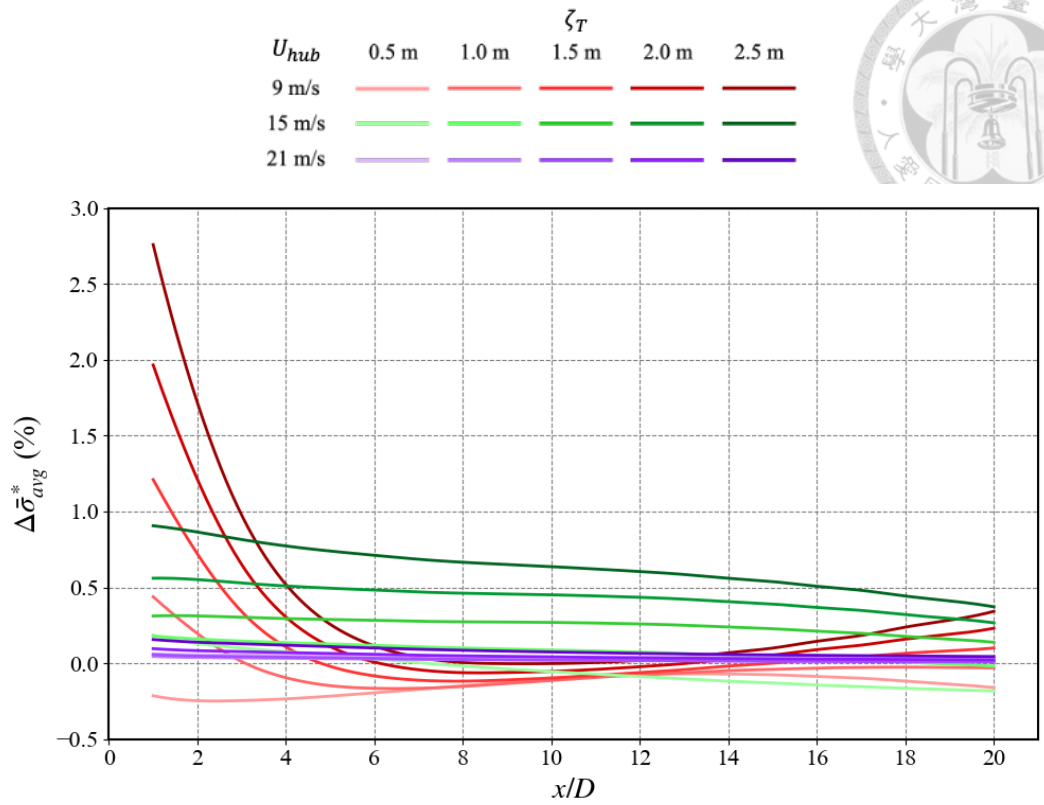

Figure 33 Downstream evolution of $\Delta\bar{\sigma}^*_{avg}$ under sway motions at 9, 15, and 21 m/s with a fixed period of 45 s

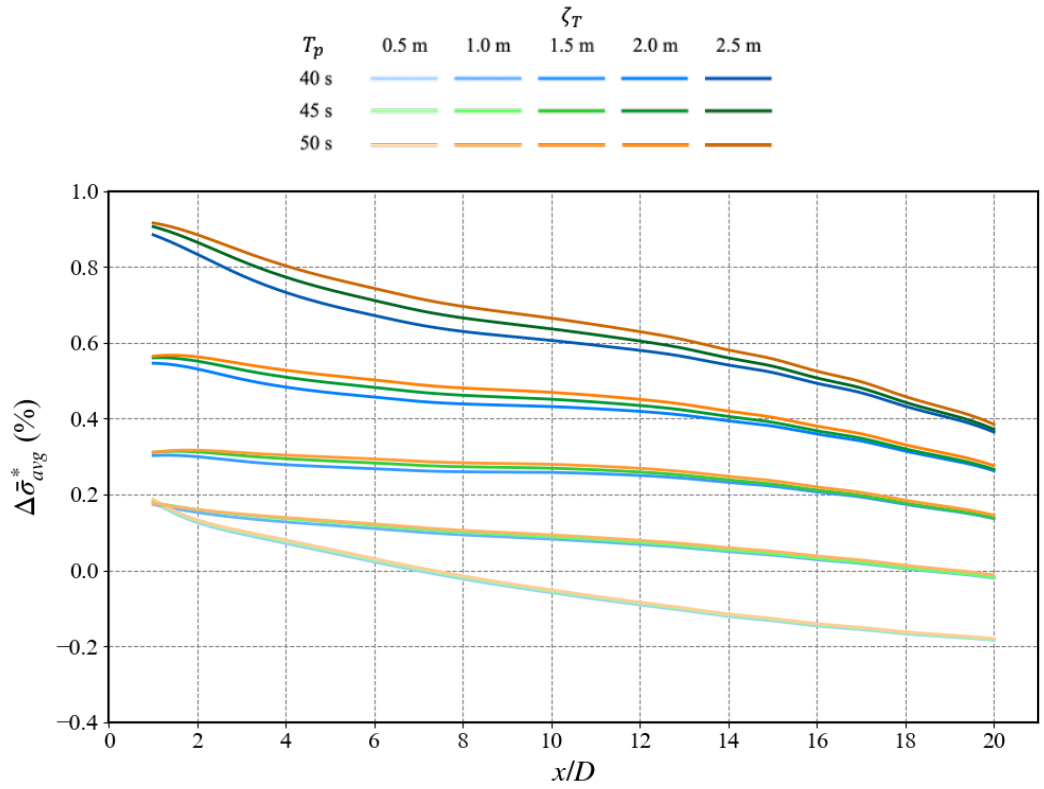

Figure 34 Downstream evolution of $\Delta\bar{\sigma}^*_{avg}$ under sway motions at 15 m/s with periods of 40, 45, and 50 s

doi:10.6342/NTU202503576

Figure 35 illustrates the downstream behavior of $\Delta\overline{U}^*_{avg}$ induced by the large amplitude sway motion with amplitudes ranging from 5 to 30 m at the wind speed of 9, 15, 21 m/s and T_p = 45 s. The results highlight the influence of sway amplitude and downstream distance on wake recovery behind the wind turbine. Under the condition of $U_{hub} = 9$ m/s, the normalized velocity increase ranges from 0.45% at $\zeta_T = 5$ m near $x = D$ to a maximum of 7.49% at $\zeta_T = 30$ m at the same location. As the flow progresses downstream, this recovery decays, with values decreasing to 0.12% at $x = 20D$ and $\zeta_T = 5$ m as well as 2.19% at $x = 20D$ and $\zeta_T = 30$ m, indicating that sway-induced effects are most significant in the near-wake region. At $U_{hub} = 15$ m/s, the wake recovery becomes considerably weakened. The peak value of $\zeta_T = 30$ m reaches 3.50% at $x = D$ and declines to 2.70% at $x = 20D$, suggesting that high wind speeds reduce the disturbance of sway motion due to high ambient momentum. The case of $U_{hub} = 21$ m/s exhibits an even more pronounced attenuation. For example, at $\zeta_T = 30$ m, the increase across $x = D$ to $x = 20D$ is only 1.24%, indicating a substantial suppression of sway-induced wake disturbance. Collectively, large sway amplitudes result in more pronounced wake recovery, but $\Delta\overline{U}^*_{avg}$ diminishes with downstream distance due to the growing wake velocity. The magnitude and extend of $\Delta\overline{U}^*_{avg}$ vary significantly across different inflow conditions. Freestream wind speed plays a decisive role in governing the wake's response to lateral excitations.

Figure 36 illustrates the downstream behavior of $\Delta\overline{U}^*_{avg}$ induced by large amplitude sway motion with amplitudes ranging from 5 to 30 m at a wind speed of 15 m/s and T_p = 40, 45, 50 s. Across three examined periods, similar trends are observed for changing sway amplitude and downstream distance. For each case, $\Delta\overline{U}^*_{avg}$ increases steadily with sway amplitude at all streamwise locations, reaching a maximum of approximately 3.5%

doi:10.6342/NTU202503576

at $x = D$ and $\zeta_T = 30$ m. As the downstream distance increases, $\Delta\overline{U}^*_{avg}$ gradually decays, with values dropping to around 2.7% at $x = 20D$ for the same sway amplitude. These results indicate that under large amplitude sway motion, the effect of the motion period on $\Delta\overline{U}^*_{avg}$is relatively minor. The behavior of $\Delta\overline{U}^*_{avg}$ across the three periods are nearly identical in magnitude and spatial variation, especially in the near-wake region. This suggests that sway-induced wake disturbance is governed primarily by motion amplitude and freestream wind speed. Large motion amplitudes clearly lead to strong momentum transfer and wake recovery, whereas high wind speeds suppress these effects through large flow inertia. While slight differences in downstream decay are observed among three periods, the motion period plays a secondary role in shaping the behavior of $\Delta\overline{U}^*_{avg}$.

doi:10.6342/NTU202503576

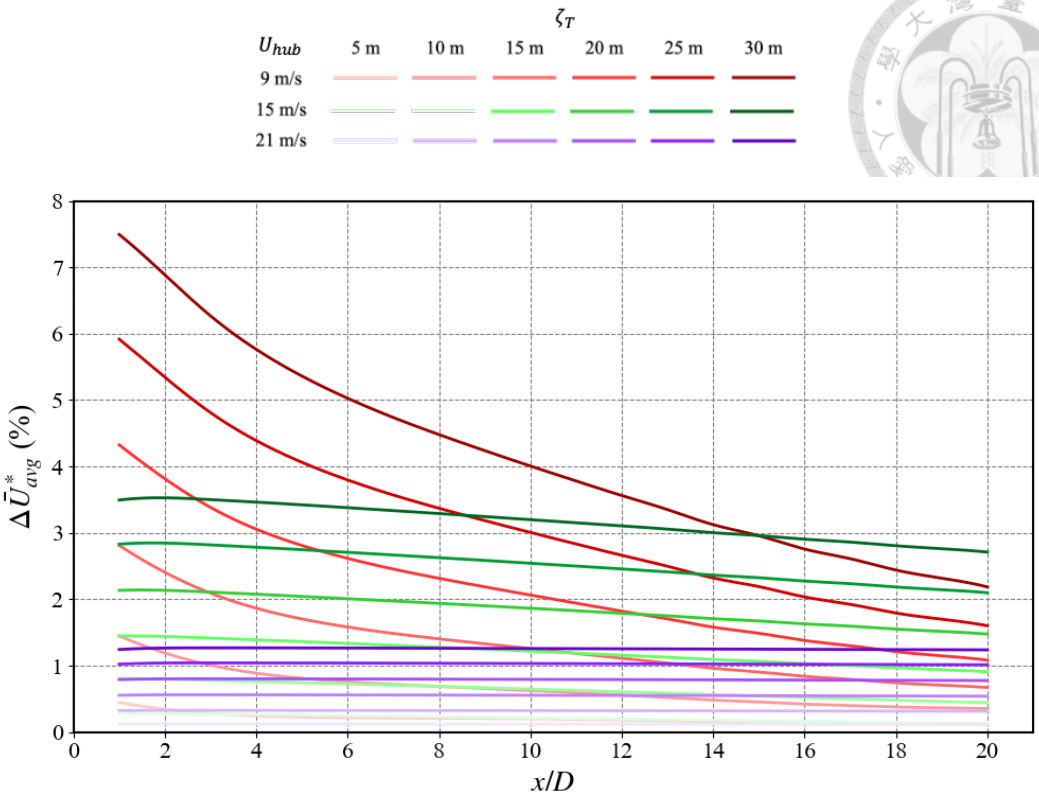

Figure 35 Downstream evolution of $\Delta\bar{U}^*_{avg}$ under large amplitude sway motions at 9, 15, and 21 m/s with a fixed period of 45 s

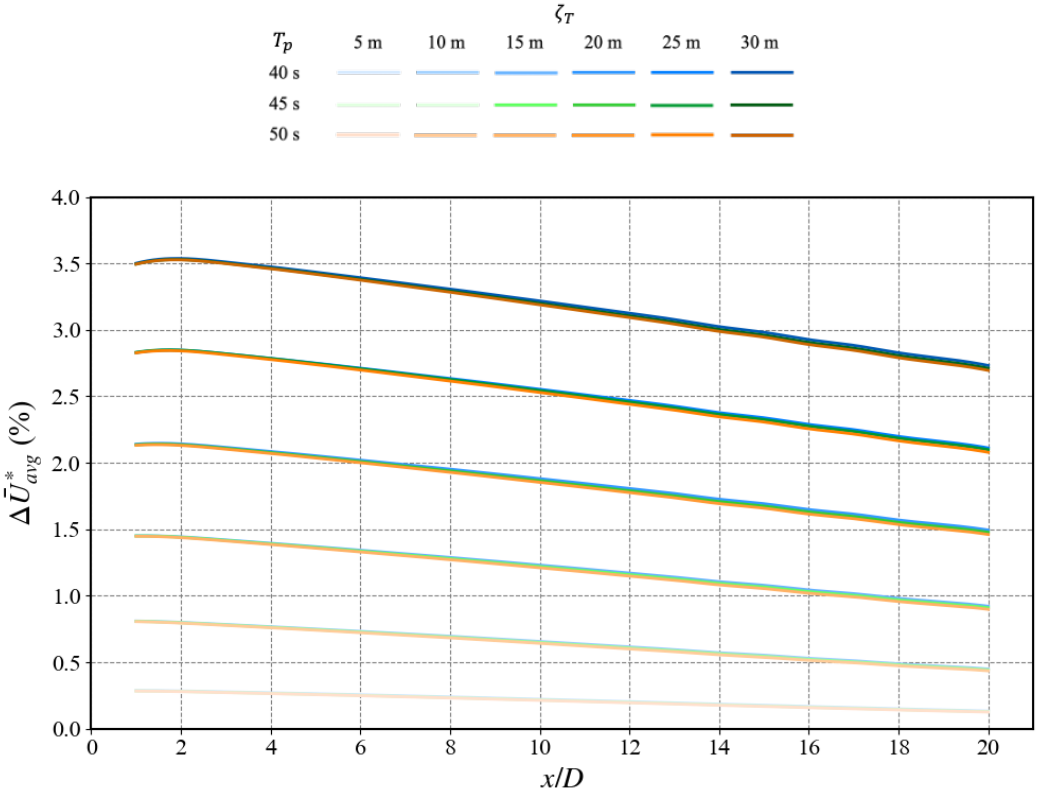

Figure 36 Downstream evolution of $\Delta\bar{U}^*_{avg}$ under large amplitude sway motions at 15 m/s with periods of 40, 45, and 50 s

doi:10.6342/NTU202503576

Figure 37 illustrates the downstream behavior of $\Delta\bar{\sigma}^*_{avg}$ induced by large amplitude sway motion with amplitudes ranging from 5 to 30 m at the wind speed of 9, 15, 21 m/s and T_p = 45 s. As the wind speed increases, $\Delta\bar{\sigma}^*_{avg}$ diminishes significantly. Under the condition of $U_{hub} = 9$ m/s, $\Delta\bar{\sigma}^*_{avg}$ reaches a peak of approximately 84% near the rotor and decays gradually downstream, indicating strong interaction between the sway motion and surrounding flow. At $U_{hub} = 15$ m/s, the peak of $\Delta\bar{\sigma}^*_{avg}$ drops to around 37%, accompanied by a more rapid decline with distance, reflecting a moderate disturbance to the downstream wake. At $U_{hub} = 21$ m/s, $\Delta\bar{\sigma}^*_{avg}$ remain below 6% even at the largest amplitude, and rapidly diminish beyond $x = 10D$, suggesting that large freestream momentum suppresses the motion-induced disturbance. These results reveal a clear negative dependence of $\Delta\bar{\sigma}^*_{avg}$ on U_{hub}. At low wind speeds, the reduced flow inertia allows sway motion to induce more visible wake perturbations. As the wind speed rises, the freestream flow becomes increasingly dominant, leading to a short flow fluctuation lifespan and reduced spatial extent of velocity variation. At $U_{hub} = 21$ m/s, the motion-induced effects become negligible. These findings underscore the governing role of freestream momentum in wake behavior responding to external excitation, with strong flow inertia at high wind speeds leading to resist lateral motion-induced disturbances.

Figure 38 illustrates the downstream behavior of $\Delta\bar{\sigma}^*_{avg}$ induced by large amplitude sway motion with amplitudes ranging from 5 to 30 m at a wind speed of 15 m/s and T_p = 40, 45, 50 s. A comparative analysis reveals that the sway motion period significantly affects both the degree and extend of wake recovery. In all cases, $\Delta\bar{\sigma}^*_{avg}$ increases with sway amplitude and decreases with downstream distance. The case of T_p = 40 s shows strong wake velocity fluctuations that last to $x = 15D$, while the case of T_p = 45 s yields slightly higher values in the mid-wake region. In contrast, the case of T_p = 50 s results

doi:10.6342/NTU202503576

in substantial downstream decay, with $\Delta\bar{\sigma}^{*}_{avg}$ dropping below 6% at $x = 20D$ for most motion amplitudes. These observations demonstrate that the period of sway motion plays a non-negligible role in shaping the spatial development of wake recovery. At U_{hub} = 15 m/s, short sway periods generate high velocity fluctuation near the rotor and deliver more gradual downstream decay. As the period increases to T_p = 45 s, the near-wake velocity fluctuation levels remain similar, but the elevated disturbance extends farther downstream, suggesting that low frequency disturbance is less prone to have a rapid dissipation.

doi:10.6342/NTU202503576

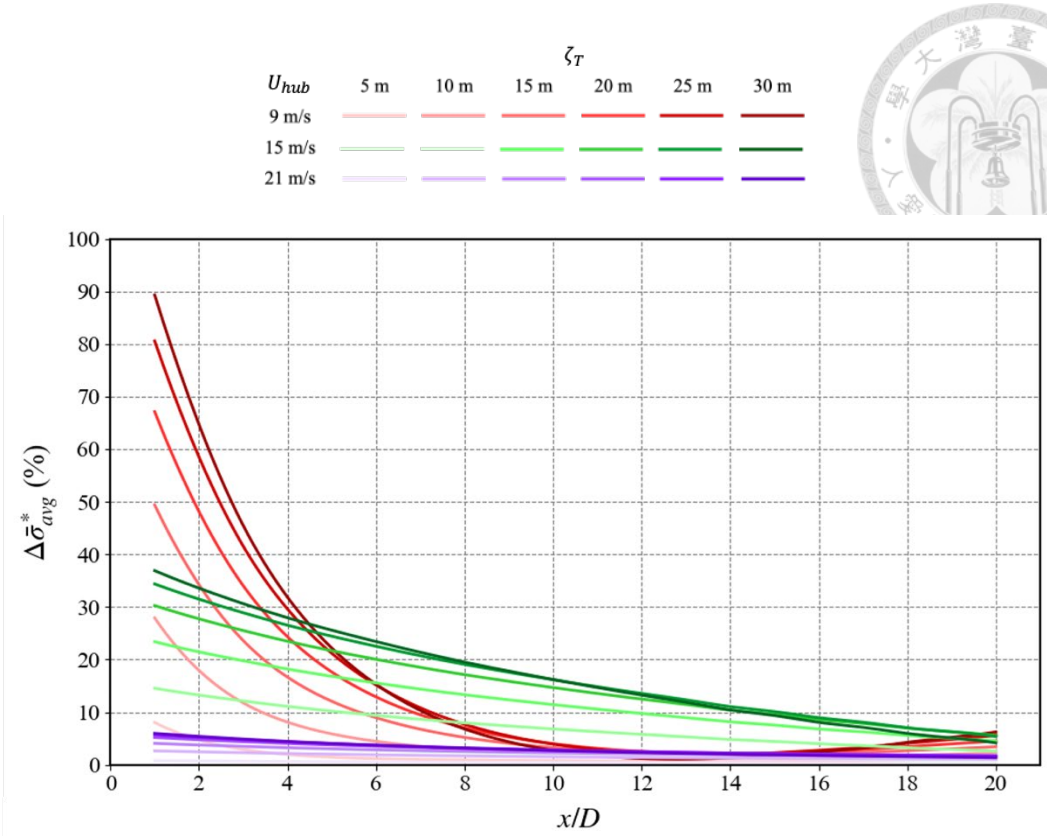

Figure 37 Downstream evolution of $\Delta\bar{\sigma}^*_{avg}$ under large amplitude sway motions at 9, 15, and 21 m/s with a fixed period of 45 s

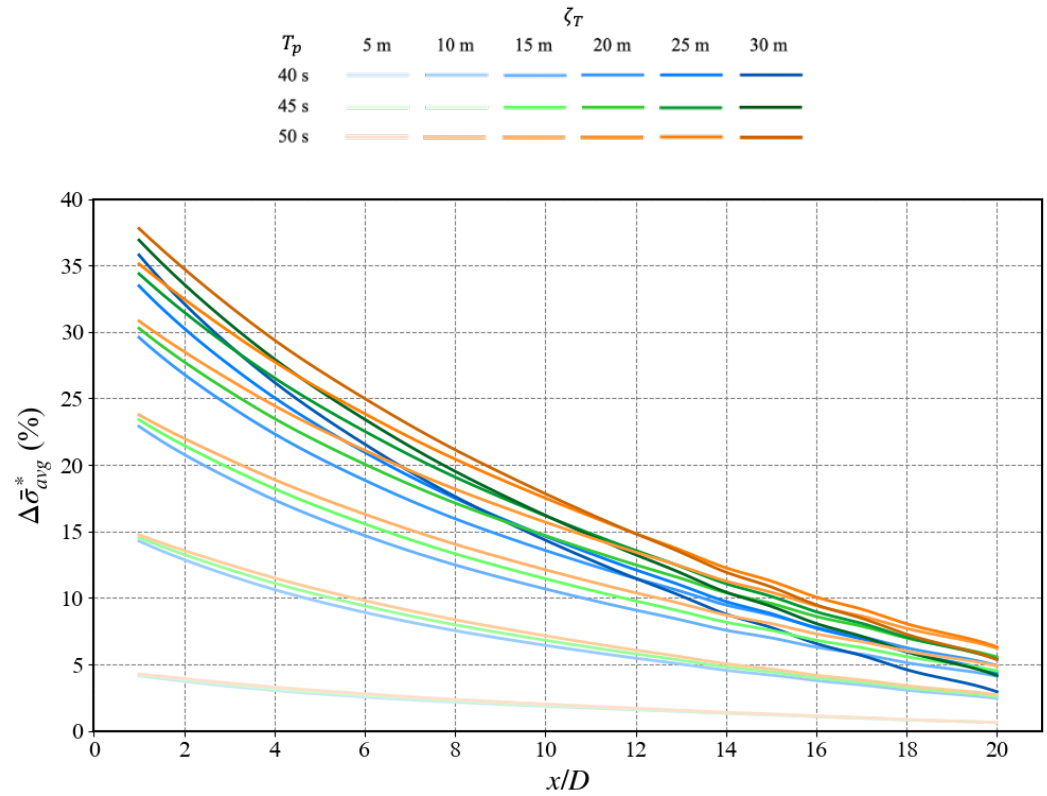

Figure 38 Downstream evolution of $\Delta\bar{\sigma}^*_{avg}$ under large amplitude sway motions at 15 m/s with periods of 40, 45, and 50 s

doi:10.6342/NTU202503576

5.1.3 Heaving Behavior

Figure 39 illustrates the downstream behavior of $\Delta\overline{U}^*_{avg}$ induced by heave motion with amplitudes ranging from 0.5 m to 2.5 m at the wind speed of 9, 15, and 21 m/s and T_p = 45 s. Across all tested wind speeds, the results consistently show that large heave amplitudes lead to substantial enhancement in wake recovery, although the effect diminishes with downstream distance. At $U_{hub} = 9$ m/s, significant contribution due to interaction is observed, with $\Delta\overline{U}^*_{avg}$ increase at $x = D$ rising from 0.015% at $\zeta_T = 0.5$ m to 0.202% at $\zeta_T = 2.5$ m. This positive influence extends downstream but attenuates gradually, with values at $x = 10D$ ranging from -0.001% to 0.039% and at $20D$ from -0.006% to 0.042%. At $U_{hub} = 15$ m/s, similar amplitude-dependent growth is seen, though the magnitudes of $\Delta\overline{U}^*_{avg}$ are reduced. $\Delta\overline{U}^*_{avg}$ at $x = D$ vary from 0.008% to 0.117%, and at $x = 20D$ from 0.001% to 0.042%. At $U_{hub} = 21$ m/s, the recovery becomes more constrained, with $x = D$ the values ranging from 0.002% to 0.047% and reaching between 0.002% and 0.044% at $x = 20D$. These observations suggest that although heave motion contributes to wake recovery across all wind conditions, its effectiveness is limited by the freestream velocity. High wind speeds imply a large kinetic energy of the incoming flow and a strong advection nature, which shortens the flow residence time across the rotor and reduces the heave-induced vertical mixing to impact the wake. In contrast, at low wind speeds, the weak advection allows the rotor motion to interact more effectively with the incoming flow, resulting in significant recovery effects in the near-wake region.

Figure 40 illustrates the downstream behavior of $\Delta\overline{U}^*_{avg}$ induced by heave motion with amplitudes ranging from 0.5 m to 2.5 m at a wind speed of 15 m/s and T_p = 40, 45, and 50 s. At a fixed wind speed of $U_{hub} = 15$ m/s, $\Delta\overline{U}^*_{avg}$ shows only minimal variation

doi:10.6342/NTU202503576

across different motion periods. For example, at $x = D$ and $\zeta_T = 2.5$ m, it reaches 0.118% under $T_p = 40$ s, which is slightly higher than 0.117% observed at $T_p = 45$ s and 50 s. This subtle trend continues downstream. At $x = 10D$, the respective values are 0.086%, 0.085%, and 0.084% for three studied periods, indicating a marginal decrease in wake recovery as the motion period increases. Despite these minor differences, the overall trend of $\Delta\overline{U}^*_{avg}$ remains consistent across all cases. These results suggest that, within the tested range, the period of vertical motion has a limited impact on wake behavior compared to the amplitude. The wake flow appears to respond primarily to the displacement magnitude of vertical motion, which governs the degree of momentum exchange and mixing, rather than the rate at which the motion occurs.

doi:10.6342/NTU202503576

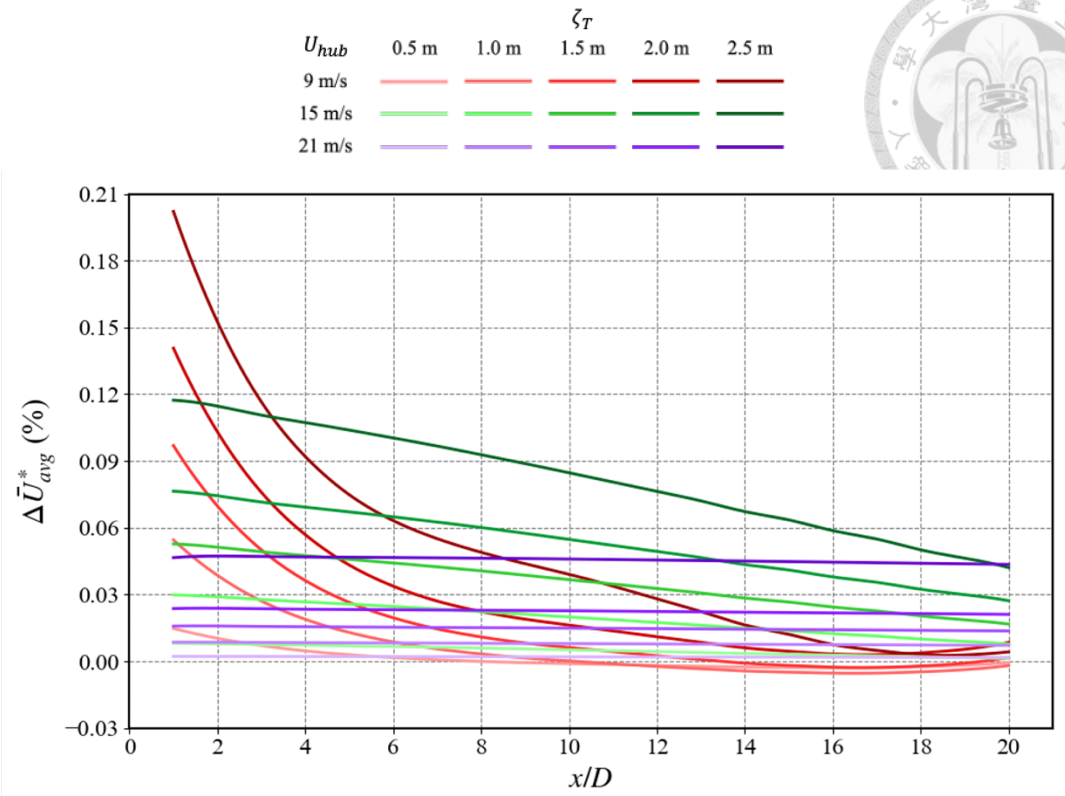

Figure 39 Downstream evolution of $\Delta\bar{U}^*_{avg}$ under heave motions at 9, 15, and 21 m/s with a fixed period of 45 s

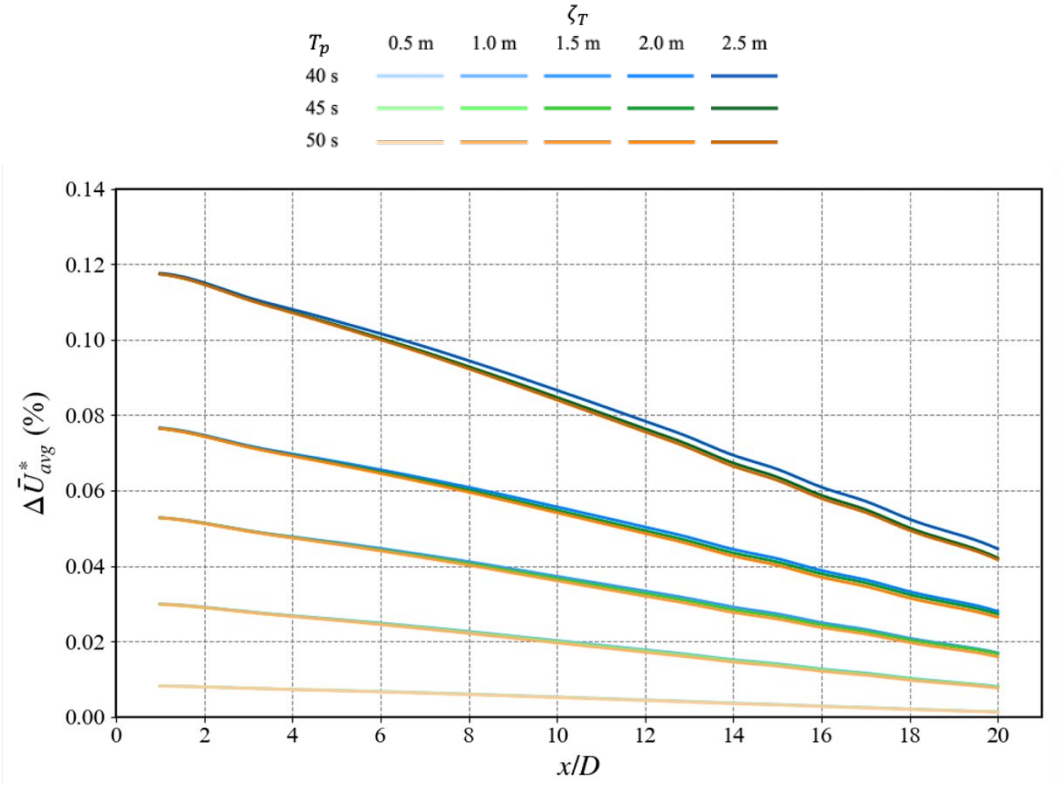

Figure 40 Downstream evolution of $\Delta\bar{U}^*_{avg}$ under heave motions at 15 m/s with periods of 40, 45, and 50 s

doi:10.6342/NTU202503576

Figure 41 illustrates the downstream behavior of $\Delta\sigma^*_{avg}$ induced by heave motion with amplitudes ranging from 0.5 m to 2.5 m at the wind speed of 9, 15, ad 21 m/s and T_p = 45 s. The results indicate that wake fluctuation behavior is most sensitive to heave motion under low freestream speeds, whereas high wind speeds suppress the mixing effects of vertical motion. At $U_{hub} = 9$ m/s, $\Delta\sigma^*_{avg}$ increases rapidly with heave amplitude in the near-wake region. For example, at $x = D$ downstream, the values rise from 0.118% at $\zeta_T = 0.5$ m to a peak of 1.816% at $\zeta_T = 2.5$ m. Although $\Delta\sigma^*_{avg}$ decreases beyond $x = 10D$, it remains positive, suggesting a sustained wake disturbance induced by heave motion. At $U_{hub} = 15$ m/s, the trend remains similar but with reduced level. At $x = D$, the value at $\zeta_T = 2.5$ m reaches 0.088 % and continues to decline further downstream. Notably, under this wind condition, $\Delta\sigma^*_{avg}$ becomes negative in the far wake at large motion amplitudes. At $U_{hub} = 21$ m/s, the wake exhibits very limited response to heave motion. In the near wake, the values range from -0.003% at $\zeta_T = 0.5$ m to -0.017% at $\zeta_T = 2.5$ m. Across the entire downstream span, the values remain negative and small, with $\Delta\sigma^*_{avg}$ at $\zeta_T = 2.5$ m amplitude decreasing to -0.056% at $x = 4D$ and stabilizing near -0.014% at $x = 20D$. These results suggest that under low wind speed conditions, moderate heave amplitudes can effectively promote coherent wake disturbance, whereas at higher inflow velocities, the strong advection effect inhibits vertical disturbance development and propogation.

Figure 42 illustrates the downstream behavior of $\Delta\bar{\sigma}^*_{avg}$ induced by heave motion with amplitudes ranging from 0.5 m to 2.5 m at a wind speed of 15 m/s and T_p = 40, 45, 50 s. The results reveal a clear dependence of $\Delta\bar{\sigma}^*_{avg}$ on the heave period. For the case of $T_p = 40$ s, $\Delta\bar{\sigma}^*_{avg}$ increases steadily with amplitude, reaching a peak of 0.32 % at $\zeta_T = 2.0$ m and $x = 14D$. In the case of $T_p = 50$ s, overall fluctuations are less

doi:10.6342/NTU202503576

pronounced, with a slightly lower maximum of 0.29 % observed at the same location. However, at $\zeta_T = 2.5$ m, $\Delta\bar{\sigma}^*_{avg}$ decreases in the downstream region and becomes negative beyond $x = 15D$. Despite these differences, the overall influence of heave motion period on wake velocity fluctuation remains relatively limited. Across all three tested periods, the spatial patterns of $\Delta\bar{\sigma}^*_{avg}$ remain broadly consistent, with only moderate variations in magnitude. Notably, at large amplitudes, $\Delta\bar{\sigma}^*_{avg}$ consistently declines in the far-wake region and frequently becomes negative beyond $x = 15D$, suggesting that excessive vertical motion may reduce the level of wake-induced fluctuations regardless of the motion frequency.

The findings are consistent with the conclusions drawn by Cioni et al. [37], who noted in the OC6 Phase III validation study that floating platform motion, particularly in heave, surge, and pitch degrees of freedom, can under certain conditions reduce the velocity fluctuation intensity in the downstream wake. The negative values seen in the normalized standard deviation at large motion amplitudes and downstream distances support this conclusion, implying that platform motions do not always enhance wake disturbance.

doi:10.6342/NTU202503576

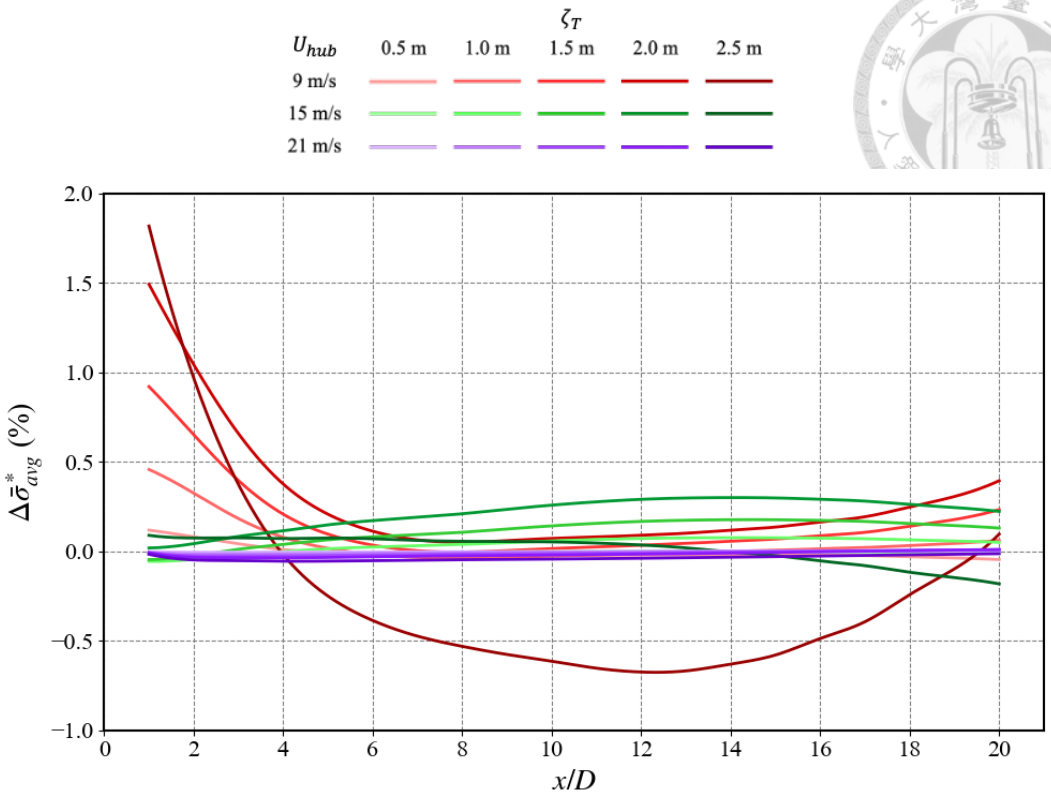

Figure 41 Downstream evolution of $\Delta\bar{\sigma}^*_{avg}$ under heave motions at 9, 15, and 21 m/s with a fixed period of 45 s

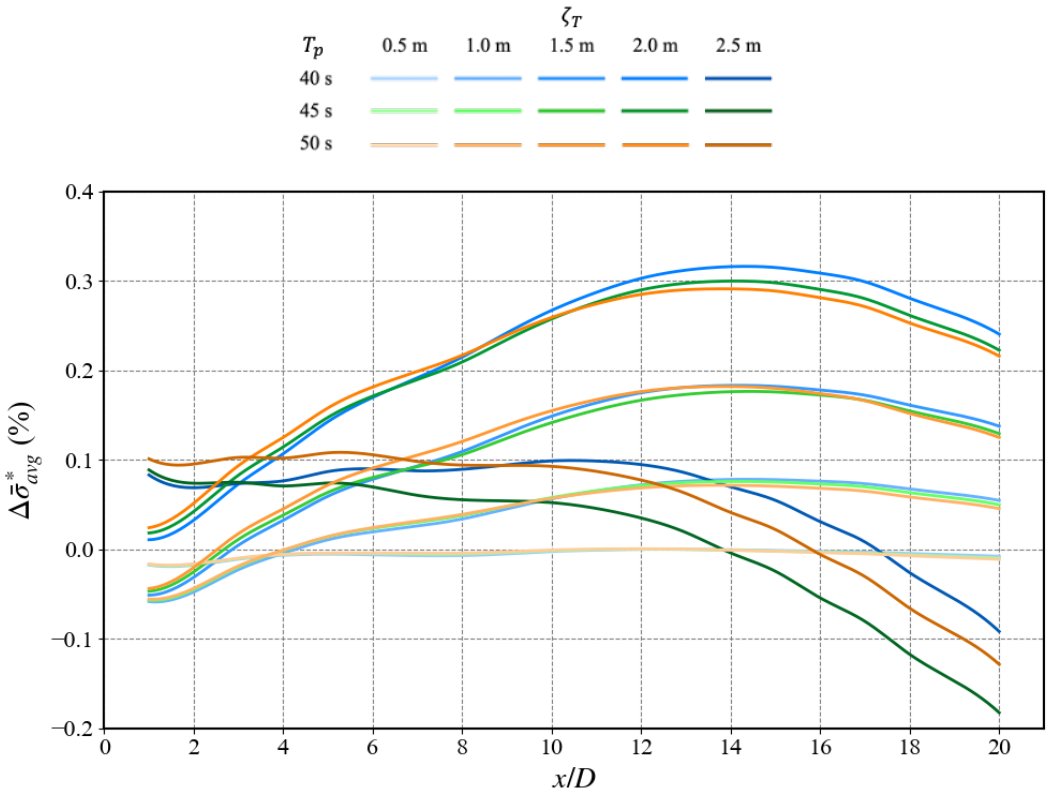

Figure 42 Downstream evolution of $\Delta\bar{\sigma}^*_{avg}$ under heave motions at 15 m/s with periods of 40, 45, and 50 s

doi:10.6342/NTU202503576

5.1.4 Summary

This section investigates the effects of single DOF translational motions, namely surge, sway, and heave, on the wake characteristics of an FOWT. Simulations were conducted under three representative wind speeds (U_{hub} = 9 m/s, 15 m/s, and 21 m/s) and three motion periods (T_p = 40 s, 45 s, and 50 s), with ζ_T ranging from 0.5 to 2.5 meters. Two primary wake indicators were evaluated: $\Delta\overline{U}^*_{avg}$ representing wake recovery, and $\Delta\bar{\sigma}^*_{avg}$ indicating wake disturbance.

The results reveal that the influence of translational motions on wake dynamics is primarily governed by inflow wind speed and platform motion amplitude. Among the three motion types, surge exhibits the most pronounced and sustained impact on both velocity recovery and turbulence levels across the entire wake region. In contrast, sway and heave predominantly affect the near wake zone, with their influence decaying rapidly downstream. As U_{hub} increases to higher than 15 m/s, the wake becomes increasingly insensitive to platform motion due to the stronger ambient flow inertia and momentum, which act to suppress the propagation of motion-induced perturbations. The role of motion period remains a secondary effect. However, shorter motion periods may occasionally trigger slightly stronger disturbances more near the rotor.

To further examine wake sensitivity to large scale motion, a series of simulations was conducted using ζ_T ranging from 5 to 30 meters. Under low wind speed conditions, particularly at U_{hub} = 9 m/s, large amplitude motions significantly enhance both wake recovery and turbulence levels. Surge motion leads to velocity increments of up to 2.56% and $\Delta\bar{\sigma}^*_{avg}$ values exceeding 5% near the rotor. Sway motion induces even more substantial responses, with wake recovery surpassing 7% and turbulence intensities reaching as high as 84%. However, as U_{hub} increases to above 15 m/s, the wake

doi:10.6342/NTU202503576

response becomes markedly subdued. Under such conditions, the wake exhibits greater flow inertia, reducing its receptivity to the upstream disturbance due to the platform motion. Most of the observed velocity and turbulence responses become very limited or negligible.

Furthermore, the motions of short periods are more effective in generating wake disturbances in the near field, whereas those of long periods yield weaker and less obvious responses. Overall, these findings highlight that platform-induced wake disturbance is highly nonlinear and strongly dependent on inflow wind speed. While large amplitude motions can significantly reshape wake behavior under moderate wind conditions, this effect is greatly diminished under high wind speeds.

As illustrated in Figure 43, the time-averaged streamwise velocity is compared along the downstream direction between the stationary case and three types of translational motions: surge, sway, and heave. In the stationary scenario, the wake recovers to approximately 7.378 m/s at a downstream distance of $x = 7D$. With surge motion, the same velocity is reached at around $x = 6.75D$. Both sway and heave motions exhibit similar behavior, achieving 7.378 m/s at approximately $x = 6.95D$. These results suggest that platform-induced translational motions can accelerate wake recovery, allowing the downstream flow to regain a high wind speed more quickly. Consequently, compared to fixed-bottom wind turbines, floating turbines with such motion characteristics may permit reduced inter-turbine spacing without compromising energy loss, offering a potential advantage in improving the spatial utilization of floating wind farms.

As shown in Figure 44, the comparison of power output under translational platform motions reveals that surge motion results in a slight increase of approximately 0.02% relative to the stationary case. In contrast, sway and heave motions lead to small reductions in power output, by approximately 0.09% and 0.04%, respectively. These

doi:10.6342/NTU202503576

results correspond to $U_{hub} = 9$ m/s, $T_p = 45$ s and $\zeta_T = 2.5$ m. The overall magnitude of variation remains limited, suggesting that small-amplitude translational motions, under the examined conditions, exert negligible influence on the power production of the moving wind turbine. Indeed, the main concern does not lie in the small power reduction observed at the leading turbine, but rather in the effect on downstream turbines. The lower panel of Figure 44 illustrates the predicted power output of a second turbine positioned at $x = 7D$ downstream, under the same conditions. It can be observed that surge motion increases the power output by approximately 0.5% at $x = 7D$, while sway and heave motions also have positive effects, each improving power output by about 0.1%. These findings highlight the relative insensitivity of the moving turbine to low-amplitude platform displacements, while also underscoring the beneficial impact of such motions on downstream wake recovery and turbine performance.

doi:10.6342/NTU202503576

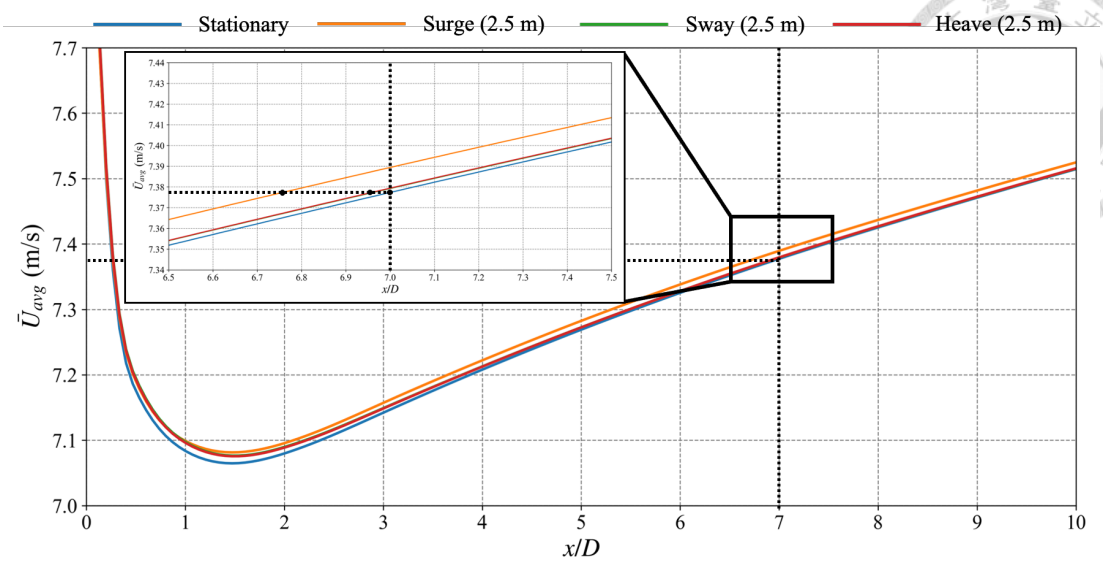

Figure 43 Dependence of $\bar{U}_{avg}$ on x/D for the stationary case and three translational motions with $U_{hub} = 9$ m/s, $T_p = 45$ s and $\zeta_T = 2.5$ m

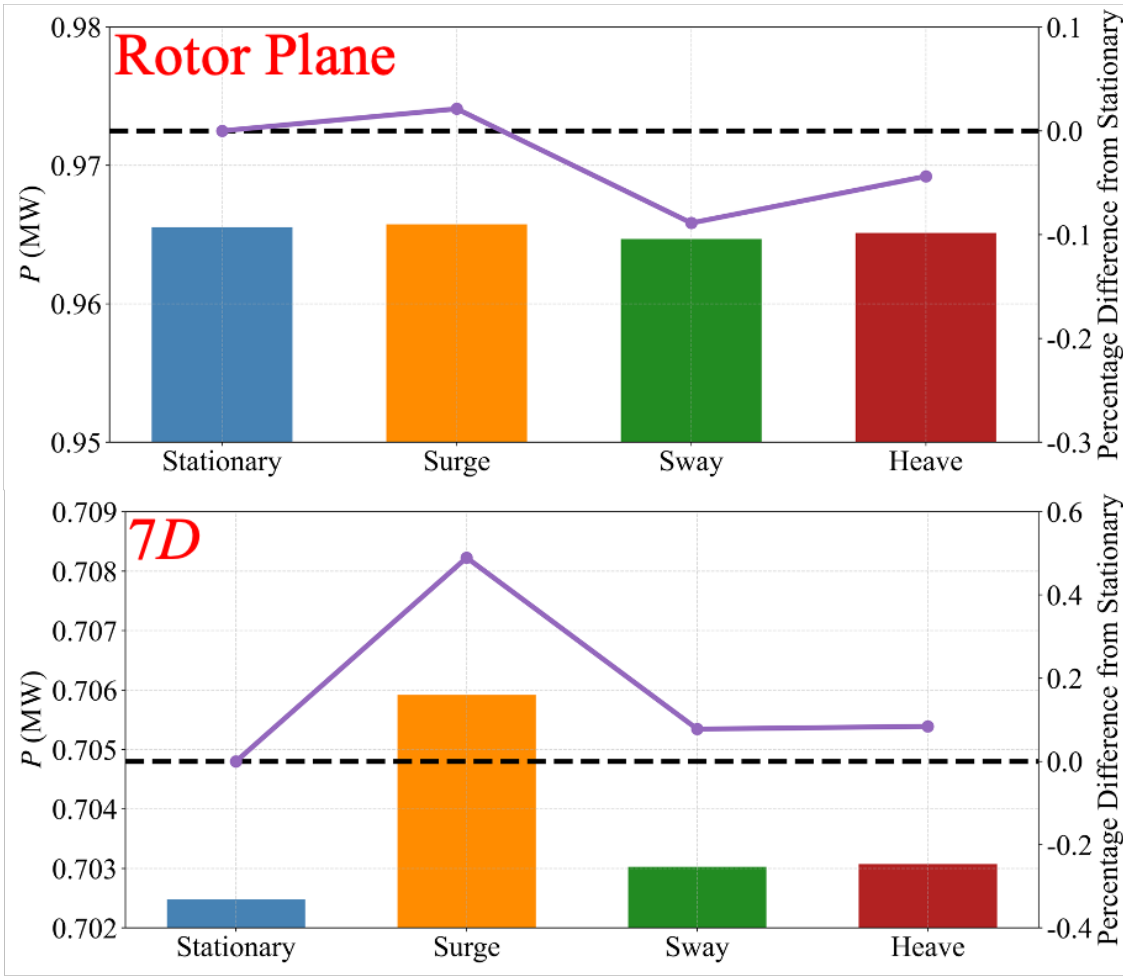

Figure 44 P of the stationary case and three translational motion cases at the rotor plane and the $x = 7D$ downstream plane

doi:10.6342/NTU202503576

As illustrated in Figure 45 and Figure 46, the wake recovery behavior is evaluated by comparing a stationary turbine with turbines subjected to six large-amplitude platform motions in both surge and sway directions. At $U_{hub} = 9$ m/s and $T_p = 45$ s, the stationary turbine reaches a time-averaged velocity of approximately 7.63 m/s at a downstream distance of $x = 13D$. In contrast, the wind turbines undergoing platform motion attain the same velocity at significantly shorter downstream positions. For the surge motion, wake recovery occurs at $x = 11.2D$, $10.7D$, $10.3D$, $9.7D$, $9.0D$, and $8.4D$, while for the sway motion, recovery distances are observed at $x = 12.5D$, $11.7D$, $10.5D$, $8.9D$, $6.5D$, and $4.0D$. These distances correspond to the motion amplitudes of 5, 10, 15, 20, 25, and 30 meters, respectively. The results demonstrate that large-amplitude translational motions in either direction can significantly accelerate wake recovery, allowing downstream turbines to regain a better inflow condition with shorter spatial distances. Compared to the stationary baseline, the presence of platform motion markedly reduces the inter-turbine spacing required to maintain equivalent aerodynamic performance. This effect provides a substantial advantage in the spatial optimization of floating offshore wind farms, improving overall energy capture and enabling more efficient utilization of the available sea area.

doi:10.6342/NTU202503576

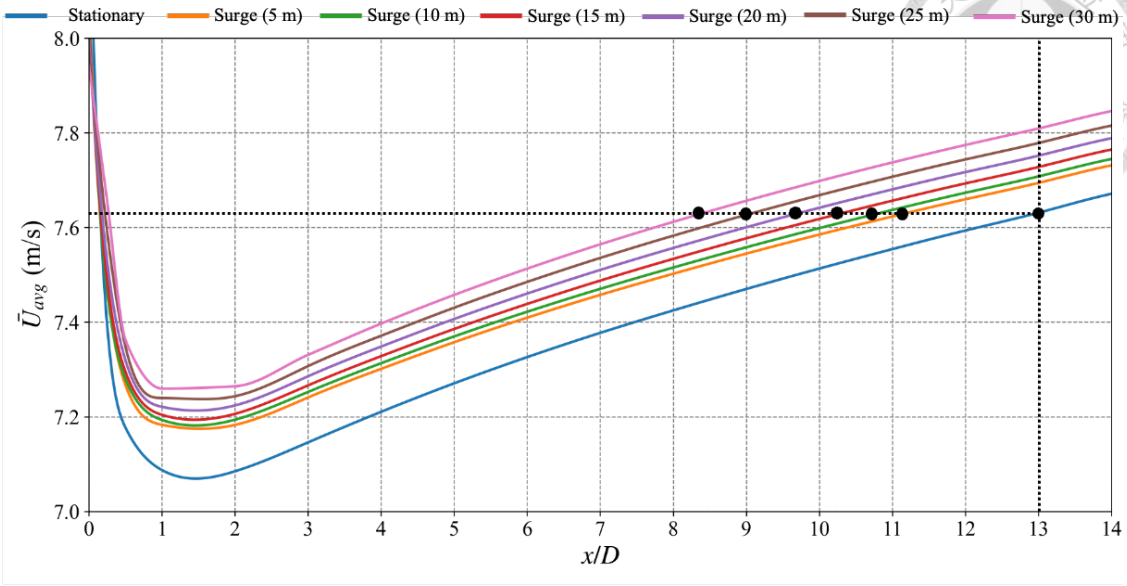

Figure 45 Dependence of $\bar{U}_{avg}$ on x/D for the stationary case and large amplitude surge motions with $U_{hub} = 9$ m/s, $T_p = 45$ s and ζ_T =5-30 m

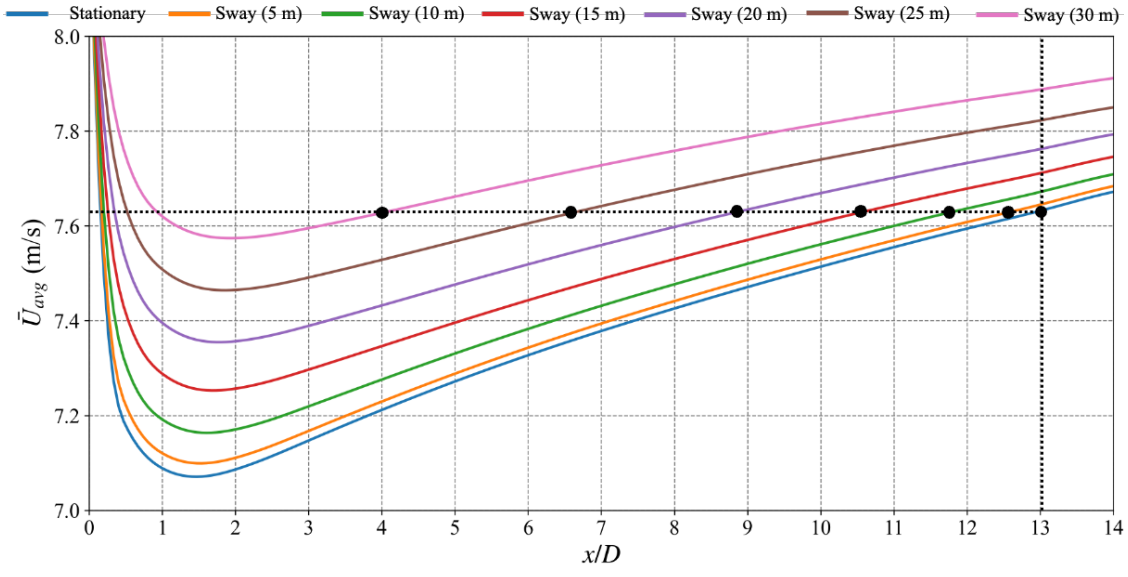

Figure 46 Dependence of $\bar{U}_{avg}$ on x/D for the stationary case and large amplitude sway motions with $U_{hub} = 9$ m/s, $T_p = 45$ s and ζ_T =5-30 m

doi:10.6342/NTU202503576

5.2 Rotational Motions

In this section, the wake characteristics of a FOWT are investigated under three different U_{hub} and three platform motion periods. The analysis specifically examines the influence of single DOF rotational motions, including roll, pitch, and yaw, on the wake structure. The simulation results and corresponding discussions are presented in Sections 5.2.1 to 5.2.3, with an integrated summary provided in Section 5.2.4.

To examine the transient development of the normalized time-averaged streamwise velocity increment $\Delta\overline{U}^*_{avg}$, the results of roll, pitch, and yaw motions are shown in Figure 47 (a), (b) and (c), respectively. Here, the case was simulated under $U_{hub} = 9$ m/s, with $\zeta_T = 1°$ and $T_p = 45$ s as a representative condition. The horizontal axis represents the number of periods, while the vertical axis denotes $\Delta\overline{U}^*_{avg}$ expressed in percentage. A total of 26 full motion cycles was computed for each case. As illustrated, all three types of rotational motion show a rapid rise during the initial cycles, followed by a gradual convergence process. At $N_T = 15$, this value becomes nearly unchanged, indicating that the system reaches a statistically steady state. Therefore, the final value at $N_T = 26$ is adopted in this study as the representative result for analyzing wake behavior. This approach ensures that the evaluated wake response reflects long-term aerodynamic effects rather than transient behaviors, thereby providing a consistent basis for comparing the influence of roll, pitch, and yaw motions on downstream flow characteristics.

doi:10.6342/NTU202503576

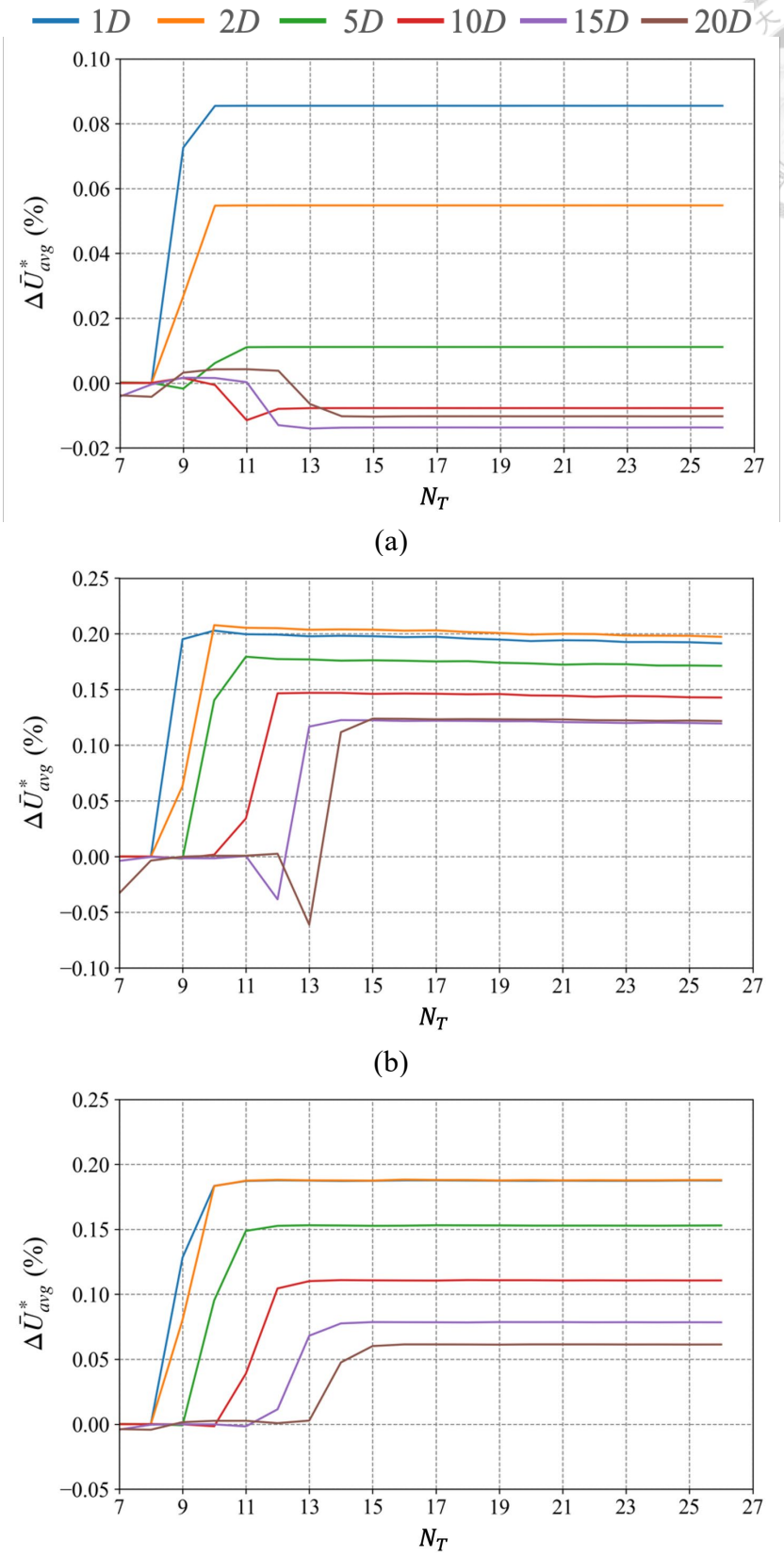

Figure 47 Evolution of $\Delta\bar{U}^*_{avg}$ over 26 periods under (a) roll, (b) pitch and (c) yaw motion with $U_{avg} = 9$ m/s, $T_p = 45$ s, and $\zeta_R = 1°$

doi:10.6342/NTU202503576

5.2.1 Rolling Behavior

Figure 48 illustrates the downstream behavior of $\Delta\overline{U}^*_{avg}$ induced by roll motion with amplitudes ranging from 1° to 5° at a wind speed of 9, 15, 21 m/s and T_p = 45 s. Across all wind speeds, the results consistently demonstrate that increasing roll amplitude enhances wake recovery, particularly within the near-wake region. At $U_{hub} = 9$ m/s, the wake recovery enhancement declines from 0.74% at $x = D$ to below 0.3% beyond $x = 10D$ for the roll case of $\zeta_R = 5°$. At low motion amplitudes, the wake recovery becomes negligible or slightly negative past $x = 7D$, indicating limited influence in the far-wake region. At $U_{hub} = 15$ m/s, the wake recovery remains positive across all the motion amplitudes up to $x = 20D$ for the roll case of $\zeta_R = 5°$, maintaining $\Delta\overline{U}^*_{avg}$ above 0.2%, suggesting a more robust and sustained recovery response enabled by a higher inflow momentum. At $U_{hub} = 21$ m/s, although roll-induced recovery is still observed, the magnitude is significantly reduced, with $\Delta\overline{U}^*_{avg}$ reaching only around 0.11% from $x = D$ to $x = 20D$. These results reveal a clear trend: roll-induced wake recovery is more effective at low wind speeds and gradually weakens as wind speed increases. Under low inflow conditions, the wake is more responsive to platform motion, allowing an effective velocity recovery to propagate downstream. In contrast, as the wind speed increases to rated and above-rated conditions, the influence of roll motion diminishes due to a greater background inertia, resulting in a more subdued recovery effect. This behavior indicates that the aerodynamic impact of roll motion is most pronounced when the inflow is featured with small axial momentum so the wake is more receptive to external perturbations.

Figure 49 illustrates the downstream behavior of $\Delta\overline{U}^*_{avg}$ induced by roll motion with amplitudes ranging from 1° to 5° at a wind speed of 15 m/s and T_p = 40, 45, 50 s.

doi:10.6342/NTU202503576

Across all cases, $\Delta\overline{U}^*_{avg}$ increases consistently with roll amplitude, and the overall spatial distribution patterns remain similar. For instance, at $\zeta_R = 5°$, $\Delta\overline{U}^*_{avg}$ reaches approximately 0.04% at $x = D$ but gradually declines to about 0.02% at $x = 20D$, illustrating the decay of wake recovery growing with distance. Although minor differences are observed among the tested motion periods, their influence on wake recovery is relatively small. The variation across periods is limited, indicating that the period of roll motion plays only a secondary role in affecting wake velocity recovery when compared to the roll amplitude which is the most dominant factor governing the wake recovery.

doi:10.6342/NTU202503576

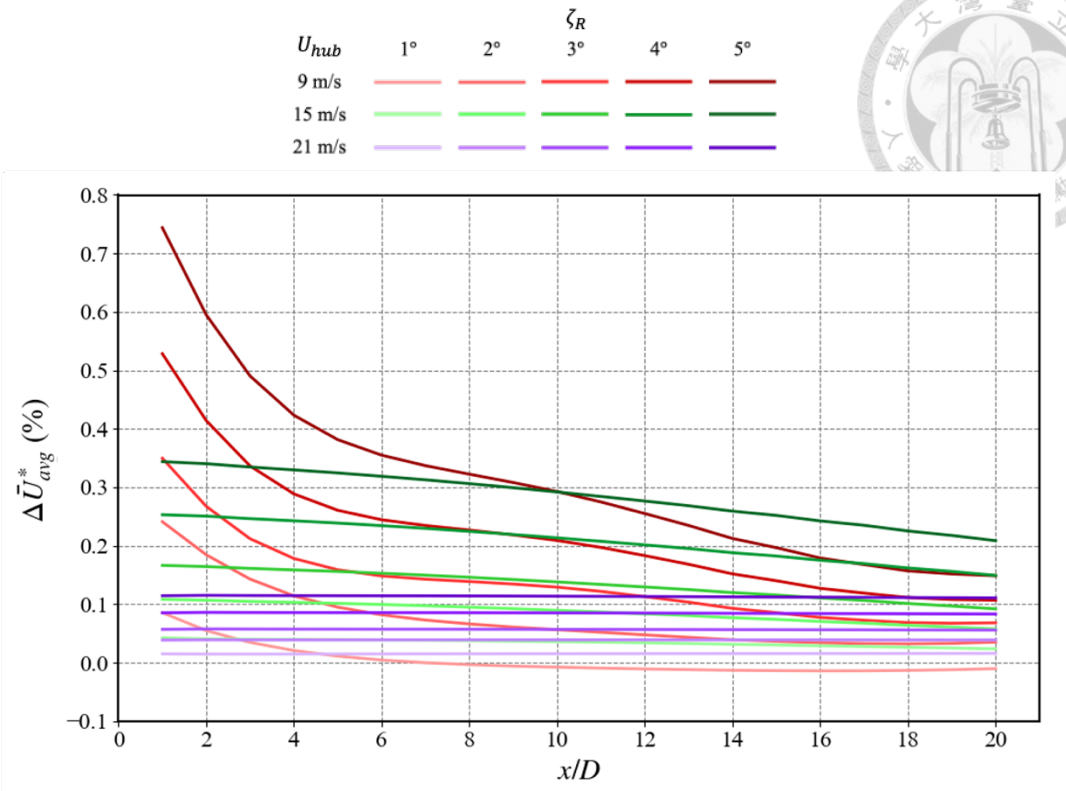

Figure 48 Downstream evolution of $\Delta\overline{U}^*_{avg}$ under roll motions at 9, 15, and 21 m/s with a fixed period of 45 s

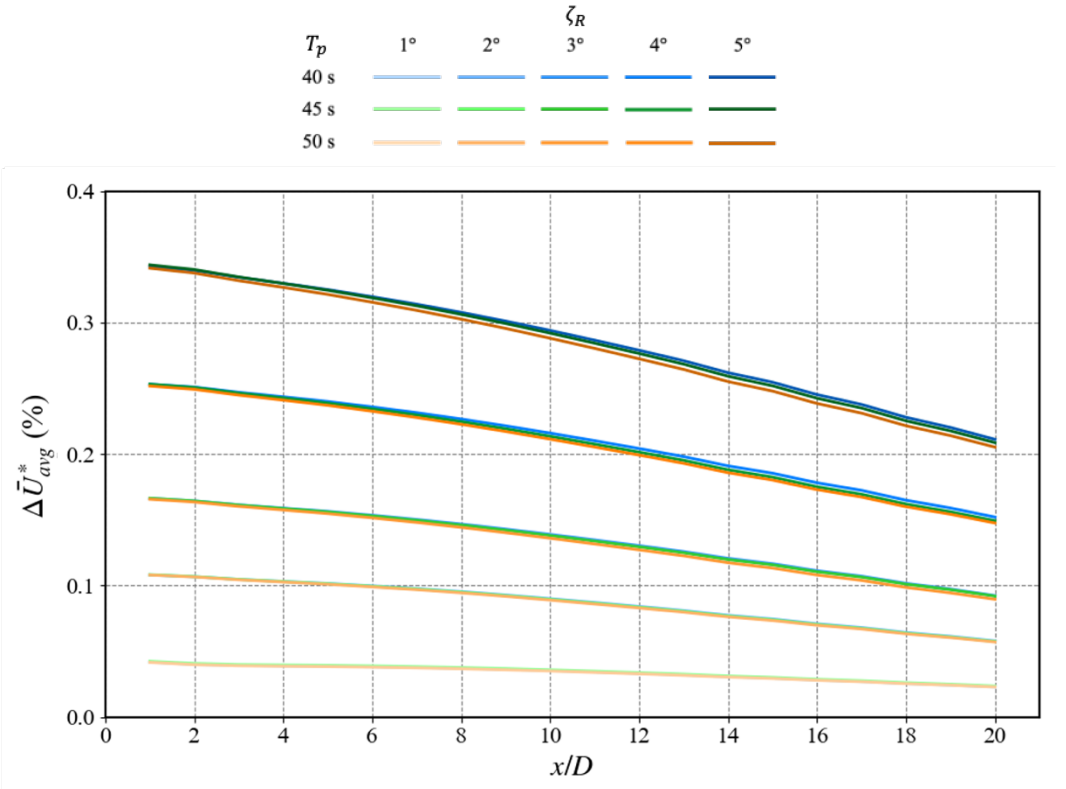

Figure 49 Downstream evolution of $\Delta\overline{U}^*_{avg}$ under roll motions at 15 m/s with periods of 40, 45, and 50 s

doi:10.6342/NTU202503576

Figure 50 illustrates the downstream behavior of $\Delta\bar{\sigma}^*_{avg}$ induced by roll motion with amplitudes ranging from 1° to 5° at the wind speed of 9, 15, and 21 m/s and T_p = 45 s. At a downstream distance of $x = D$, the wake exhibits a clear dependence on both roll amplitude and inflow velocity, with the peak values of $\Delta\bar{\sigma}^*_{avg}$ reaching 12.1% at $U_{hub} = 9$ m/s, 6.14% at $U_{hub} = 15$ m/s, and 1.3% at $U_{hub} = 21$ m/s. This reflects a strong suppression of wake fluctuations as wind speed increases. In the far-wake region at $x = 20D$, $\Delta\bar{\sigma}^*_{avg}$ decreases to 1.86%, 2.17%, and 0.7% for the respective wind speeds, demonstrating a consistent trend of decay growing with distance. Across all cases, the influence of roll motion diminishes in the downstream direction, and high wind speeds further reduce the magnitude of wake fluctuation. These observations indicate that at $T_p = 45$ s, increasing wind speed leads to a significant reduction in wake fluctuation levels in the near and far wake regions. At low wind speeds, the platform-induced motion has a strong influence on the wake flow, generating large disturbances and delaying wake recovery. In contrast, high wind speeds tend to suppress the motion-induced effects and enhance a stable wake. This trend suggests that the relative importance of platform roll motion in contributing to the wake recovery weakens as inflow energy increases.

Figure 51 illustrates the downstream behavior of $\Delta\bar{\sigma}^*_{avg}$ induced by roll motion with amplitudes ranging from 1° to 5° at a wind speed of 15 m/s and T_p = 40, 45, 50 s. At the downstream location of $x = D$, $\Delta\bar{\sigma}^*_{avg}$ reaches 6.20% in the case of $T_p = 50$ s, and $\zeta_R = 5°$, followed closely by 6.14% for $T_p = 45$ s and 6.03% for $T_p = 40$ s. These values indicate that long-period motions still induce considerable near-wake disturbances. At $x = 20\,D$, $\Delta\bar{\sigma}^*_{avg}$ consistently decreases across all cases and converges to approximately 2.1%, indicating similar levels of wake recovery regardless of the motion period. Overall, the simulations demonstrate that shorter motion periods tend to sustain

doi:10.6342/NTU202503576

higher turbulence intensity from the near-wake to the far-wake region, although differences become less pronounced with the downstream distance. These observations suggest that low-frequency roll motions lead to reduced flow disturbance, whereas high-frequency motions induce more substantial platform-driven disturbances that amplify velocity fluctuations, particularly in the upstream region.

doi:10.6342/NTU202503576

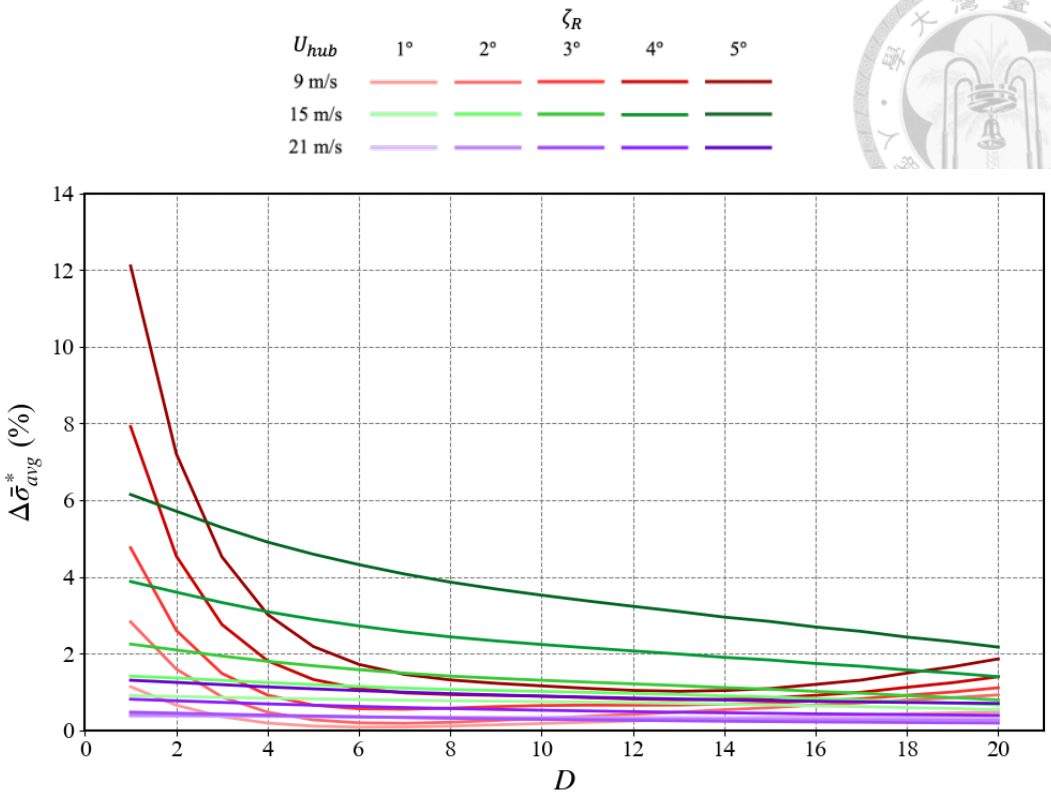

Figure 50 Downstream evolution of $\Delta\bar{\sigma}^*_{avg}$ under roll motions at 9, 15, and 21 m/s with a fixed period of 45 s

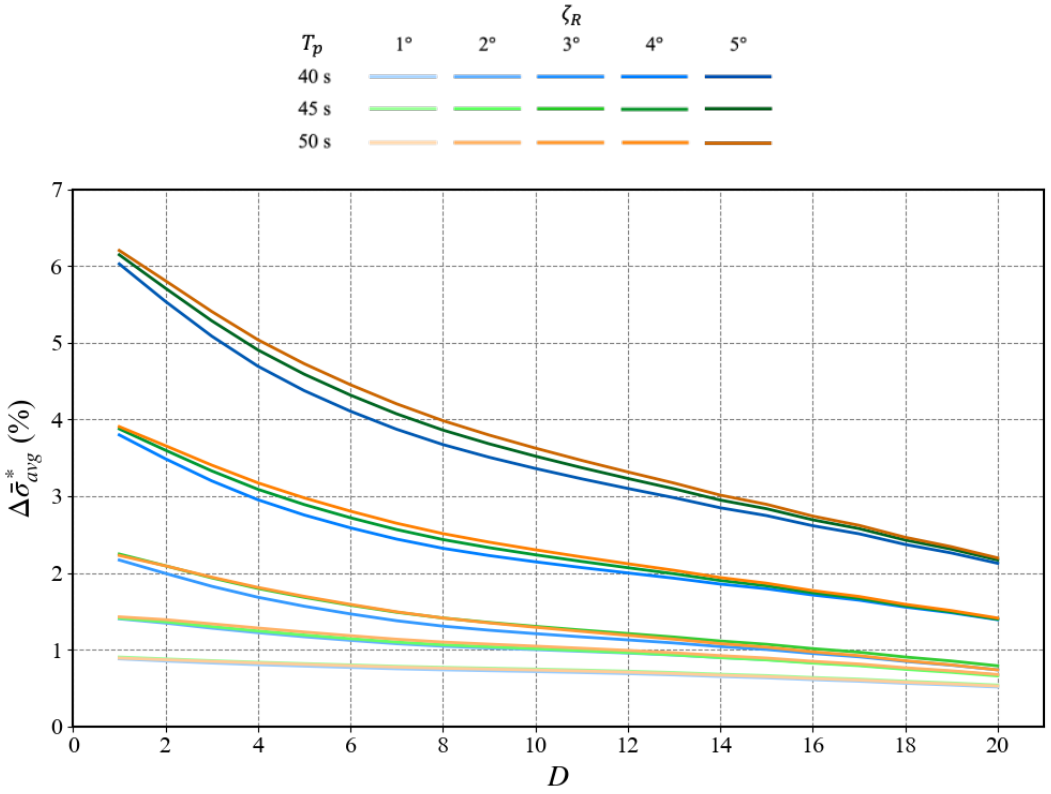

Figure 51 Downstream evolution of $\Delta\bar{\sigma}^*_{avg}$ under roll motions at 15 m/s with periods of 40, 45, and 50 s

doi:10.6342/NTU202503576

5.2.2 Pitching Behavior

Figure 52 illustrates the downstream behavior of $\Delta\overline{U}^*_{avg}$ induced by pitch motion with amplitudes ranging from 1° to 5° at the wind speed of 9, 15, 21 m/s and T_p = 45 s. The results demonstrate that the pitch-induced wake behavior is highly sensitive to inflow velocity. At $U_{hub} = 9$ m/s, pitch motions significantly enhance wake velocity, with $\Delta\overline{U}^*_{avg}$ increasing from 0.19% to 1.88% as the amplitude increases from 1° to 5°, and remaining above 1.2% even at $x = 20D$. At $U_{hub} = 15$ m/s, the wake response becomes more complicated. Negative values of $\Delta\overline{U}^*_{avg}$ dominate the near-wake region, but positive values gradually emerge in the downstream region, reaching 0.11% at $x = 20D$ for $\zeta_R = 4°$ and 0.18% for $\zeta_R = 5°$. In contrast, at $U_{hub} = 21$ m/s, the influence of pitch motion is limited, with the highest $\Delta\overline{U}^*_{avg}$ reaching only 0.08% at $x = 20D$ for $\zeta_R = 5°$. These results highlight that pitch-induced wake recovery is most effective at low wind velocity, where platform motion can contribute extra momentum to promote wake recovery. At moderate wind speeds, the wake recovery exhibits a delayed onset and becomes more dependent on pitch amplitude. Under high inflow wind speed conditions, stronger ambient momentum suppresses motion-induced perturbations, rendering the effect of pitch motion almost negligible.

Figure 53 illustrates the downstream behavior of $\Delta\overline{U}^*_{avg}$ induced by pitch motion with amplitudes ranging from 1° to 5° at a wind speed of 15 m/s and T_p = 40, 45, 50 s. In all cases, $\Delta\overline{U}^*_{avg}$ is negative in the near-wake region due to the blockage effect introduced by the pitch motion. For example, at $x = D$, $\Delta\overline{U}^*_{avg}$ for $\zeta_R = 3°$is approximately -0.16% across all three motion periods. However, wake recovery become more evident in the far-wake region and with high pitch amplitudes. For the case of $T_p = 50$ s, wake recovery is relatively moderate and gradual, with positive values appearing

doi:10.6342/NTU202503576

beyond $x = 11D$ and reaching a peak of 0.17% at $x = 20D$ for $\zeta_R = 5°$. The case of $T_p = 45$ s shows slightly stronger recovery, with $\Delta\overline{U}^*_{avg}$ giving a higher peak of 0.20% at the same location. The case of $T_p = 40$ s exhibits the most pronounced effect, with $\Delta\overline{U}^*_{avg}$ becoming positive from $x = 9D$ at $\zeta_R = 5°$, and reaching 0.22% at $x = 20D$, marking the highest wake recovery among the three motion periods. These results indicate that changes in motion period have only a minor effect on wake recovery under $U_{hub} =$ 15 m/s. For all tested motion periods, the downstream trends of $\Delta\overline{U}^*_{avg}$ are highly similar. Negative values are observed near the rotor, followed by gradual downstream recovery as the pitch motion amplitude increases. The wake behavior for $T_p = 40$ s shows a similar spatial feature to other periods. This suggests that pitch motion amplitude plays a more dominant role than motion period in influencing wake behavior within the tested range.

Under low wind speed conditions, large pitch motion amplitudes lead to significant and sustained recovery in wake velocity across the entire downstream region. This wake behavior observed for $\zeta_R \geq 3°$ can be attributed to the nonlinear characteristics of wake mixing and the turbine's limited aerodynamic response to dynamic flow excitation. According to Frederik et al. [38], dynamic pitch control enhances wake turbulence and recovery. However, when pitch motion amplitudes become too excessive, the increase in structural loads may be unable to justify aerodynamic benefits. Similarly, Abraham et al. [39] pointed out that the wake exhibits a delayed response to high-frequency or large-amplitude pitch inputs, which reduces the effectiveness of additional excitation. His findings align with the current observation that while moderate pitch motion improves wake mixing, its impact tends to become saturated once the motion amplitude exceeds a certain threshold.

doi:10.6342/NTU202503576

The negative $\Delta\overline{U}^*_{avg}$values observed in the near-wake region at moderate and high wind speed may be attributed to transient flow disruption induced by the platform's pitch motion. Although the present study only considers uncoupled pitch motion, similar wake behavior has been reported in studies involving combined motions. For example, Zhao et al. [40] observed that in-phase surge and pitch motion could lead to the early formation and expansion of a reverse flow region near the upper edge of the wake, resulting in localized velocity deficits. While their setup involved multi-axis excitation, the underlying mechanism remains relevant. Platform-induced disturbances can alter tip vortex spacing and affect shear-layer development, which in turn may destabilize the near-wake region and delay momentum recovery. In the present case, pitch motion alone may be sufficient to trigger such effects under moderate wind speed conditions, leading to the onset of negative $\Delta\overline{U}^*_{avg}$ in the early downstream region.

doi:10.6342/NTU202503576

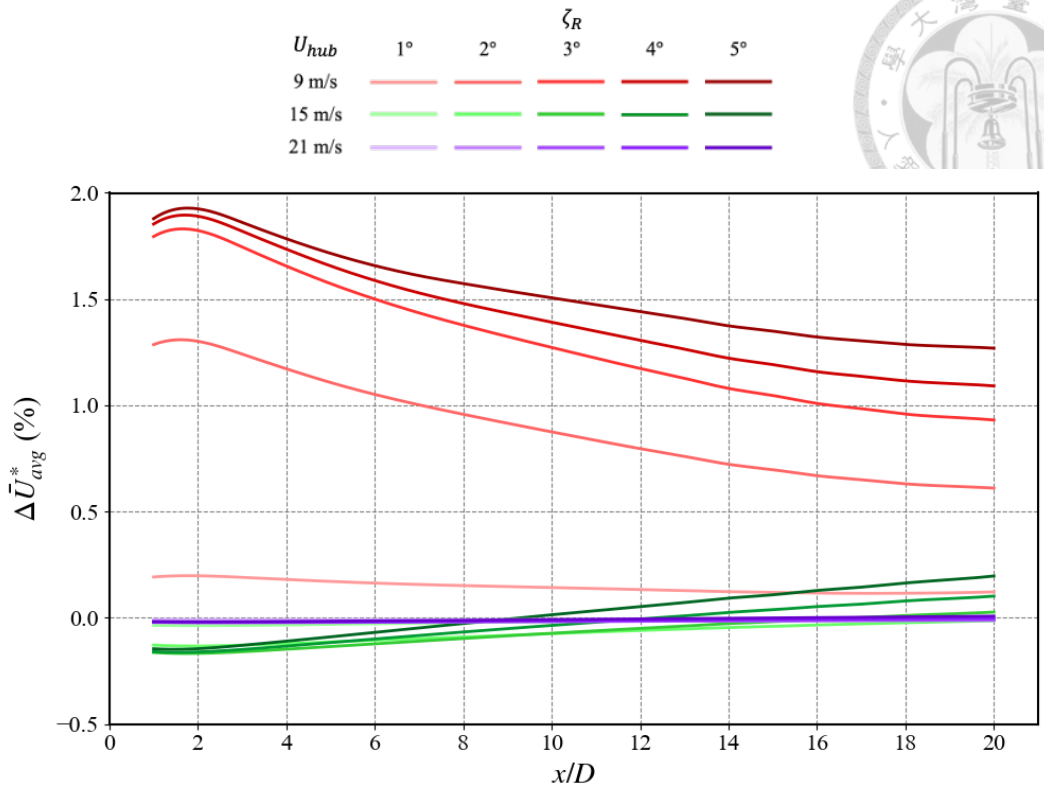

Figure 52 Downstream evolution of $\Delta\bar{U}^*_{avg}$ under pitch motions at 9, 15, and 21 m/s with a fixed period of 45 s

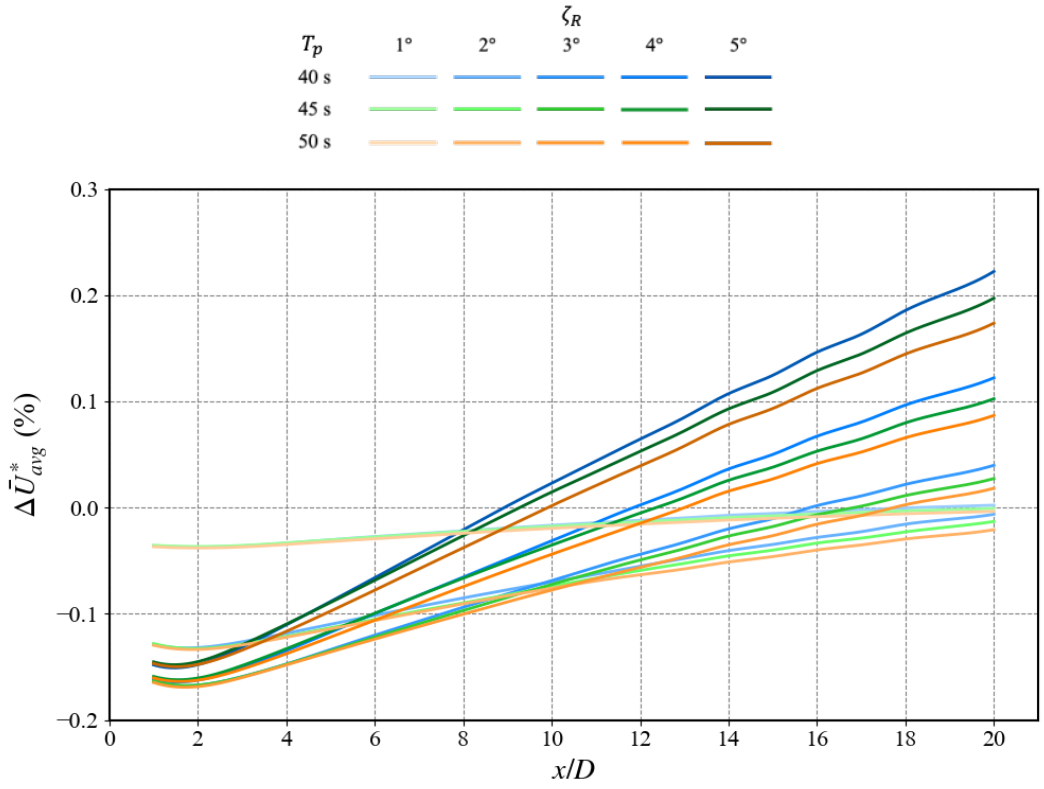

Figure 53 Downstream evolution of $\Delta\bar{U}^*_{avg}$ under pitch motions at 15 m/s with periods of 40, 45, and 50 s

doi:10.6342/NTU202503576

Figure 54 illustrates the downstream behavior of $\Delta\bar{\sigma}^*_{avg}$ induced by pitch motion with amplitudes ranging from 1° to 5° under the wind speeds of 9, 15, and 21 m/s and T_p = 45 s. At $U_{hub} = 9$ m/s, $\Delta\bar{\sigma}^*_{avg}$ gradually increases along the downstream direction, reaching a peak of approximately 3.28% at $x = 20D$ for $\zeta_R = 5°$. At $U_{hub} = 15$ m/s, $\Delta\bar{\sigma}^*_{avg}$ is significantly more pronounced, with $\Delta\bar{\sigma}^*_{avg}$ rising from 1.43% at $x = D$ to 5.46% at $x = 20D$ under the same pitch motion condition. In contrast, the case of $U_{hub} = 21$ m/s exhibits considerably low variation throughout the domain, with peak values only reaching about 0.77% at $x = 20D$ for $\zeta_R = 5°$. These results indicate that rated wind speed produces the highest wake disturbance under dynamic pitch motion, likely due to a better balance between the surrounding flow inertia and perturbation strength. At low wind speeds, the velocity perturbation propagates but remains moderate in strength, while at high wind speeds, strong inflow momentum suppresses fluctuation growth trigged by a continued platform motion.

Figure 55 illustrates the downstream behavior of $\Delta\bar{\sigma}^*_{avg}$ induced by pitch motion with amplitudes ranging from 1° to 5° under a wind speed of 15 m/s and $T_p = 40, 45, 50$ s. Across all pitch motion amplitudes and downstream locations, the case of $T_p = 40$ s consistently produces the highest fluctuation levels, followed by the cases of $T_p = 45$ s and 50 s. For example, in the case of $\zeta_R = 5°$ at $x = 20D$, $\Delta\bar{\sigma}^*_{avg}$ reaches 6.00% for $T_p = 40$ s, decreases to 5.46% for $T_p = 45$ s, and further drops to 5.02% for $T_p = 50$ s. A similar trend is observed at $x = 10D$, where the values are 3.88%, 3.51%, and 3.27% for the cases of $T_p = 40, 45$ and 50 s, respectively. While the general trend of $\Delta\bar{\sigma}^*_{avg}$ are similar across all cases, the magnitude of wake fluctuations is clearly influenced by the motion period. Specifically, short period induces strong and intense aerodynamic perturbations, resulting in substantial temporal velocity variation within the wake. In

doi:10.6342/NTU202503576

contrast, long period generates a smooth pitch motion dynamics and a constrained unsteady wake behavior.

doi:10.6342/NTU202503576

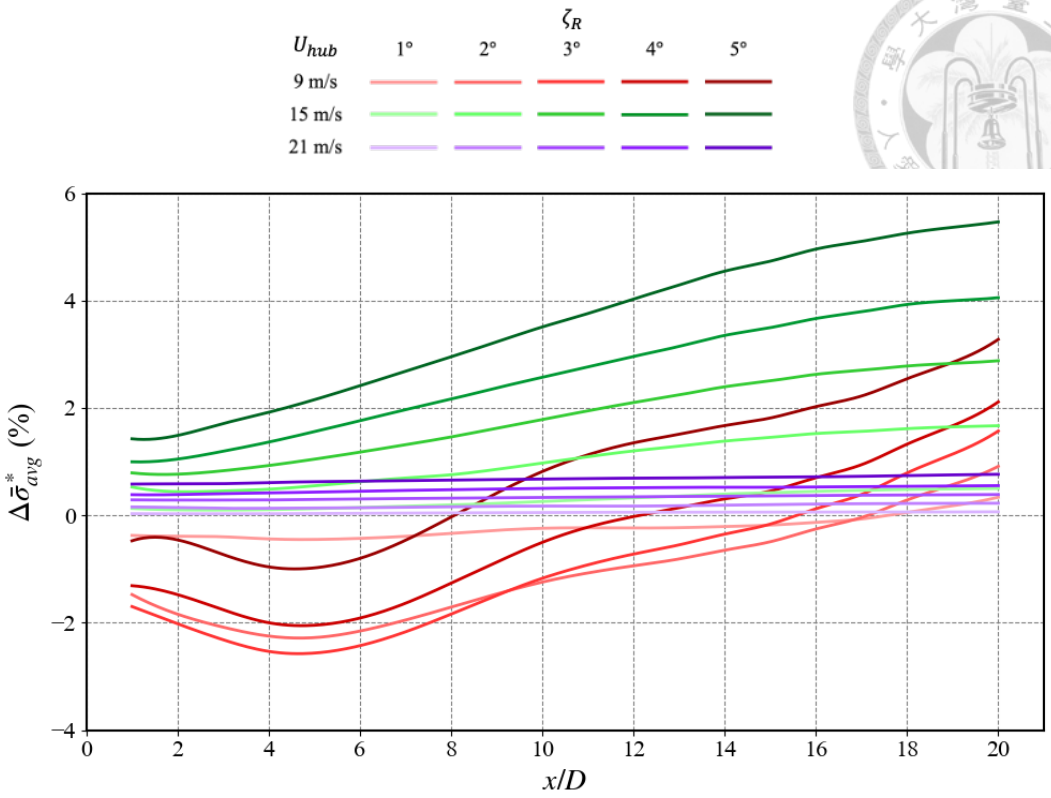

Figure 54 Downstream evolution of $\Delta\bar{\sigma}^*_{avg}$ under pitch motions at 9, 15, and 21 m/s with a fixed period of 45 s

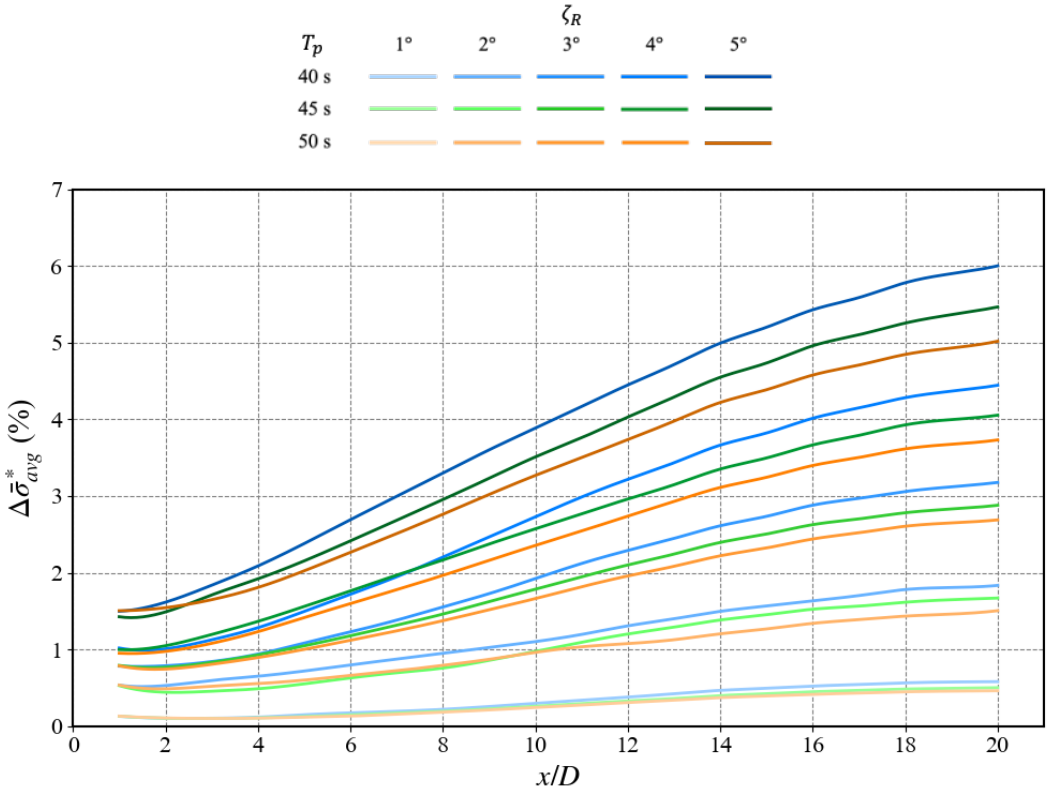

Figure 55 Downstream evolution of $\Delta\bar{\sigma}^*_{avg}$ under pitch motions at 15 m/s with periods of 40, 45, and 50 s

doi:10.6342/NTU202503576

5.2.3 Yawing Behavior

Figure 56 illustrates the downstream behavior of $\Delta\overline{U}^*_{avg}$ induced by yaw motion with amplitudes ranging from 1° to 5° at the wind speed of 9, 15, 21 m/s and T_p = 45 s. At $U_{hub} = 9$ m/s, $\Delta\overline{U}^*_{avg}$ increase significantly with the yaw motion amplitude, particularly for $\zeta_R = 4°$ and 5°, where the recovery peaks near $x = D$ and gradually decreases downstream, indicating a strong near-wake recovery. At $U_{hub} = 15$ m/s, the wake exhibits a velocity deficit in the near-wake region, followed by modest recovery beyond approximately $x = 6D$, suggesting a limited contribution to the wake recovery. At $U_{hub} = 21$ m/s, $\Delta\overline{U}^*_{avg}$ remains negative for a long downstream distance, with a sign change occurring only beyond $x = 9D$ and recovery magnitudes remaining relatively small. These results demonstrate that the impact of yaw motion on wake recovery is highly sensitive to inflow wind speed. At low wind speed, yaw-induced asymmetry in the wake leads to the formation of counter-rotating vortex pairs, which enhance lateral mixing and accelerate downstream velocity recovery. This phenomenon can be attributed to the development of asymmetric wake structures and counter-rotating vortex pairs that promote lateral mixing and effective velocity recovery, as reported by Bartl et al. [41] and Howland et al. [42]. These studies show that under low wind speed conditions, yaw-induced wake deflection and vortex dynamics are more pronounced and effective in accelerating wake dissipation. In contrast, high wind speeds impose a delayed response due to strong wake inertia and more stable coherent structures, resulting in postponed and less significant wake recovery.

Figure 57 illustrates the downstream behavior of $\Delta\overline{U}^*_{avg}$ induced by yaw motion with amplitudes ranging from 1° to 5° at a wind speed of 15 m/s and T_p = 40, 45, 50 s. Overall, short yaw motion periods lead to earlier and slightly more pronounced wake

doi:10.6342/NTU202503576

velocity increments, particularly in the mid- to far-wake regions. The case of $T_p = 40$ s exhibits the earliest transition of $\Delta\overline{U}^*_{avg}$ from a negative to positive value, with a sign change occurring around $x = 6D$ and reaching a peak of approximately 0.025% at $x = 20D$ for $\zeta_R = 5°$. In comparison, the case of $T_p = 45$ s shows a similar pattern but with a slightly delayed recovery and a lower peak of 0.032% as $x = 20D$, while the case of $T_p = 40$ s displays the weakest wake adjustment, with a more gradual increase yet ultimately achieving the highest recovery of 0.035% at the same location. These results suggest that varying the yaw motion period between 40 and 50 seconds influences the behavior of wake recovery. Short periods accelerate the dynamic response of the wake by inducing high-frequency perturbations, which promote earlier wake deflection and mixing. Although the differences among the cases are modest in absolute values, the trend indicates that motion period plays a secondary but noticeable role in governing yaw-induced wake dynamics.

doi:10.6342/NTU202503576

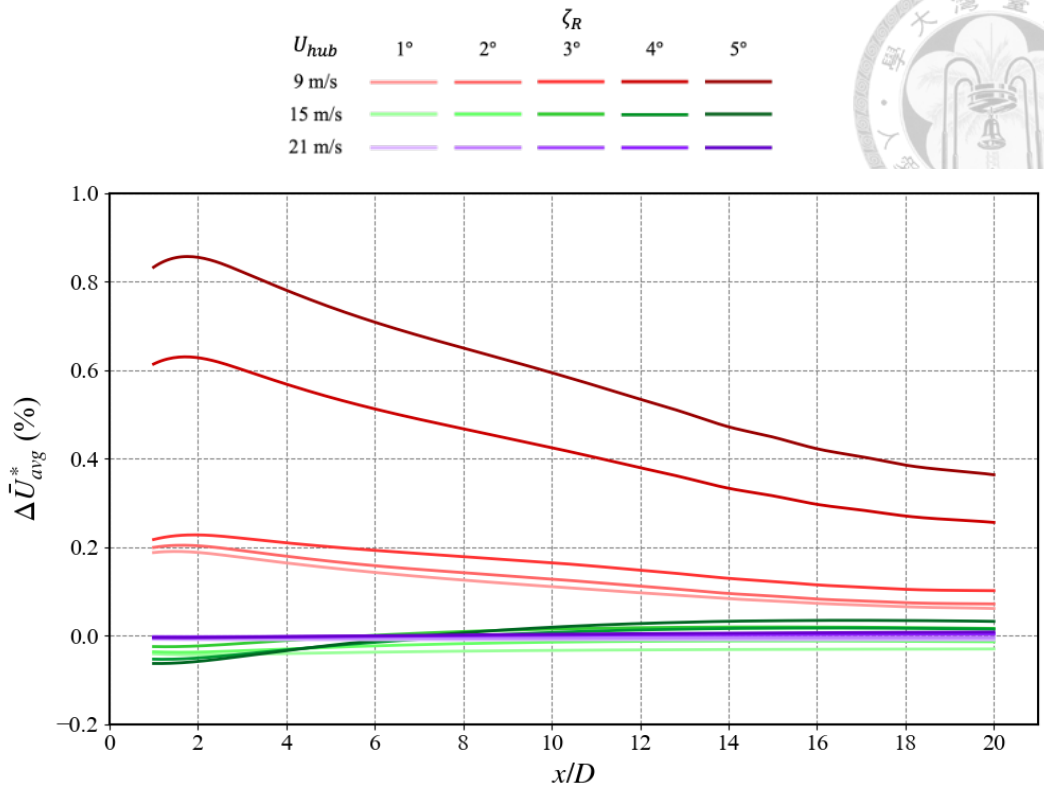

Figure 56 Downstream evolution of $\Delta\bar{U}^*_{avg}$ under yaw motions at 9, 15, and 21 m/s with a fixed period of 45 s

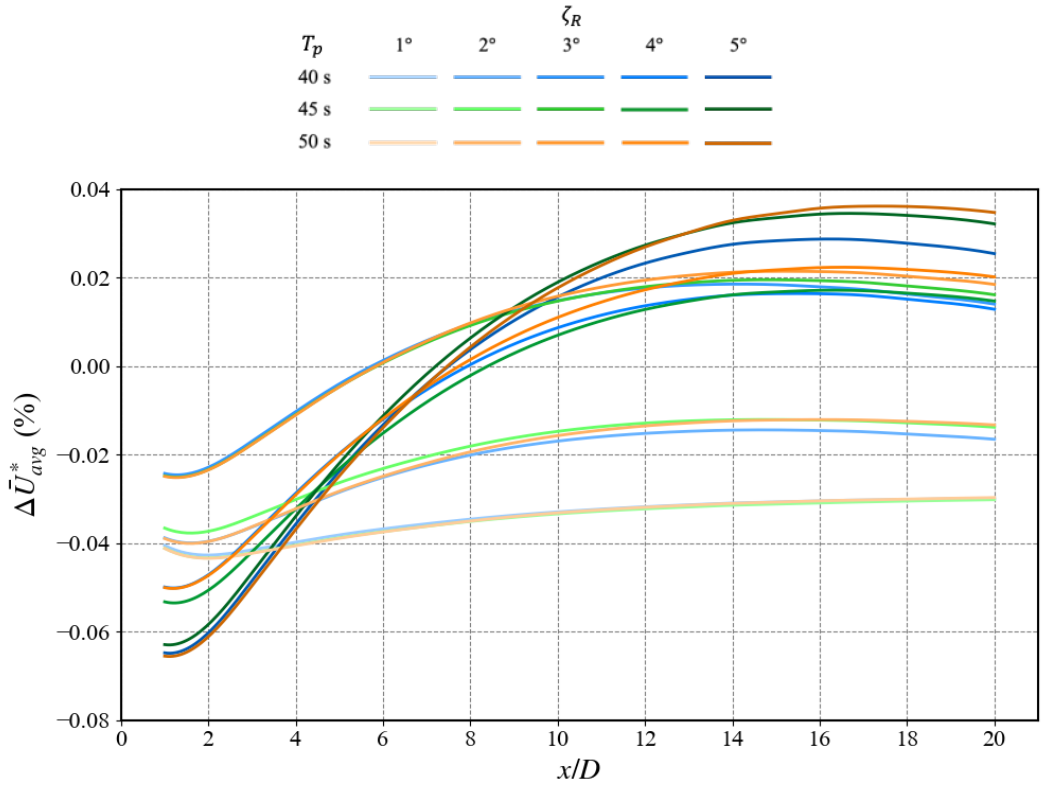

Figure 57 Downstream evolution of $\Delta\bar{U}^*_{avg}$ under yaw motions at 15 m/s with periods of 40, 45, and 50 s

doi:10.6342/NTU202503576

Figure 58 illustrates the downstream behavior of $\Delta\bar{\sigma}^*_{avg}$ induced by yaw motion with amplitudes ranging from 1° to 5° at the wind speed of 9, 15, 21 m/s and T_p = 45 s. The results reveal a strong dependence of mean streamwise velocity fluctuations on inflow wind speed. At $U_{hub} = 9$ m/s, $\Delta\bar{\sigma}^*_{avg}$ increases gradually with yaw motion amplitude and downstream distance, peaking at approximately 0.72% at $x = 20D$ for $\zeta_R = 5°$. At $U_{hub} = 15$ m/s, $\Delta\bar{\sigma}^*_{avg}$ are significantly amplified. The values rise rapidly beyond $x = 5D$ and exceed 1.51% at $x = 16D$ under the same yaw condition, indicating a substantial wake disturbance. In contrast, at $U_{hub} = 21$ m/s, $\Delta\bar{\sigma}^*_{avg}$ is markedly suppressed. The maximum $\Delta\bar{\sigma}^*_{avg}$ reaches only 0.087% at $x = 20D$, which is nearly an order of magnitude lower than the value observed at $U_{hub} = 15$ m/s. Despite similar spatial distributions, the overall magnitude remains limited, reflecting a reduced wake response to periodic yaw motion excitation. These observations suggest a non-monotonic relationship between inflow velocity and yaw-induced disturbance. At moderate wind speeds, the interaction between shear layer instability and yaw-induced cross-stream vorticity promotes strong vortex shedding and wake meandering, resulting in elevated fluctuation levels. However, at high wind speeds, increased flow inertia stabilizes the wake structure and suppresses perturbation growth, thereby diminishing unsteady wake behavior.

Figure 59 illustrates the downstream behavior of $\Delta\bar{\sigma}^*_{avg}$ induced by yaw motion with amplitudes ranging from 1° to 5° at a wind speed of 15 m/s and T_p = 40, 45, 50 s. Under this inflow condition, the yaw-induced wake fluctuation clearly increases with the yaw motion period. The peak $\Delta\bar{\sigma}^*_{avg}$ consistently occurs near $x = 17D$ for $\zeta_R = 5°$, with values rising from 1.43% for $T_p = 40$ s, to 1.51% for $T_p = 45$ s, and reaching 1.66% for $T_p = 50$ s. This trend indicates that long yaw motion periods enhance the flow

doi:10.6342/NTU202503576

unsteadiness and persistence of wake fluctuations. The downstream location of peak disturbance suggests that long periods allow more coherent wake structures to develop and persist, thereby amplifying the motion energy carried downstream. In contrast, short yaw periods induce more frequent but less spatially sustained perturbations, resulting in early saturation of wake recovery and decay of wake fluctuations. While the differences in peak magnitude are moderate, the overall trend is similar across all cases: increasing yaw motion period leads to enhance unsteady wake behavior, reflecting a positive correlation between yaw motion timescale and fluctuation intensity.

The experimental work by Medici and Alfredsson [43] demonstrated that under low freestream velocities, yaw-induced wake asymmetry does not necessarily lead to increased disturbance in the near wake. Their findings revealed that although yaw motion creates lateral deflection and asymmetrical flow structures, the limited flow inertia and reduced shear layer development at low wind speeds suppress the formation of large-scale instabilities. This suggests that yaw-induced disturbance may only become significant under moderate to high inflow conditions where the shear flow and vorticity amplification become more dominant.

doi:10.6342/NTU202503576

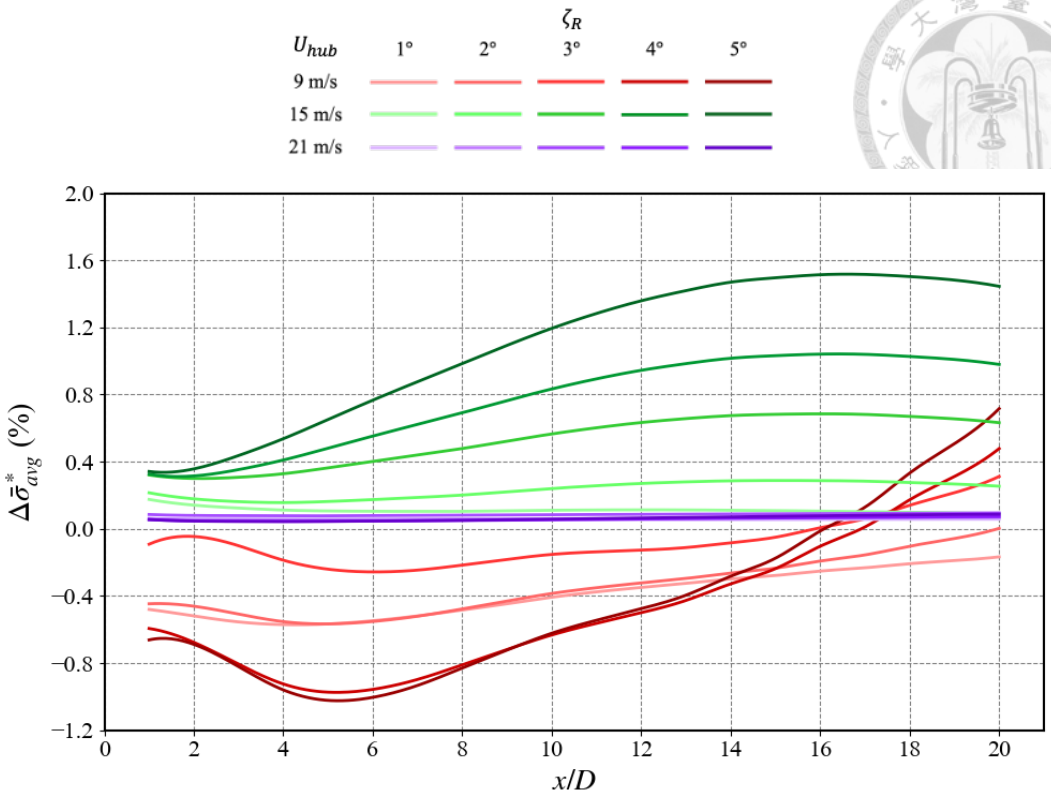

Figure 58 Downstream evolution of $\Delta\bar{\sigma}^*_{avg}$ under yaw motions at 9, 15, and 21 m/s with a fixed period of 45 s

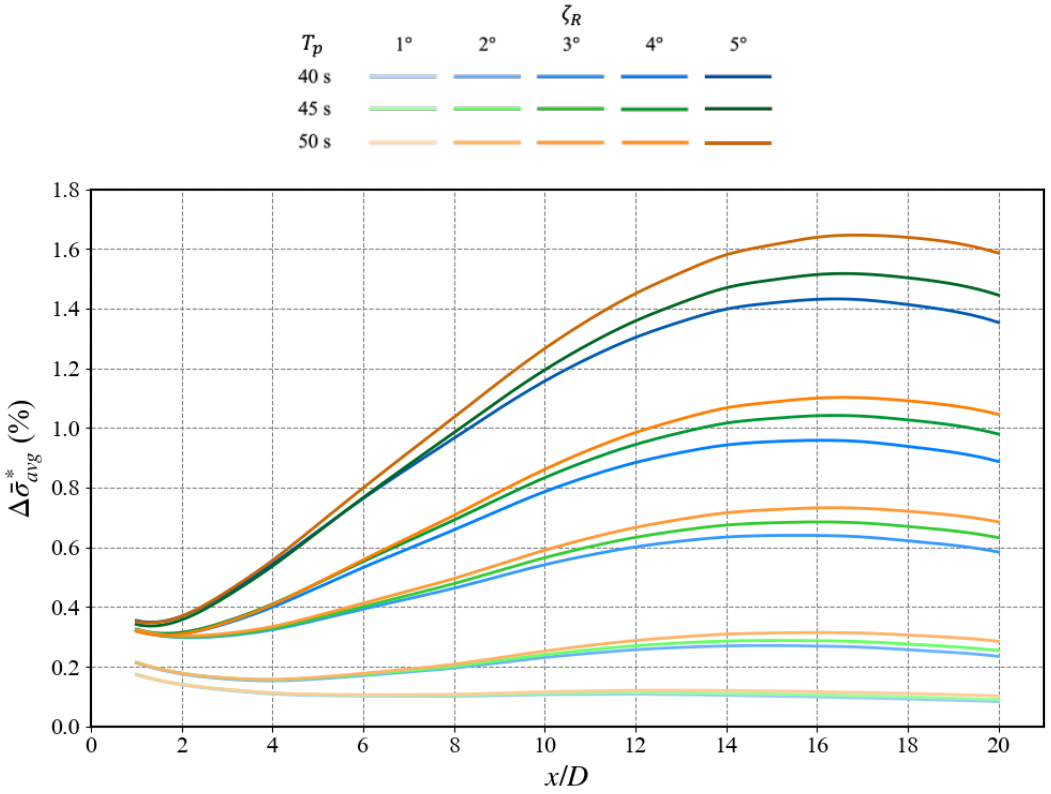

Figure 59 Downstream evolution of $\Delta\bar{\sigma}^*_{avg}$ under yaw motions at 15 m/s with periods of 40, 45, and 50 s

doi:10.6342/NTU202503576

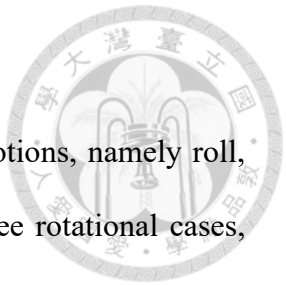

5.2.4 Summary

This section investigates the effects of uncoupled rotational motions, namely roll, pitch, and yaw, on the wake behaviors of FOWT. Among these three rotational cases, pitch and yaw motions cause the most significant modulation of the wake, followed by roll motion. This influence is especially evident in the near-wake and mid-wake regions, where increased flow asymmetry and intensified turbulence are observed. Pitch and yaw motions introduce cross-stream velocity components and enhance vortex interactions, which promote wake deformation and mixing. These effects lead to localized zones of acceleration and deceleration within the wake, depending on the phase and amplitude of the platform motion. Although roll motion is less dominant in the wake recovery, it still contributes to increased wake disturbance under specific flow conditions. The aerodynamic response of the wake to rotational motion is closely related to the inflow wind speed. At low and moderate wind speeds, such as $U_{hub} = 9$ and 15 m/s, the wake behavior is more sensitive to the platform motion, leading to strong turbulence and great variation in the velocity field. However, at a high wind speed of $U_{hub} = 21$ m/s, the effects of rotational motion become markedly weaker. In this case, the strong flow inertia stabilizes the wake and reduces its receptiveness to external perturbations. Additionally, while changes in motion period produce only minor differences in the far wake, short motion periods can intensify disturbances in the near-wake region.

As shown in Figure 60, wake behavior is compared between the stationary turbine and three cases of rotational motions, i.e., roll, pitch, and yaw. Under an inflow wind speed of $U_{hub} = 9$ m/s, with $\zeta_R = 5°$ and $T_p = 45$ s, the stationary turbine reaches a time-averaged velocity of approximately 7.378 m/s at a downstream distance of $x = 7D$. In comparison, the turbine subjected to roll motion reaches the same wind speed earlier, at $x = 6.5D$. Pitch motion leads to the fastest recovery, with the target velocity achieved

doi:10.6342/NTU202503576

at $x = 4.6D$, while yaw motion yields a recovery distance of around $x = 6D$.These results indicate that rotational motions, particularly pitch and yaw, can substantially enhance wake recovery, enabling downstream turbines to regain inflow velocity over shorter streamwise intervals. Compared to the stationary configuration, the presence of platform rotation reduces the required inter-turbine spacing to achieve the required aerodynamic performance.

As shown in Figure 61, the total power output of the wind turbine is compared under stationary conditions and three distinct rotational platform motions, i.e., roll, pitch, and yaw. At $U_{hub} = 9$ m/s with $T_p = 45$ s and ζ_R =5°, a clear trend in power generation is observed. Relative to the stationary baseline, roll motion results in a modest decrease in power output of approximately 0.3% at the rotor plane. Pitch motion leads to the largest reduction, with a drop of about 2.7%, while yaw motion produces a decrease of approximately 2.1%. These results demonstrate that rotational platform motions can adversely affect the aerodynamic performance of the moving turbine itself. Among the three motions, pitch and yaw exhibit more pronounced negative impacts, likely due to their direct influence on rotor inflow alignment. However, when considering the downstream turbine located at 7D, the effect of rotational platform motions appears beneficial. At the same motion with amplitude of 5°, roll motion increases the power output of the downstream turbine by approximately 1%, pitch motion yields the most pronounced positive effect with an increase of about 4.8%, and yaw motion contributes an improvement of roughly 2.1%. These results indicate that, although the upstream turbine experiences a reduction in power generation under platform motions, the associated wake recovery improving inflow conditions of the downstream turbine lead to higher power production of the subsequent turbines.

doi:10.6342/NTU202503576

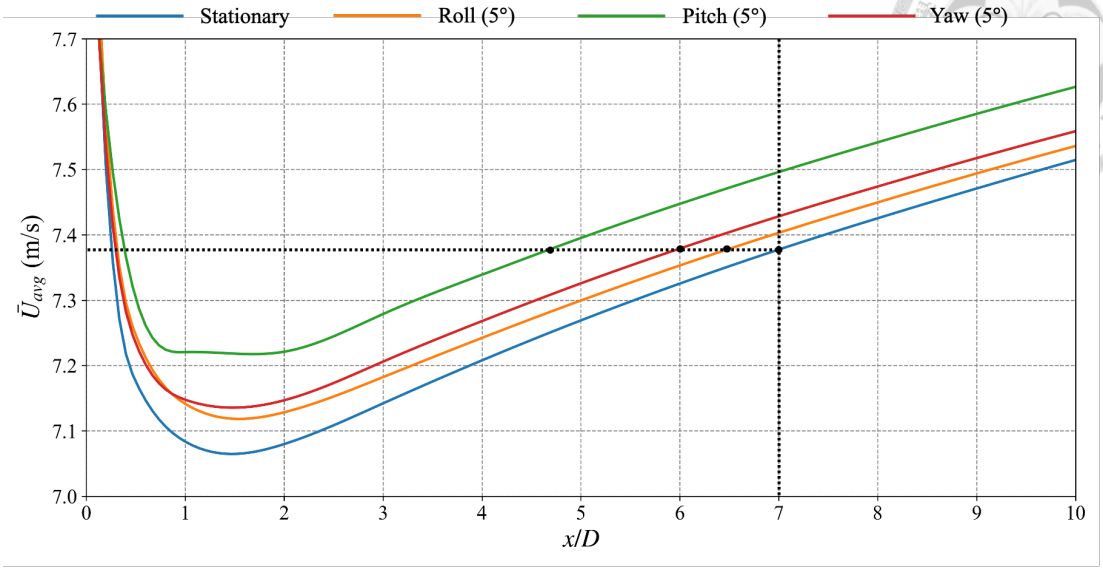

Figure 60 Dependence of $\bar{U}_{avg}$ on x/D for the stationary case and three rotational motions with $U_{hub} = 9$ m/s, $T_p = 45$ s and $\zeta_R = 5°$

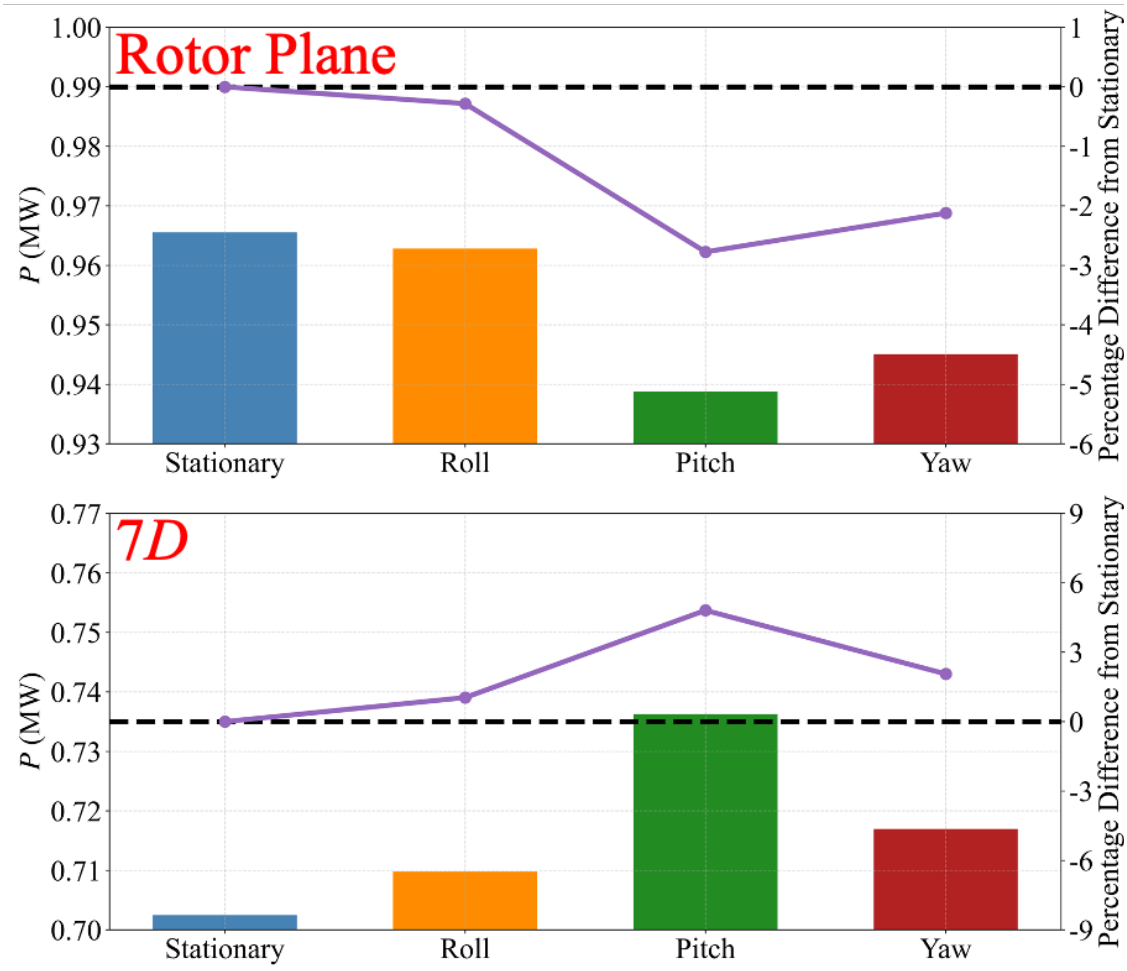

Figure 61 P of the stationary case and three rotational motion cases at the rotor plane and the $7D$ downstream plane

doi:10.6342/NTU202503576

6 Fitting Analysis

In this study, a quadratic polynomial fitting method is employed to establish a polynomial dependence of the field variable on its parameters. In this fitting framework, $\Delta\overline{U}_{avg}^{F}$ denotes the predicted difference in normalized time-averaged velocity and serves as the dependent variable of the quadratic polynomial equation, which comprises a constant term (C_0) accounting for the baseline offset, linear terms (C_1, C_2) representing the proportional contributions of motion amplitude and downstream distance, respectively, quadratic terms (C_3, C_4) that capture the nonlinear growth or decay associated with independent variables, and an interaction term (C_5) that describes the coupled effect of motion amplitude and downstream distance. The adopted formula is given as follows:

$$\Delta\overline{U}_{avg}^{F} = C_0 + C_1 \cdot \zeta + C_2 \cdot \left(\frac{x}{D}\right) + C_3 \cdot \zeta^2 + C_4 \cdot \left(\frac{x}{D}\right)^2 + C_5 \cdot \zeta \cdot \left(\frac{x}{D}\right). \tag{36}$$

This fitting analysis not only provides a compact mathematical representation of the simulation results but also highlights the relative contribution of each factor and their impacts on wake recovery. Through the fitted coefficients, one can assess which factors dominate the recovery of downstream wind speed under various platform motion conditions. The use of a quadratic polynomial is designed to adequately capture both linear and nonlinear behaviors observed in the wake flow for the purpose of maintaining computational simplicity and interpretability. Table 10 summarizes the constants of the fitted quadratic polynomials for various cases.

doi:10.6342/NTU202503576

Table 10 The constants of the fitted quadratic polynomials

Figure		C_0	C_1	C_2	C_3	C_4	C_5	R^2	Motion	U_{hub} (m/s)	T_p (s)
62	(a)	47.90	120.4	0.253	-0.96	-0.27	-1.33	0.9786	Surge	9	45
	(b)	-10.4	-18.9	5.746	0.517	-0.31	0.953	0.9049		15	45
	(c)	-4.08	-25.1	-1.48	0.668	-0.01	0.529	0.5800		21	45
	(d)	-15.1	-19.9	7.332	0.566	-0.39	1.188	0.9422		15	40
	(e)	-10.4	-18.9	5.746	0.517	-0.31	0.953	0.9049		15	45
	(f)	-26.4	-17.7	7.659	0.472	-0.36	0.774	0.8664		15	50
63	(a)	-4.67	12.39	-2.70	0.296	0.179	-0.72	0.9960	Sway	9	45
	(b)	-67.9	75.89	1.896	1.726	-0.09	-1.72	0.9986		15	45
	(c)	-373	353.6	1.830	3.024	-0.10	-0.70	0.9991		21	45
	(d)	-71.2	76.35	2.577	1.716	-0.12	-1.69	0.9986		15	40
	(e)	-67.9	75.89	1.896	1.726	-0.09	-1.72	0.9986		15	45
	(f)	-64.3	75.16	1.466	1.746	-0.07	-1.75	0.9986		15	50
64	(a)	15.21	16.54	-4.14	9.021	0.219	-2.26	0.9650	Heave	9	45
	(b)	-10.9	31.73	0.887	8.228	-0.01	-1.80	0.9966		15	45
	(c)	52.05	-89.1	0.643	100.8	-0.02	-0.88	0.9793		21	45
	(d)	-10.6	30.50	0.955	8.748	-0.02	-1.76	0.9965		15	40
	(e)	-10.9	31.73	0.887	8.228	-0.01	-1.80	0.9966		15	45
	(f)	-10.1	31.04	0.795	8.422	-0.01	-1.82	0.9966		15	50
65	(a)	-57.7	91.89	-3.60	3.190	0.277	-3.78	0.9951	Roll	9	45
	(b)	-12.8	46.94	2.164	5.419	-0.07	-1.64	0.9988		15	45
	(c)	-2.40	16.46	0.184	1.414	-0.01	-0.07	0.9976		21	45
	(d)	-15.0	47.75	2.329	5.323	-0.08	-1.60	0.9986		15	40
	(e)	-12.8	46.94	2.164	5.419	-0.07	-1.64	0.9988		15	45
	(f)	-13.1	47.45	2.009	5.237	-0.06	-1.65	0.9985		15	50
66	(a)	-32.9	98.23	-4.49	-9.91	0.132	-0.60	0.9791	Pitch	9	45
	(b)	5.829	-13.9	0.128	1.769	-0.01	0.424	0.9923		15	45
	(c)	6.881	-17.9	-0.41	2.411	0.004	0.368	0.9807		21	45
	(d)	6.422	-14.2	0.062	1.782	-0.01	0.463	0.9946		15	40
	(e)	5.829	-13.9	0.128	1.769	-0.01	0.424	0.9923		15	45
	(f)	5.642	-13.7	0.133	1.717	-0.01	0.407	0.9914		15	50

doi:10.6342/NTU202503576

67	(a)	16.53	-2.96	-0.53	3.501	0.033	-0.54	0.9680	Yaw	9	45
	(b)	-84.6	21.93	5.211	-3.30	-0.24	0.835	0.9165		15	45
	(c)	-157	54.86	0.764	-6.24	-0.07	1.273	0.9396		21	45
	(d)	-87.8	24.55	5.367	-3.65	-0.24	0.737	0.9114		15	40
	(e)	-84.6	21.93	5.211	-3.30	-0.24	0.835	0.9165		15	45
	(f)	-88.1	24.27	5.250	-3.76	-0.24	0.901	0.9330		15	50

doi:10.6342/NTU202503576

To quantitatively evaluate the accuracy of the quadratic polynomial under surge motion, the coefficient of determination (R^2) was computed for each case and summarized in Table 10. At a wind speed of $U_{hub} = 9$ m/s and a fixed period $T_p = 45$ s, the fitted polynomial has $R^2 = 0.9786$. This reflects a reasonable correlation among ζ, x/D, and $\Delta\overline{U}^*_{avg}$ at low wind speeds. When the wind speed increases to $U_{hub} = 15$ m/s, the fitting accuracy decreases slightly. Specifically, $R^2 = 0.9422$, 0.9049, and 0.8664 are found for $T_p = 40$ s, 45 s, and 50 s, respectively. Notably, at the high wind speed of $U_{hub} = 21$ m/s and $T_p = 45$ s, the polynomial fit exhibits the lowest $R^2 = 0.5800$. This marked reduction in R^2 highlights that at high wind speeds, the interaction becomes highly nonlinear, and a simple quadratic form is insufficient to fully characterize its nonlinear behavior. Nevertheless, it can still be observed from the fitted constants that under low wind speed conditions, the linear coefficient C_1 remains positive, indicating that for every 1-meter increase in surge amplitude, the downstream wind speed increases by approximately 0.12%. This demonstrates that surge motion at low wind speeds indeed produces a positive gain in the velocity field.

doi:10.6342/NTU202503576

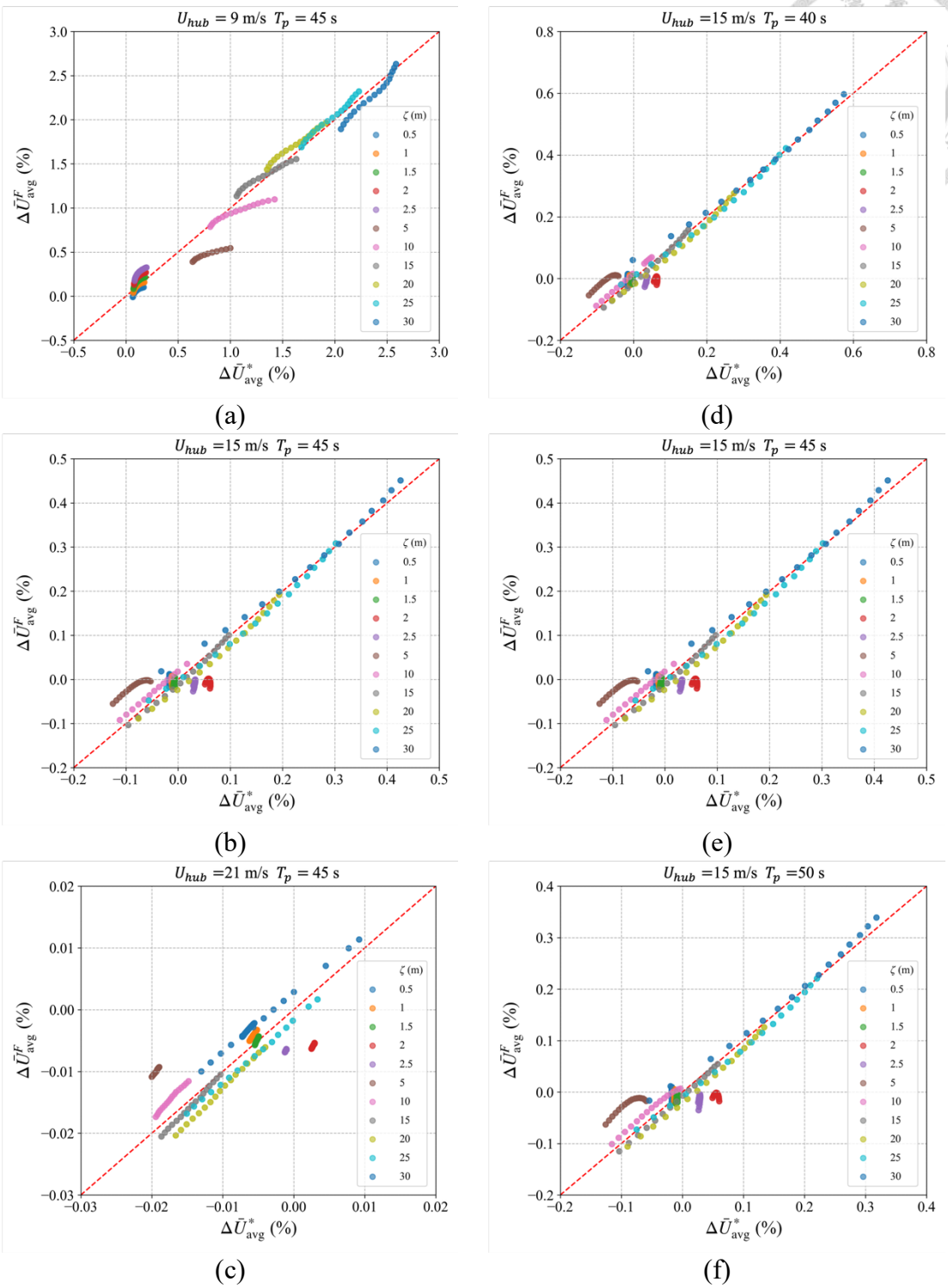

Figure 62 $\Delta\bar{U}^F_{avg}$ under surge motions at (a) 9 m/s, (b) 15 m/s, and (c) 21 m/s with period fixed at 45 s, and at 15 m/s with periods of (d) 40 s, (e) 45 s, and (f) 50 s

doi:10.6342/NTU202503576

Figure 63 illustrates the prediction of the quadratic polynomial under sway motion. Compared to the surge motion, the sway motion models exhibit remarkably high R^2 values across all tested wind speeds and motion periods. At $U_{hub} = 9$ m/s and $T_p = 45$ s, the polynomial fit achieves $R^2 = 0.9960$. Similarly, for $U_{hub} = 15$ m/s, the fitted result is found to give $R^2 = 0.9986$ for $T_p = 40$ s, 45 s, and 50 s. At the highest wind speed $U_{hub} = 21$ m/s and $T_p = 45$ s, the model even achieves the highest value of $R^2 = 0.9991$. Therefore, it can be concluded that the quadratic polynomial provides a reliable description of the downstream velocity increase behavior induced by sway motion. These results suggest that, unlike surge motion, the interaction under sway motion remains relatively linear, or at least adequately represented by the quadratic terms, even at elevated wind speeds and motion amplitudes. This strong agreement also highlights that sway motion primarily influences the lateral velocity component in a manner that is less nonlinear than the longitudinal effects of surge motion.

Furthermore, examination of the fitted constants reveals that the linear and quadratic amplitude terms (C_1 and C_3) remain positive in all cases, indicating that larger sway amplitudes consistently lead to greater increases in downstream wind speed. The coefficient C_2, associated with the streamwise distance, is negative under low wind speed conditions, suggesting that the velocity gain decays rapidly with distance. However, at medium and high wind speeds, C_2 becomes positive, but its magnitude remains relatively small. Notably, the interaction term C_5 is negative in all cases, implying that while increasing the sway amplitude enhances the gain of wind speed, but this effect diminishes at large downstream distances.

doi:10.6342/NTU202503576

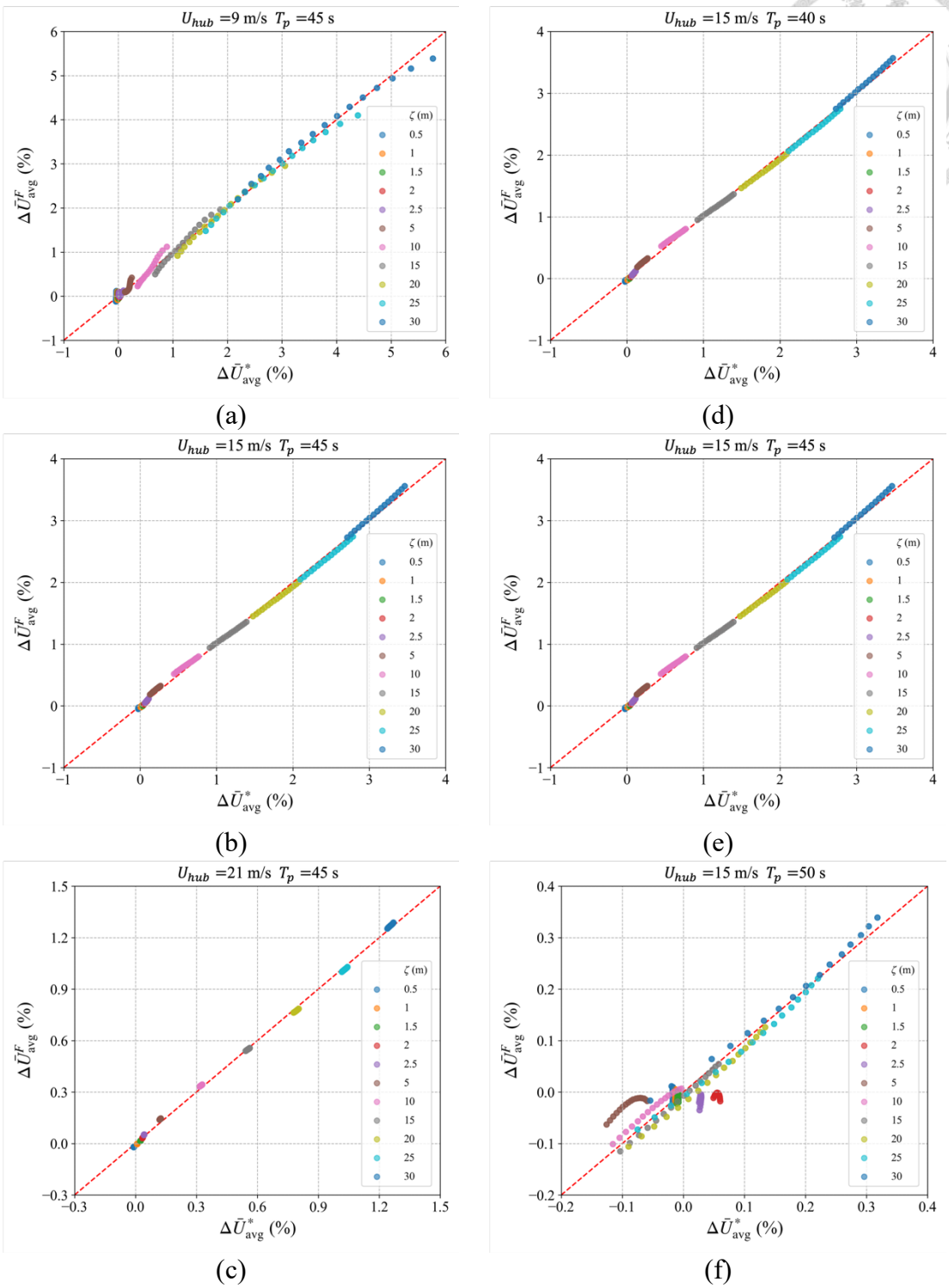

Figure 63 $\Delta\bar{U}^F_{avg}$ under sway motions at (a) 9 m/s, (b) 15 m/s, and (c) 21 m/s with period fixed at 45 s, and at 15 m/s with periods of (d) 40 s, (e) 45 s, and (f) 50 s

doi:10.6342/NTU202503576

Figure 64 illustrates the prediction of the quadratic polynomial under heave motion. Similar to the sway motion, the heave motion models exhibit high R^2 values across all tested wind speeds and periods, albeit with slightly large variation at both low and high wind speeds. At $U_{hub} = 9$ m/s and $T_p = 45$ s, the polynomial fit achieves $R^2 = 0.9650$, indicating good agreement between the simulated and predicted $\Delta\overline{U}^F_{avg}$. For $U_{hub} = 15$ m/s, the fitting remains reliable, with $R^2 = 0.9965$, 0.9966, 0.9966 for $T_p = 40$ s, 45 s, and 50 s, respectively. At the highest wind speed $U_{hub} = 21$ m/s and $T_p = 45$ s, the model achieves $R^2 = 0.9793$, which, although slightly lower than at $U_{hub} = 15$ m/s, still demonstrates high reliability. Therefore, it can be concluded that the quadratic polynomial provides a reliable description of the downstream velocity increase behavior induced by heave motion. These results indicate that, like sway motion, the interaction under heave motion seems to be adequately represented by quadratic terms, even at elevated wind speeds and motion amplitudes.

Furthermore, an examination of the fitted constants reveals that their trends for heave and sway motions are very similar. The linear and quadratic amplitude terms (C_1 and C_3) are positive under all conditions, indicating that larger heave amplitudes consistently lead to more significant increases in downstream wind speed. This supports the conclusion that heave motion, like sway motion, enhances the wake velocity with the increase of the the motion amplitude. Notably, the interaction term (C_5) remains negative under all conditions, implying that although increasing the heave amplitude enhances the velocity gain, this effect diminishes with increasing downstream distance.

doi:10.6342/NTU202503576

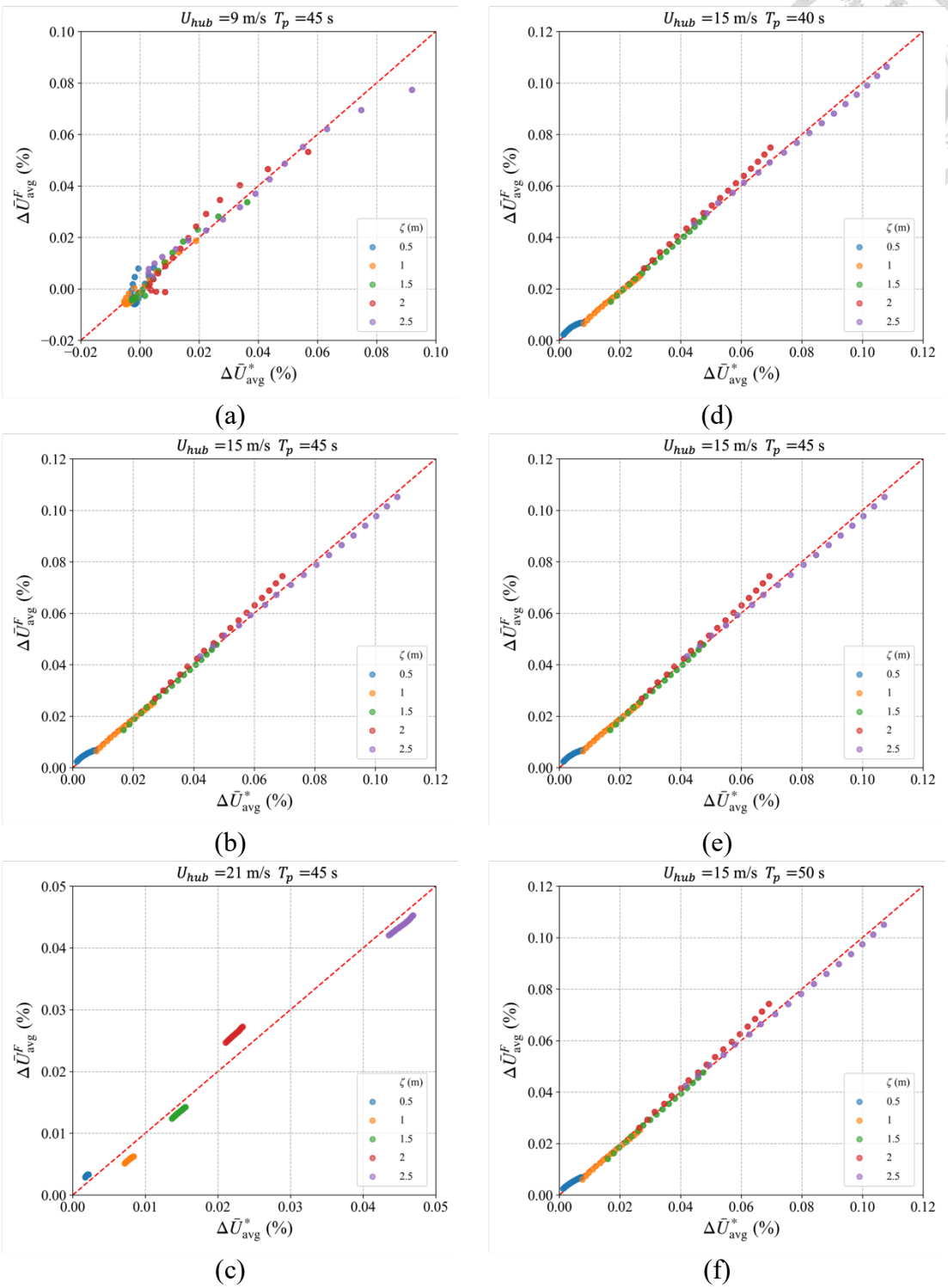

Figure 64 $\Delta\bar{U}^F_{avg}$ under heave motions at (a) 9 m/s, (b) 15 m/s, and (c) 21 m/s with period fixed at 45 s, and at 15 m/s with periods of (d) 40 s, (e) 45 s, and (f) 50 s

doi:10.6342/NTU202503576

Figure 65 illustrates the prediction of the quadratic polynomial under roll motion. Similar to the sway and heave motions, the roll motion models exhibit high R^2 values across all tested wind speeds and periods, demonstrating the adequacy of a quadratic form in describing the simulation results. At $U_{hub} = 9$ m/s and $T_p = 45$ s, the polynomial fit achieves $R^2 = 0.9951$. For $U_{hub} = 15$ m/s, the fitting gives $R^2 = 0.9986$, 0.9988, 0.9985 for $T_p = 40$ s, 45 s, and 50 s, respectively. Even at the highest wind speed $U_{hub} = 21$ m/s and $T_p = 45$ s, the model maintains a high $R^2 = 0.9976$, confirming its reliability under high wind conditions. Therefore, it can be concluded that the quadratic polynomial provides a robust and accurate description of the downstream velocity increase induced by roll motion. These results indicate that, like sway and heave motions, the interaction under roll motion seems to be adequately captured by the quadratic terms.

Further analysis of the fitted constants reveals that both C_1 and C_3 representing the linear and quadratic amplitude effects, remain positive in all cases, indicating that larger roll amplitudes consistently lead to greater increases in downstream wind speed. This trend is highly similar to that observed in sway and heave motions. Additionally, the interaction term C_5 remains negative in all cases, implying that while increasing the roll amplitude enhances the velocity gain, this effect diminishes at larger downstream distances. Such findings suggest that the beneficial effect of roll motion on the wake recovery is also spatially localized and attenuates with distance, as observed in other motion modes.

doi:10.6342/NTU202503576

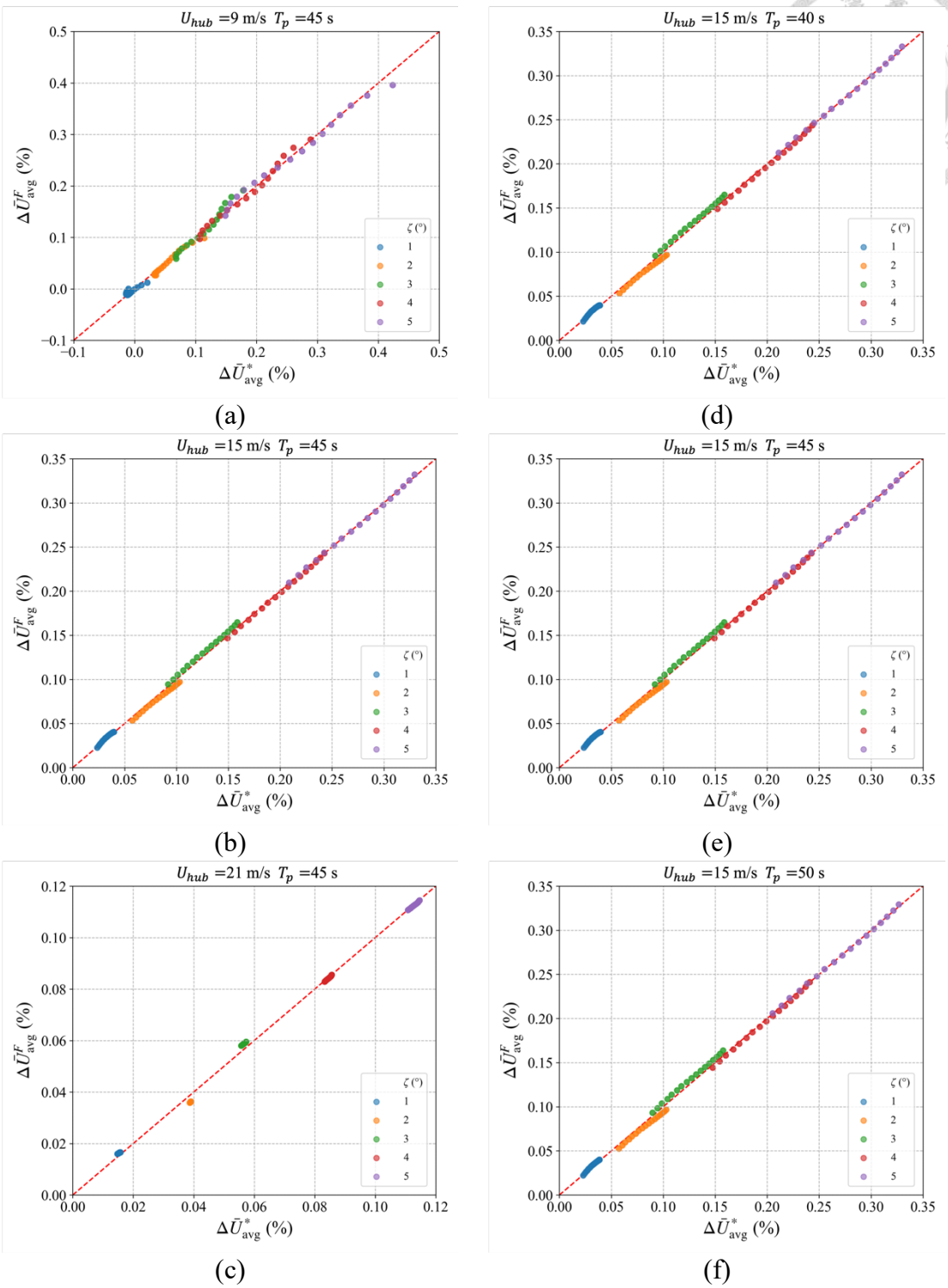

Figure 65 $\Delta\bar{U}^F_{avg}$ under roll motions at (a) 9 m/s, (b) 15 m/s, and (c) 21 m/s with period fixed at 45 s, and at 15 m/s with periods of (d) 40 s, (e) 45 s, and (f) 50 s

doi:10.6342/NTU202503576

Figure 66 illustrates the prediction of the quadratic polynomial models under pitch motion. While the fitted equations of the pitch motion still achieving relatively high R^2 values across all tested wind speeds and motion periods, they exhibit slightly large deviations compared to sway, heave, and roll motions. At $U_{hub} = 9$ m/s and $T_p = 45$ s, the polynomial fit achieves $R^2 = 0.9791$, indicating good agreement between the simulated and predicted $\Delta\bar{U}^F_{avg}$. For $U_{hub} = 15$ m/s, $R^2 = 0.9946$, 0.9923, and 0.9914 are found for $T_p = 40$ s, 45 s, and 50 s, respectively. Even at the highest wind speed $U_{hub} = 21$ m/s and $T_p = 45$ s, the fitted equation has $R^2 = 0.9807$, confirming a reasonable prediction under high wind conditions. These results demonstrate that the quadratic polynomial still provides an adequate description of the downstream velocity behavior induced by pitch motion, though the nature of the flow interaction appears to differ from other motion modes.

A closer examination of the fitted constants reveals distinctive characteristics of pitch motion. The quadratic amplitude term C_3 remains consistently positive under all conditions, indicating that larger pitch amplitudes lead to greater downstream velocity increases at higher-order terms. However, unlike other motions, the linear amplitude term C_1 becomes negative under medium-to-high wind speed conditions, suggesting that pitch motion exerts an adverse effect on the near-wake flow field. Additionally, the interaction term C_5 is positive, which implies that the beneficial effects of pitch amplitude become more pronounced at larger downstream distances. This trend is found different from the attenuation observed in sway, heave, and roll motions. These findings highlight that the aerodynamic response to pitch motion involves more complicated spatial and directional effects, distinct from other motion modes.

doi:10.6342/NTU202503576

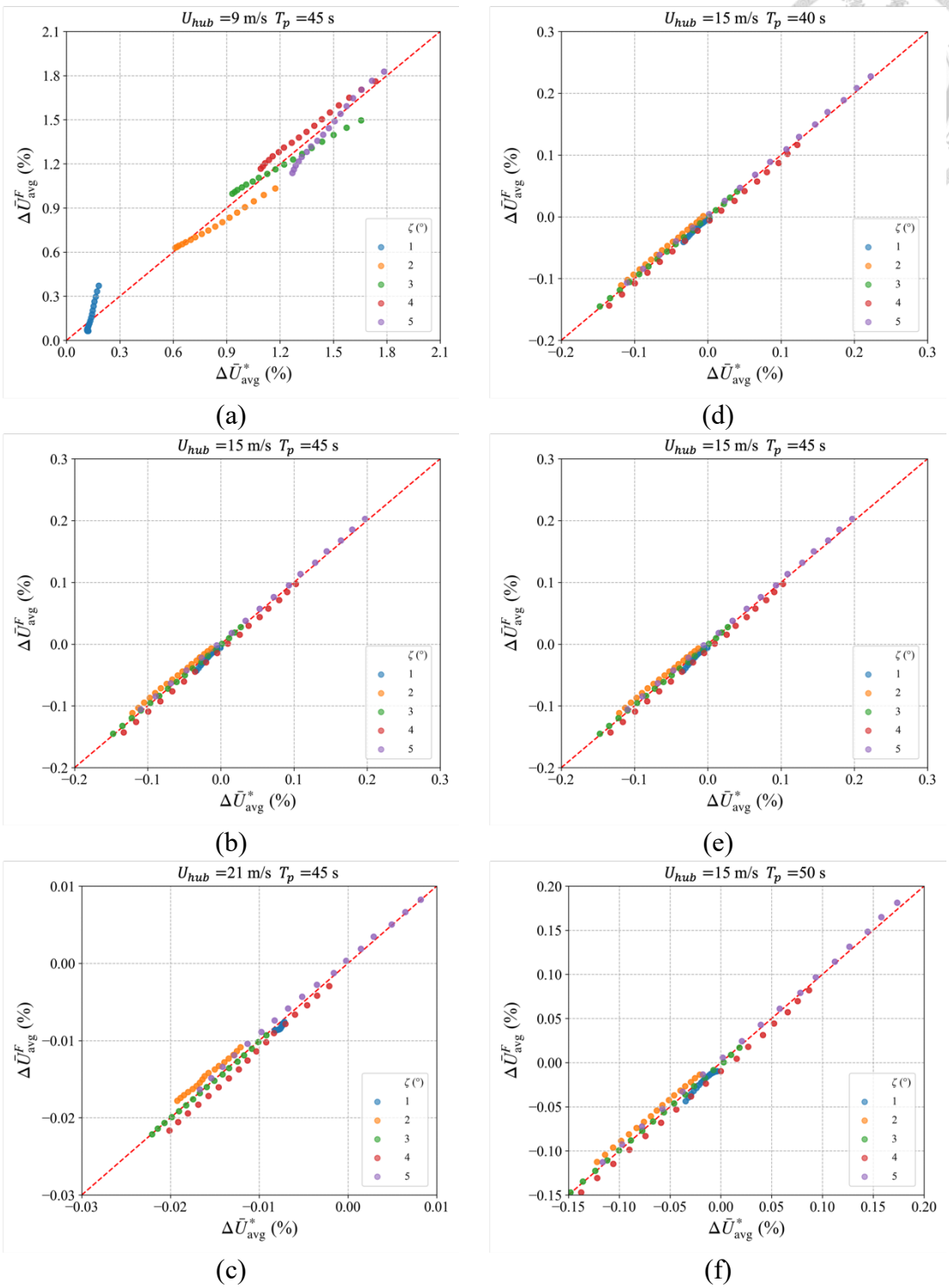

Figure 66 $\Delta\bar{U}^F_{avg}$ under pitch motions at (a) 9 m/s, (b) 15 m/s, and (c) 21 m/s with period fixed at 45 s, and at 15 m/s with periods of (d) 40 s, (e) 45 s, and (f) 50 s

doi:10.6342/NTU202503576

Figure 67 illustrates the prediction of the quadratic polynomial under yaw motion. Overall, the R^2 values for yaw motion are notably lower than those of the other motion types discussed earlier, indicating that a simple quadratic polynomial is not sufficient to fully capture the complex flow response associated with yaw. At $U_{hub} = 9$ m/s and $T_p = 45$ s, the polynomial fit achieves $R^2 = 0.9680$, which still represents a reasonable fit. When the wind speed increases to $U_{hub} = 15$ m/s, the performance decreases slightly, with $R^2 = 0.9114$, 0.9165, and 0.9330 with $T_p = 40$ s, 45 s, and 50 s, respectively. At the highest wind speed $U_{hub} = 21$ m/s and $T_p = 45$ s, R^2 is 0.9396, but remains lower than the values achieved by other degrees of freedom under comparable conditions. These results suggest that the aerodynamic response to yaw motion is quite nonlinear and governed by more complicated interactions, making it harder for a quadratic form to fully represent its physical behavior. However, the relatively low R^2 values imply that additional higher-order terms are necessary to improve predictive accuracy under yaw motion.

doi:10.6342/NTU202503576

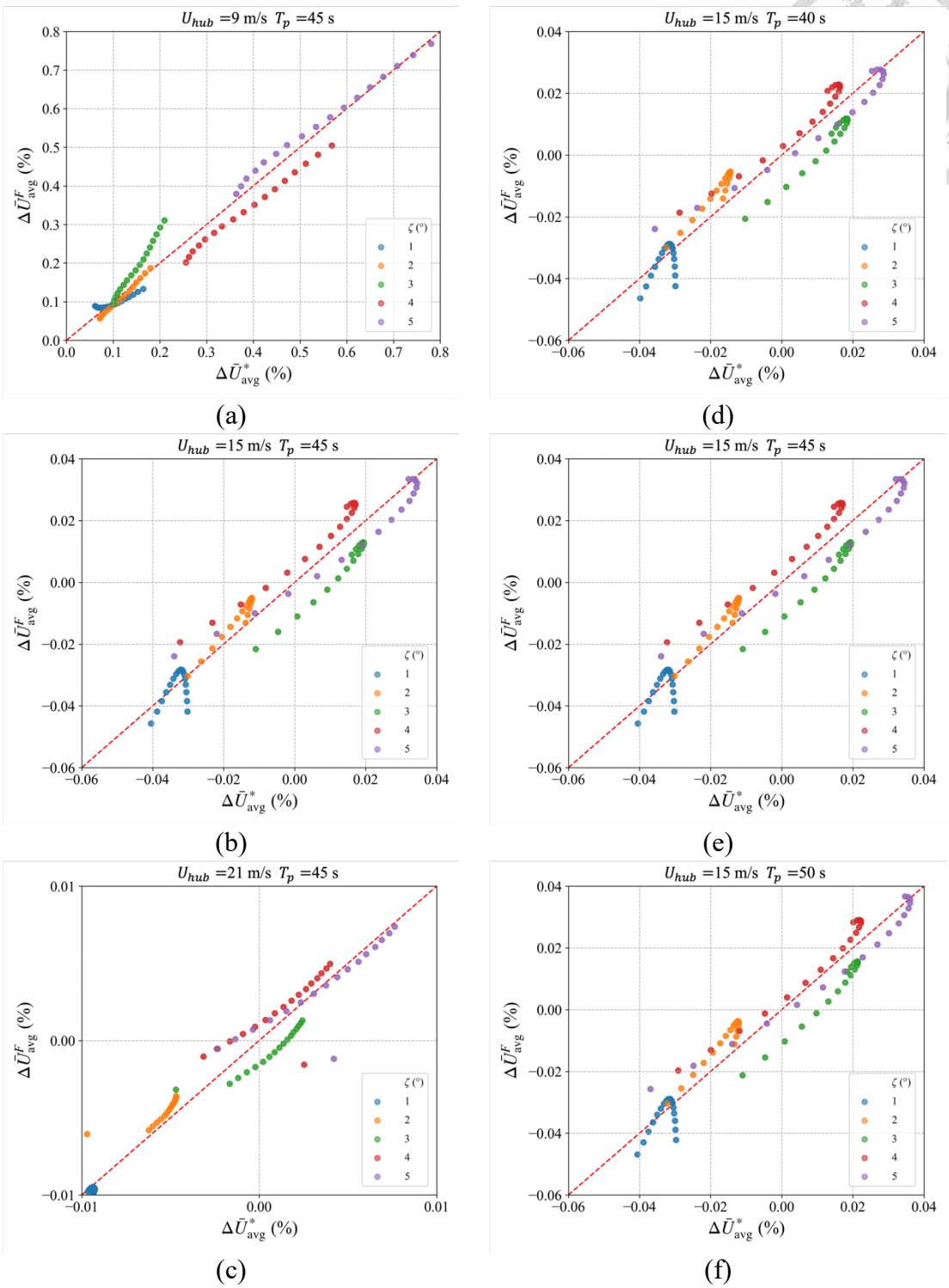

Figure 67 $\Delta\bar{U}^F_{avg}$ under yaw motions at (a) 9 m/s, (b) 15 m/s, and (c) 21 m/s with period fixed at 45 s, and at 15 m/s with periods of (d) 40 s, (e) 45 s, and (f) 50 s

doi:10.6342/NTU202503576

7 Comparison with Previous Studies

A comparison is made between the present study and the work of Lin et al. [34], who investigated the influence of surging and pitching behaviors on the power output and wake characteristics of a 15 MW floating wind turbine using STAR-CCM+ with the IEA 15 MW reference turbine. In their simulations, the rotor rotation was resolved using a sliding mesh technique, and the wake field was examined at various downstream locations. A notable feature in [34] is a convex wake recovery profile arising from approximately $3D$ to $8D$ downstream. [34] employed the detailed geometries of the blades, nacelle, and tower, which introduce additional drag forces and consequently contribute to further velocity deficits in the downstream wake region. As shown in Figure 68 , the mean streamwise velocities in [34] were reduced to as low as 4 m/s, whereas the present study delivers a mean wake velocity above 7 m/s.

In contrast, the present study, which adopts a different modeling approach and numerical configuration, did not exhibit such convex wake recovery profile in the same downstream region. As shown in Figure 69, the wake recovery profiles in the present study display an almost linear dependence on the downstream distance. This difference may be attributed to the rotor modeling strategy, the turbulence modeling approach or the level of numerical dissipation inherent to the adopted computational framework.

doi:10.6342/NTU202503576

7. Comparison with Previous Studies

The previous study [34] is believed to better represent the actual wake behavior, because the present study uses an actuator disk to avoid the need to resolve the geometry of rotor blades. It is possible that the present study underestimates the local momentum deficit recovery in the far wake, leading to a weaker velocity gradient between the wake core and the surrounding flow. As a result, the deceleration region appears to shift synchronously with the platform motions, and the level of turbulent mixing in the downstream wake remains relatively subdued. This reduced mixing hence produces a linear velocity recovery profile. Consequently, the wake recovery curve obtained in this study may underestimate certain localized acceleration behavior, which in turn implies the need for further validation against high-fidelity numerical methods or experimental measurements to ensure that wake dynamics are accurately captured.

While the overall wake recovery trends between these two studies are basically consistent, the absence of the convex velocity rise in the present results indicates that the numerical setup adopted in this study may be unable to fully reproduce the physical characteristics of the floating wind turbine wake under real operating conditions. This underscores the need for further improvement of the modeling approach and validation against high-fidelity simulations or experimental data to ensure the accuracy of the proposed numerical approach.

doi:10.6342/NTU202503576

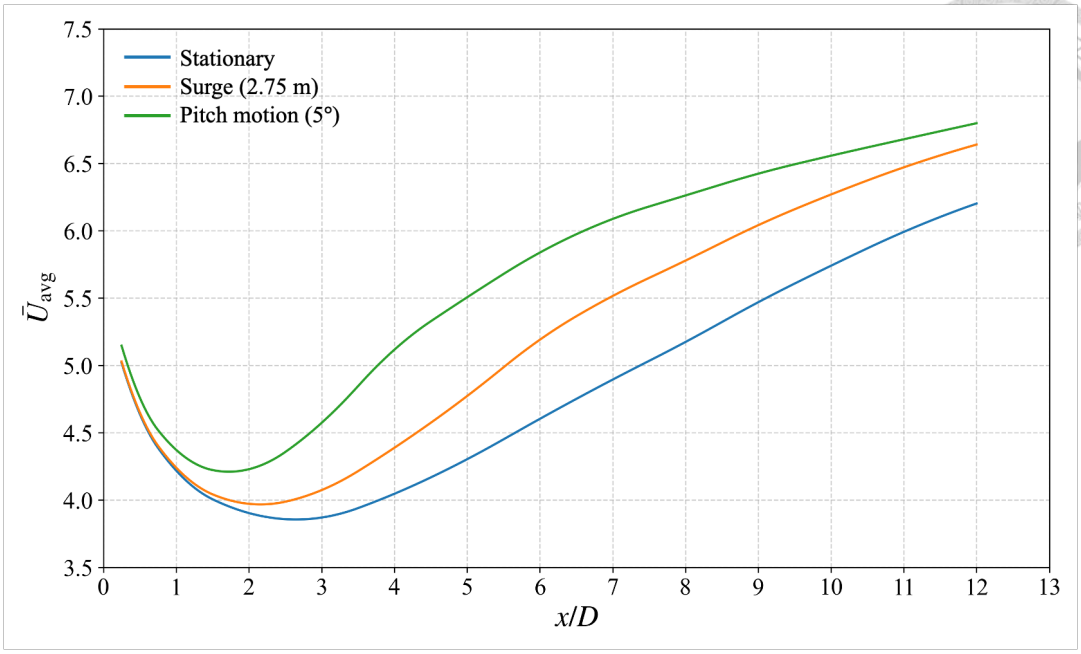

Figure 68 Comparison of $\bar{U}_{avg}$ among the stationary, surge, and pitch cases given in [34]

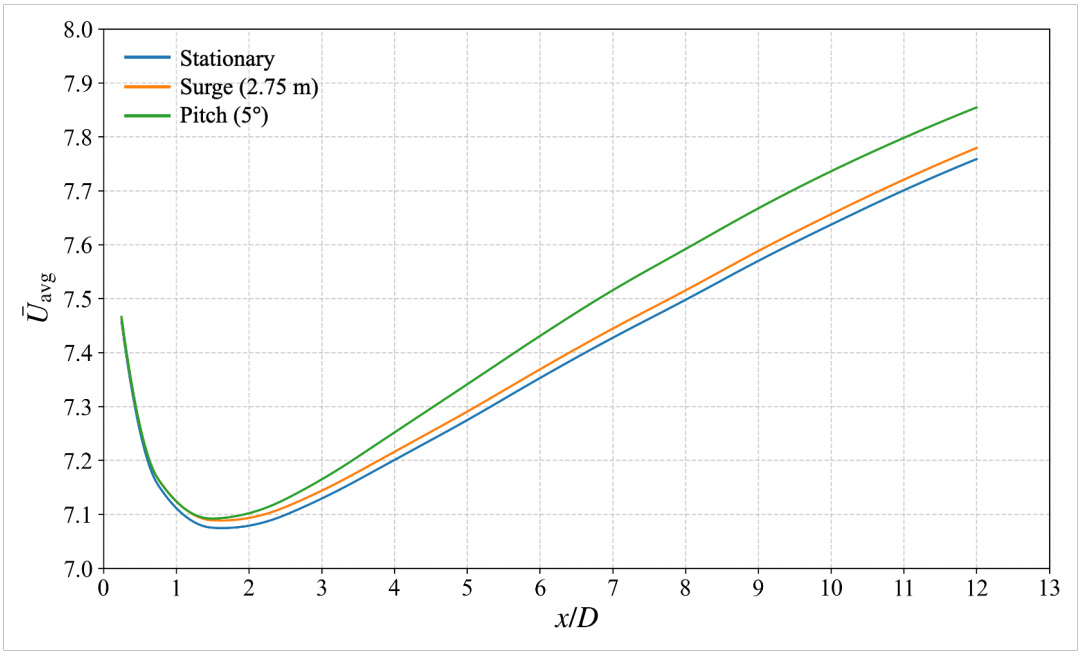

Figure 69 Comparison of $\bar{U}_{avg}$ among the stationary, surge, and pitch cases

doi:10.6342/NTU202503576

8 Conclusion

This study presents a comprehensive numerical investigation into the wake behaviors of a FOWT subjected to 6 single-DOF platform motions. By employing an actuator disk model within the STAR-CCM+ framework, the effects of both translational and rotational motions on wake behavior were systematically examined under various inflow wind speeds, motion amplitudes, and motion periods. The analysis provides critical insights into how platform-induced dynamics influence wake recovery, velocity fluctuations, and overall aerodynamic performance.

1. Based on the normalized mean velocity deficit $\Delta\overline{U}^{*}_{avg}$, it was found that pitch and yaw motions generate strong disturbances in the downstream flow beyond 6*D*, which enhance wake mixing and accelerate wind speed recovery. This indicates that these motions can be exploited to improve downstream wake conditions.
2. Analysis of the normalized turbulence intensity $\Delta\bar{\sigma}^{*}_{avg}$ suggests that sway and roll motions contribute to enhance turbulence levels and fatigue loads on downstream turbines. Therefore, controlling and minimizing sway and roll amplitudes is essential to reduce fatigue-induced damage and prolong turbine lifespan.
3. At high wind speeds, the accompanied flow inertia and stability of the atmospheric boundary layer significantly mitigate the effects induced by platform motions. This demonstrates that the response of wake recovery to platform dynamics diminishes as wind speed rises, making motion-induced wake impacts less pronounced under strong wind conditions.

doi:10.6342/NTU202503576

4. The results confirm that wind speed and motion amplitude are the dominant factors influencing downstream wake behavior, whereas the effect of motion period remains relatively minor. This suggests that future design and control strategies of FOWTs needs to take the impact of platform motion into account.
5. The findings also indicate that the motions of FOWTs have the potential to enhance wake recovery downstream, enabling the possibility of reducing inter-turbine spacing in wind farms. Such a reduction could improve the spatial efficiency of wind farm layouts and lower the levelized cost of energy, despite the trade-off of slightly reduced power output of the upstream FOWTs.
6. The correlation among motion amplitude**,** downstream distance, and $\Delta\overline{U}^{*}_{avg}$ can be described by a quadratic polynomial, particularly for sway, heave, roll, and pitch motions. This demonstrates that the fitted quadratic equations can capture the complex wake dynamics induced by platform motions and can be used as predictive tools in design and optimization processes.

doi:10.6342/NTU202503576

9 Future Work

One future research is suggested to further investigate the complex interactions between wake dynamics and platform motion of FOWTs. Preliminary findings indicate that the downstream wake characteristics are influenced not only by geometric and operational parameters, but also by the platform's motion response under environmental loading. Notably, the wake generated by an upstream floating turbine can significantly alter both the inflow velocity field and the dynamic response of downstream units within an array configuration. To accurately capture these two-way effects, a coupled modeling framework that accounts for both motion-induced wake field and the aerodynamic and hydrodynamic in order to get a deeper insight into the wake-motion coupling mechanism and to optimize and spatial design of floating wind farm layouts is another suggestion of future work.

Future research activities can extend to the simulations of wake-motion interactions in FOWT arrays. Comparative studies between fixed and floating configurations can be also performed, focusing on the differences in platform kinematics, wake propagation, and downstream turbine performance. These efforts will support the quantitative evaluation of FOWT's motion affects wake development, and conversely as well as wake influence on the dynamic behavior of downstream platforms. Moreover, in light of the industry's progression toward higher-capacity wind turbines, future simulations can be extended to 10-MW to 15-MW class FOWTs to assess motion-wake coupling effects on the performance and design of FOWT arrays.

doi:10.6342/NTU202503576

References

[1] "Global Offshore Wind Report 2024", GWEC, 2024.

[2] Global Wind Energy Council and Ocean Renewable Energy Action Coalition, "Offshore wind technical potential in Taiwan," Brussels, Belgium, Jun. 2021.

[3] W. J. M. Rankine, "On the mechanical principles of the action of propellers," *Trans. Inst. Naval Architects*, vol. 6, 1865.

[4] R. E. Froude, "On the part played in propulsion by differences of fluid pressure," *Trans. Inst. Naval Architects*, vol. 30, pp. 390, 1889.

[5] K. C. Lee, "A wake model for wind turbine power prediction," M.S. thesis, Dept. of Engineering Science and Ocean Engineering, National Taiwan University, 2018.

[6] Y. C. Chiang, "Wind farm power prediction via actuator disk model," M.S. thesis, Dept. of Engineering Science and Ocean Engineering, National Taiwan University, 2019.

[7] Y. C. Hsu, "Wind farm wake prediction via a large eddy simulation approach," M.S. thesis, Dept. of Engineering Science and Ocean Engineering, National Taiwan University, 2021.

[8] W. H. Pan, "Study on wake interaction among wind farms of Zhangbin offshore area via RANS approach coupled with actuator disk model," M.S. thesis, Dept. of Engineering Science and Ocean Engineering, National Taiwan University, 2022.

[9] D. A. L. Gurau, "Application of Symmetry-Preserving Discretization to Wind Turbine Flow Simulation," M.S. thesis, Dept. of Engineering Science and Ocean Engineering, College of Engineering, National Taiwan University, 2023.

[10] H. D. Nedjari, O. Guerri, and M. Saighi, "Full rotor modelling and generalized actuator disc for wind turbine wake investigation," *Energy Reports*, vol. 6, pp. 232-255, 2020.

[11] A. Rezaeiha and D. Micallef, "Wake interactions of two tandem floating offshore wind turbines: CFD analysis using actuator disc model," *Renewable Energy*, vol. 179, pp. 859-876, 2021.

[12] I. Neunaber, M. Hölling, J. Whale, and J. Peinke, "Comparison of the turbulence in the wakes of an actuator disc and a model wind turbine by higher order statistics: A wind tunnel study," *Renewable Energy*, vol. 179, pp. 1650-1662, 2021.

[13] G. Dong, Z. Li, J. Qin, and X. Yang, "Predictive capability of actuator disk models for wakes of different wind turbine designs," *Renewable Energy*, vol. 188, pp. 269-281, 2022.

[14] H. Meng, T. Chen, X. Chen, M. Ge, Y. Han, and Y. Liu, "Simplified Polynomial-asymptotic-distribution Actuator Disc (SPAD) method for wind turbine wake simulation based on k-ε-f_p turbulence model," *Renewable Energy*, vol. 236, Art. no. 121479, 2024.

[15] R. Kyle, Y. C. Lee, and W.-G. Früh, "Propeller and vortex ring state for floating offshore wind turbines during surge," *Renewable Energy*, vol. 155, pp. 645–657, 2020.

[16] Q. Sun, G. Li, L. Duan, and Z. He, "The coupling of tower-shadow effect and surge motion intensifies aerodynamic load variability in downwind floating

doi:10.6342/NTU202503576

offshore wind turbines," *Energy*, vol. 282, Art. no. 128788, 2023.
[17] K. Wang, M. Zhao, S. Chen, and R. Zha, "Aerodynamic performance analysis of a floating wind turbine with coupled blade rotation and surge motion," *Engineering Applications of Computational Fluid Mechanics*, vol. 18, no. 1, Art. no. 2301524, 2024.
[18] Y. Fang, L. Duan, Z. Han, Y. Zhao, and H. Yang, "Numerical analysis of aerodynamic performance of a floating offshore wind turbine under pitch motion," *Energy*, vol. 192, Art. no. 116621, 2020.
[19] W. Shi, J. Jiang, K. Sun, and Q. Ju, "Aerodynamic performance of semi-submersible floating wind turbine under pitch motion," *Sustainable Energy Technologies and Assessments*, vol. 48, Art. no. 101556, 2021.
[20] S. Fu, Z. Li, W. Zhu, X. Han, X. Liang, H. Yang, and W. Shen, "Study on aerodynamic performance and wake characteristics of a floating offshore wind turbine under pitch motion," *Renewable Energy*, vol. 205, pp. 317-325, 2023.
[21] L. Lin, K. Wang, and D. Vassalos, "Detecting wake performance of floating offshore wind turbine," *Ocean Engineering*, vol. 156, pp. 263-276, 2018.
[22] Z. Chen, X. Wang, Y. Guo, and S. Kang, "Numerical analysis of unsteady aerodynamic performance of floating offshore wind turbine under platform surge and pitch motions," *Renewable Energy*, vol. 163, pp. 1849-1870, 2021.
[23] A. Arabgolarcheh, S. Jannesarahmadi, and E. Benini, "Modeling of near wake characteristics in floating offshore wind turbines using an actuator line method," *Renewable Energy*, vol. 185, pp. 871-887, 2022.
[24] F. R. Menter, "Two-Equation Eddy-Viscosity Turbulence Models for Engineering Applications," *AIAA Journal*, vol. 32, no. 8, pp. 1598-1605, 1994.
[25] Y. T. Wu and F. Porté-Agel, "Modeling Turbine Wakes and Power Losses within a Wind Farm Using LES: An Application to the Horns Rev Offshore Wind Farm," *Renewable Energy*, vol. 75, pp. 945-955, 2015.
[26] Simcenter STAR-CCM+ User Guide, ver. 2410, Siemens, Berlin, Germany, 2023.
[27] Y. C. Chiang, Y. C. Hsu and S. W. Chau, "Power Prediction of Wind Farms via a Simplified Actuator Disk Model," *Journal of Marine Science and Engineering*, vol. 8, Art. No. 610, 2020.
[28] R. J. Barthelmie, K. Hansen, S. T. Frandsen, O. Rathmann, J. G. Schepers, W. Schlez, J. Phillips, K. Rados, A. Zervos, E. S. Politis, and P. K. Chaviaropoulos. "Modeling and Measuring Flow and Wind Turbine Wakes in Large Wind Farms Offshore," *Wind Energy*, vol. 12, no. 5, pp. 431-444, 2009.
[29] A. Subbulakshmi, M. Verma, M. Keerthana, S. Sasmal, P. Harikrishna and S. Kapuria, "Recent advances in experimental and numerical methods for dynamic analysis of floating offshore wind turbines-An integrated review," *Renewable and Sustainable Energy Reviews*, vol. 164, p. 112525, 2022.
[30] DNV GL, *Coupled Analysis of Floating Wind Turbines*, DNVGL-RP-0286, 2019.
[31] M. Ikhennicheu, M. Lynch, S. Doole, F. Borisade, D. Matha, J. L. Dominguez, R. D. Vicente, T. Habekost, L.Ramirez, S. Potestio, C. Molins and P. Trubat, *Review of the State of the Art of Mooring and Anchoring Designs, Technical Challenges and Identification of Relevant DLCs*, Corewind Project, 2020.
[32] T. Ishihara and S. Zhang, "Prediction of dynamic response of semi-submersible floating offshore wind turbine using augmented Morison's equation with

doi:10.6342/NTU202503576

frequency dependent hydrodynamic coefficients," *Renewable Energy*, vol. 131, pp. 1186-1207, 2019.

[33] H. Y. Tong, T. Y. Lin and S. W. Chau, "Normal operating performance study of 15 MW floating wind turbine system using semisubmersible Taida floating platform in Hsinchu offshore area," *Journal of Marine Science and Engineering*, vol. 11, no. 2, Art. no. 457, 2023.

[34] T. S. Lin, H. Y. Tong, S. K. Wong and S. W. Chau, "Influence of surging and pitching behaviors on the power output and wake characteristics of a 15 MW floating wind turbine," *Journal of Marine Science and Engineering*, vol. 13, no. 6, Art. no. 1059, 2025.

[35] H. Li, Y. Zhang, and L. Chen, "Wake dynamics of a floating wind turbine under surge motion," *Renewable Energy*, vol. 170, pp. 498-513, 2021.

[36] S. Guntur, A. R. Natarajan, and P. E. Réthoré, "An investigation into the effects of floating platform motion on wind turbine wake dynamics using LES," *Wind Energy Science*, vol. 3, pp. 627-641, 2018.

[37] A. Cioni, R. Bayati, A. Robertson, K. Dykes, and J. Jonkman, "OC6 Phase III: Validation of floating offshore wind modelling in a coupled simulation framework using data from the DeepCwind floating semisubmersible wind turbine test campaign," *Wind Energy Science*, vol. 8, pp. 1659-1688, 2023.

[38] J. Frederik, M. van Dooren, P. Chamorro, and J. Meyers, "Helix: breaking the rotational symmetry of wake turbulence," *Wind Energy Science*, vol. 5, pp. 1217-1233, 2020.

[39] R. Abraham, A. Petros, and C. Meneveau, "Response characteristics of wind turbine wakes to time-varying pitch control," *Renewable Energy*, vol. 172, pp. 1033-1043, 2021.

[40] Z. Zhao, D. Liu, Y. Zhu, and W. Liu, "Study on the near wake aerodynamic characteristics of floating offshore wind turbine under combined surge and pitch motion," *Energy Reports*, vol. 8, pp. 17083-17094, 2022.

[41] J. Bartl and C. S. Sætran, "Experimental measurements of wake deflection by static yaw misalignment of a model wind turbine," *Wind Energy Science*, vol. 3, no. 1, pp. 329-337, 2018.

[42] M. F. Howland, L. M. Dabiri, and J. O. Dabiri, "Wind farm power optimization through wake steering using adjoint-based methods," *arXiv preprint,* arXiv:1603.06632, 2016.

[43] D. Medici and P. H. Alfredsson, "Measurements on a wind turbine wake: 3D effects and bluff body vortex shedding," *Wind Energy*, vol. 9, no. 3, pp. 219-236, 2006.

doi:10.6342/NTU202503576

Appendix

doi:10.6342/NTU202503576

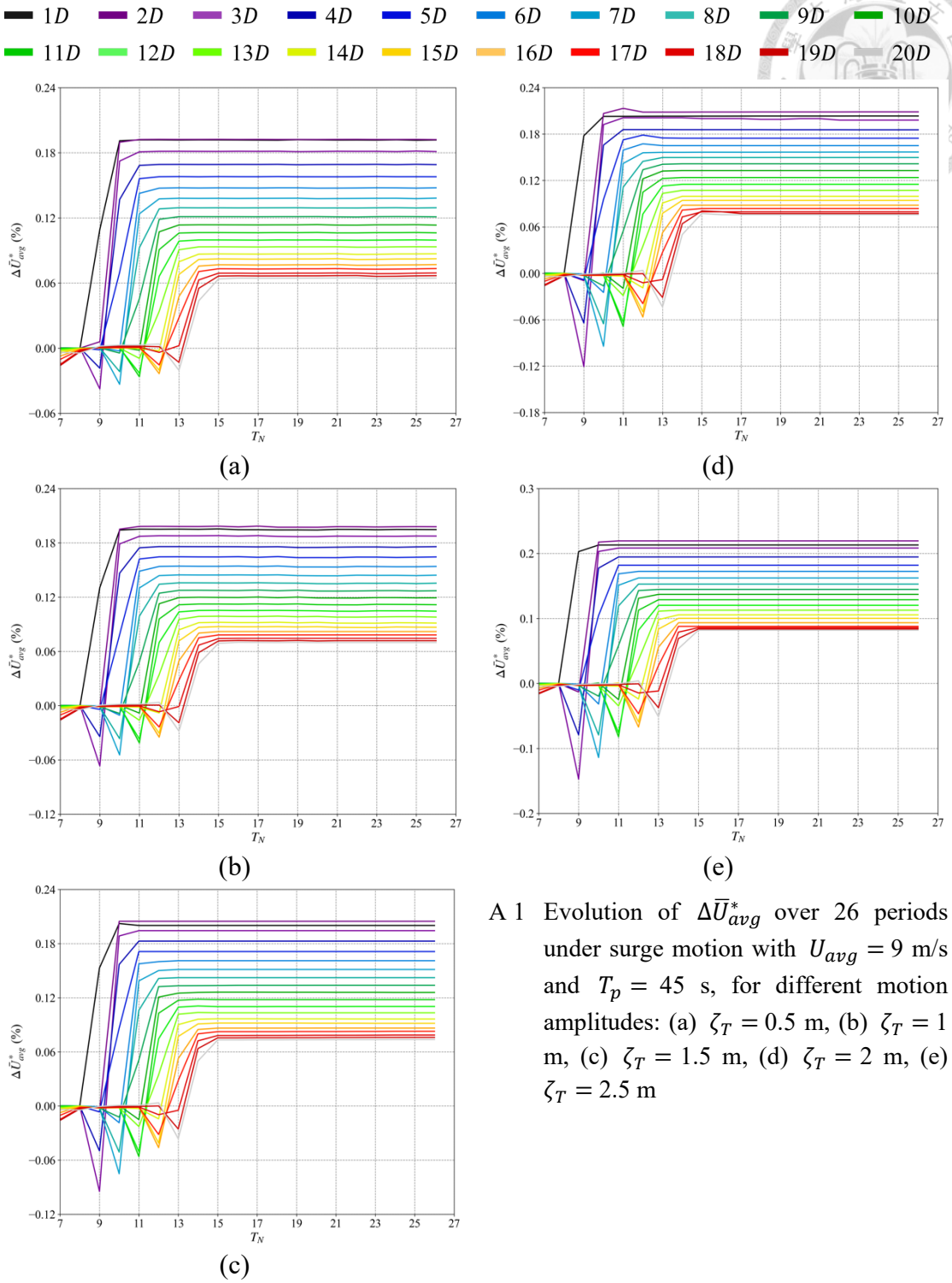

A 1 Evolution of $\Delta\bar{U}^*_{avg}$ over 26 periods under surge motion with $U_{avg} = 9$ m/s and $T_p = 45$ s, for different motion amplitudes: (a) $\zeta_T = 0.5$ m, (b) $\zeta_T = 1$ m, (c) $\zeta_T = 1.5$ m, (d) $\zeta_T = 2$ m, (e) $\zeta_T = 2.5$ m

doi:10.6342/NTU202503576

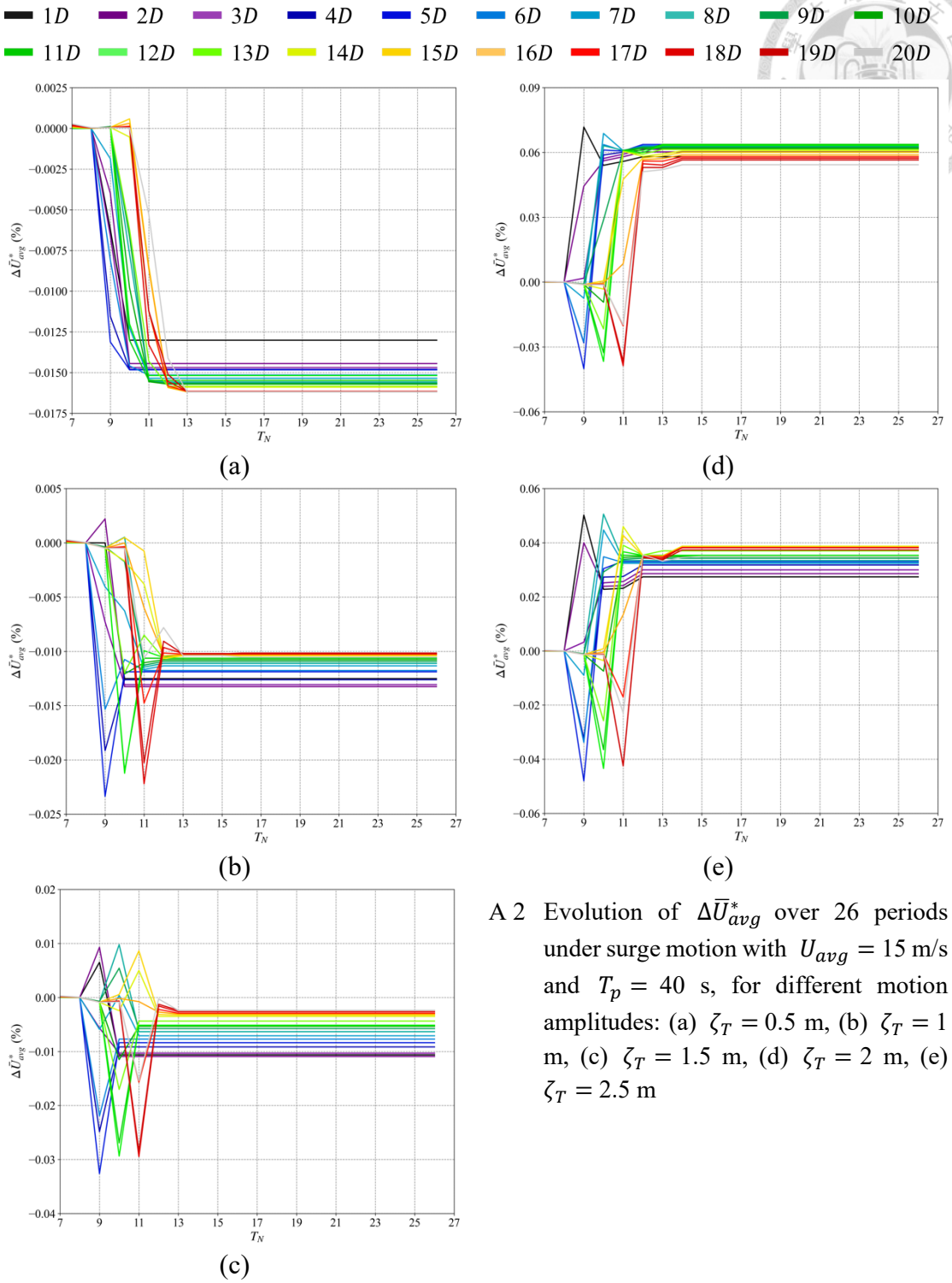

A 2 Evolution of $\Delta\bar{U}^*_{avg}$ over 26 periods under surge motion with $U_{avg} = 15$ m/s and $T_p = 40$ s, for different motion amplitudes: (a) $\zeta_T = 0.5$ m, (b) $\zeta_T = 1$ m, (c) $\zeta_T = 1.5$ m, (d) $\zeta_T = 2$ m, (e) $\zeta_T = 2.5$ m

doi:10.6342/NTU202503576

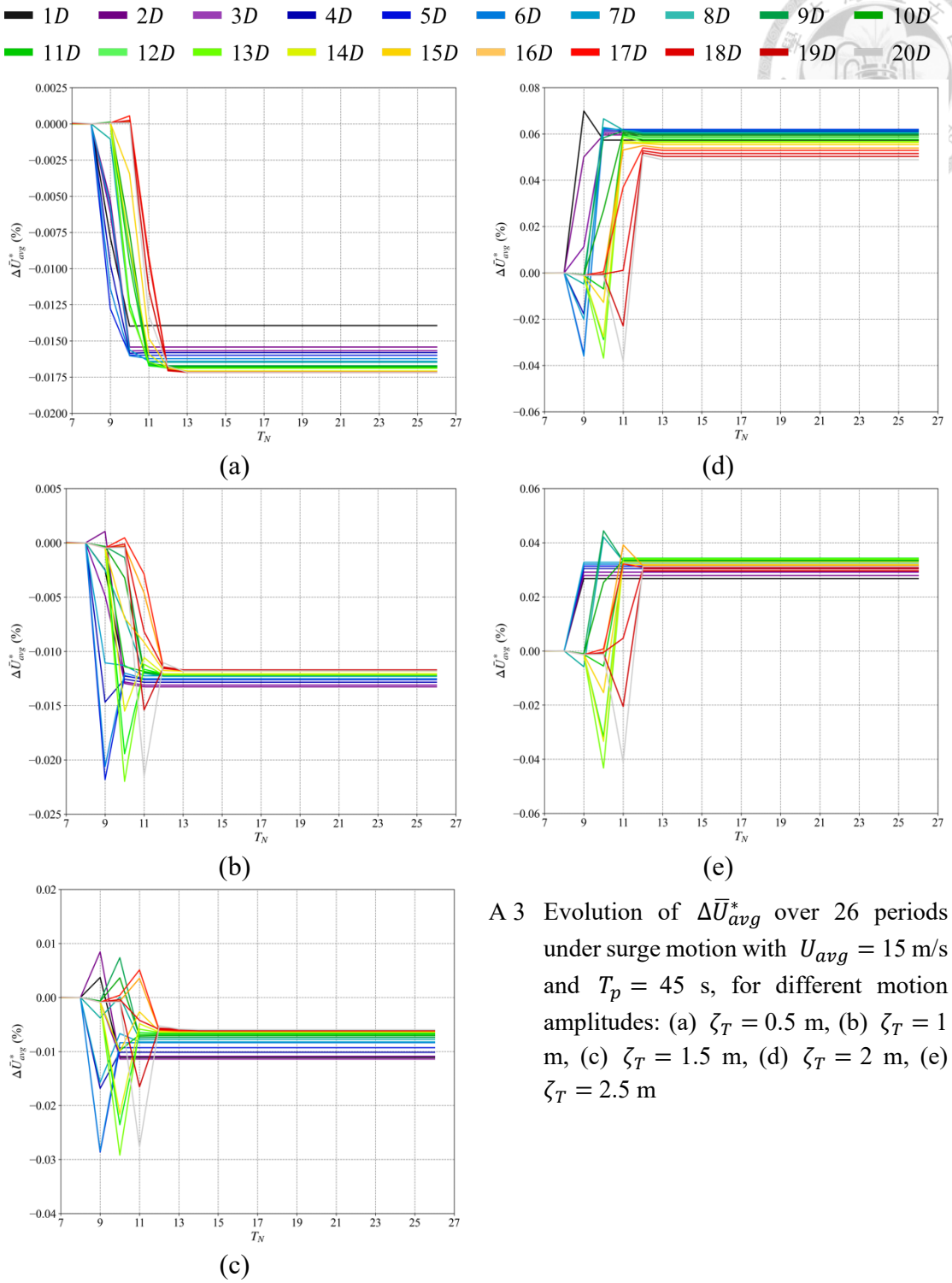

A 3 Evolution of $\Delta\bar{U}^*_{avg}$ over 26 periods under surge motion with $U_{avg} = 15$ m/s and $T_p = 45$ s, for different motion amplitudes: (a) $\zeta_T = 0.5$ m, (b) $\zeta_T = 1$ m, (c) $\zeta_T = 1.5$ m, (d) $\zeta_T = 2$ m, (e) $\zeta_T = 2.5$ m

doi:10.6342/NTU202503576

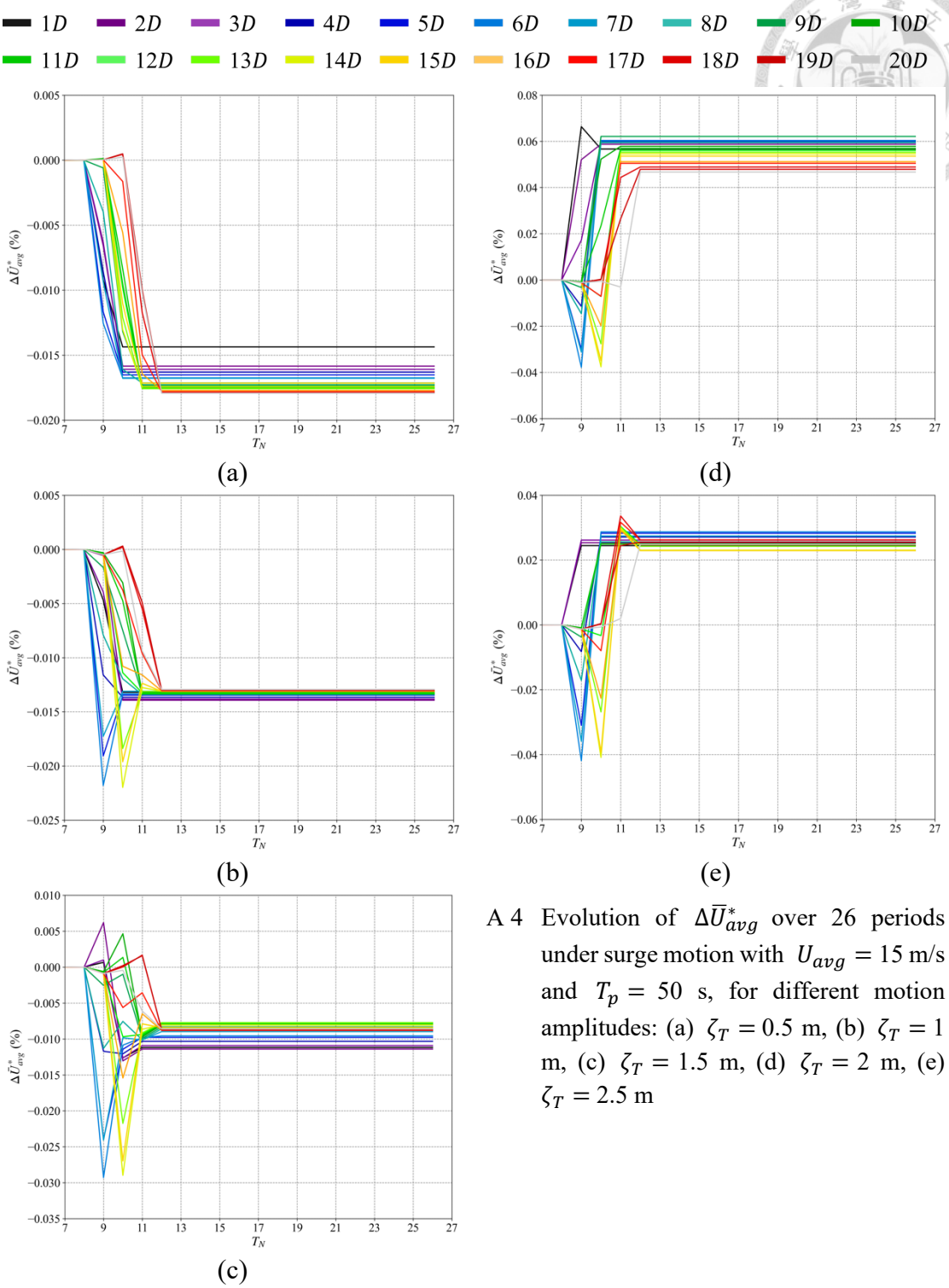

A 4 Evolution of $\Delta\bar{U}^*_{avg}$ over 26 periods under surge motion with $U_{avg} = 15$ m/s and $T_p = 50$ s, for different motion amplitudes: (a) $\zeta_T = 0.5$ m, (b) $\zeta_T = 1$ m, (c) $\zeta_T = 1.5$ m, (d) $\zeta_T = 2$ m, (e) $\zeta_T = 2.5$ m

doi:10.6342/NTU202503576

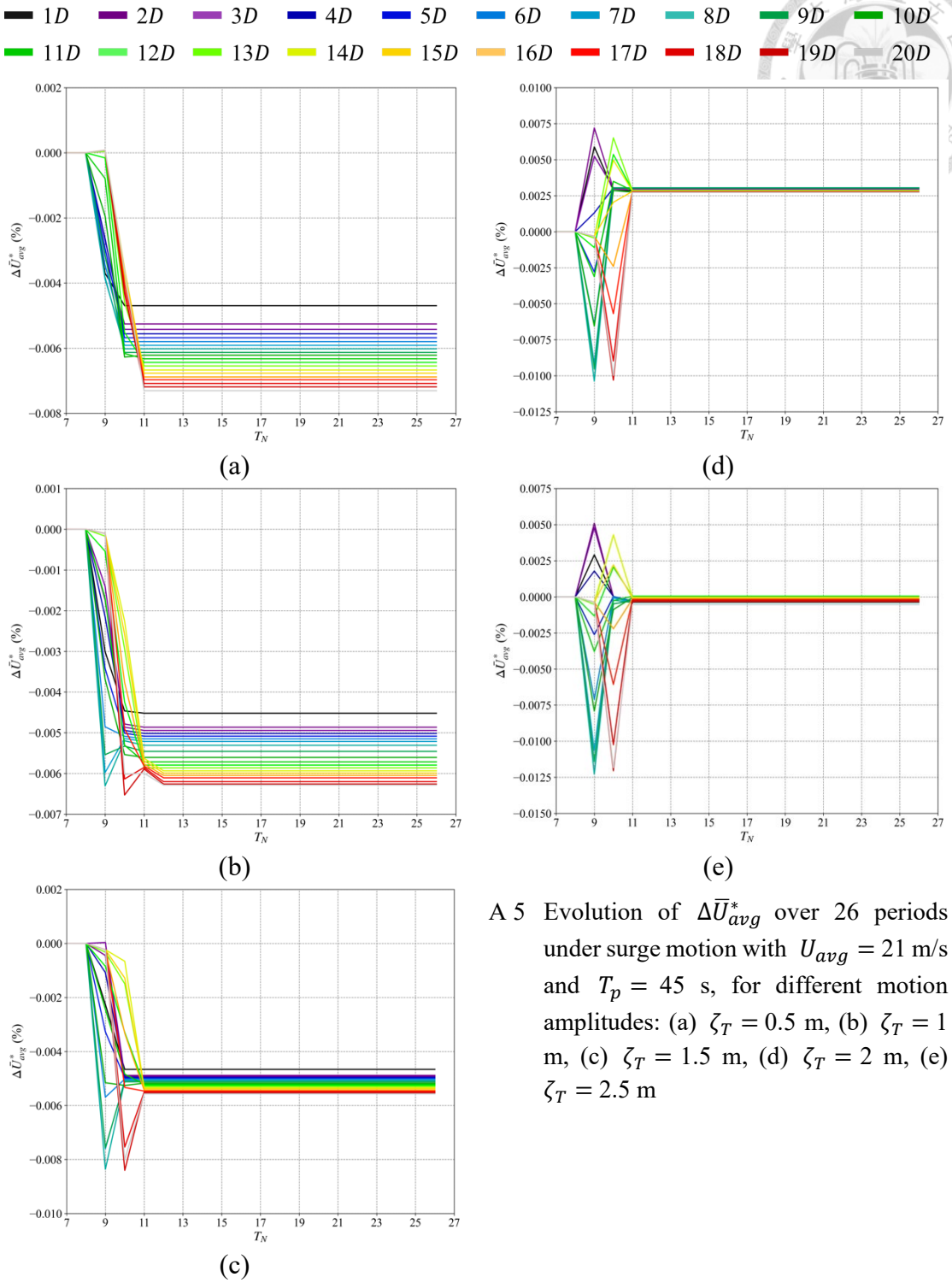

A 5 Evolution of $\Delta\bar{U}^*_{avg}$ over 26 periods under surge motion with $U_{avg} = 21$ m/s and $T_p = 45$ s, for different motion amplitudes: (a) $\zeta_T = 0.5$ m, (b) $\zeta_T = 1$ m, (c) $\zeta_T = 1.5$ m, (d) $\zeta_T = 2$ m, (e) $\zeta_T = 2.5$ m

doi:10.6342/NTU202503576

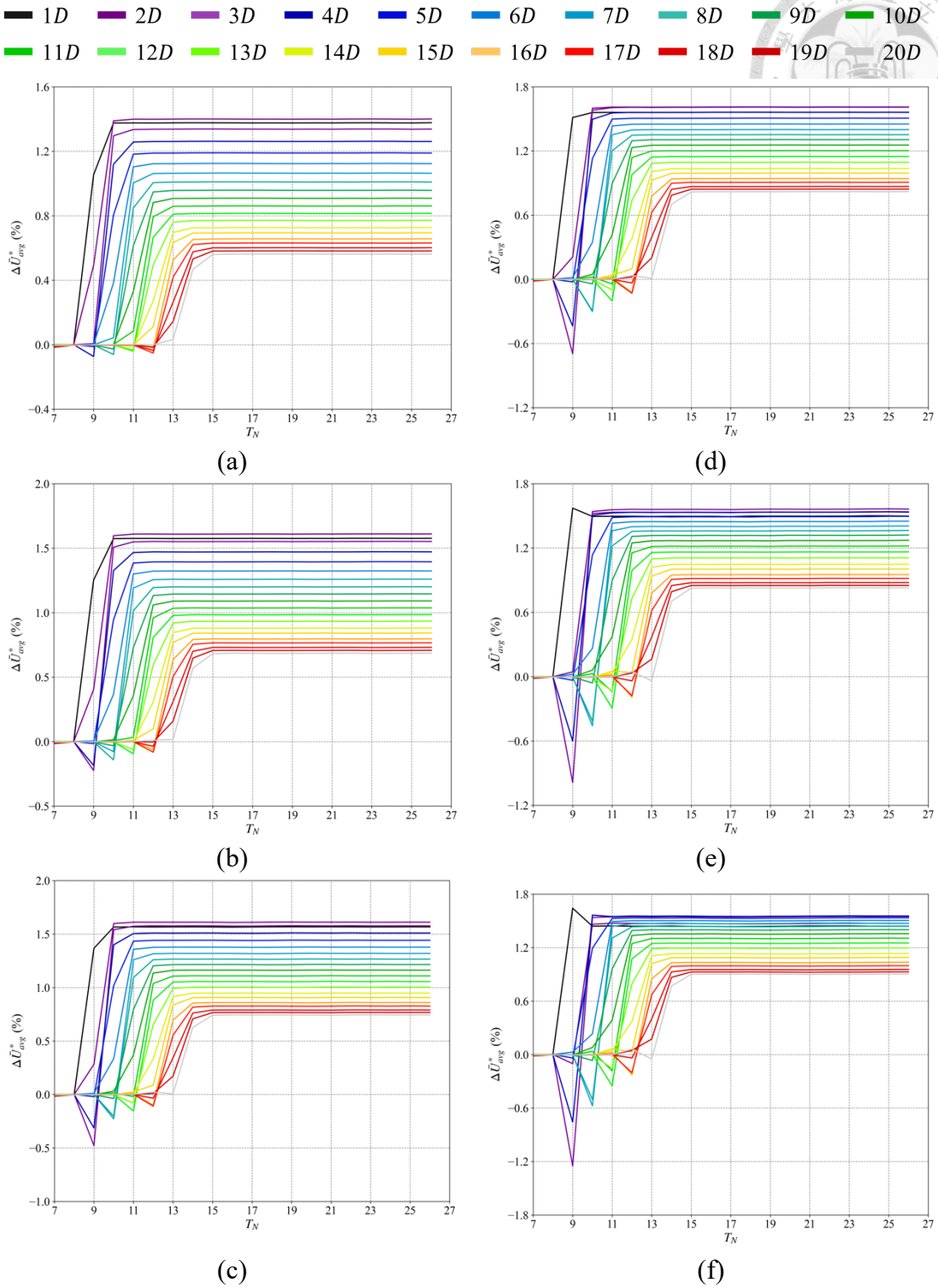

A 6 Evolution of $\Delta\bar{U}^*_{avg}$ over 26 periods under surge motion with $U_{avg} = 9$ m/s and $T_p = 45$ s, for different motion amplitudes: (a) $\zeta_T = 5$ m, (b) $\zeta_T = 10$ m, (c) $\zeta_T = 15$ m, (d) $\zeta_T = 20$ m, (e) $\zeta_T = 25$ m, (f) $\zeta_T = 30$ m

doi:10.6342/NTU202503576

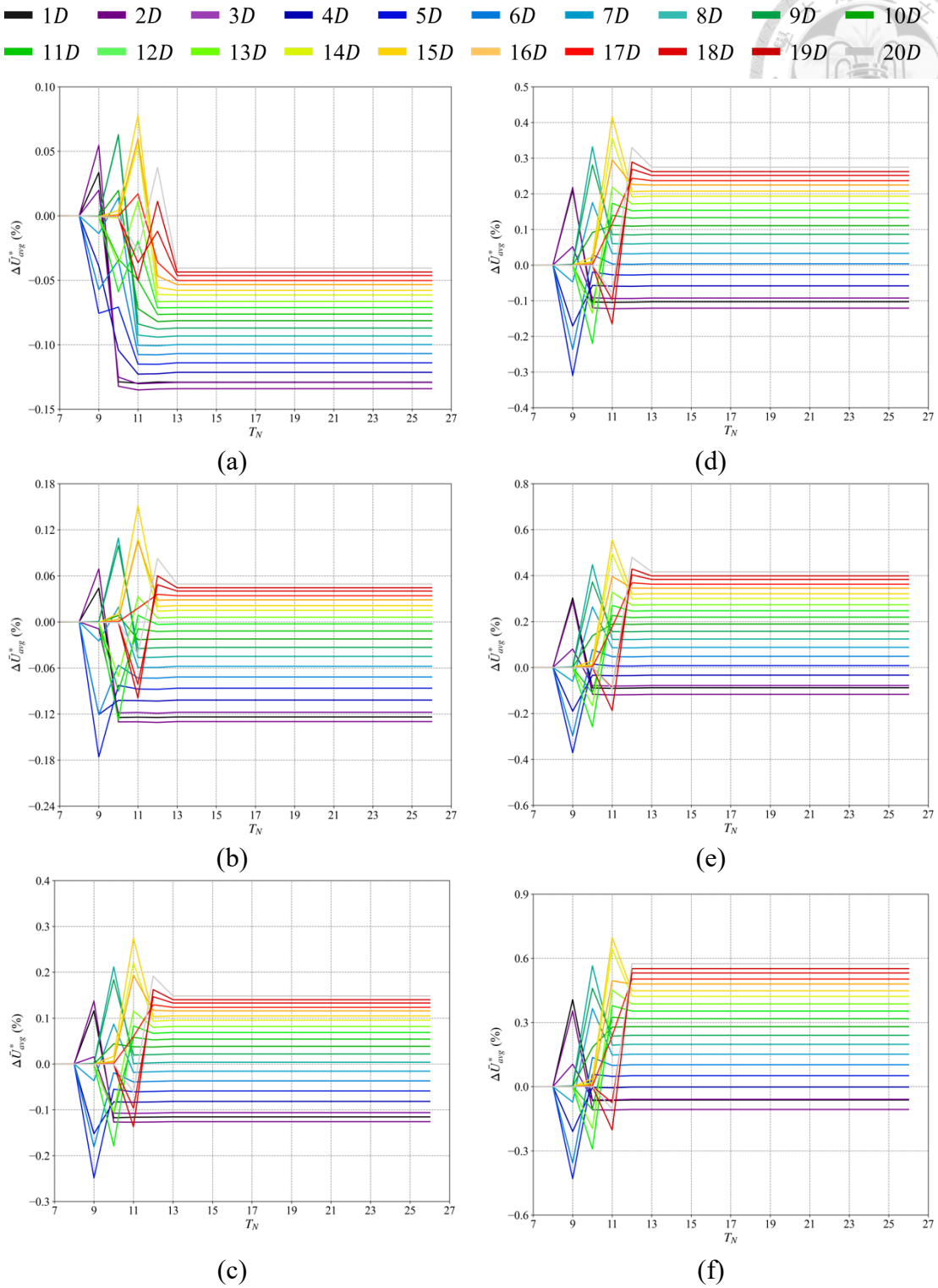

A 7 Evolution of $\Delta\bar{U}^*_{avg}$ over 26 periods under surge motion with $U_{avg} = 15$ m/s and $T_p = 40$ s, for different motion amplitudes: (a) $\zeta_T = 5$ m, (b) $\zeta_T = 10$ m, (c) $\zeta_T = 15$ m, (d) $\zeta_T = 20$ m, (e) $\zeta_T = 25$ m, (f) $\zeta_T = 30$ m

doi:10.6342/NTU202503576

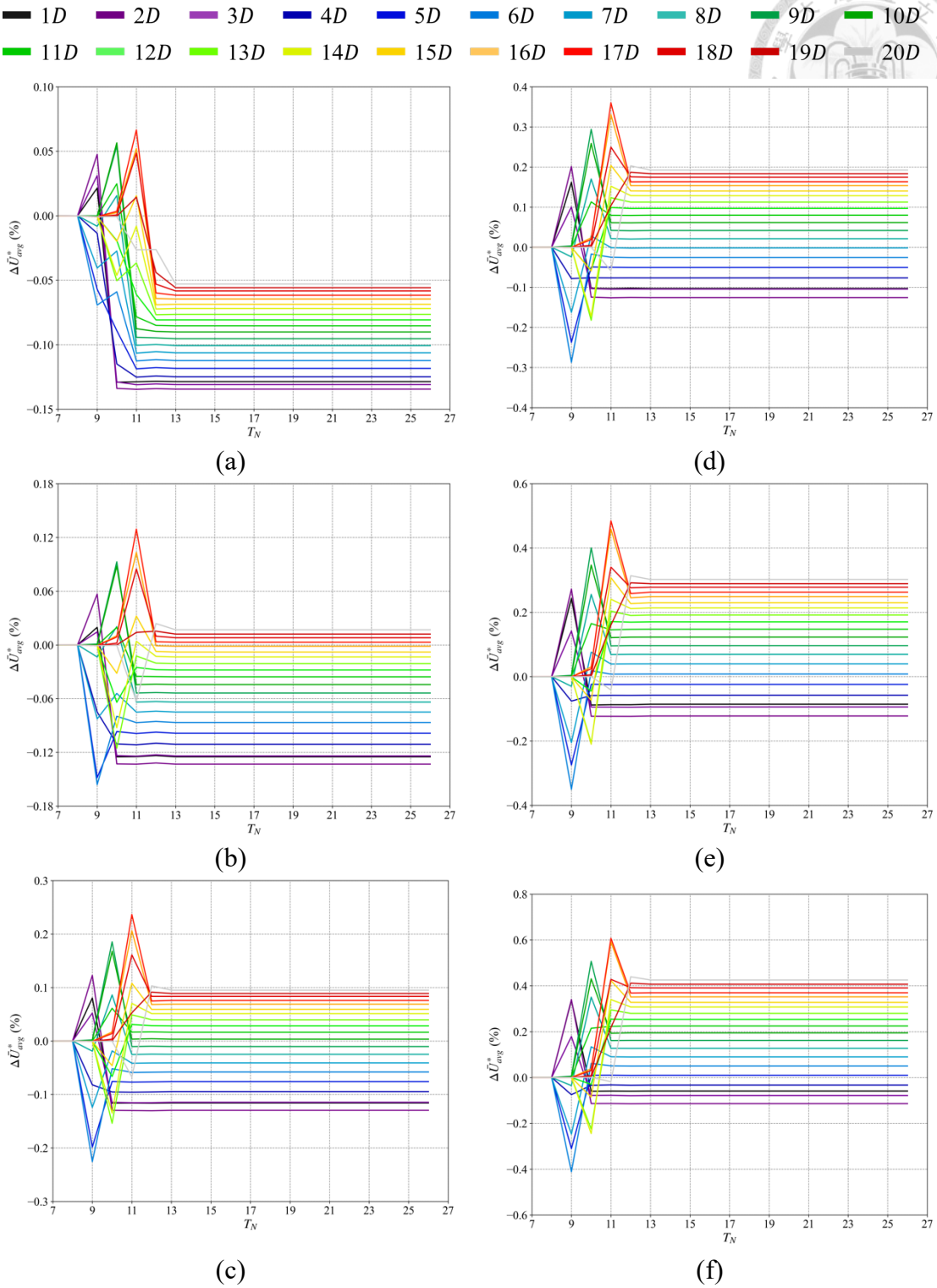

A 8 Evolution of $\Delta\bar{U}^*_{avg}$ over 26 periods under surge motion with $U_{avg} = 15$ m/s and $T_p = 45$ s, for different motion amplitudes: (a) $\zeta_T = 5$ m, (b) $\zeta_T = 10$ m, (c) $\zeta_T = 15$ m, (d) $\zeta_T = 20$ m, (e) $\zeta_T = 25$ m, (f) $\zeta_T = 30$ m

doi:10.6342/NTU202503576

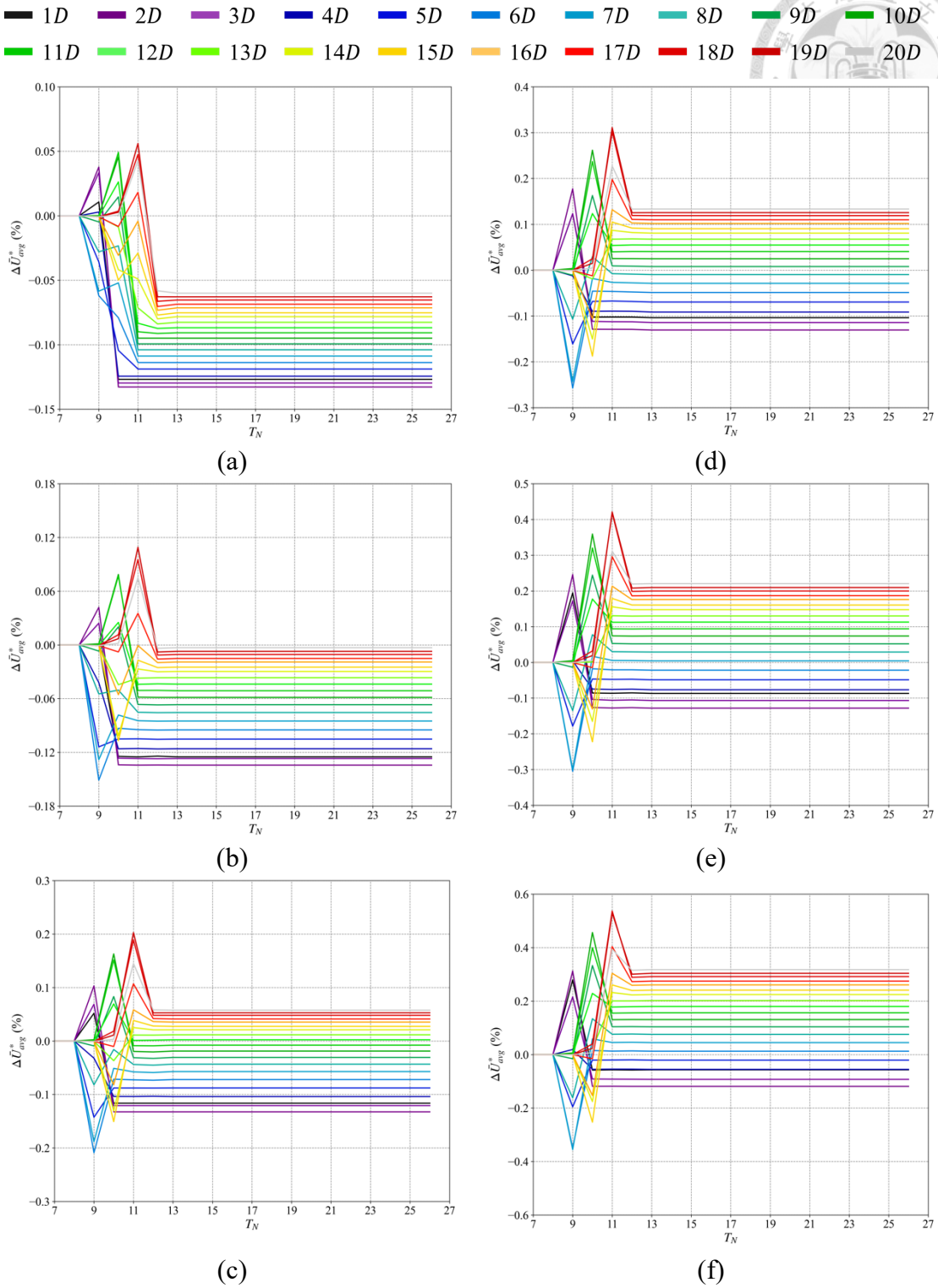

A 9 Evolution of $\Delta\bar{U}^*_{avg}$ over 26 periods under surge motion with $U_{avg} = 15$ m/s and $T_p = 50$ s, for different motion amplitudes: (a) $\zeta_T = 5$ m, (b) $\zeta_T = 10$ m, (c) $\zeta_T = 15$ m, (d) $\zeta_T = 20$ m, (e) $\zeta_T = 25$ m, (f) $\zeta_T = 30$ m

doi:10.6342/NTU202503576

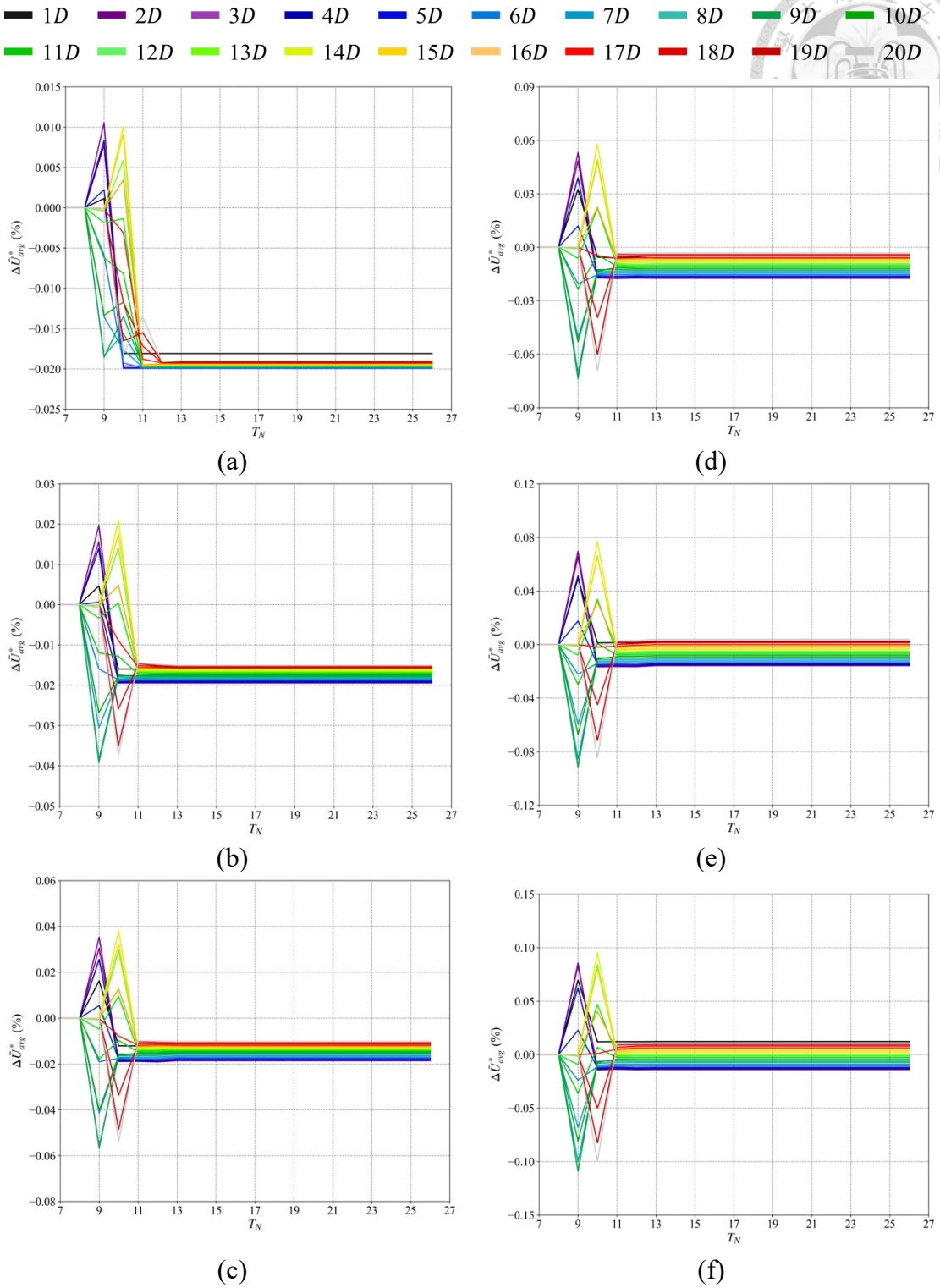

A 10 Evolution of $\Delta\bar{U}^*_{avg}$ over 26 periods under surge motion with $U_{avg} = 21$ m/s and $T_p = 45$ s, for different motion amplitudes: (a) $\zeta_T = 5$ m, (b) $\zeta_T = 10$ m, (c) $\zeta_T = 15$ m, (d) $\zeta_T = 20$ m, (e) $\zeta_T = 25$ m, (f) $\zeta_T = 30$ m

doi:10.6342/NTU202503576

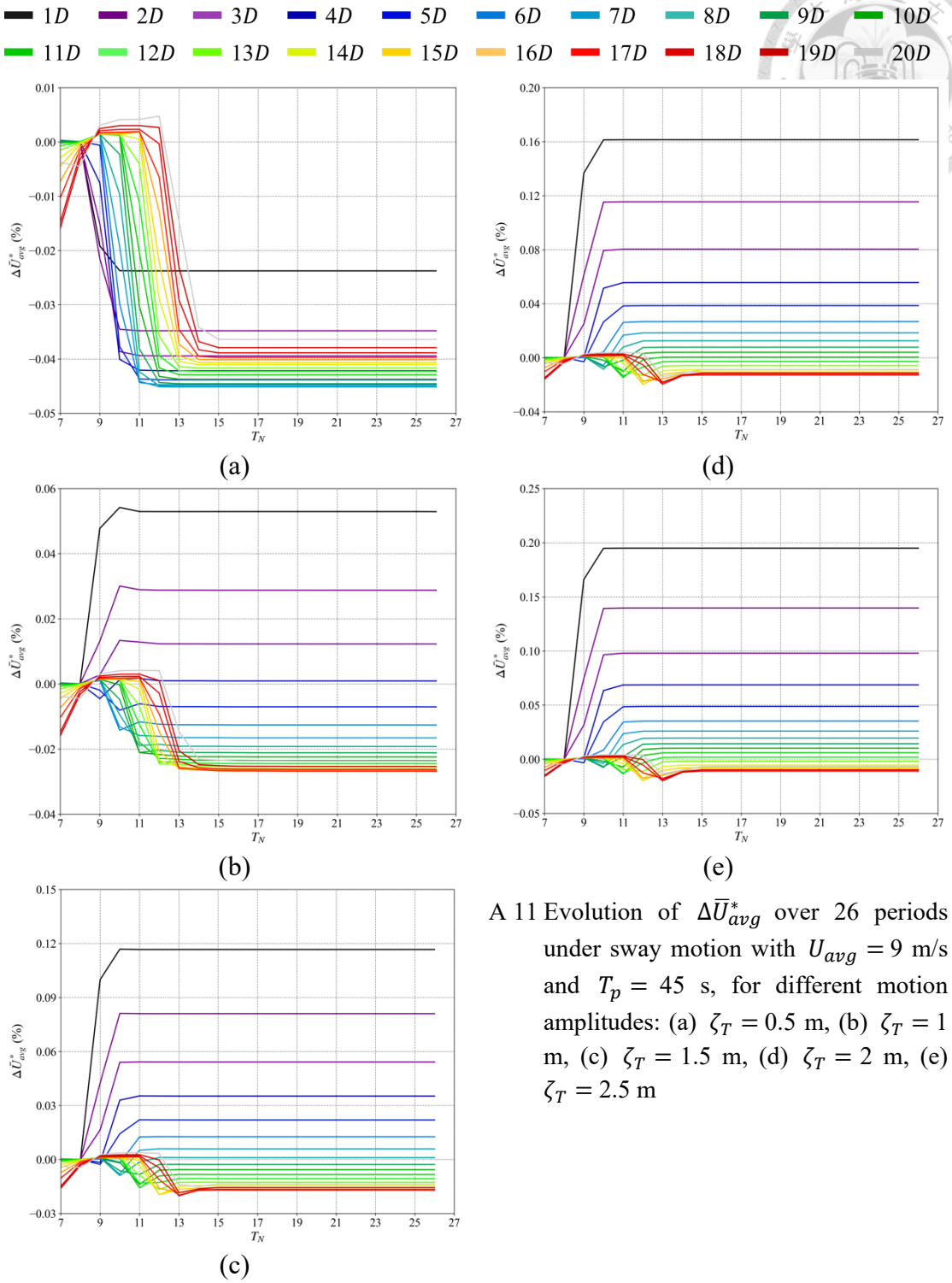

A 11 Evolution of $\Delta\bar{U}^*_{avg}$ over 26 periods under sway motion with $U_{avg} = 9$ m/s and $T_p = 45$ s, for different motion amplitudes: (a) $\zeta_T = 0.5$ m, (b) $\zeta_T = 1$ m, (c) $\zeta_T = 1.5$ m, (d) $\zeta_T = 2$ m, (e) $\zeta_T = 2.5$ m

doi:10.6342/NTU202503576

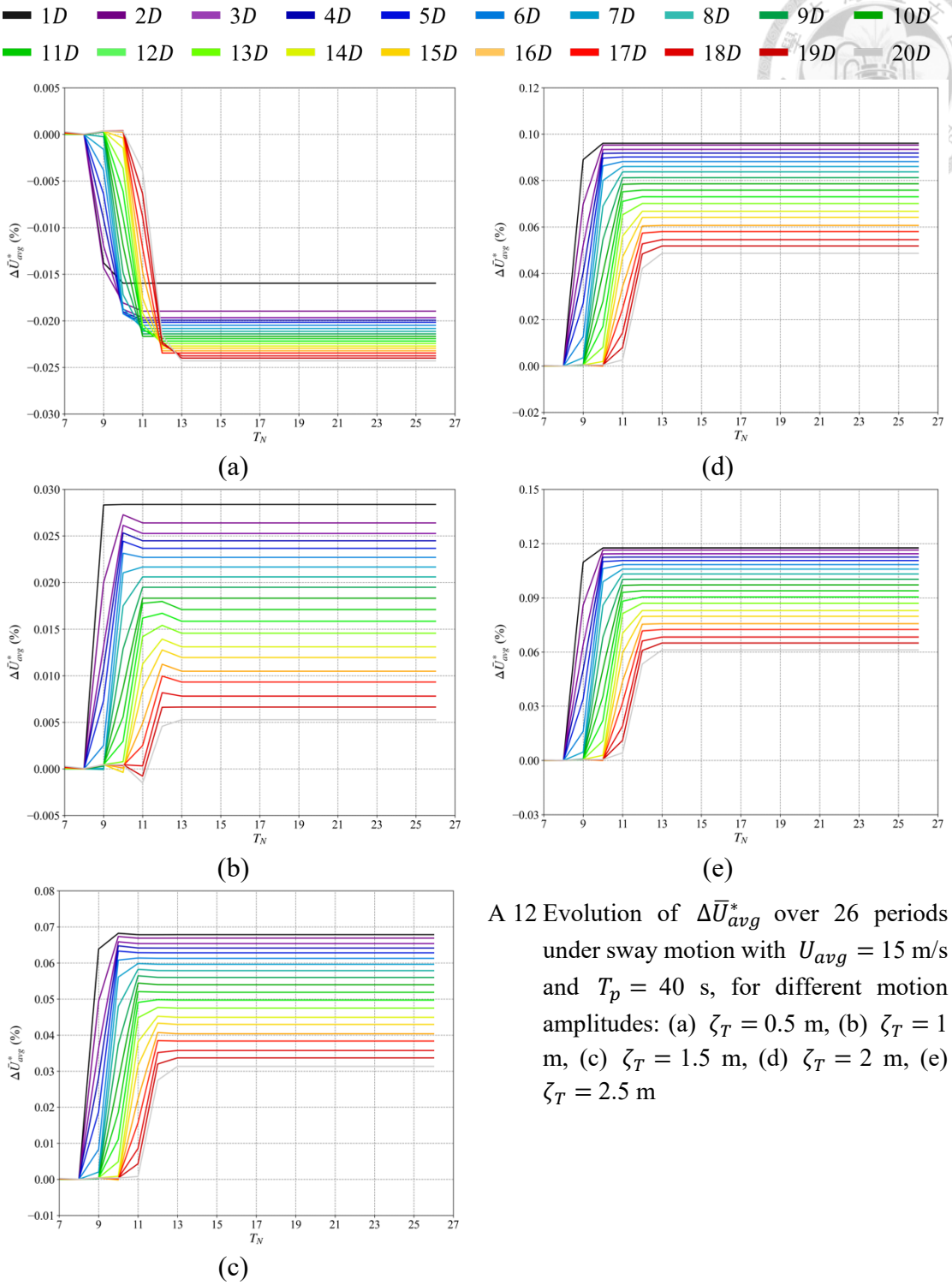

A 12 Evolution of $\Delta\bar{U}^*_{avg}$ over 26 periods under sway motion with $U_{avg} = 15$ m/s and $T_p = 40$ s, for different motion amplitudes: (a) $\zeta_T = 0.5$ m, (b) $\zeta_T = 1$ m, (c) $\zeta_T = 1.5$ m, (d) $\zeta_T = 2$ m, (e) $\zeta_T = 2.5$ m

doi:10.6342/NTU202503576

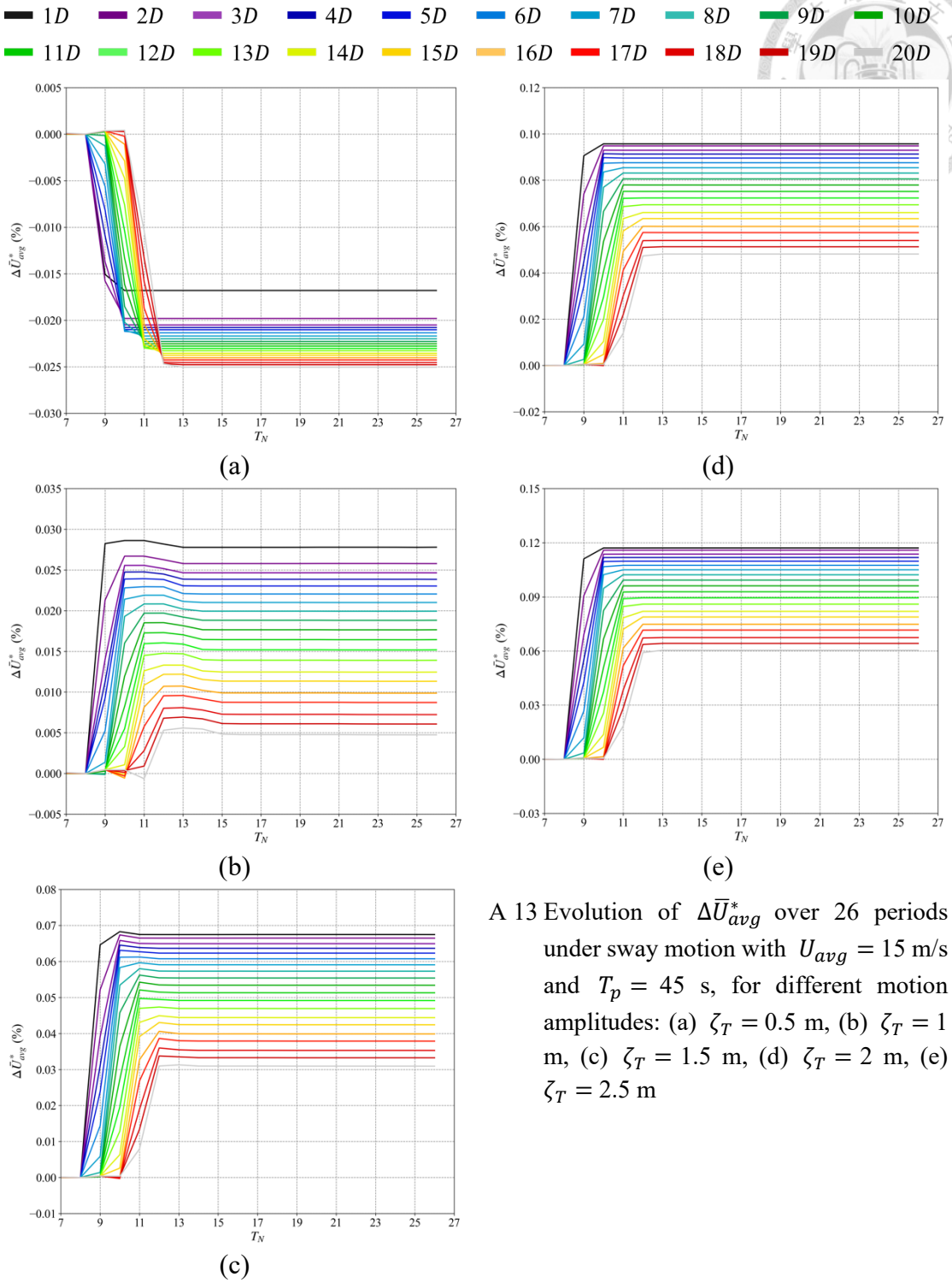

A 13 Evolution of $\Delta\bar{U}^*_{avg}$ over 26 periods under sway motion with $U_{avg} = 15$ m/s and $T_p = 45$ s, for different motion amplitudes: (a) $\zeta_T = 0.5$ m, (b) $\zeta_T = 1$ m, (c) $\zeta_T = 1.5$ m, (d) $\zeta_T = 2$ m, (e) $\zeta_T = 2.5$ m

doi:10.6342/NTU202503576

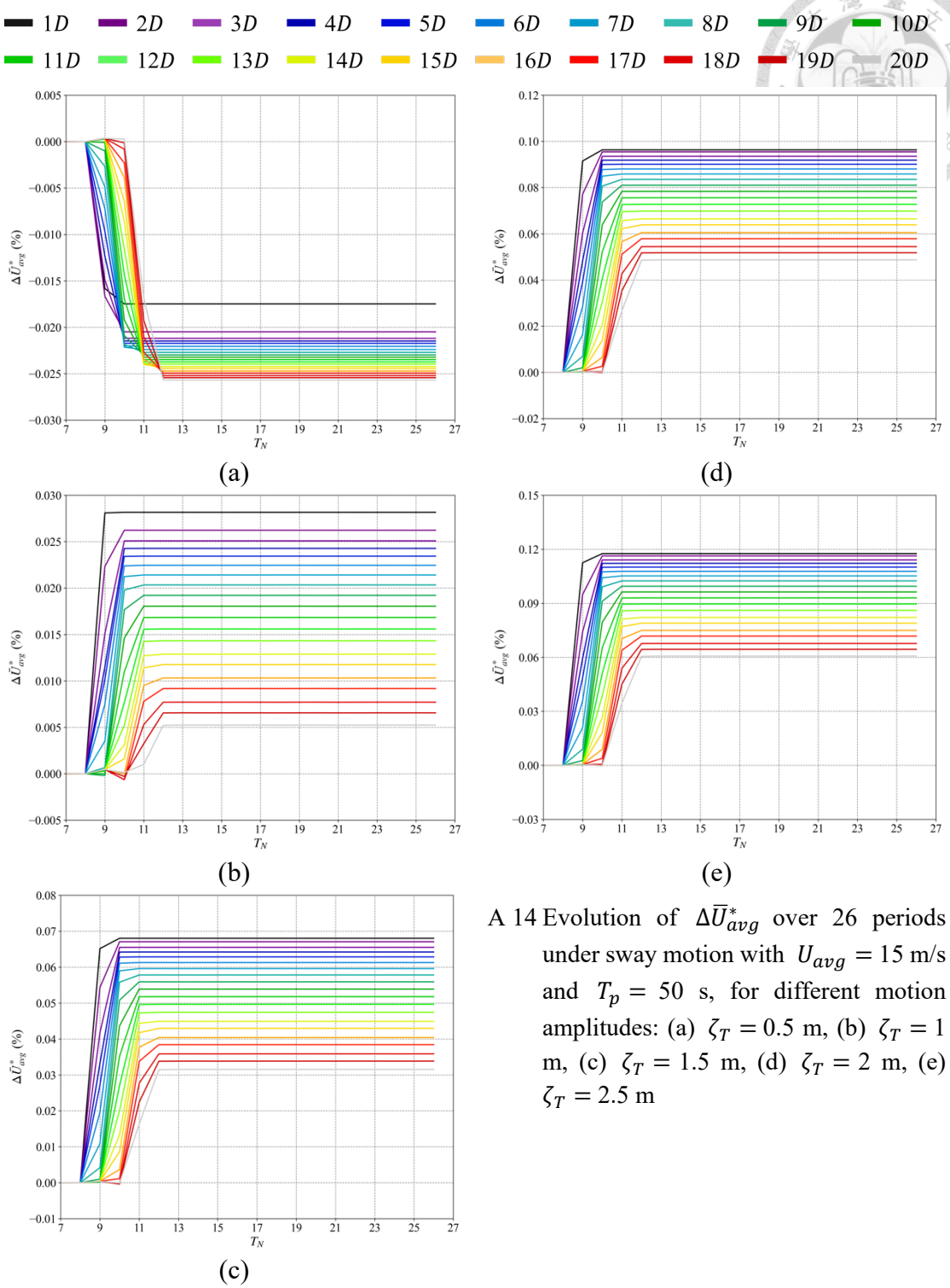

A 14 Evolution of $\Delta\bar{U}^*_{avg}$ over 26 periods under sway motion with $U_{avg} = 15$ m/s and $T_p = 50$ s, for different motion amplitudes: (a) $\zeta_T = 0.5$ m, (b) $\zeta_T = 1$ m, (c) $\zeta_T = 1.5$ m, (d) $\zeta_T = 2$ m, (e) $\zeta_T = 2.5$ m

doi:10.6342/NTU202503576

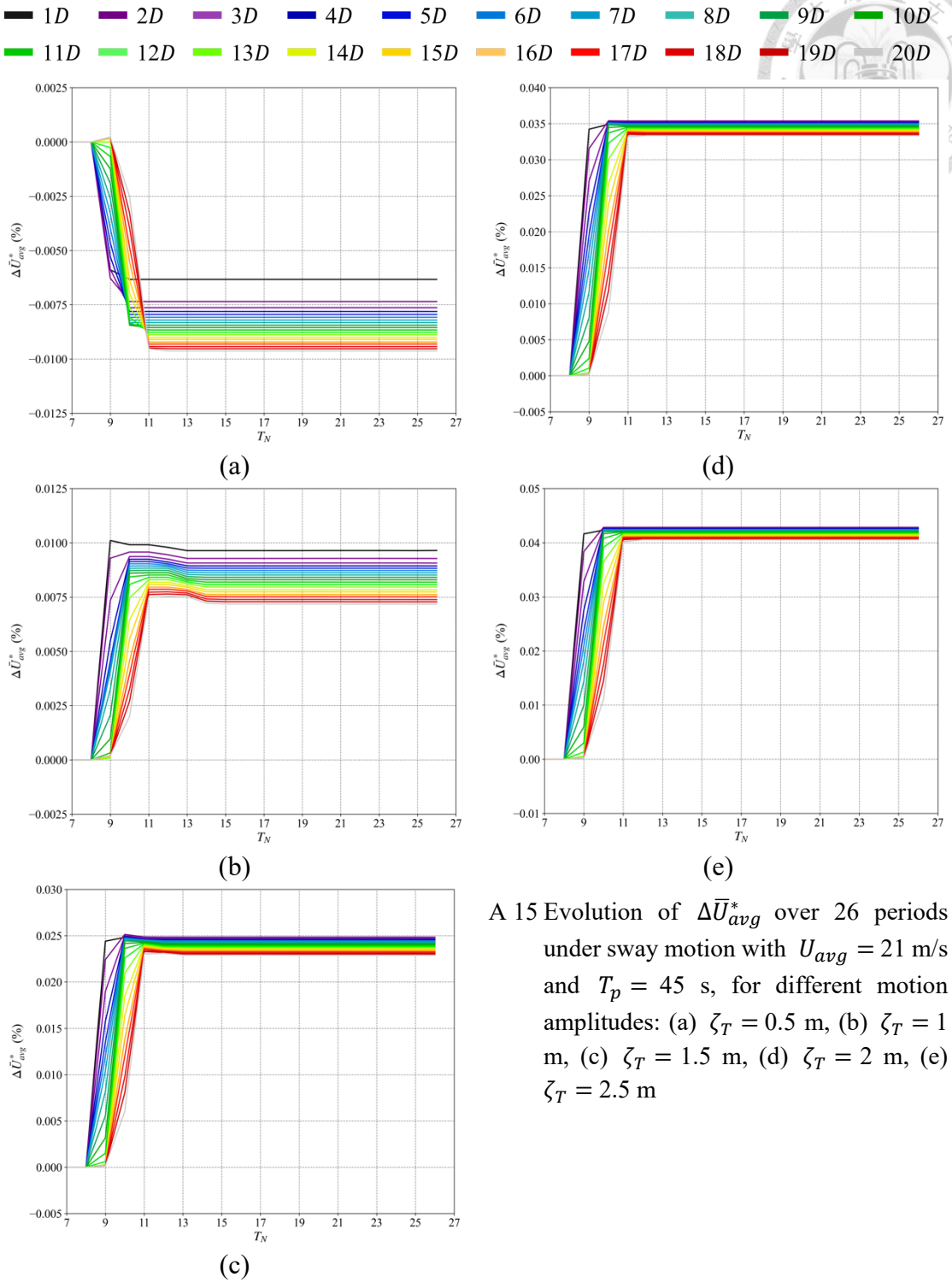

A 15 Evolution of $\Delta\bar{U}^*_{avg}$ over 26 periods under sway motion with $U_{avg} = 21$ m/s and $T_p = 45$ s, for different motion amplitudes: (a) $\zeta_T = 0.5$ m, (b) $\zeta_T = 1$ m, (c) $\zeta_T = 1.5$ m, (d) $\zeta_T = 2$ m, (e) $\zeta_T = 2.5$ m

doi:10.6342/NTU202503576

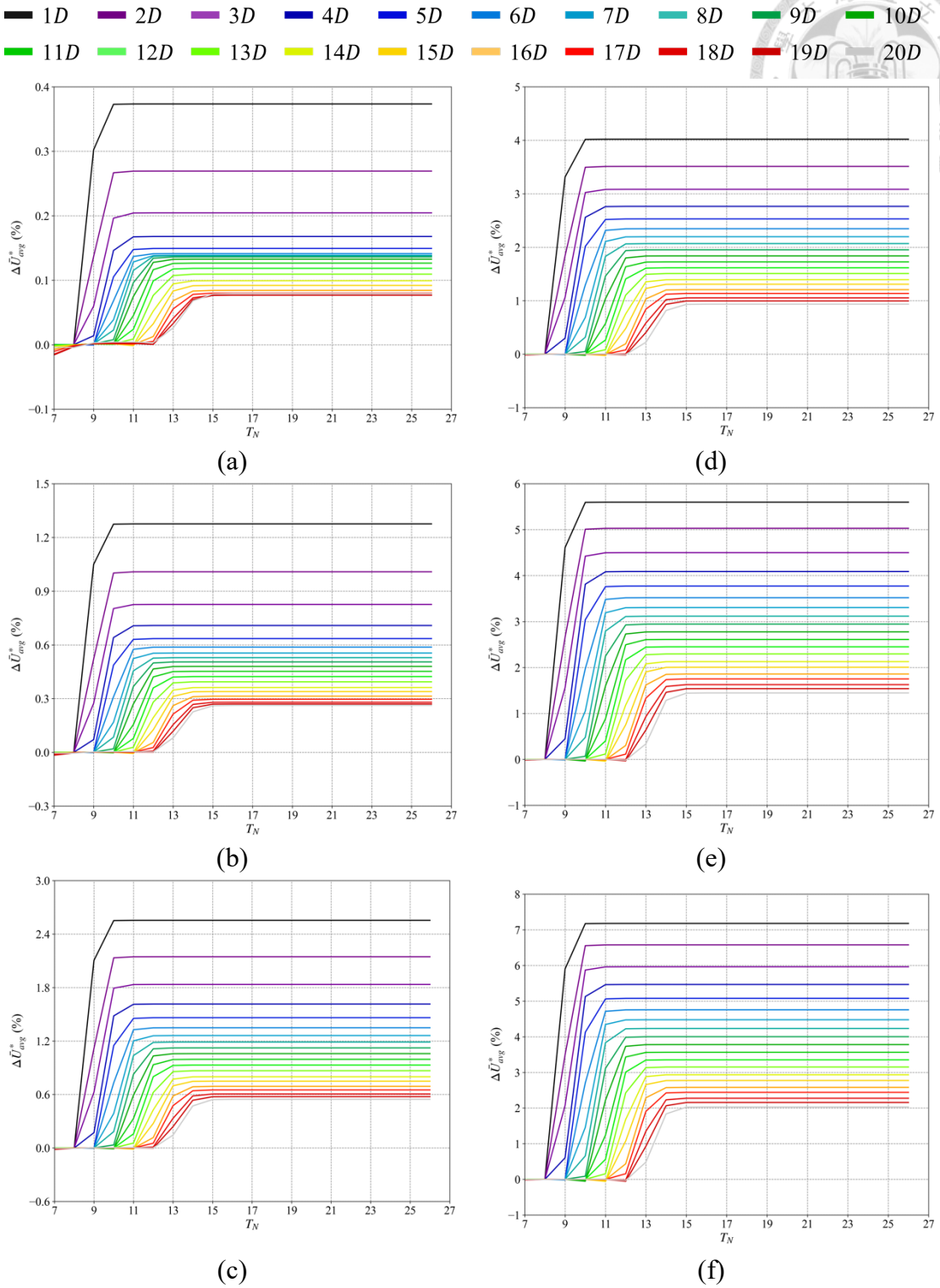

A 16 Evolution of $\Delta\bar{U}^*_{avg}$ over 26 periods under sway motion with $U_{avg} = 9$ m/s and $T_p = 45$ s, for different motion amplitudes: (a) $\zeta_T = 5$ m, (b) $\zeta_T = 10$ m, (c) $\zeta_T = 15$ m, (d) $\zeta_T = 20$ m, (e) $\zeta_T = 25$ m, (f) $\zeta_T = 30$ m

doi:10.6342/NTU202503576

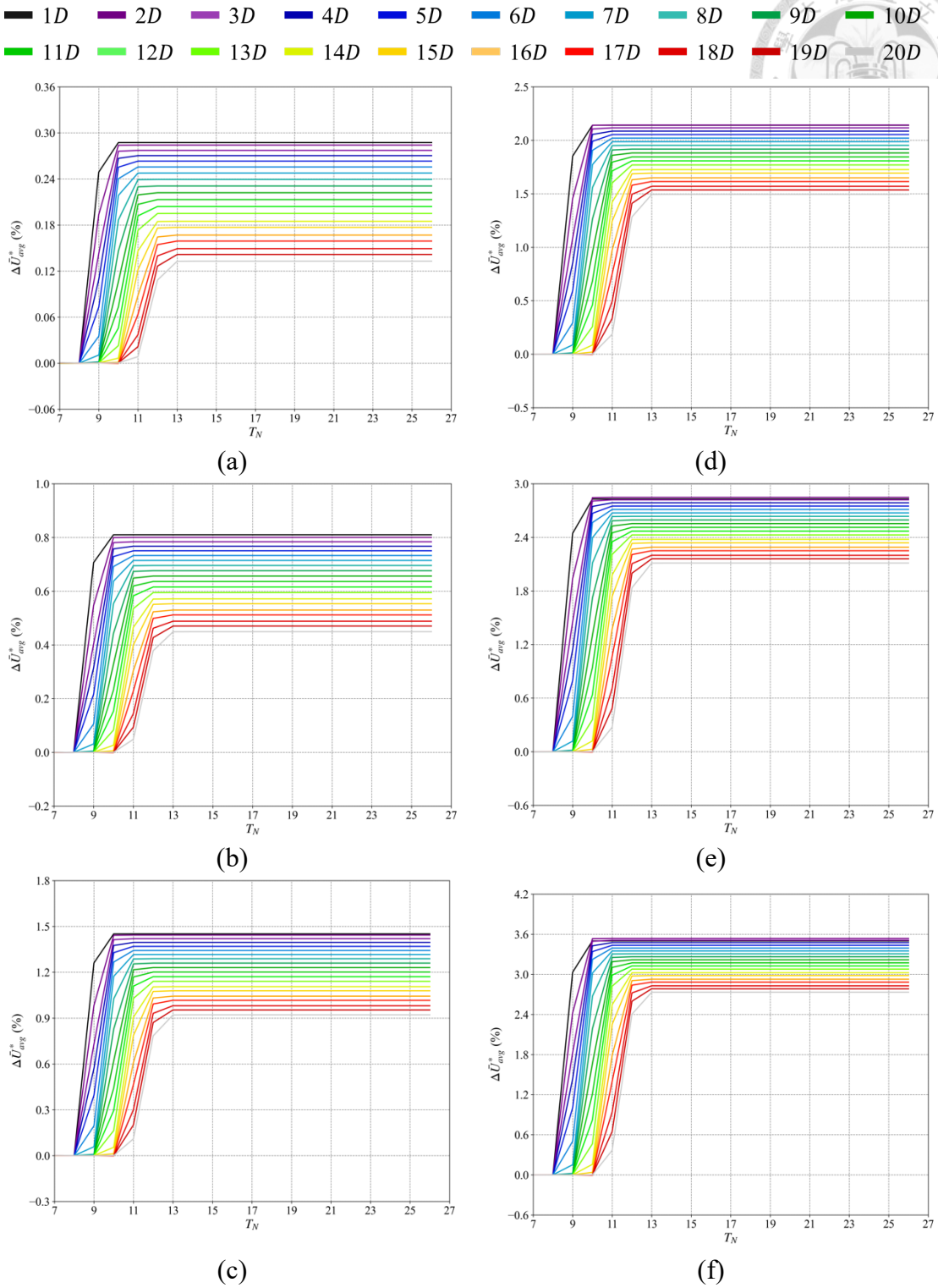

A 17 Evolution of $\Delta\bar{U}^*_{avg}$ over 26 periods under sway motion with $U_{avg} = 15$ m/s and $T_p = 40$ s, for different motion amplitudes: (a) $\zeta_T = 5$ m, (b) $\zeta_T = 10$ m, (c) $\zeta_T = 15$ m, (d) $\zeta_T = 20$ m, (e) $\zeta_T = 25$ m, (f) $\zeta_T = 30$ m

doi:10.6342/NTU202503576

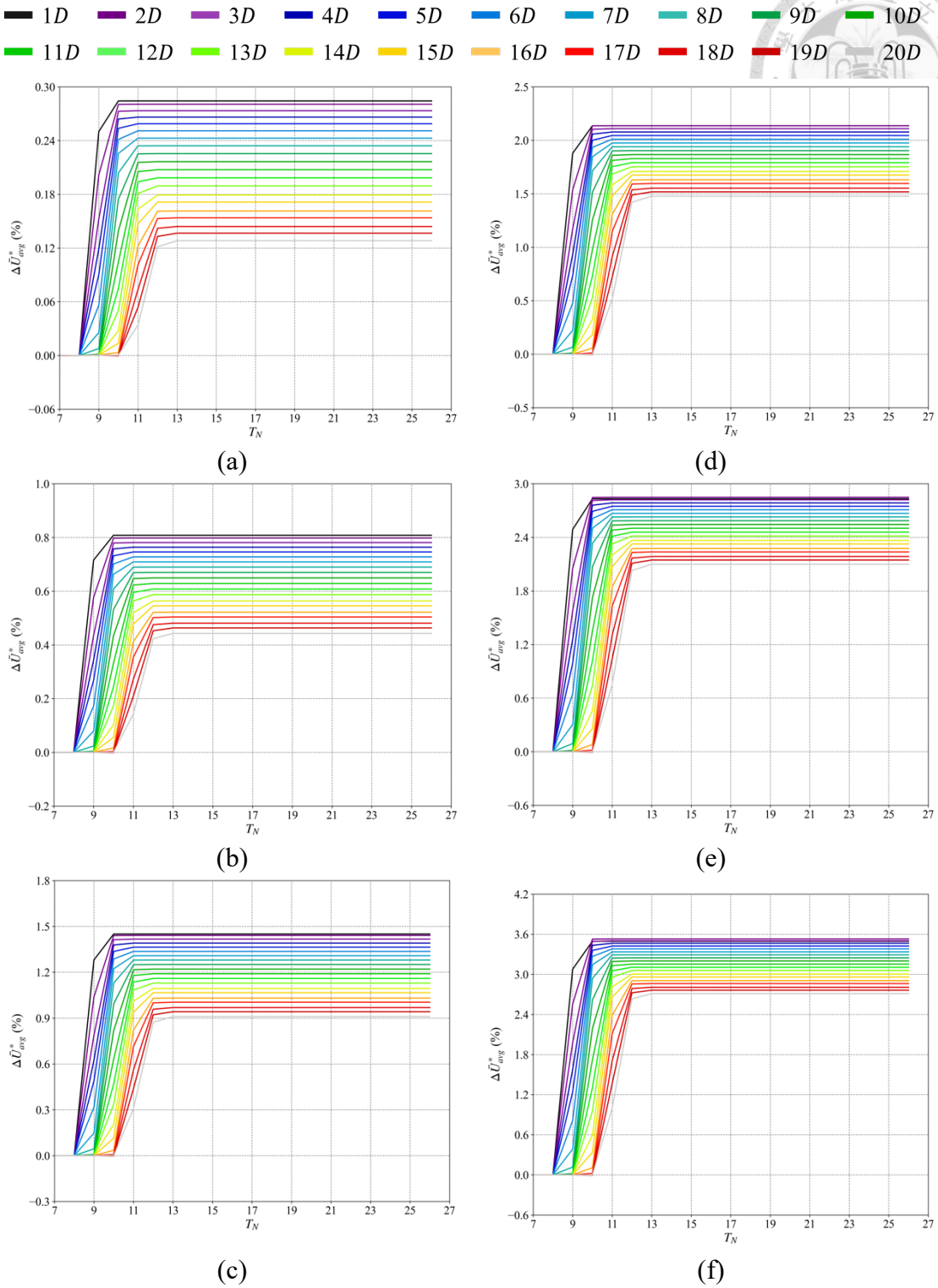

A 18 Evolution of $\Delta\bar{U}^*_{avg}$ over 26 periods under sway motion with $U_{avg} = 15$ m/s and $T_p = 45$ s, for different motion amplitudes: (a) $\zeta_T = 5$ m, (b) $\zeta_T = 10$ m, (c) $\zeta_T = 15$ m, (d) $\zeta_T = 20$ m, (e) $\zeta_T = 25$ m, (f) $\zeta_T = 30$ m

doi:10.6342/NTU202503576

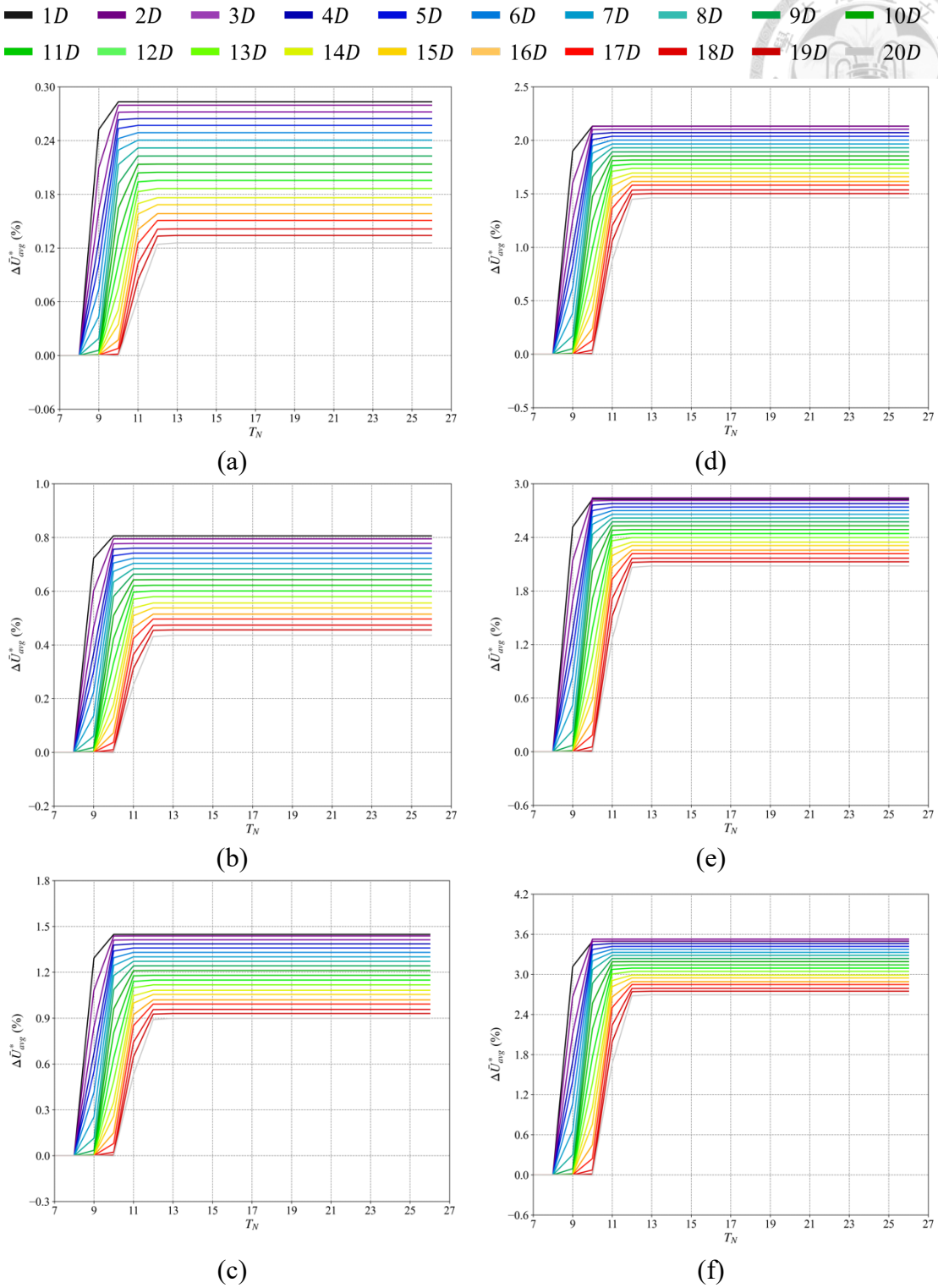

A 19 Evolution of $\Delta\bar{U}^*_{avg}$ over 26 periods under sway motion with $U_{avg} = 15$ m/s and $T_p = 50$ s, for different motion amplitudes: (a) $\zeta_T = 5$ m, (b) $\zeta_T = 10$ m, (c) $\zeta_T = 15$ m, (d) $\zeta_T = 20$ m, (e) $\zeta_T = 25$ m, (f) $\zeta_T = 30$ m

doi:10.6342/NTU202503576

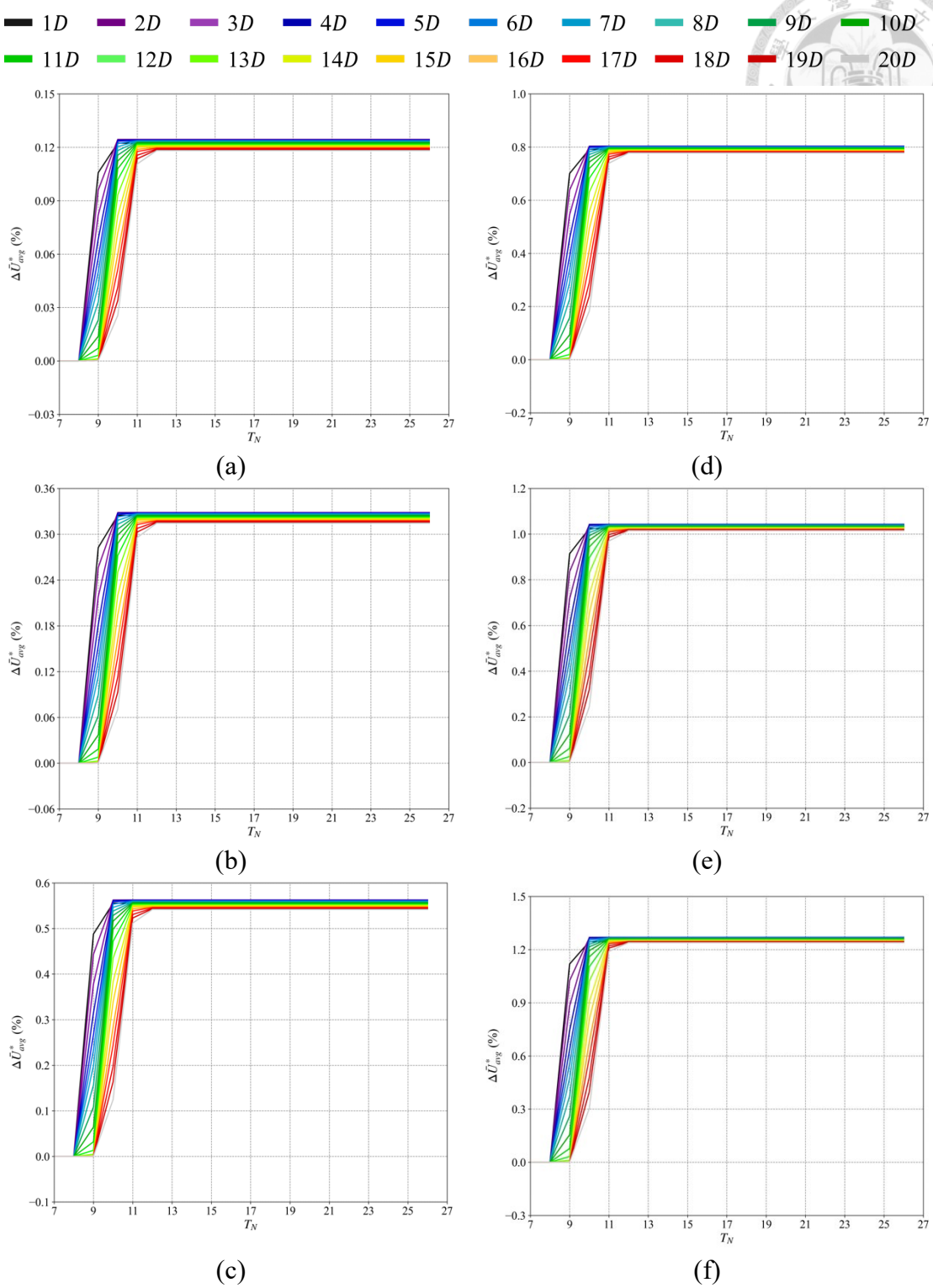

A 20 Evolution of $\Delta\bar{U}^*_{avg}$ over 26 periods under sway motion with $U_{avg} = 21$ m/s and $T_p = 45$ s, for different motion amplitudes: (a) $\zeta_T = 5$ m, (b) $\zeta_T = 10$ m, (c) $\zeta_T = 15$ m, (d) $\zeta_T = 20$ m, (e) $\zeta_T = 25$ m, (f) $\zeta_T = 30$ m

doi:10.6342/NTU202503576

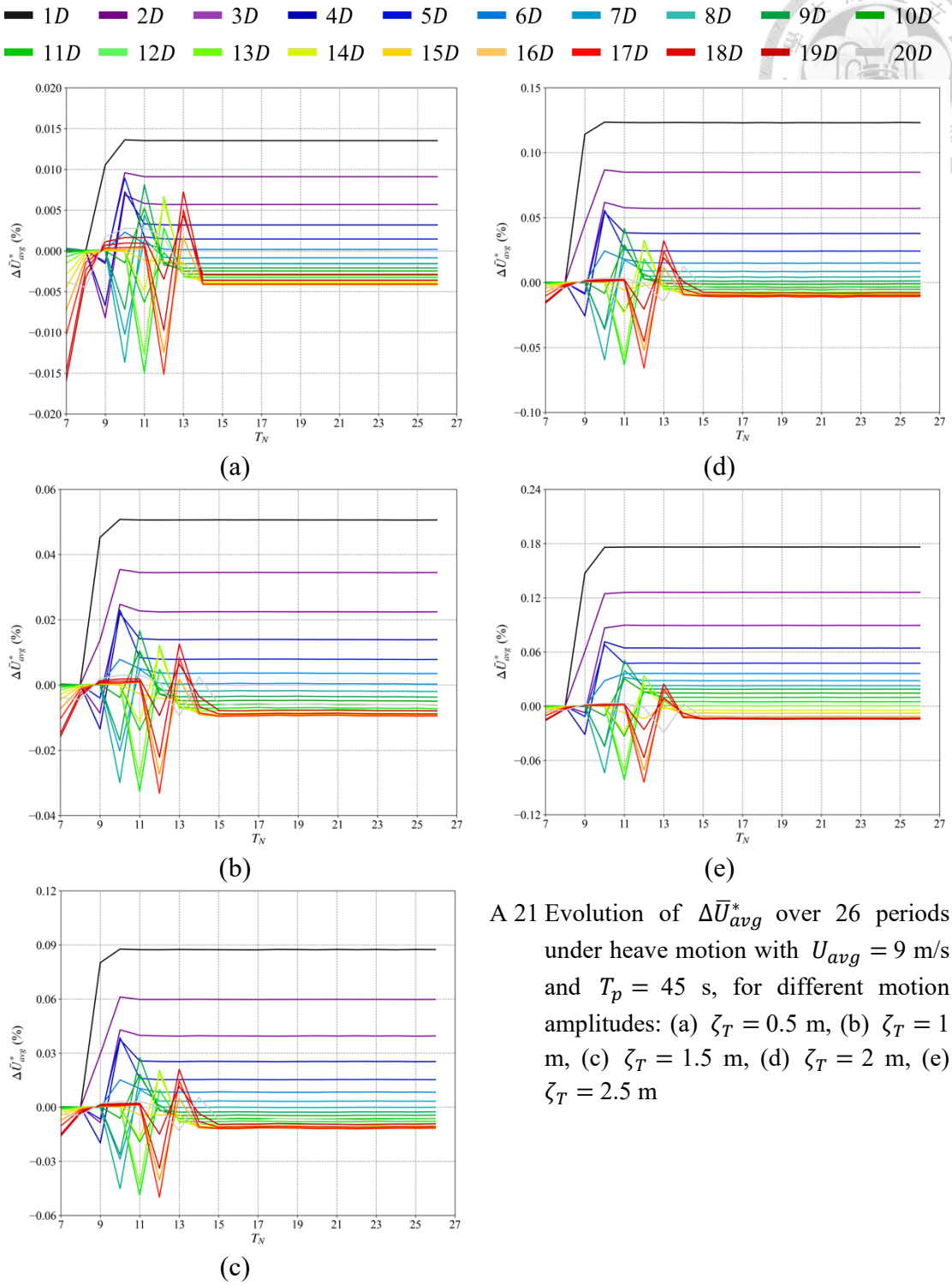

A 21 Evolution of $\Delta\bar{U}^*_{avg}$ over 26 periods under heave motion with $U_{avg} = 9$ m/s and $T_p = 45$ s, for different motion amplitudes: (a) $\zeta_T = 0.5$ m, (b) $\zeta_T = 1$ m, (c) $\zeta_T = 1.5$ m, (d) $\zeta_T = 2$ m, (e) $\zeta_T = 2.5$ m

doi:10.6342/NTU202503576

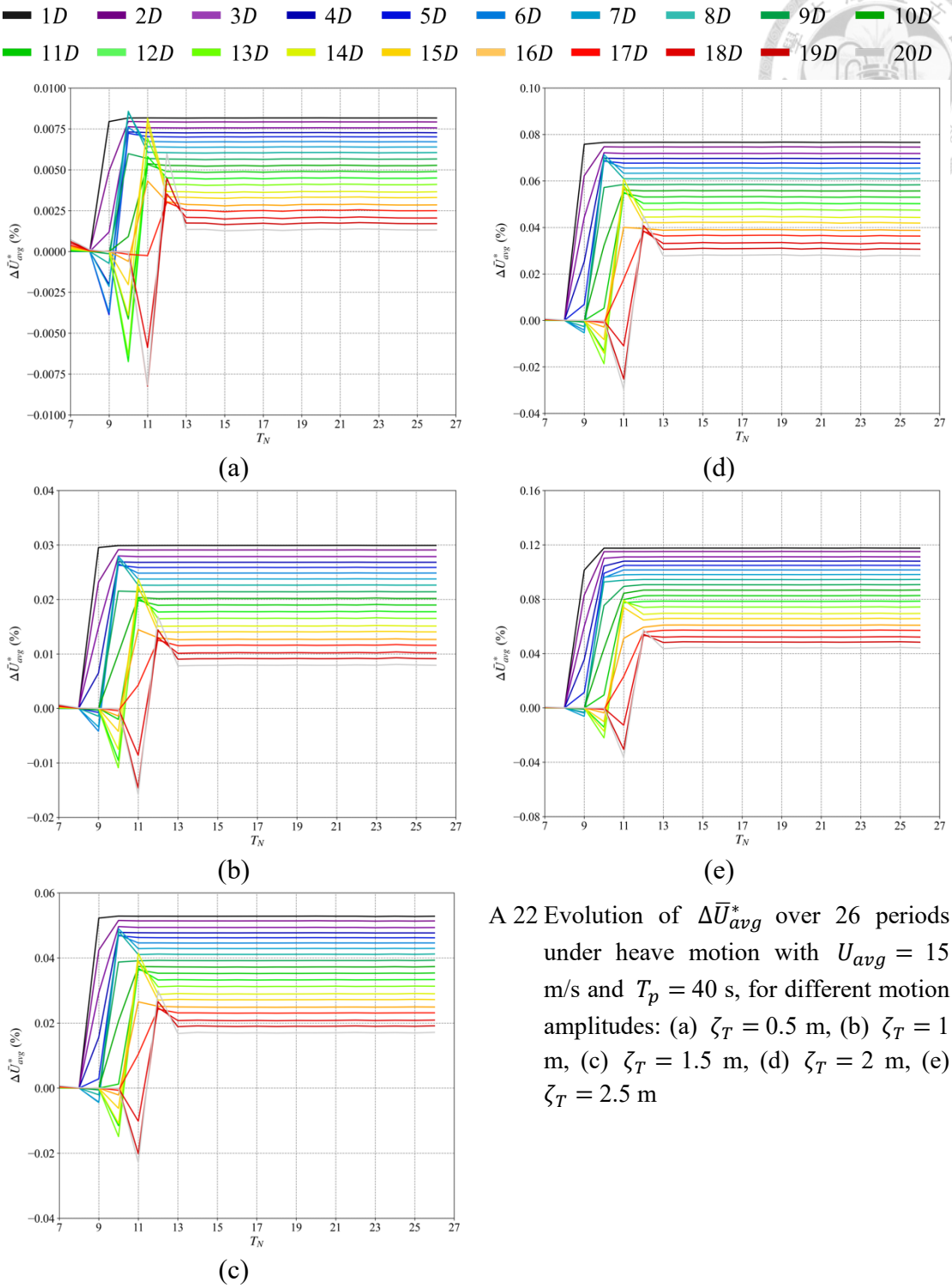

A 22 Evolution of $\Delta\bar{U}^*_{avg}$ over 26 periods under heave motion with $U_{avg} = 15$ m/s and $T_p = 40$ s, for different motion amplitudes: (a) $\zeta_T = 0.5$ m, (b) $\zeta_T = 1$ m, (c) $\zeta_T = 1.5$ m, (d) $\zeta_T = 2$ m, (e) $\zeta_T = 2.5$ m

doi:10.6342/NTU202503576

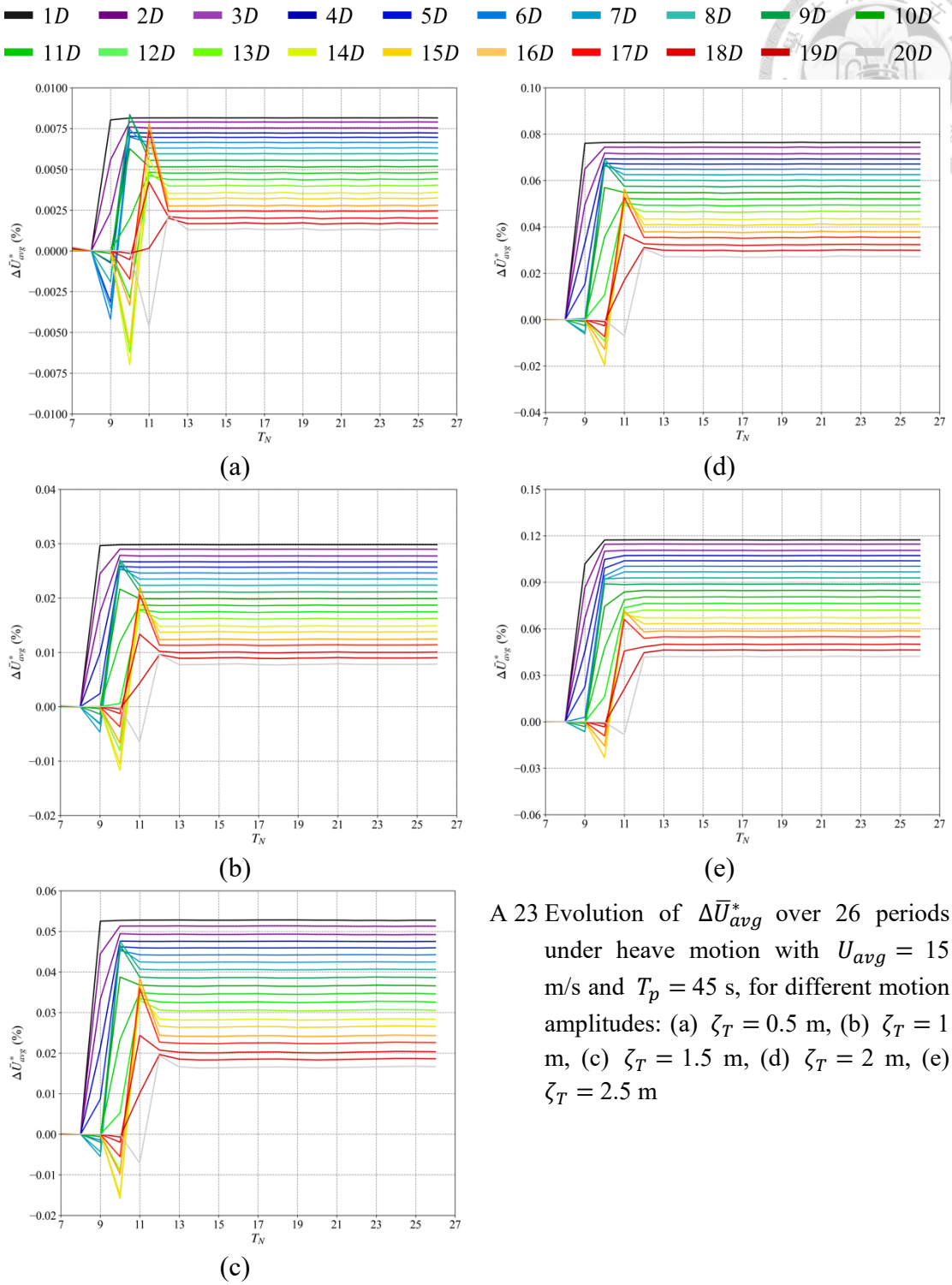

A 23 Evolution of $\Delta\bar{U}^*_{avg}$ over 26 periods under heave motion with $U_{avg} = 15$ m/s and $T_p = 45$ s, for different motion amplitudes: (a) $\zeta_T = 0.5$ m, (b) $\zeta_T = 1$ m, (c) $\zeta_T = 1.5$ m, (d) $\zeta_T = 2$ m, (e) $\zeta_T = 2.5$ m

doi:10.6342/NTU202503576

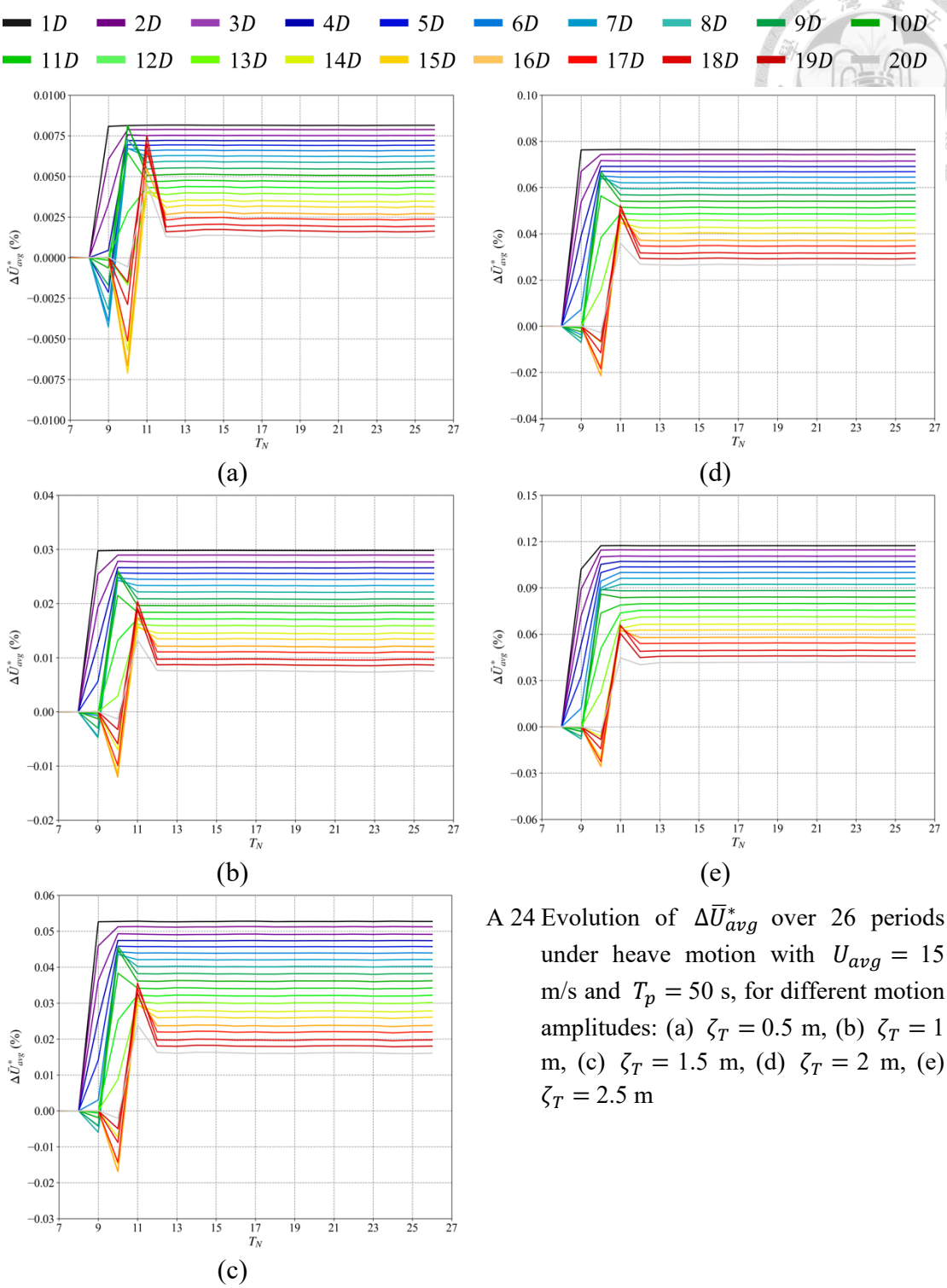

A 24 Evolution of $\Delta\bar{U}^*_{avg}$ over 26 periods under heave motion with $U_{avg} = 15$ m/s and $T_p = 50$ s, for different motion amplitudes: (a) $\zeta_T = 0.5$ m, (b) $\zeta_T = 1$ m, (c) $\zeta_T = 1.5$ m, (d) $\zeta_T = 2$ m, (e) $\zeta_T = 2.5$ m

doi:10.6342/NTU202503576

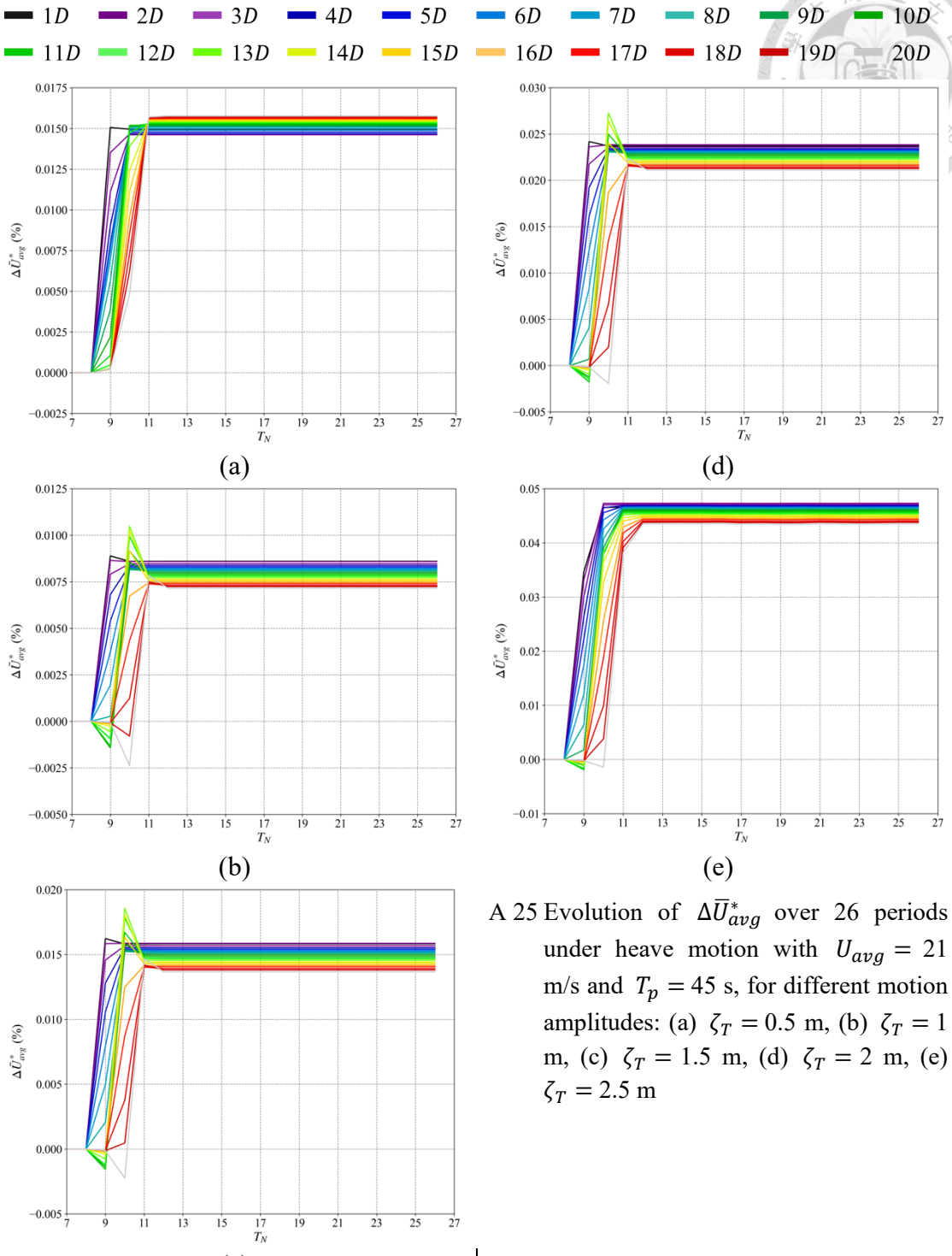

A 25 Evolution of $\Delta\bar{U}^*_{avg}$ over 26 periods under heave motion with $U_{avg} = 21$ m/s and $T_p = 45$ s, for different motion amplitudes: (a) $\zeta_T = 0.5$ m, (b) $\zeta_T = 1$ m, (c) $\zeta_T = 1.5$ m, (d) $\zeta_T = 2$ m, (e) $\zeta_T = 2.5$ m

doi:10.6342/NTU202503576

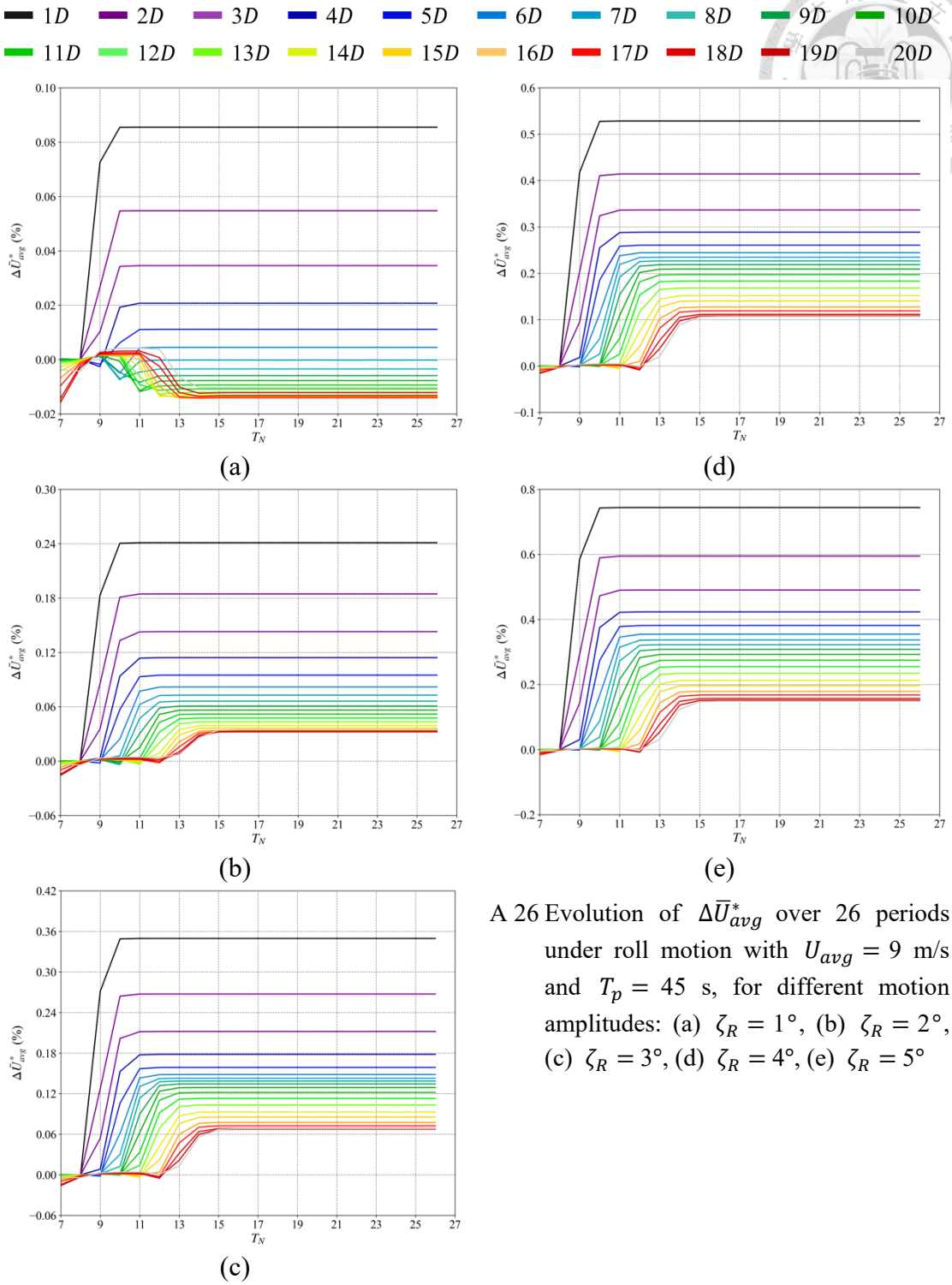

A 26 Evolution of $\Delta\bar{U}^*_{avg}$ over 26 periods under roll motion with $U_{avg} = 9$ m/s and $T_p = 45$ s, for different motion amplitudes: (a) $\zeta_R = 1°$, (b) $\zeta_R = 2°$, (c) $\zeta_R = 3°$, (d) $\zeta_R = 4°$, (e) $\zeta_R = 5°$

doi:10.6342/NTU202503576

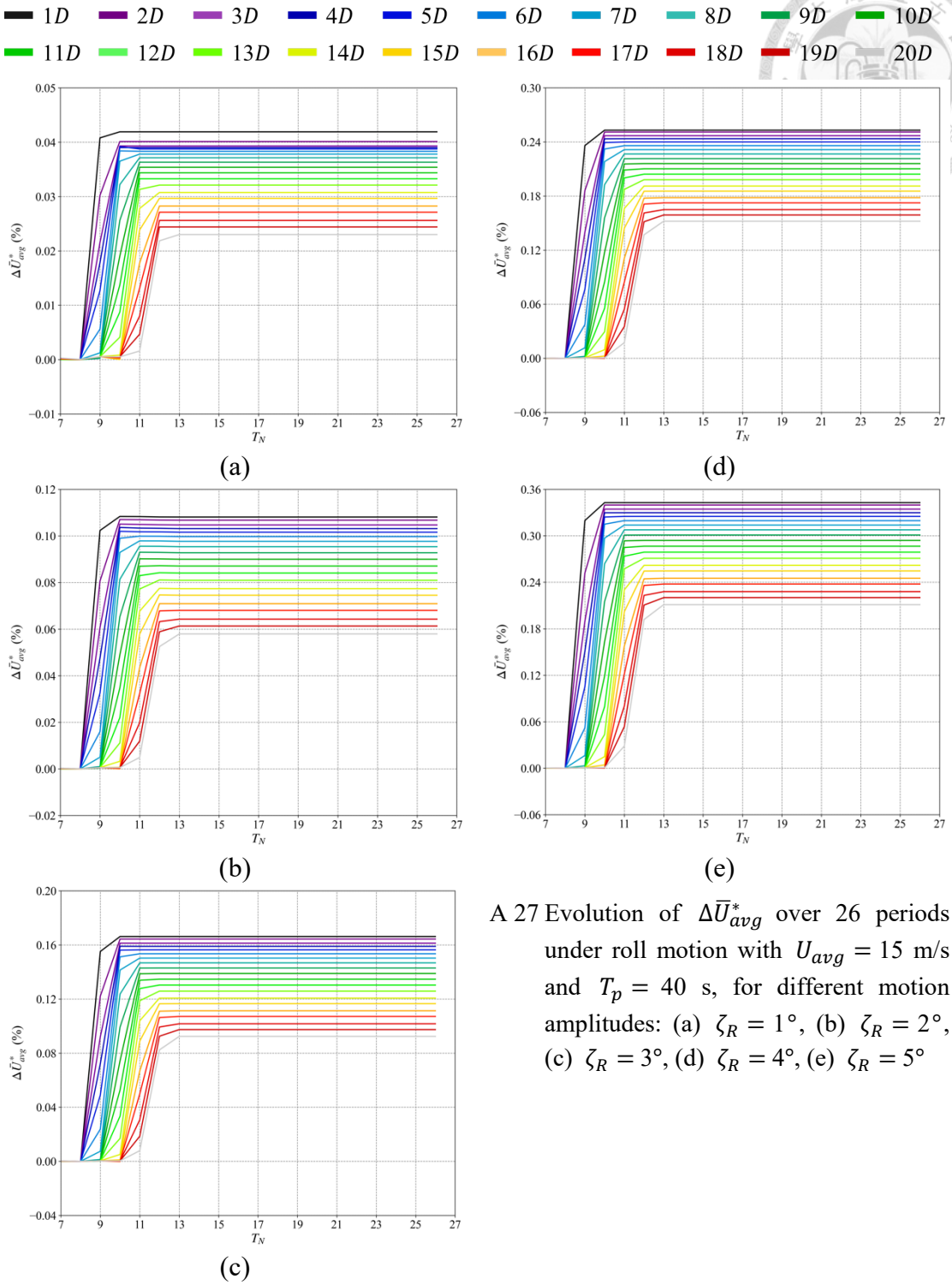

A 27 Evolution of $\Delta\bar{U}^*_{avg}$ over 26 periods under roll motion with $U_{avg} = 15$ m/s and $T_p = 40$ s, for different motion amplitudes: (a) $\zeta_R = 1°$, (b) $\zeta_R = 2°$, (c) $\zeta_R = 3°$, (d) $\zeta_R = 4°$, (e) $\zeta_R = 5°$

doi:10.6342/NTU202503576

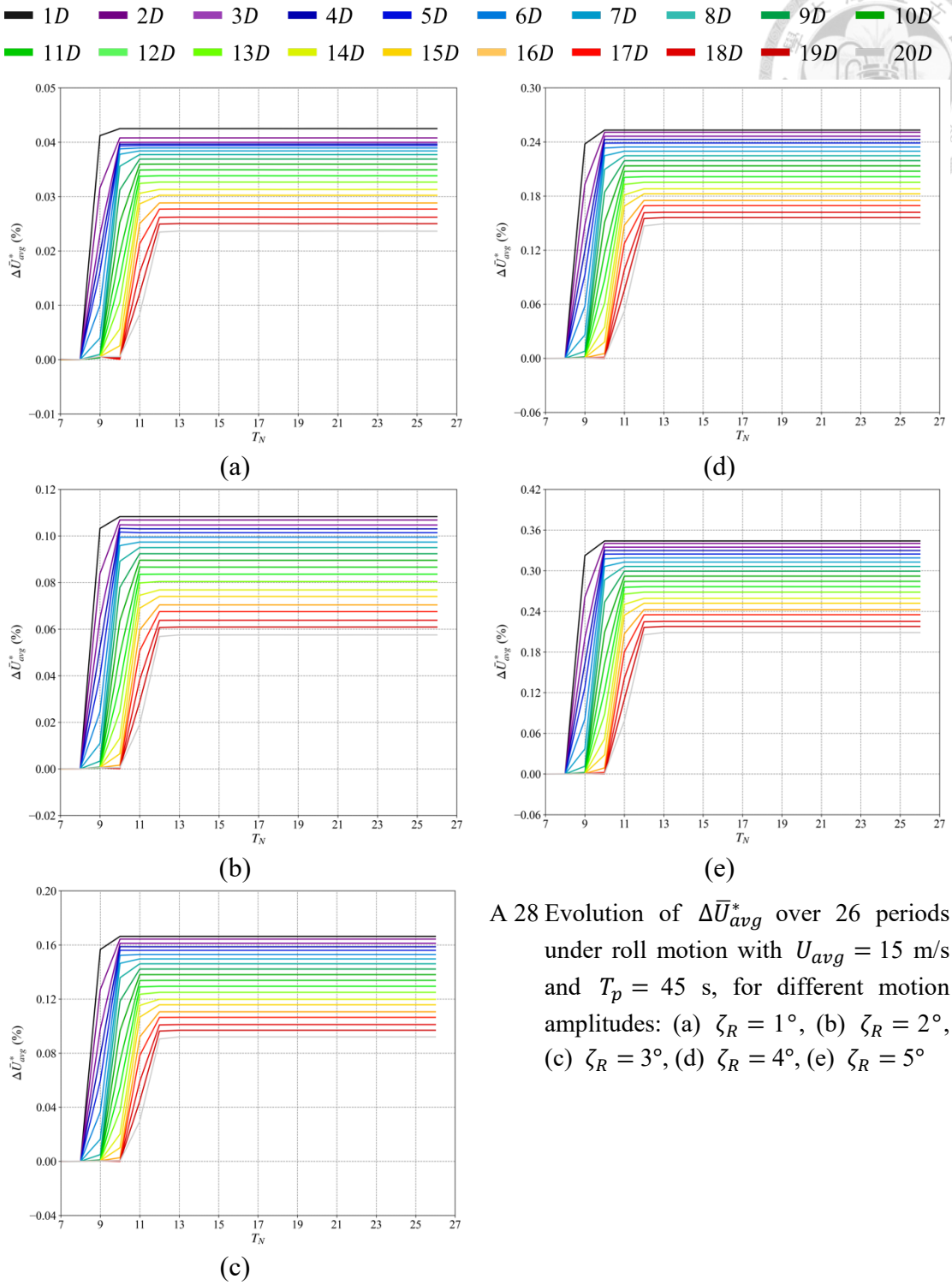

A 28 Evolution of $\Delta\bar{U}^*_{avg}$ over 26 periods under roll motion with $U_{avg} = 15$ m/s and $T_p = 45$ s, for different motion amplitudes: (a) $\zeta_R = 1°$, (b) $\zeta_R = 2°$, (c) $\zeta_R = 3°$, (d) $\zeta_R = 4°$, (e) $\zeta_R = 5°$

doi:10.6342/NTU202503576

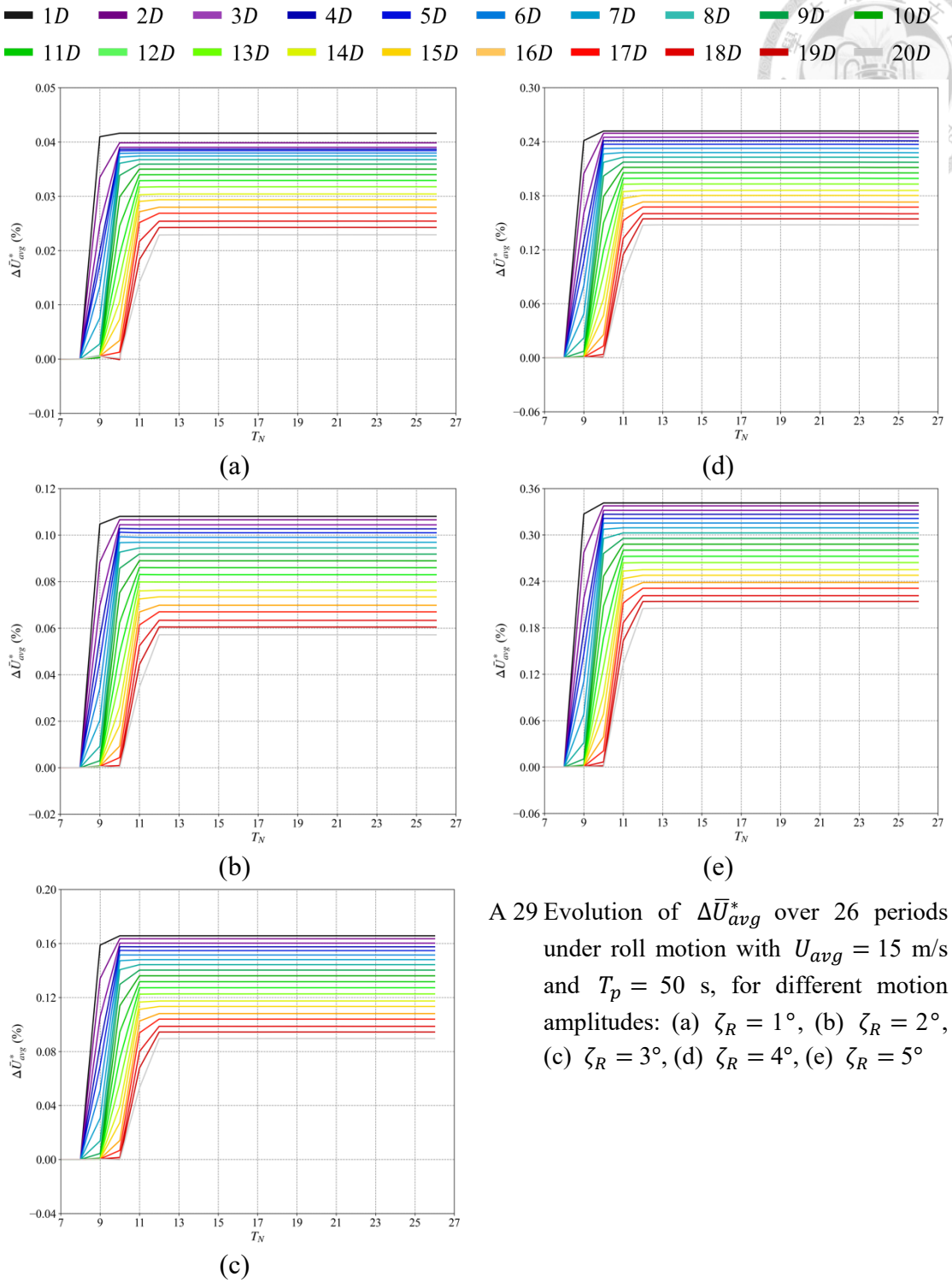

A 29 Evolution of $\Delta\bar{U}^*_{avg}$ over 26 periods under roll motion with $U_{avg} = 15$ m/s and $T_p = 50$ s, for different motion amplitudes: (a) $\zeta_R = 1°$, (b) $\zeta_R = 2°$, (c) $\zeta_R = 3°$, (d) $\zeta_R = 4°$, (e) $\zeta_R = 5°$

doi:10.6342/NTU202503576

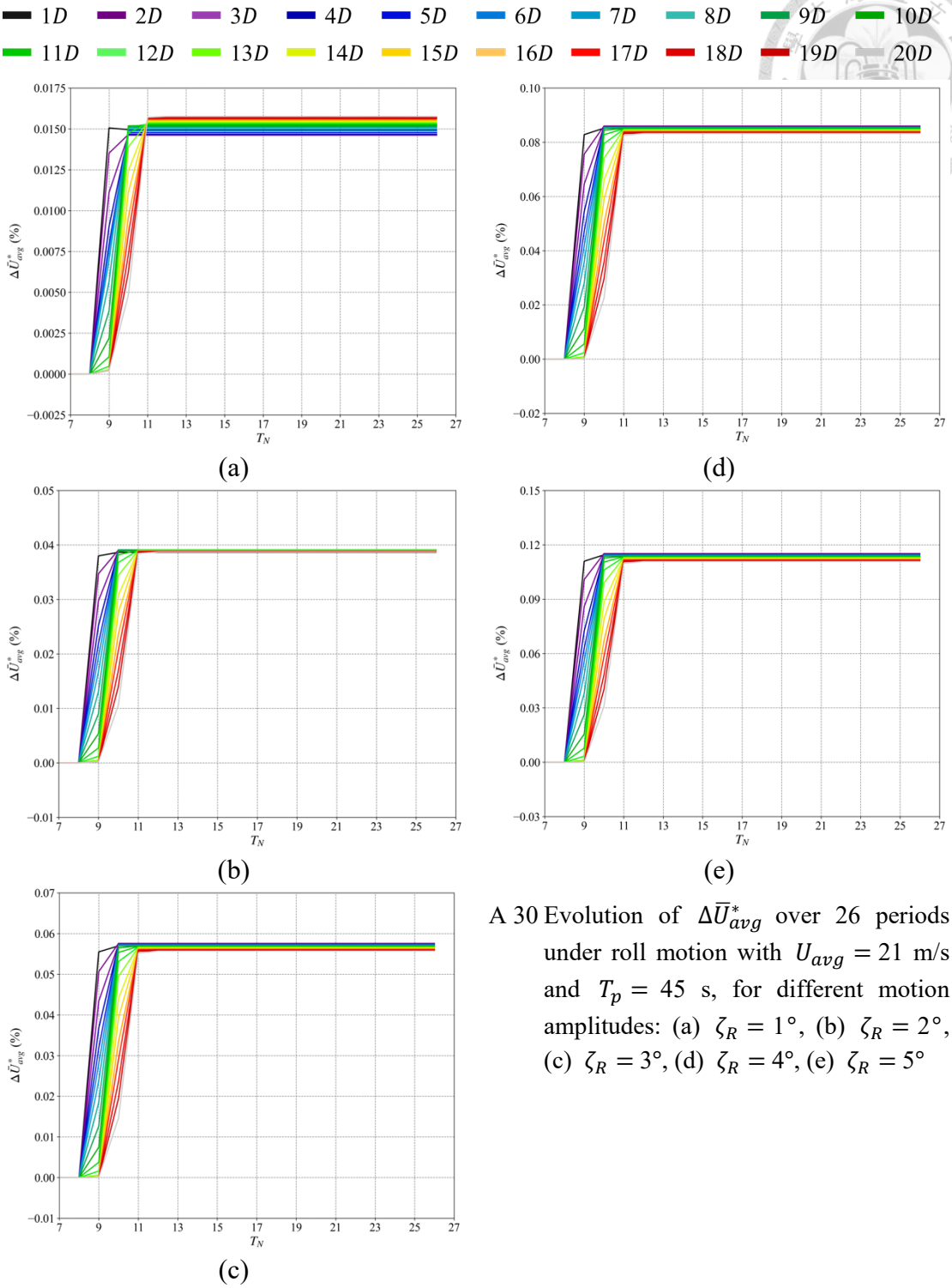

A 30 Evolution of $\Delta\bar{U}^*_{avg}$ over 26 periods under roll motion with $U_{avg} = 21$ m/s and $T_p = 45$ s, for different motion amplitudes: (a) $\zeta_R = 1°$, (b) $\zeta_R = 2°$, (c) $\zeta_R = 3°$, (d) $\zeta_R = 4°$, (e) $\zeta_R = 5°$

doi:10.6342/NTU202503576

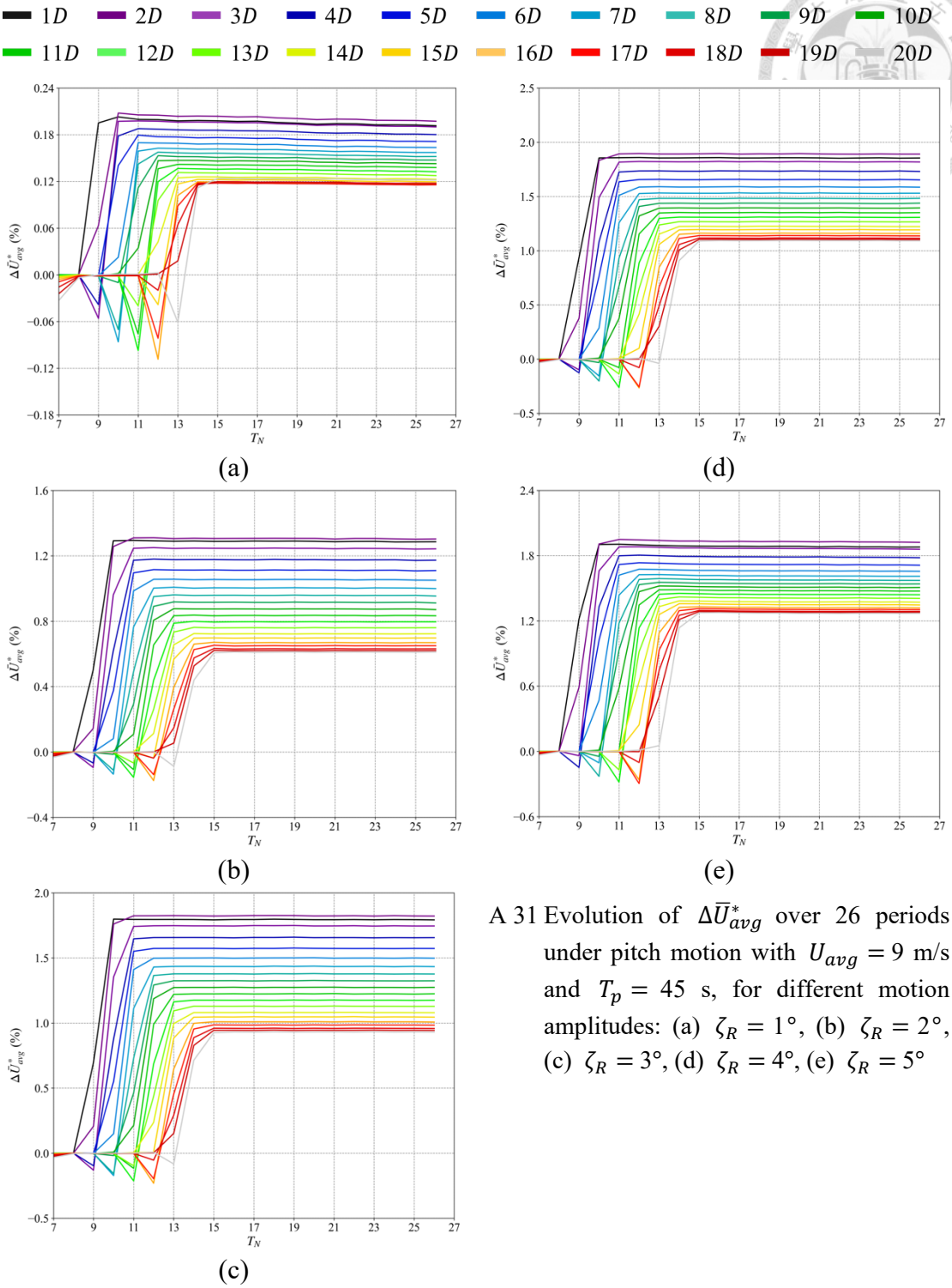

A 31 Evolution of $\Delta\bar{U}^*_{avg}$ over 26 periods under pitch motion with $U_{avg} = 9$ m/s and $T_p = 45$ s, for different motion amplitudes: (a) $\zeta_R = 1°$, (b) $\zeta_R = 2°$, (c) $\zeta_R = 3°$, (d) $\zeta_R = 4°$, (e) $\zeta_R = 5°$

doi:10.6342/NTU202503576

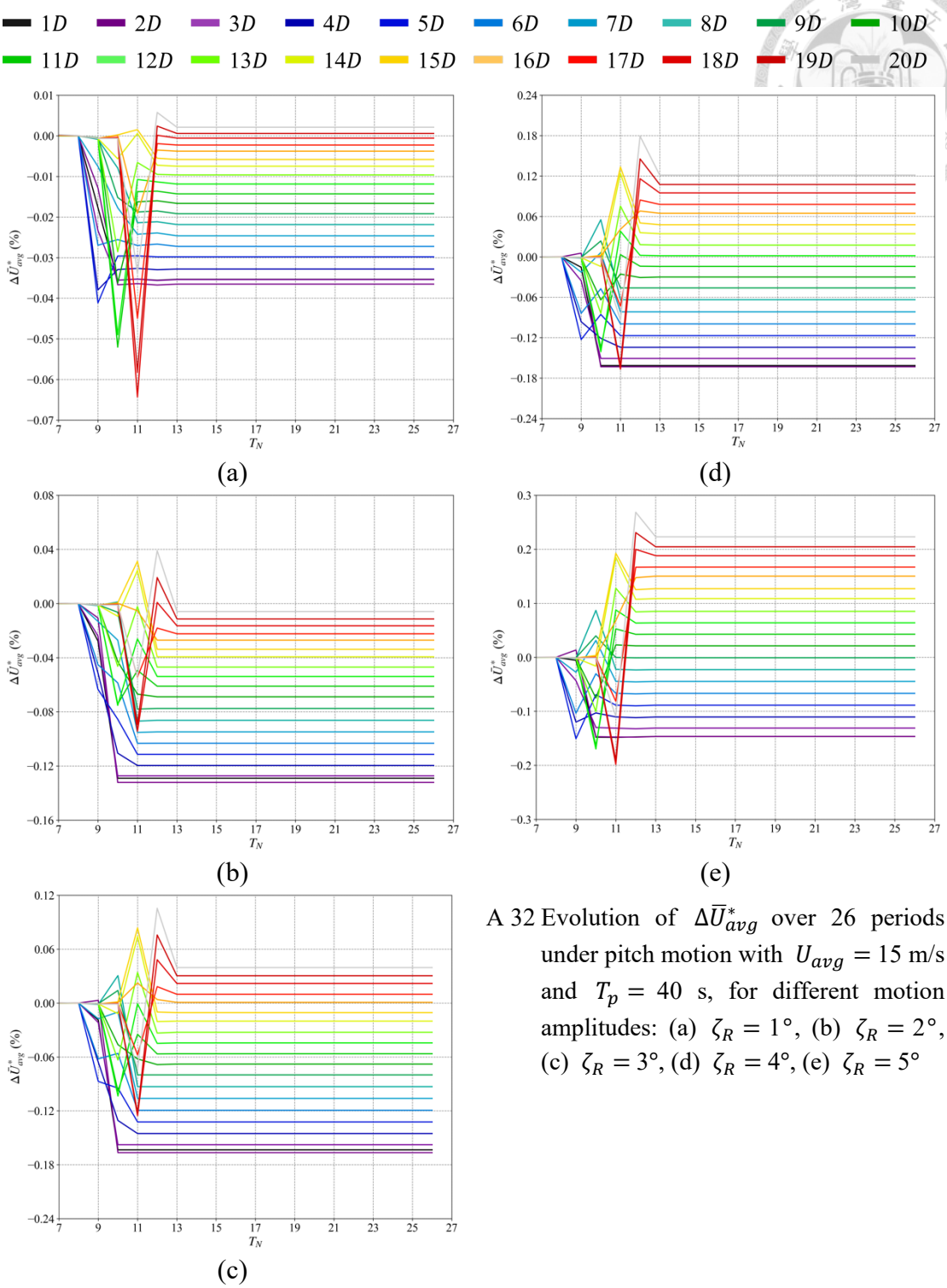

A 32 Evolution of $\Delta\bar{U}^*_{avg}$ over 26 periods under pitch motion with $U_{avg} = 15$ m/s and $T_p = 40$ s, for different motion amplitudes: (a) $\zeta_R = 1°$, (b) $\zeta_R = 2°$, (c) $\zeta_R = 3°$, (d) $\zeta_R = 4°$, (e) $\zeta_R = 5°$

doi:10.6342/NTU202503576

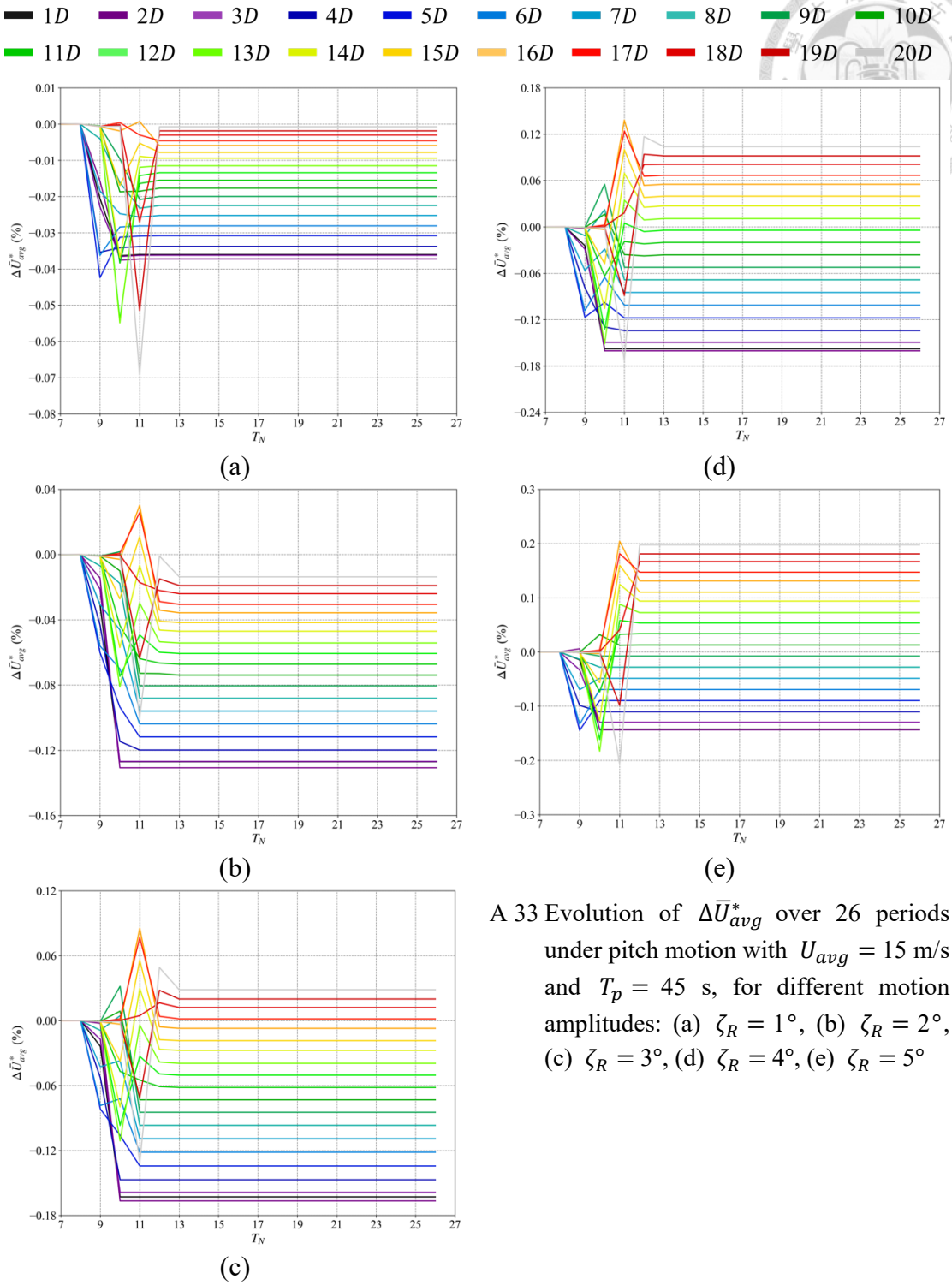

A 33 Evolution of $\Delta\bar{U}^*_{avg}$ over 26 periods under pitch motion with $U_{avg} = 15$ m/s and $T_p = 45$ s, for different motion amplitudes: (a) $\zeta_R = 1°$, (b) $\zeta_R = 2°$, (c) $\zeta_R = 3°$, (d) $\zeta_R = 4°$, (e) $\zeta_R = 5°$

doi:10.6342/NTU202503576

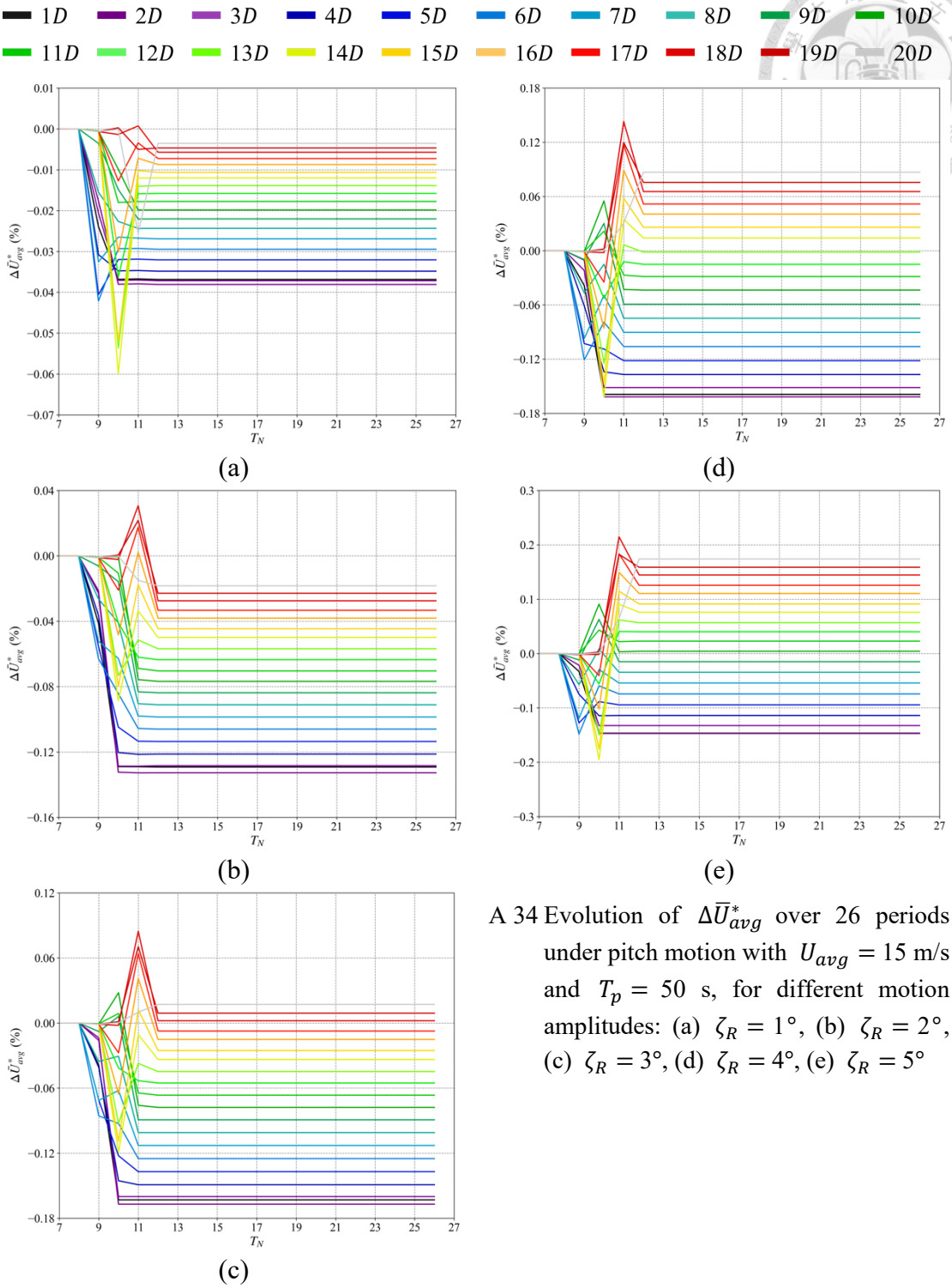

A 34 Evolution of $\Delta\bar{U}^*_{avg}$ over 26 periods under pitch motion with $U_{avg} = 15$ m/s and $T_p = 50$ s, for different motion amplitudes: (a) $\zeta_R = 1°$, (b) $\zeta_R = 2°$, (c) $\zeta_R = 3°$, (d) $\zeta_R = 4°$, (e) $\zeta_R = 5°$

doi:10.6342/NTU202503576

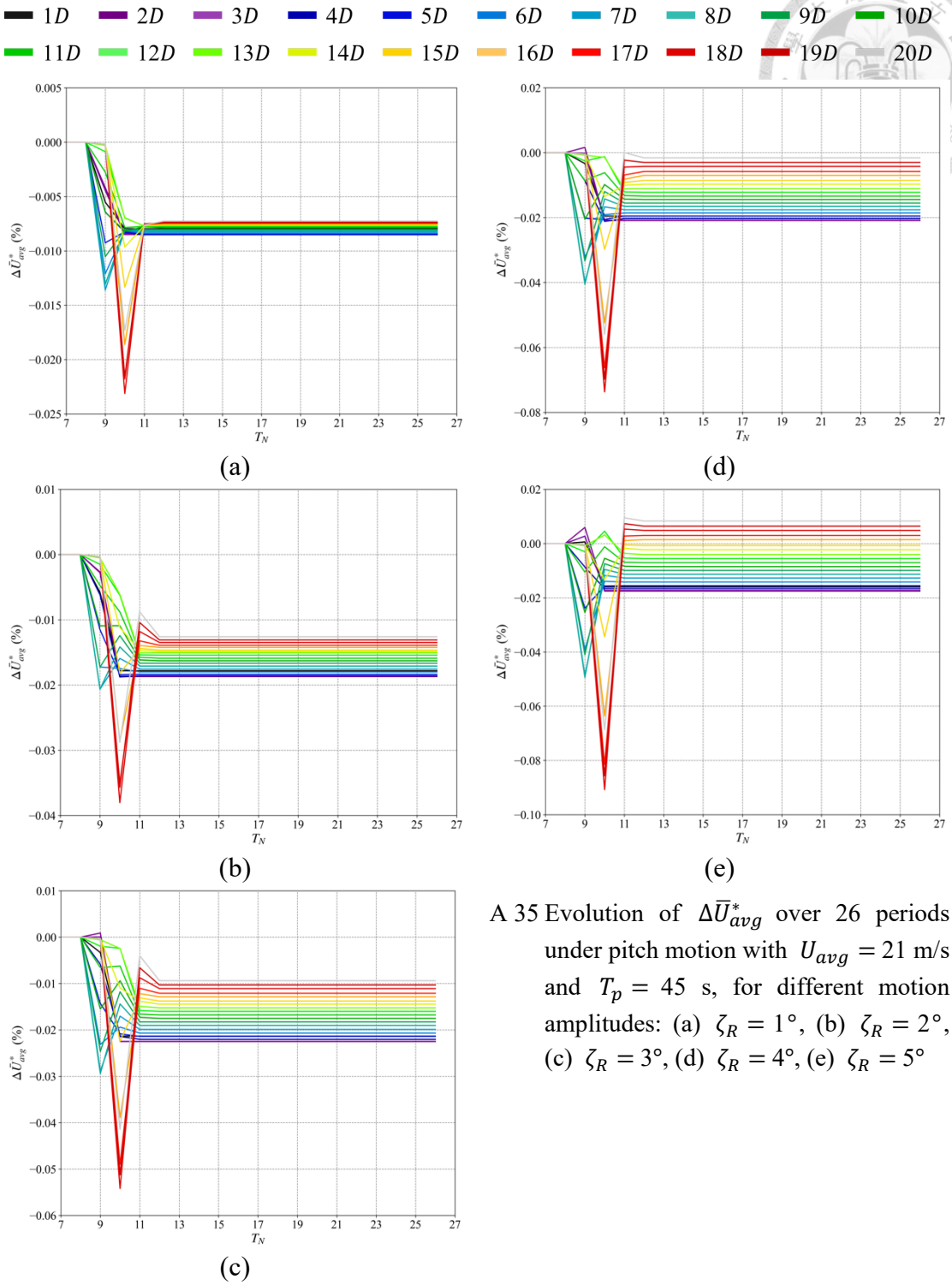

A 35 Evolution of $\Delta\bar{U}^*_{avg}$ over 26 periods under pitch motion with $U_{avg} = 21$ m/s and $T_p = 45$ s, for different motion amplitudes: (a) $\zeta_R = 1°$, (b) $\zeta_R = 2°$, (c) $\zeta_R = 3°$, (d) $\zeta_R = 4°$, (e) $\zeta_R = 5°$

doi:10.6342/NTU202503576

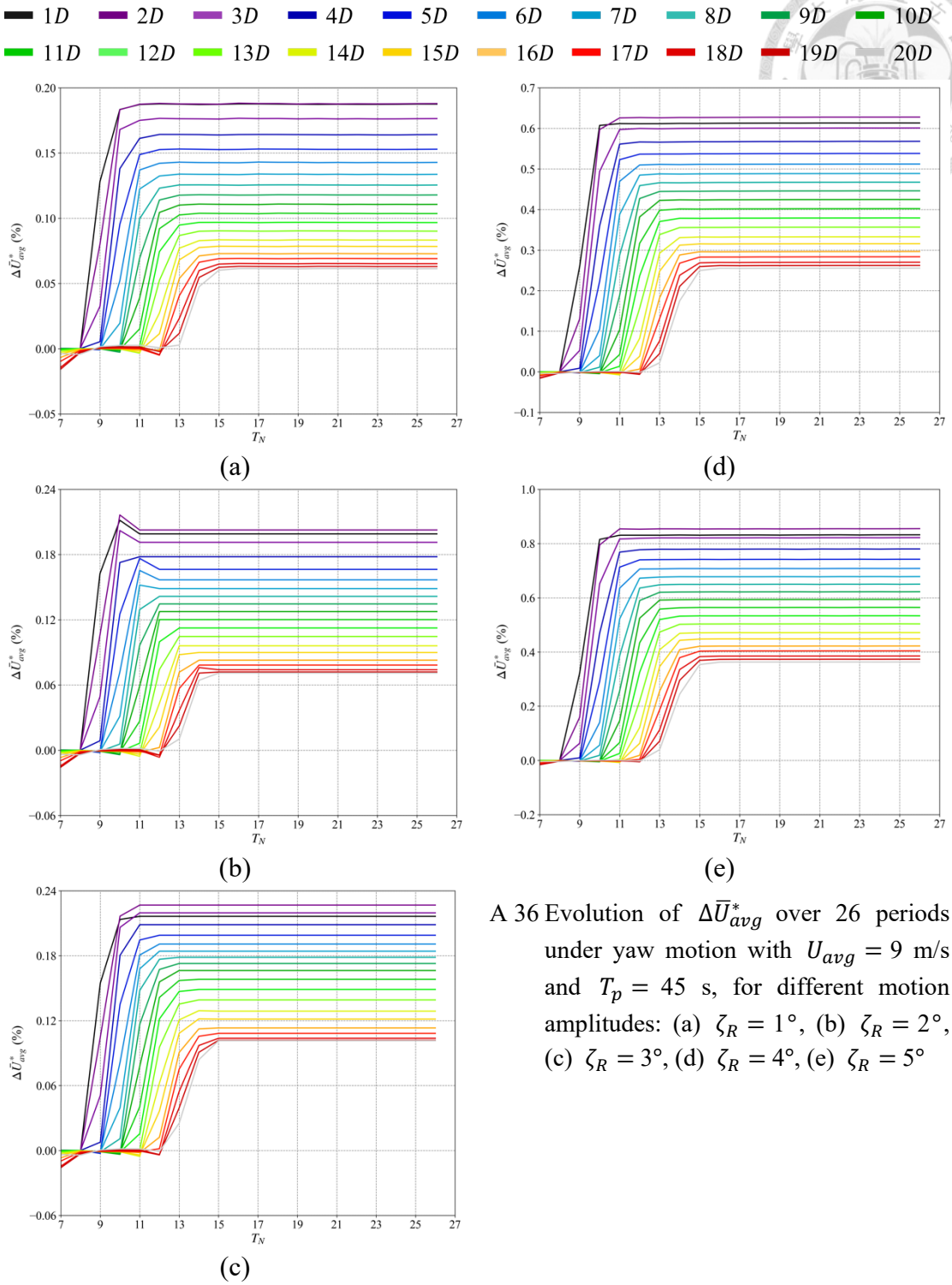

A 36 Evolution of $\Delta\bar{U}^*_{avg}$ over 26 periods under yaw motion with $U_{avg} = 9$ m/s and $T_p = 45$ s, for different motion amplitudes: (a) $\zeta_R = 1°$, (b) $\zeta_R = 2°$, (c) $\zeta_R = 3°$, (d) $\zeta_R = 4°$, (e) $\zeta_R = 5°$

doi:10.6342/NTU202503576

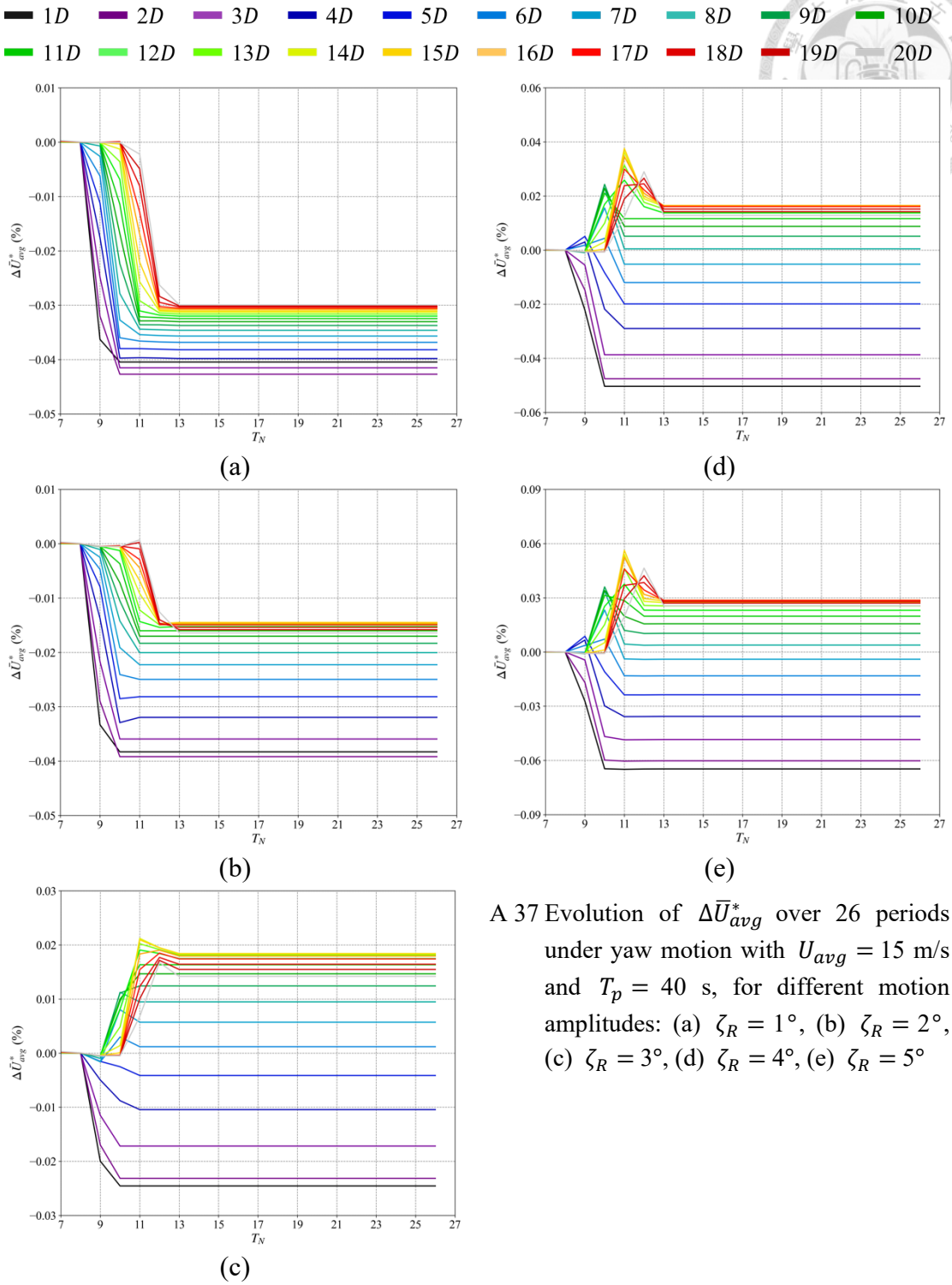

A 37 Evolution of $\Delta\bar{U}^*_{avg}$ over 26 periods under yaw motion with $U_{avg} = 15$ m/s and $T_p = 40$ s, for different motion amplitudes: (a) $\zeta_R = 1°$, (b) $\zeta_R = 2°$, (c) $\zeta_R = 3°$, (d) $\zeta_R = 4°$, (e) $\zeta_R = 5°$

doi:10.6342/NTU202503576

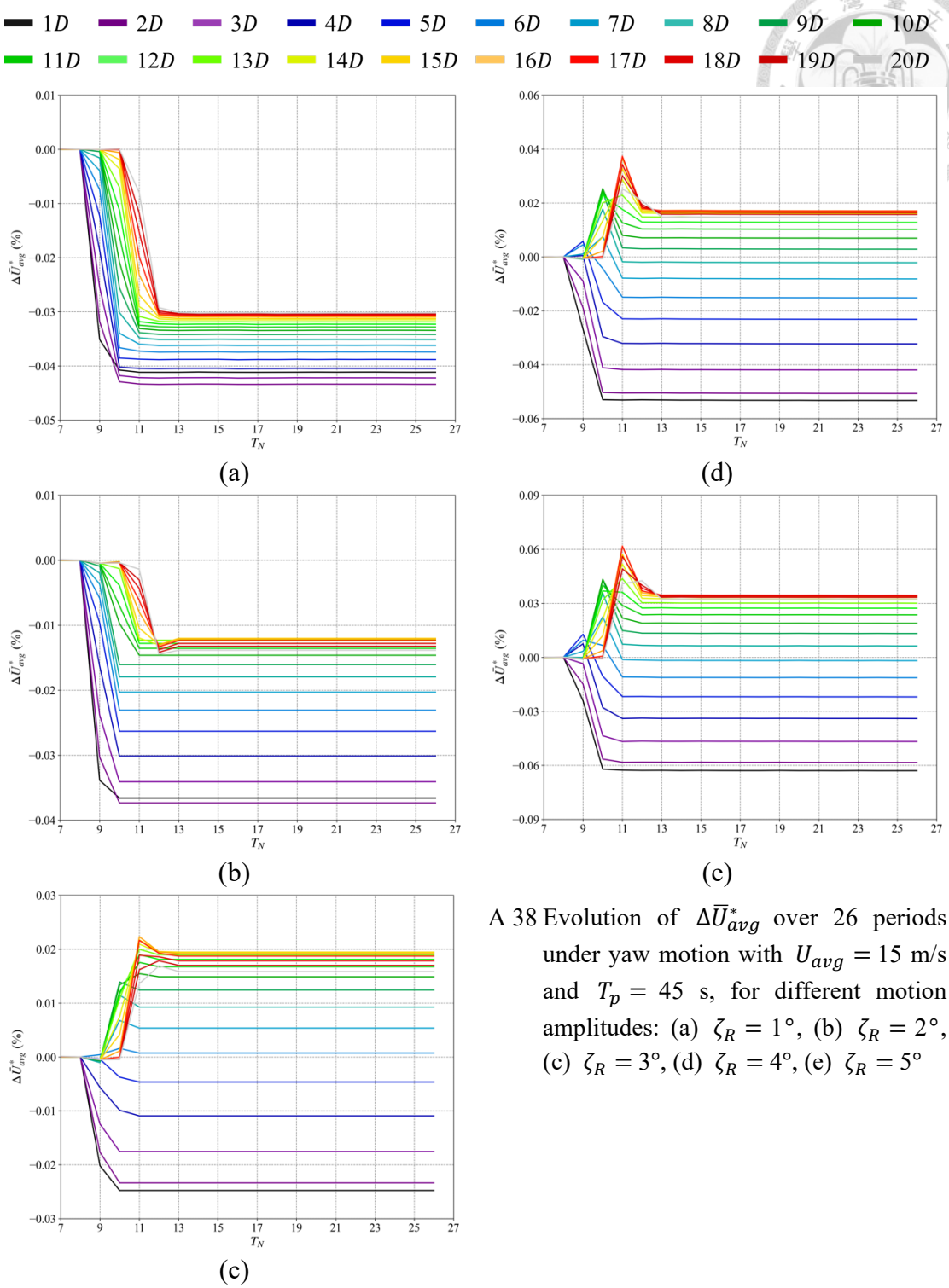

A 38 Evolution of $\Delta\bar{U}^*_{avg}$ over 26 periods under yaw motion with $U_{avg} = 15$ m/s and $T_p = 45$ s, for different motion amplitudes: (a) $\zeta_R = 1°$, (b) $\zeta_R = 2°$, (c) $\zeta_R = 3°$, (d) $\zeta_R = 4°$, (e) $\zeta_R = 5°$

doi:10.6342/NTU202503576

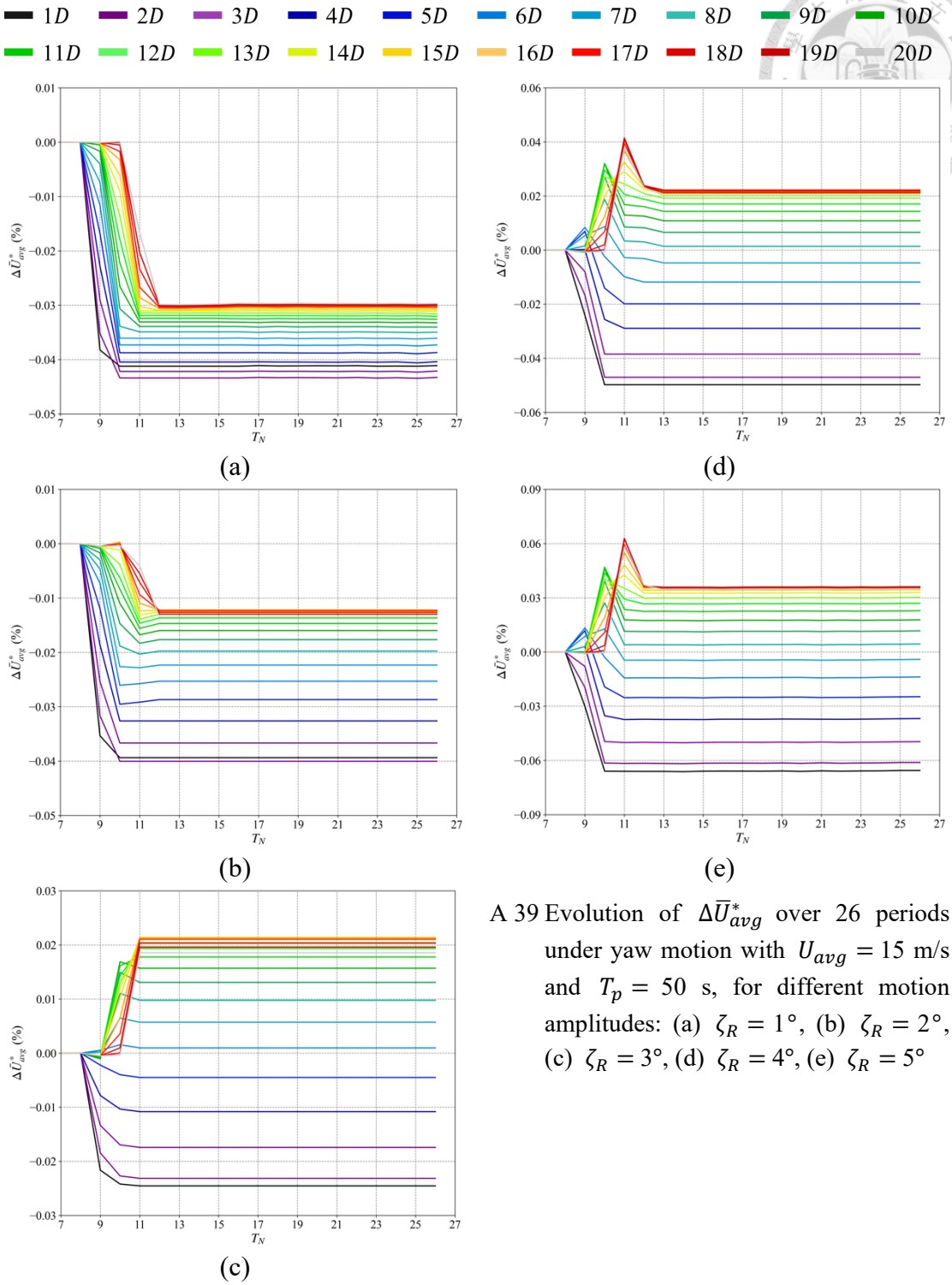

A 39 Evolution of $\Delta\bar{U}^*_{avg}$ over 26 periods under yaw motion with $U_{avg} = 15$ m/s and $T_p = 50$ s, for different motion amplitudes: (a) $\zeta_R = 1°$, (b) $\zeta_R = 2°$, (c) $\zeta_R = 3°$, (d) $\zeta_R = 4°$, (e) $\zeta_R = 5°$

doi:10.6342/NTU202503576

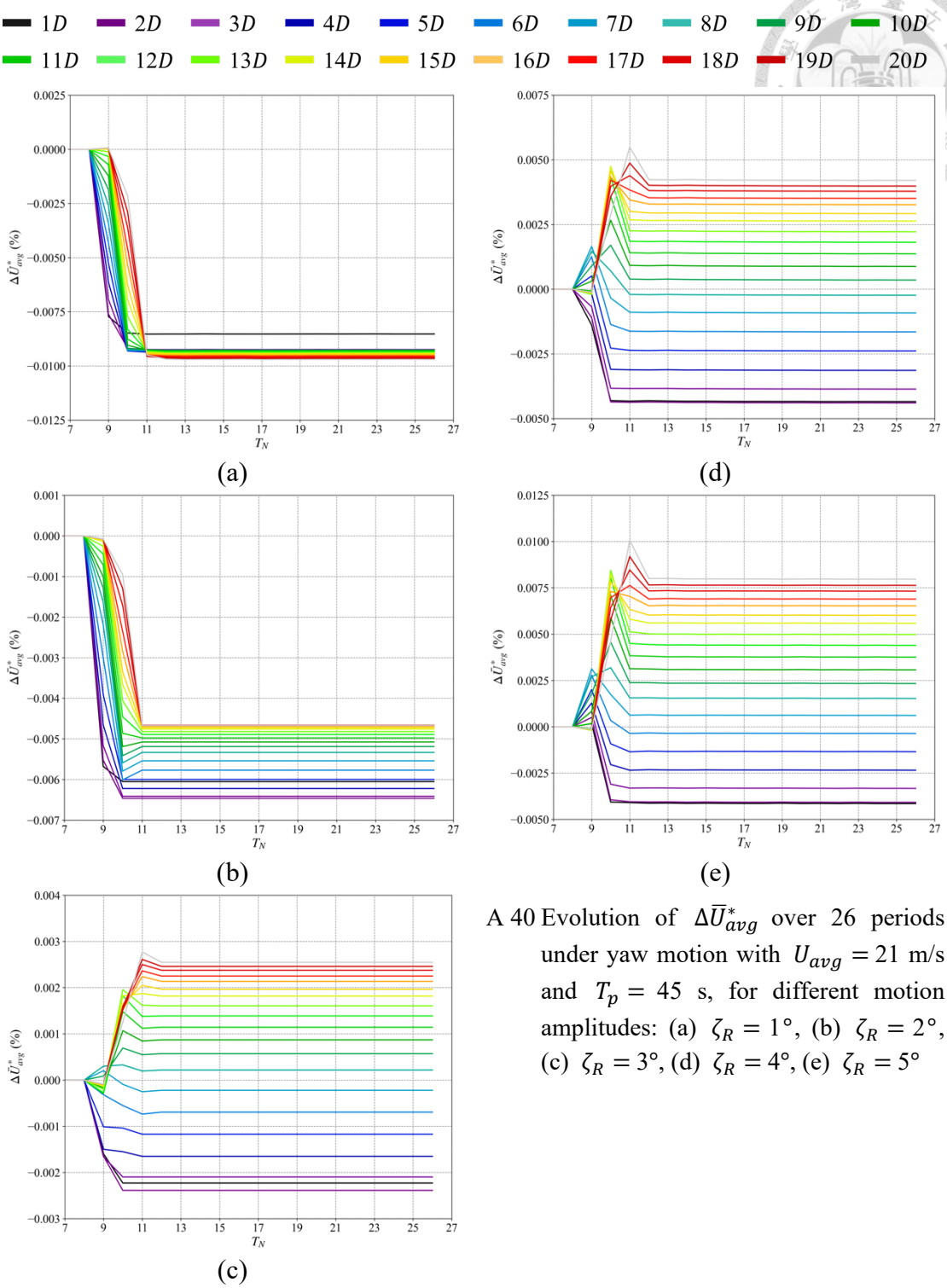

A 40 Evolution of $\Delta\bar{U}^*_{avg}$ over 26 periods under yaw motion with $U_{avg} = 21$ m/s and $T_p = 45$ s, for different motion amplitudes: (a) $\zeta_R = 1°$, (b) $\zeta_R = 2°$, (c) $\zeta_R = 3°$, (d) $\zeta_R = 4°$, (e) $\zeta_R = 5°$

doi:10.6342/NTU202503576